Multi-Octave, CEP-Stable Source for High-Energy Field Synthesis

Ayman Alismail

München 2020

Multi-Octave, CEP-Stable Source for High-Energy Field Synthesis

Ayman Alismail

Dissertation
an der Fakultät für Physik
der Ludwig–Maximilians–Universität
München

vorgelegt von
Ayman Alismail
aus Ushaiqer, Saudi-Arabien

München, den 12 Dezember 2019

Erstgutachter: Prof. Dr. Ferenc Krausz

Zweitgutachter: Prof. Dr. Oleg Pronin

Tag der mündlichen Prüfung: 05 Februar 2020

To my wonderful wife Hayat

"The difference between ordinary and extraordinary is that little extra."

~ Jimmy Johnson

Zusammenfassung

Die Erzeugung hochenergetischer Lichtpulse mit Bandbreiten von mehreren Oktaven ist zur Zeit Gegenstand intensiver Forschung und von großem Interesse für neuartige Anwendungen in der Attosekunden-Spektroskopie sowie im Bereich der kohärenten Kontrolle von Molekülen (Coherent Control). Eine der seit langem bestehenden Herausforderungen auf diesem Gebiet ist die Verfügbarkeit einer phasenstabilen Lichtquelle, welche hochenergetische Pulse mit hoher Durchschnittsleistung und mehreren Oktaven Bandbreite zuverlässig erzeugt. Im Rahmen dieser Arbeit wird ein phasenstabiles Front-End zur Erzeugung von Multioktaven-Lichttransienten entwickelt, welches auf der Yb:YAG Dünnscheibenlaser-Technologie (Thin-Disk Laser) basiert. In diesem Zusammenhang wird die Verstärkung eines zwei Oktaven breiten Spektrums auf 25 μJ Pulsenergie in zwei einstufigen OPCPA-Stufen (Optical Parametric Chirped Pulse Amplification) sowie die Pulskompression auf 18 fs bei 2 μm Wellenlänge (6 fs bei 1 μm Wellenlänge) demonstriert. Durch eine inhärente Kopplung von Seed- und Pumplichtpulsen sowie der beiden Verstärkerkanäle werden die zeitlichen Fluktuationen in diesem Aufbau hauptsächlich durch Langzeitdrifts verursacht, was eine stabile Erzeugung der Lichttransienten ermöglicht. Darüberhinaus wird auch die zeitliche und räumliche Stabilität dieses Synthesizers gezeigt, was die Detektion eines schnell oszillierenden Feldes bei 0.15 PHz in einem 3 ps langen Zeitfenster ermöglicht. Der Synthesizer ist imstande, Lichttransienten mit einer Dauer von weniger als einer Schwingungsperiode zu erzeugen und ist sowohl in der Spitzenleistung als auch in der mittleren Leistung skalierbar.

Als erste Anwendung hierfür wird das Konzept der feldaufgelösten Breitband-Nahinfrarotspektroskopie vorgestellt. Dabei werden Moleküle durch die Femtosekundenpulse im Nahinfrarot (NIR) angeregt und das komplexe elektrische Feld der Molekülantwort mit der Methode des Electro-Optic Sampling (EOS) direkt gemessen. Die oben erwähnten Few-Cycle-Pulse um 2 μm und 1 μm Wellenlänge, die von den OPCPA-Stufen erzeugt werden, werden sowohl für die Anregung als auch für das EOS verwendet. Zur Überprüfung der Anwendbarkeit dieser neuen Technologie wird Wasser in einer Pufferlösung aus Essigsäure verwendet. Hierbei wird das komplexe elektrische Feld der Kombinationsbande der Wassermoleküle bei 1930 nm gemessen. Es ergibt sich bei dieser zeitbereichs-basierten Methode eine Detektionsgenauigkeit, welche mit konventionellen Methoden im Frequenzbereich ver-

gleichbar ist. Durch Verwendung eines Lasersystems mit höheren Wiederholraten kann die Genauigkeit nochmals erheblich gesteigert werden. Dies ist nach bestem Wissen der erste Nachweis einer komplexen Feldantwort eines Moleküls im Nahinfrarotbereich. Diese neuartige Methode ermöglicht hochauflösende Oberton- und Kombinationsbandenspektroskopie mit einzigartiger Empfindlichkeit und Spezifität über den gesamten Bereich des molekularen Fingerabdrucks.

Abstract

The development of high-energy, multi-octave light transients is currently the subject of intense research driven by emerging applications in attosecond spectroscopy and coherent control. One of the long-standing challenges in this field has been the availability of turn-key, high-power and high-energy multi-octave sources with carrier-envelope phase stability. Here, a phase-stable, multi-octave frontend based on Yb:YAG thin-disk amplifier for a light-transient generation is developed. In this regard, the amplification of a two-octave spectrum to 25 μJ of energy in two single-stage optical parametric chirped-pulse amplifiers and the temporal compression to 18 fs and 6 fs at 2 μm and 1 μm, respectively, is demonstrated. In this scheme, the temporal jitter is dominated only by long-term drift, allowing for a stable light transient generation. This is due to the intrinsic temporal synchronization between the seed and pump pulses, and the two amplification channels. Moreover, the temporal and spatial stability of the synthesizer, allowing for sub-cycle detection of the fast oscillating electric field at 0.15 PHz over a 3 ps time window, is proved. The source is capable of delivering sub-cycle light transients with 3 fs temporal duration. The presented scheme is scalable in peak and average power.

To present a first application, the concept of broadband near-infrared (NIR) field-resolved spectroscopy is introduced. Here, molecules are excited by femtosecond pulses in NIR region and the complex electric field of their response is directly measured via electro-optic sampling (EOS). The previously mentioned few-cycle pulses centered at 2 μm and 1 μm, generated from optical parametric chirped-pulse amplifiers, are utilized for femtosecond excitation and EOS, respectively. Water in a buffer solution of acetic acid is chosen to demonstrate the first proof of principle measurement with the new technique. The complex electric field of the combination band of water molecules at 1930 nm at different molecular concentrations is detected. The detection sensitivity of this time-domain technique being comparable to conventional spectral-domain techniques is exhibited. Utilizing a laser frontend with higher repetition rates, the detection sensitivity can be dramatically improved. To the best of my knowledge, this is the first detection of the complex electric field of the molecular response in NIR spectral range. The novel method holds promise for high-resolution overtone and combination bands spectroscopy and microscopy with unique sensitivity and specificity over the total molecular fingerprint region.

Contents

List of Figures

List of Tables

List of Abbreviations

AOPDF	acousto-optic programmable dispersive filter
AR	anti-reflective
ASE	amplified spontaneous emission
BaF_2	barium fluoride
BBO	beta barium borate
BOC	balanced optical cross-correlation
CEP	carrier-envelope phase
CPA	chirped pulse amplification
CW	continuous wave
DFG	difference-frequency generation
EOS	electro-optic sampling
F_2	flint
FID	free-induction decay
FWHM	full width at half maximum
GD	group delay
GDD	group delay dispersion
HD	high-dispersive
HR	high-reflective
LBO	lithium triborate
MIR	mid-infrared
NIR	near-infrared
NOPA	non-collinear optical parametric amplification
OPA	optical parametric amplification
OPCPA	optical parametric chirped pulse amplification
PC	Pockels cell
PPLN	periodically poled lithium niobate
RMS	root mean square

ROC	radius of curvature
SFG	sum-frequency generation
SH	second-harmonic
SH-FROG	second-harmonic frequency-resolved optical gating
SHG	second-harmonic generation
SISYFOS	Simulation System for Optical Science
SPM	self-phase modulation
TFP	thin-film polarizer
THG	third-harmonic generation
Ti:Sa	titanium-doped sapphire
VIS	visible
XFROG	cross-correlation frequency-resolved optical gating
XPM	cross-phase modulation
XPW	cross-polarized wave
XUV	extreme-ultraviolet
Yb:YAG	ytterbium-doped yttrium aluminum garnet

Chapter 1

Introduction

1.1 Motivation

Controlling, shaping, and measuring the electric field of light at terahertz frequencies opened new possibilities for a variety of applications from fundamental science to real-world applications [1]. Their extension to petahertz frequencies has been enhanced the depth of our insight into microscopic ultrafast dynamics at femtosecond and attosecond time scale. It was the controlling of the slippage of the electric field of light relative to its envelope (carrier-envelope phase (CEP)-stability) that paved the way for isolated attosecond pulse generation [2]. Nowadays, attosecond extreme-ultraviolet (XUV) pulses are generated routinely in laboratories and allow for controlling and observation of electron dynamics [3–7]. Nevertheless, attosecond metrology and spectroscopy has been confined to the employment of low-energy attosecond pulses in the XUV spectral region [8]. Pushing the frontiers of attosecond spectroscopy to new areas like attosecond X-ray diffraction [9] or XUV-pump/XUV-probe spectroscopy [10, 11] to capture the four-dimensional microscopic dynamics of electrons outside the atomic core [12] calls for isolated XUV or X-ray attosecond pulses, with sufficient yield. High-energy light transients hold promise for extending the photon energy of isolated attosecond pulses to a multi-keV regime with a higher photon flux compared to other conventional drivers [13].

1.2 Concept

In recent times, many strategies have been taken into consideration toward generating high-energy light transients. Light transients with tens of microjoules of energy have been generated by spectral shaping, or field synthesis of multi-octave pulses [14–16]. However, increasing their energy to multi-millijoules at several kilohertz repetition rates calls for energy- and power-scalable scheme [17, 18]. Conceptual combination of temporal field synthesis

and optical parametric chirped pulse amplification (OPCPA) holds promise for accessing the desirable light transients, which is proposed and explicated in Ref. [18]. OPCPAs are capable of delivering few-cycle pulses, scalable in energy and power. As a result, a coherent combination of few-cycle pulses from several OPCPA channels allows for the generation of sub-cycle light transients with higher energy and power [17–20].

A proposed waveform synthesizer scheme is shown in Fig. 1.1 [9, 21]. In this approach, the entire spectrum is split into different spectral regions and each region is amplified in an associated OPCPA channel. Here, the spectral phase is compensated for each channel separately. The parallel channels [17, 19, 20] permit superior flexibility concerning dispersion management. Eventually, a coherent combination between all channels results in a synthesized light transient. A relative temporal synchronization between these channels is significantly important to compensate for any time and phase jitters in the precision of the half-cycle of the fields at the synthesis point. Various optical light transients can be generated by adjusting the relative spectral amplitude and the relative phase between the OPCPA arms.

Realizing such a concept requires high-energy lasers to pump and seed several OPCPA chains at different carrier frequencies. Based on this concept, the energy of the light transients was boosted to nearly 1 mJ by employing a 20 mJ, 1 kHz, 150 fs titanium-doped sapphire (Ti:Sa) amplifier [23, 24]. However, boosting the energy and average power of light transients beyond this value calls for a different frontend due to the limitations of simultaneous energy and power scalability in Ti:Sa amplifiers [25]. The ytterbium-doped yttrium aluminum garnet (Yb:YAG) laser sources in geometries of slab or thin-disk are capable of simultaneously providing high-energy and high-power pulses [26–28].

This work reports on the development of an all ytterbium based light field synthesizer for generating high-energy light transients [29, 30]. To the best of my knowledge, this is the first proof of principle prototype allowing simultaneous scaling of the energy and the peak power of light-field synthesizers. Furthermore, the first application of such a source in molecular spectroscopy is demonstrated. In this proof of principle experiment, the complex electric field of the molecular response of water in near-infrared (NIR) spectral region is resolved [31–33]. The setup operates in ambient air, keeping a promise to open new paths in NIR molecular spectroscopy.

The waveform synthesizer's prototype is shown in Fig. 1.2 [9, 21]. The synthesizer consists of: i) an Yb:YAG thin-disk regenerative amplifier, ii) CEP-stable supercontinuum generation module, iii) OPCPA modules for different spectral regions, and iv) coherent combination stage to synthesize the output few-cycle pulses of OPCPA channels [18, 34]. Relative temporal synchronization between: i) the seed and the pump pulses of OPCPA, and ii) different OPCPA channels, is vitally important as it defines the ultimate stability of the synthesized light transients. In the presented system, the stability of the amplified spectrum at each OPCPA channel is assured by the direct generation of the multi-octave

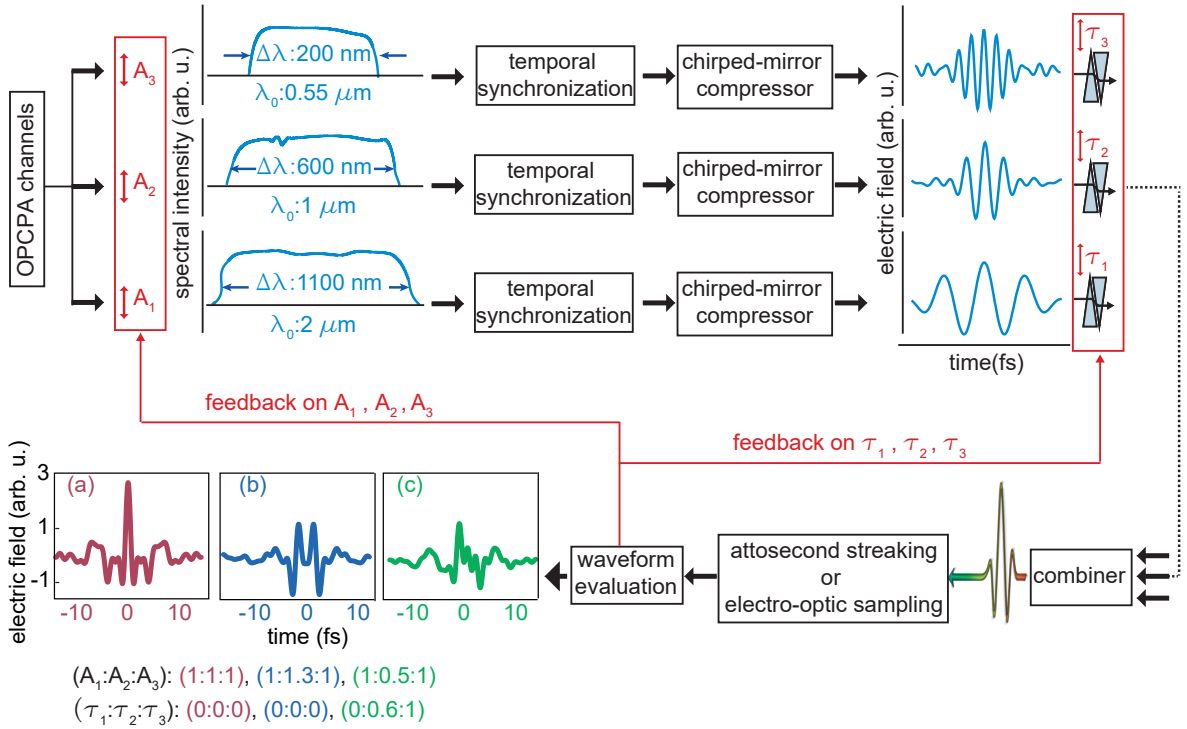

Figure 1.1: Proposed layout of waveform synthesizer for shaping the light transient. It consists of three channels cover the spectral regions of visible, near-infrared, and mid-infrared centered at 550 nm, 1000 nm, and 2000 nm, respectively. After the parametric amplification, each spectrum passes through a delay line to temporally synchronize between the three channels. Subsequently, each spectral region is individually compressed to its Fourier transform-limit by utilizing a chirped mirror compressor. A relative delay can be introduced between the three arms via separately fine-tuning the corresponded pair of glass wedges. Thereafter, two broadband dichroic beam combiners allow spatially combining the three beams. The resultant waveform is evaluated by the method of attosecond streaking [2] or electro-optic sampling [22]. A wide range of light transients can be produced by applying feedback on the relative spectral amplitude (A_1, A_2, A_3) and the relative phase (τ_1, τ_2, τ_3) of each channel to achieve the desired light transient. Three examples of light transients are shown in panels (a), (b), and (c). This figure is adapted from [9].

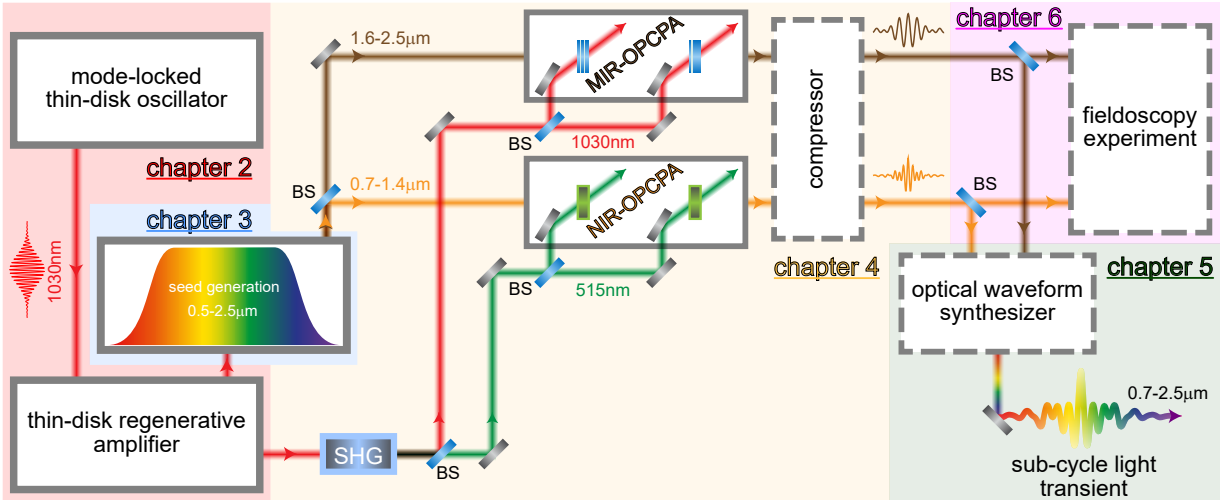

Figure 1.2: Prototype waveform synthesizer based-on optical parametric chirped pulse amplification. The route starts from generating the 2 μJ seed pulses from Yb:YAG thin-disk oscillator. Subsequently, the seed pulses are amplified in the Yb:YAG thin-disk regenerative amplifier to 20 mJ of pulse energy at a repetition rate of 5 kHz. A small portion of this energy is used to directly generate the CEP-stable supercontinuum which then is split into two spectral regions centered at 1000 nm and 2000 nm to seed the near-infrared (NIR) and mid-infrared (MIR) OPCPA channels, respectively. Each spectrum is amplified in the corresponding channel, thereafter, compressed to their Fourier transform-limit. Afterwards, the few-cycle pulses generated from the two channels are coherently combined in the optical waveform synthesizer. The resultant waveform spans from 700 nm to 2500 nm and supports sub-cycle pulses. The shaded areas indicate the outline of this thesis. BS: beam splitter, SHG: second-harmonic generation.

seed spectrum from the pump laser, in addition to the temporal synchronization between the OPCPA channels.

1.3 Thesis outline

The thesis is outlined as following:

Chapter 2: is devoted to the development of the Yb:YAG thin-disk amplifier as the pump source of the light field synthesizer. The amplifier delivers 1 ps pulses with an energy of 20 mJ at a repetition rate of 5 kHz. The chapter prefaces with an overview of Yb:YAG gain medium and its advantages when it is applied to thin-disk geometry. This followed by presenting the generation of the seed pulses, their energy scaling in the regenerative amplifier, and their dispersion management before and after the amplification. Eventually, impacts associated with pulse amplification such as chaotic behavior and gain narrowing is addressed.

Chapter 3: presents the CEP-stable multi-octave seed generation. The chapter begins with some theoretical foundations about nonlinear optics. In the two following sections, the direct seed generation from a home-built, diode-pumped Yb:YAG thin-disk regenerative amplifier is discussed. The generated broadband spectrum spans from 500 nm to 2500 nm. Lastly, an alternative approach with higher optical efficiency to generate few-cycle, microjoule, CEP-stable pulses centered at 2 μm from the Yb:YAG regenerative amplifier is presented. The generated coherent light carries an energy of 5.4 μJ.

Chapter 4: discusses two OPCPA channels of the field synthesizer covering two spectral regions of comparable bandwidth in the mid-infrared (MIR) and NIR with central wavelengths at 2 μm and 1 μm, respectively. The chapter starts with a theoretical background of optical parametric amplification (OPA). The channels are pumped by the Yb:YAG thin-disk regenerative amplifier via its fundamental and frequency-doubled pulses. Afterwards, the parametric amplification of each channel to the total energy of 25 μJ is demonstrated. Eventually, the ability to scale the energy of the few-cycle pulses to millijoule-level is numerically demonstrated.

Chapter 5: addresses the prototype waveform synthesizer based-on OPCPA. Temporal drifts and relative timing fluctuations between the two arms of the synthesizer are discussed. It is shown that the temporal jitter fluctuations are restrained to long-term drifts.

Chapter 6: introduces the concept of NIR field-resolved spectroscopy and presents the proof of principle experiment. This chapter provides a theoretical framework

about the NIR spectroscopy. Besides, I show how this concept allows accessing the information of the intensity and phase of the electric field of light in a single-shot measurement.

Chapter 2

Yb:YAG Thin-Disk Regenerative Amplifier

In the previous chapter, I generally presented the prototype of the high-energy field synthesizer (Fig. 1.2), where its path starts with all-Yb:YAG thin-disk regenerative amplifier as a pump source for high-energy field synthesis. This chapter considers the development of the Yb:YAG thin-disk regenerative amplifier seeded by an Yb:YAG thin-disk Kerr-lens mode-locked oscillator.

The presented work in this chapter is based on the reported results in the two published articles:

- H. Fattahi, A. Alismail, H. Wang, J. Brons, O. Pronin, T. Buberl, L. Vámos, G. Arisholm, A. M. Azzeer, and F. Krausz, "High-power, 1-ps, all-Yb:YAG thin-disk regenerative amplifier," *Optics Letters* **41**(6), pp. 1126—1129, 2016.

- A. Alismail, H. Wang, J. Brons, and H. Fattahi, "20 mJ, 1 ps Yb:YAG thin-disk regenerative amplifier," *Journal of Visualized Experiments: JoVE* (125), 2017.

2.1 Yb:YAG thin-disk

Since the discovery of Peter Moulton in 1986, Ti:Sa crystal has been the workhorse in the generation of femtosecond pulses, which was formerly dominated by dye lasers [18, 35]. Ultrashort pulses with a pulse duration around 6 fs were directly delivered from Ti:Sa Kerr-lens mode-locked oscillator [36, 37]. In general, the crystal is pumped at 532 nm by frequency-doubling of Nd:YAG laser. Nevertheless, the simultaneous scalability of the average and peak power is restricted in this medium. This drawback calls for a new generation of femtosecond lasers, where the gain medium is directly pumped by an efficient

laser source. In the following, I treat the Yb:YAG gain medium that is utilized in the frontend lasers and I address its use in thin-disk geometry.

2.1.1 Yb:YAG gain medium

Ytterbium-doped materials are capable of delivering picosecond laser pulses with high average power and high-energy in comparison to a wide variety of laser media. Consequently, they are superior pump sources for OPCPA. The introduction of ytterbium-doped lasers in different geometries are about to change the current state of the field [18, 38–43]. Yb:YAG is a quasi-three-level laser with long upper-state lifetime and it has good thermal conductivity. It can be pumped by cost-effective diode lasers. Additionally, the quantum defect is considerably low, which is a great benefit for diminishing the heat load in high-power lasers and increasing the conversion efficiency [44]. Yb:YAG has two possible pumping lines: i) broad absorption line around 940 nm with a quantum defect of approximately 9 %, ii) narrow zero-phonon line at 969 nm with a lower quantum defect of around 6 %. Figure 2.1 (a) shows the energy level of ytterbium-doped crystals. It has a dominated emission line at 1030 nm with a bandwidth of approximately 8 nm [45], see Fig. 2.1 (b). Pumping at a low quantum defect (at 969 nm) is desired, however, the narrow absorption cross-section requires a costly laser diode with a stabilized emission wavelength [46]. The absorption band at 940 nm has a sufficient spectral bandwidth, about 18 nm (full width at half maximum (FWHM)), which is realistic for diode lasers, therefore, it is most commonly used.

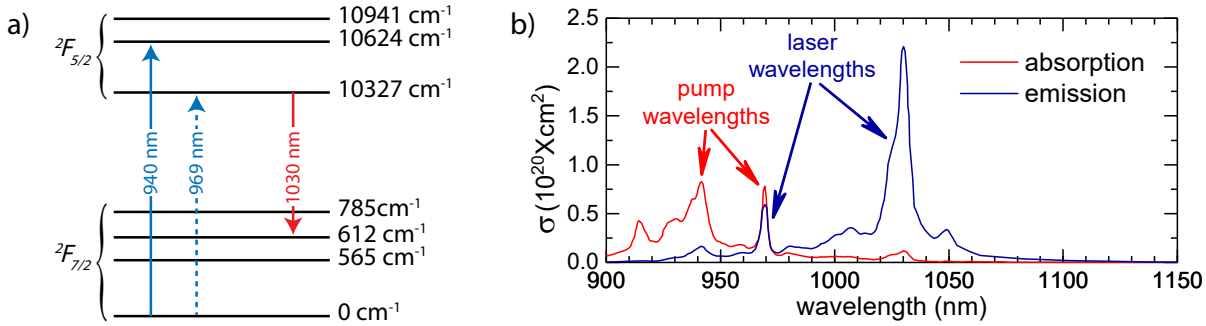

Figure 2.1: Yb:YAG gain medium. a) Yb:YAG energy level diagram. b) Emission and absorption cross-section (σ) of Yb:YAG medium [47].

2.1.2 Thin-disk geometry

In solid-state lasers, the geometry of the gain medium plays an important role in thermal management. Proper geometry has a large ratio between the cooling area and the pumped

volume. Numerous designs have been developed in this respect. Yb:YAG lasers can be classified into several categories such as rod, slab, fiber and thin-disk geometries [47].

In the rod geometry, a radial temperature gradient can be observed as the heat is extracted through the outer surface, which consequently limits the beam quality. Moreover, at high output power operation, thermal lensing becomes unavoidable [48]. On the other hand, heat removal becomes more functional in slab geometry through the upper and lower surfaces, as the temperature gradient is mostly limited to the vertical direction in the edge-pumping configuration. In this configuration, the slab is pumped via the two side surfaces resulting in a homogeneous heat distribution along the laser direction. However, the asymmetry in the geometry and the thermal lensing lead to a strong elliptical laser mode [49]. Innoslab lasers overcome this drawback with improved beam quality [26, 50]. The pulse energy of 70 mJ at a repetition rate of 1 kHz was generated by cryogenically cooling an Yb:YAG crystal, at the expense of complexity and the associated bandwidth [51]. By employing a single-mode Yb:YAG fiber laser, high output power with diffraction-limited beam quality was achieved [52]. Nevertheless, as a result of the nonlinearity of the fiber, its peak power bounds to gigawatt-level, introducing the demand for a bulk laser with better geometry.

The performance of Yb:YAG laser in thin-disk geometry is remarkable due to the efficient cooling of the gain medium. Therefore, the average and peak power can be simultaneously scaled. Here, the disk is bonded to a high thermal conductivity diamond substrate, which is attached from the back to a water-cooled heat sink. The thin-disk design is illustrated in Fig. 2.2 (a). In this geometry, heat flows efficiently in one-dimension along the prorogation direction due to the small ratio of the crystal thickness to the crystal diameter. Consequently, this allows for energy and average power scaling to joule-level and kilowatt-level, respectively, while maintaining a decent beam quality via tens of multi-passes through either one disk or two disks [28, 39, 53]. The amplified spontaneous emission (ASE) limits the energy scaling as this effect is remarkable in such a quasi-three-level gain medium [54]. In order to inhibit the gain losses via the disk, the front and the back surfaces of the disk are deposited with anti-reflective (AR) and high-reflective (HR) coatings for the spectral range of the seed and pump pulses, respectively. To accomplish a high pump absorption in the gain medium, the thin-disk is placed in a head with a multi-pass arrangement, where the pump beam is reimaged by a combination of a parabolic mirror and prism retroreflectors allowing for tens of double-passes via the thin-disk, resulting in absorption efficiency of 90 % (Fig. 2.2 (b)). Furthermore, the occurrence of self-focusing inside the gain medium during the amplification process is restrained due to the slenderness of the thin-disk in contrast to other gain medium geometries, resulting in excellent spatial and temporal profiles of the amplified pulses.

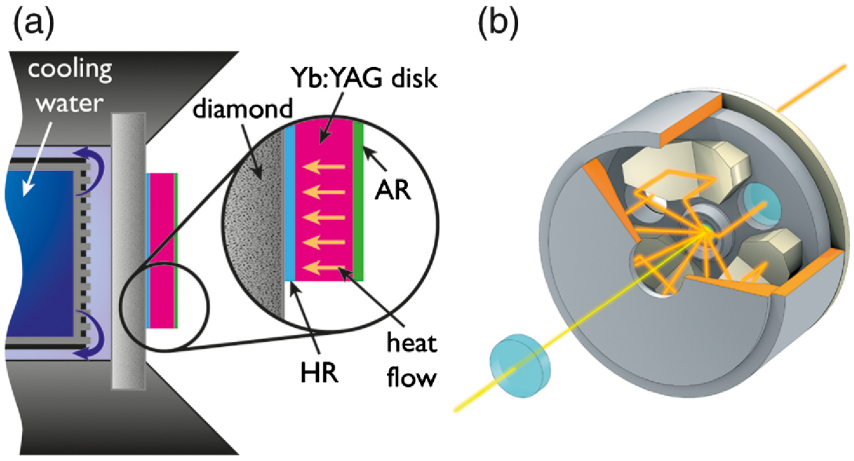

Figure 2.2: Thin-disk geometry. a) The thin-disk design. b) The multi-passes pumping head. AR: anti-reflective coating, HR: high-reflective coating. This figure is adapted from [18].

2.2 Chirped-pulse amplification

Energy scaling of short pulses is restricted to the accumulated nonlinearity of the amplified pulses, which leads to the risk of self-focusing. Therefore, the pulse peak intensity exceeds the damage threshold of the optical components. The peak intensity is mainly governed by the beam size and pulse duration of the source. The peak intensity of the amplified pulse is inversely proportional to the square of the beam size, therefore, increasing the beam diameter potentially benefits overcoming this limitation. Many materials are restricted in the available aperture. Moreover, large apertures lead to a manufacturing challenge in some material specifications, in terms of surface quality and homogeneity. In 1985, a technique invented by Gérard Mourou and Donna Strickland and denominated with chirped pulse amplification (CPA) [55]. Figure 2.3 illustrates the concept of the CPA technique, which initiates with a temporal stretching of the laser pulses before the amplification process in order to reduce the nonlinearity inside the amplifier. Eventually, after the amplification, the introduced dispersion is compensated in a compressor resulting in short, extreme high-energy and high peak power pulses. Here, the pulse energy could be boosted to microjoule-level and its peak power reached terawatt-level.

Implementing Yb:YAG with thin-disk geometry in a CPA configuration paves the way for generating picosecond pulses with hundreds of watts of average power and hundreds of millijoules of energy [28, 56]. The first part of this section is devoted to the seed pulses of such an amplifier delivered by the Yb:YAG thin-disk Kerr-lens mode-locked oscillator. Other seed strategies can be used to seed the amplifier, such as fiber amplifiers. The following parts of this section cover the aspects of the CPA starting from the temporal

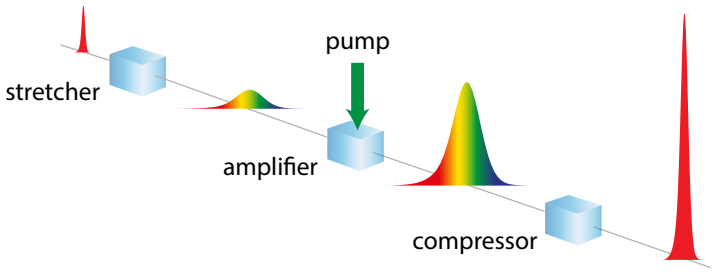

Figure 2.3: Concept of chirped-pulse amplification technique. The seed pulses are temporally chirped prior entering the amplifier, then after the optical gain, they are temporally compressed to their Fourier transform-limit.

stretching then followed by the pulse amplification and the pulse compression.

2.2.1 Kerr-lens mode-locked Yb:YAG thin-disk oscillator

Reproducible daily performance is essential for an appropriate amplifier source to pump OPCPAs. To achieve this goal, several parameters should be taken into account in the design of the frontend oscillator, for instance:

- microjoule-level pulse energy
- sub-picosecond laser pulses
- superb beam pointing stability
- excellent mechanical and thermal stability

Nowadays, short pulses with high average and peak power have been simultaneously generated from mode-locked oscillators utilizing a gain medium of Yb:YAG in thin-disk configuration [57–59].

The schematic of the oscillator is depicted in Fig. 2.4. The standing waves are formed in a linear cavity, confined between a wedge-shaped output coupler (Layertec GmbH) with transmission of 13 %, and a highly reflective flat-shaped end mirror. Optical gain is achieved with about plane Yb:YAG thin-disk gain medium (TRUMPF Scientific Lasers GmbH) with a thickness of 100 μm, optically pumped by fiber-coupled laser diodes (Dilas Diodenlaser GmbH, M1F8H12-940.5-500C-IS11.34) at a wavelength of 940 nm. Short pulses at a wavelength of 1030 nm are obtained by balancing the nonlinear effects and the dispersion in the resonator (i.e. soliton condition) [62]. Three high-dispersive (HD) mirrors with a total intra-cavity group delay dispersion (GDD) of -18000 fs^2 per round-trip

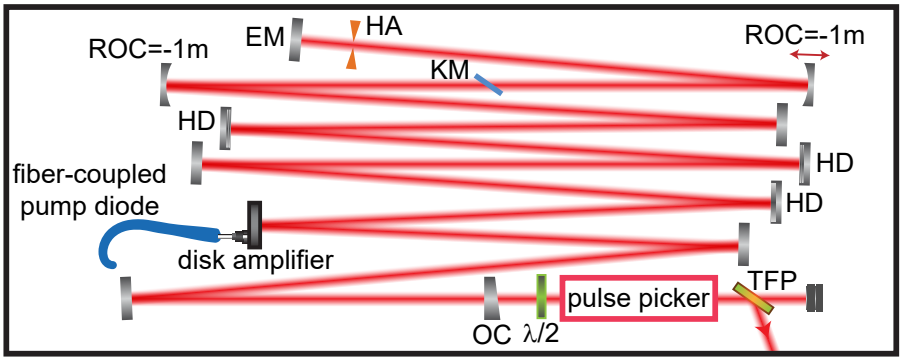

Figure 2.4: Schematic layout of Kerr-lens mode-locked Yb:YAG thin-disk oscillator. The 10 m linear cavity of the oscillator consists of a 13 % transmission output coupler, three high-dispersive mirrors with a group delay dispersion of -3000 fs^2, 1 mm sapphire Kerr medium, and a copper hard aperture. A pulse picker, containing a BBO crystal with a thickness of 25 mm, is utilized to decline the repetition rate to 5 kHz. TFP: thin-film polarizer, $\lambda/2$: half-wave plate, OC: output coupler, HD: high-dispersive mirror, ROC: radius of curvature, KM: Kerr medium, HA: hard aperture, EM: end mirror. This figure is adapted from [60].

facilitate this compensation. A Kerr lensing occurs in a sapphire plate (Meller Optics Inc.) with a thickness of 1 mm placed around the focus of a telescope consists of two concave mirrors ($ROC = -1$ m). High-intense modes experience a strong focusing in Kerr medium, which leads to low losses at a copper hard aperture and the soft aperture of the pump spot, in contrast to the low-intense modes (i.e. continuous wave (CW)). For launching mode-locking, the mirror on a translation stage (marked in Fig. 2.4) is perturbed by a mechanical push.

Table 2.1: Cavity parameters of Kerr-lens mode-locked Yb:YAG thin-disk oscillator. The distance represents the separation from the previous adjacent component. ROC: radius of curvature, OC: output coupler, TD: thin-disk, M: curved mirror, KM: Kerr medium, EM: end mirror. This table is adapted from [61].

component	OC	TD	M_1	KM	M_2	EM
ROC (mm)	∞	-17000	-1000	∞	-1000	∞
distance (mm)	0	3600	5000	510	510	800

Figure 2.5 shows the calculated mode radius along the oscillator's cavity, which has a total length of 10 m. A laser cavity simulation software, developed by Dr. M. Ueffing, was used to simulate the design of the oscillator cavity and the regenerative amplifier cavity in

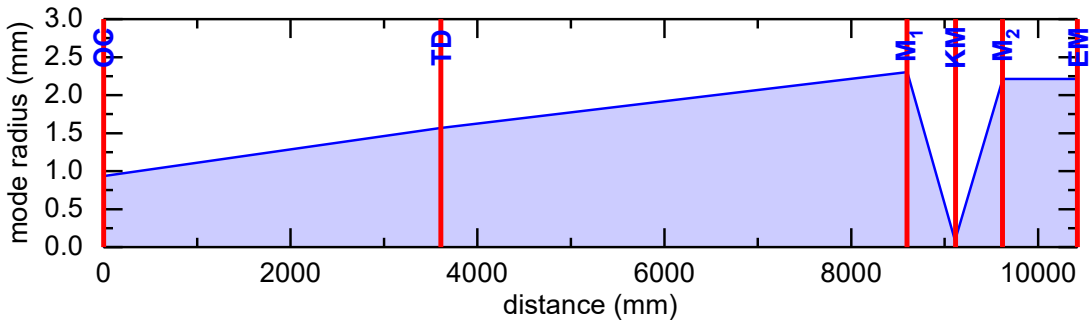

Figure 2.5: Cavity design of Kerr-lens mode-locked Yb:YAG thin-disk oscillator. The propagation distance versus the calculated mode radius. Position of cavity components are marked in red. OC: output coupler, TD: thin-disk, M: curved mirror, KM: Kerr medium, EM: end mirror. This figure is adapted from [61].

Sec. 2.2.3. The distance separation between the cavity's components and their curvature values are summarized in Table 2.1. The pulse duration of the oscillator is 350 fs (FWHM) characterized by utilizing a second-harmonic frequency-resolved optical gating (SH-FROG) containing a beta barium borate (BBO) (BaB_2O_4) crystal with a thickness of 100 μm. Figure 2.6 (a) and (b) illustrate the retrieved temporal and the spectral profiles. The retrieved spectrum is in excellent agreement with the measured spectrum. The measured and retrieved SH-FROG spectrographs of the oscillator's pulses are shown in Fig. 2.6 (c) and (d) with an error of $G_{error} = 6.8 \times 10^{-3}$.

The oscillator delivers approximately 2 μJ pulses, an average power of 30 W, at a 15 MHz repetition rate, and a 4 nm spectral bandwidth (FWHM). Its performance shows pulse-to-pulse stability of 1 % (root mean square (RMS)) and beam-pointing fluctuations of less than 0.4 % over a period of 1 h (see Fig. 2.7). The turn-key operation of the oscillator is attained by the optimum heat management of the laser's components including the laser housing. The output of the oscillator is reproducible on a daily basis, with no need for additional alignment or optimization. Also, the pulse-to-pulse energy stability and spatial pointing stability of the seed laser fulfills the preconditions to achieve the stable operation of the regenerative amplifier, which is subsequently demonstrated in Sec. 2.2.3.

The megahertz repetition rate of the seed pulses is necessarily reduced to kilohertz-level to assist the high-energy amplification in the regenerative amplifier. Thus, the pulse train emitted from the oscillator is picked to 5 kHz by a electro-optical pulse picker (Bergmann Messgeräte Entwicklung KG). The functionality of the pulse picker relies on electro-optic modulation, which is known as the Pockels effect. This effect will be subsequently considered in Sec. 3.1.1. Here, the pulse picker applies a transverse high voltage, corresponding to a half-wave polarization switching, on a BBO crystal (CASTECH Inc.) with a thickness

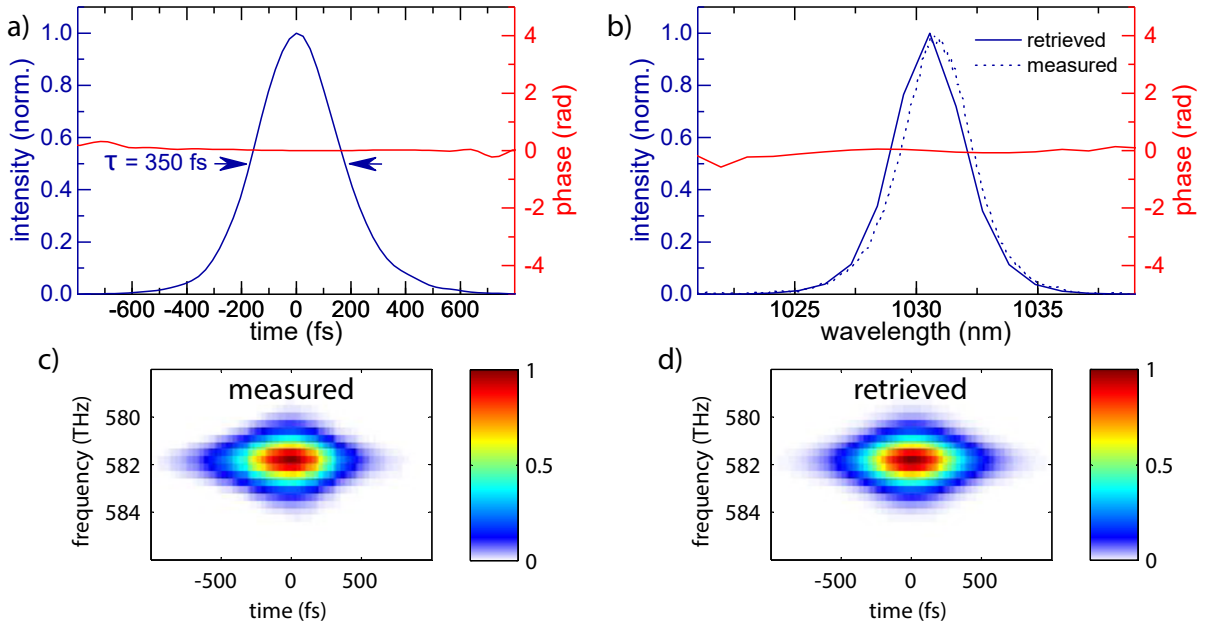

Figure 2.6: Pulse characterization of Kerr-lens mode-locked Yb:YAG thin-disk oscillator. (a) The retrieved temporal intensity profile and its temporal phase. (b) The retrieved and the measured spectrum including the spectral phase. (c) The measured and (d) the retrieved second-harmonic frequency-resolved optical gating spectrographs of the oscillator pulses ($G_{error} = 6.8 \times 10^{-3}$).

of 25 mm. The half-wave voltage ($U_{\lambda/2}$) is given by:

$$U_{\lambda/2} = \frac{\lambda\, d}{2\, \gamma_{22}(\lambda)\, n_o^3(\lambda)\, L} \tag{2.1}$$

where λ is laser's wavelength, d is electrode separation, γ_{22} is the electro-optic coefficient for BBO crystal as a function of wavelength, n_o is refractive index of the ordinary ray as a function of wavelength, and L is the thickness of the crystal [63]. The required half-wave voltage at 1030 nm, for BBO's electro-optic coefficient 2.7 pm/V [64], and $d = 10$ mm, is about 16.8 kV.

2.2.2 Optical pulse stretcher

In order to avoid the nonlinearity during the amplification process, the peak intensity of the seed pulses should be held below the damage threshold. Therefore, the seed pulses should be stretched to several nanoseconds by introducing a large amount of GDD over the spectrum of the seed pulses. Several options can provide this requirement such as a pair of diffraction gratings, fiber Bragg gratings, and volume Bragg gratings. For seed pulse

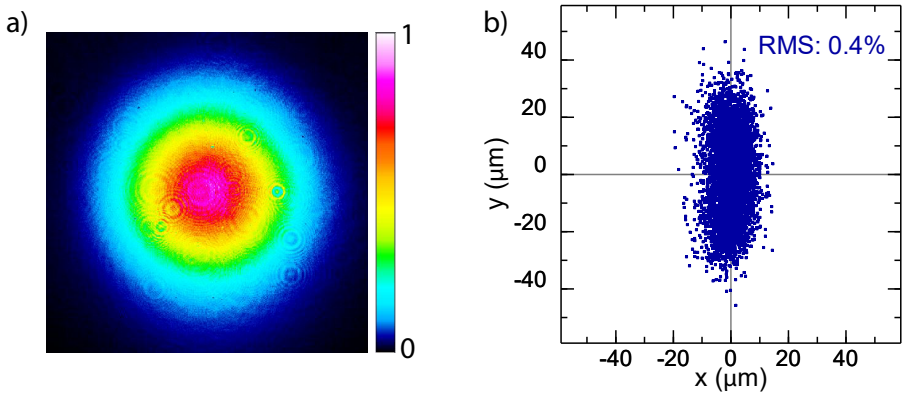

Figure 2.7: Beam pointing measurement of Kerr-lens mode-locked Yb:YAG thin-disk oscillator. (a) The spatial profile of the oscillator's output. (b) Near-field beam pointing of the oscillator's output over a 1 h of measurement.

energy within a microjoule-level, fiber Bragg gratings become an unlikely option because of its low damage threshold. Volume Bragg gratings are durable for this energy level, however, the beam quality deteriorates after a double-pass configuration. Consequently, the seed pulses were initially stretched with a normal dispersion before the amplification process in a Martinez-type stretcher [65], containing two lenses ($f = 2.2\,\mathrm{m}$) confined between two anti-parallel gold gratings (Horiba Jobin Yvon GmbH) with a line density of 1740 lines/mm. The introduced GDD in a Martinez-type stretcher is governed by:

$$GDD \;=\; X\; l_{eff}\; \frac{\lambda_0}{2\;\pi\;c_0^2}\; \left(\frac{N\;\lambda_0}{cos\beta_0}\right)^2 \tag{2.2}$$

where X is the number of passes of the traveled pulses, l_{eff} is the effective distance between the gratings, λ_0 is the central wavelength, c_0 is the velocity of light, N is the line density of the grating, and β_0 is the first-order diffraction angle of the central wavelength.

The pulses traveled 5.9 m through the stretcher resulting in a - 500 ps/nm of stretching factor with a total GDD of 2.52×10^8 fs^2 and a pulse duration of 2 ns (see Fig. 2.8 top-block). The temporal duration of the output pulses (τ_{out}) can be calculated from:

$$\tau_{out} \;=\; \tau_{in}\; \sqrt{1+\left(\frac{4\;ln\,2\;GDD}{\tau_{in}^2}\right)^2} \tag{2.3}$$

where τ_{in} is the temporal duration of the input pulses.

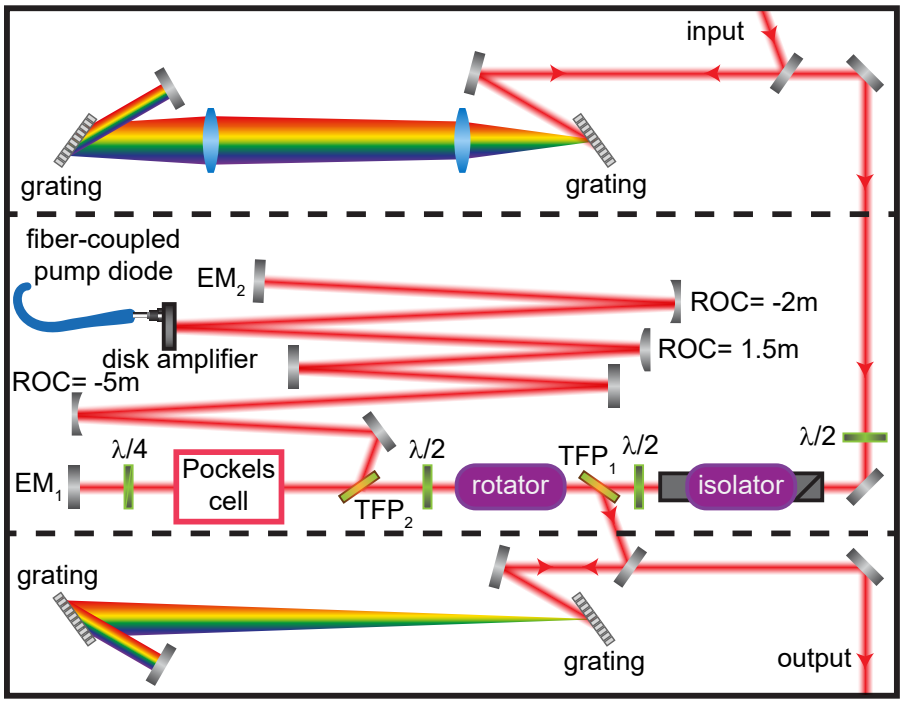

Figure 2.8: Schematic layout of chirped-pulse amplification. Top block: the pulse stretcher setup containing two anti-parallel gold gratings (1740 lines/mm), where the seed pulses are temporally stretched to about 2 ns. Middle block: the regenerative amplifier, where the seed pulse is confined in the amplifier cavity for amplification when the high voltage of the Pockels cell is applied. Bottom block: the pulse compressor containing two parallel dielectric gratings (1740 lines/mm), where the amplified pulses are temporally compressed down to 1 ps. $\lambda/2$: half-wave plate, TFP: thin-film polarizer, $\lambda/4$: quarter-wave plate, EM: end mirror, ROC: radius of curvature. This figure is adapted from [60].

2.2.3 Regenerative amplifier

The stretched pulses were guided to the resonator of the regenerative amplifier passing through a coupling path (see Fig. 2.8 middle-block). This path consists of two optical isolators, where the first (confined between two half-wave plates) was used to prevent the oscillator from any back reflection, and the second is a combination of a Faraday rotator (Electro-Optics Technology Inc.) and a thin-film polarizer (TFP), which was utilized to separate the seed and amplified pulses. Here, the p-polarized seed pulse was transmitted through the TFP_2 (see Fig. 2.8) inside the amplifier's cavity with an unchanged polarization. After the pulse was double passed through the unoperated Pockels cell (PC) (Bergmann Messgeräte Entwicklung KG) and a quarter-wave plate, its polarization was rotated to s-polarization. This ensures that the pulse enters the cavity when reflecting from

the back surface of the TFP_2. Polarization maintaining of the pulse at s-polarized state guarantees trapping the pulse into the cavity. Applying a high voltage on the crystal of the PC corresponds to a quarter-wave rotation allowing for compensating of any polarization rotation induced by the quarter-wave plate, i.e. the pulse circulates into the cavity. PC employs a BBO crystal (CASTECH Inc.) with thickness of 20 mm and a clear aperture of $10\times10\,mm^2$. The estimated quarter-wave voltage ($U_{\lambda/4}$), expressed from Eq. 2.1 divided by factor of 2 is about 10.5 kV. The time window of the applied voltage controls the number of round-trips of the pulse inside the cavity. This window should guarantee the interning of the pulse and starts before the second round-trip. For ideal stable operation, a round-trip number was selected to allow for energy built-up of the pulse to saturation. Afterwards, the amplified pulse was ejected outside the cavity through the TFP_2 by switching off the applied voltage of the PC. Strictly speaking, the amplified pulse transmits through the TFP_2 due to its p-polarization. In this situation, both the PC and the TFP_2 function as either 0 % or 100 % output coupler. The output pulses were reflected from the back surface of the TFP_1 and got separated from the incoming seed pulses.

The cavity design of the amplifier is depicted in Fig. 2.9, including the calculated beam radius along a 6 m cavity length. Table 2.2 summarizes the position of the cavity's components and their curvature values. An Yb:YAG thin-disk (TRUMPF Scientific Lasers GmbH) was placed inside the cavity as a gain medium with a thickness of 100 μm and an approximately 7 % doping rate. The disk has a clear aperture of 9 mm and a radius of curvature (ROC) of - 2000 mm. The seed pulses were amplified in the regenerative amplifier after 106 round-trips, corresponding to a time window of applying a voltage of 4 μs, to an average power of 125 W, while being pumped by a CW fiber-coupled diode (Laserline GmbH, LDM1000-500) with a 280 W at a wavelength of 940 nm, corresponding to approximately 48 % of optical-to-optical efficiency. The pump spot on the disk has a flat-top spatial profile and a 3.5 mm of the beam diameter.

The amplifier was placed in an airtight housing and operated at room temperature. Operating the amplifier in saturation-level after 106 round-trips results in stable amplified pulses. The pulse-to-pulse stability of the amplifier is less than 1 % (RMS) within a time window of 2 s. The amplifier exhibits excellent long-term power stability after 10 h of continuous operation (Fig. 2.10 (a)). Inset of Fig. 2.10 (a) demonstrates the power stability over a time period of 30 min by normalizing the power to its average. The amplified beam has an excellent spatial profile, with a M^2 of 1 ($M_x^2 = 1.08$ and $M_y^2 = 1.09$) (see Fig. 2.10 (b)). The beam quality evaluation was done by using a laser M^2 measuring system (Ophir Optronics Solutions Ltd., M^2-200s). The transverse intensity profile of the amplified beam is demonstrated in the inset of Fig. 2.10 (b). In addition to the operation of the regenerative amplifier in saturation, careful optimization of the cooling systems and the power supply of the diodes plays a major role in the achieved stability of the amplifier.

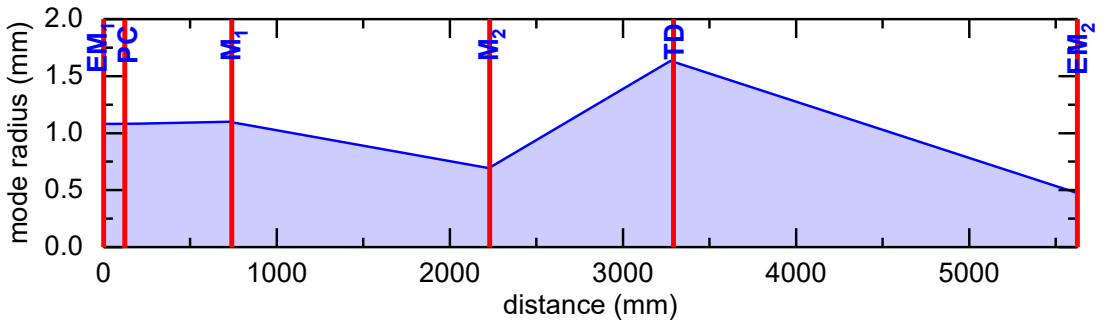

Figure 2.9: Cavity design of Yb:YAG thin-disk regenerative amplifier. The propagation distance versus the calculated mode radius. Position of cavity components are marked in red. EM: end mirror, PC: Pockels cell, M: curved mirror, TD: thin-disk. This figure is adapted from [61].

Table 2.2: Cavity parameters of Yb:YAG thin-disk regenerative amplifier. The distance represents the separation from the previous adjacent component. ROC: radius of curvature, EM: end mirror, PC: Pockels cell, M: curved mirror, TD: thin-disk. This table is adapted from [61].

component	EM_1	PC	M_1	M_2	TD	EM_2
ROC (mm)	∞	∞	-5000	1500	-2000	-2000
distance (mm)	0	200	525	1500	1050	2350

2.2.4 Amplified pulse compression

After amplification, the output pulses were sent to a Treacy-type pulse compressor [66], consists of two parallel dielectric gratings (Plymouth Grating Laboratory Inc.), with a line density of 1740 lines/mm (see Fig. 2.8 bottom-block). The compressor introduces an anomalous dispersion to the amplified pulses. Using identical dispersion in the stretcher and the compressor allows for excellent dispersion compensation. Figure 2.11 illustrations the temporal and the spectral details of the compressed pulses, which were characterized by using a SH-FROG employing a BBO crystal with a thickness of 100 μm resulting in a 1 ps (FWHM) of pulse duration, where the Fourier transform-limit is 0.98 ps. Considering an output efficiency of 80 % of the compressor, the compressed pulses have 20 mJ of pulse energy at a wavelength of 1030 nm, and 1.5 nm spectral bandwidth (FWHM) operating at 5 kHz repetition rate.

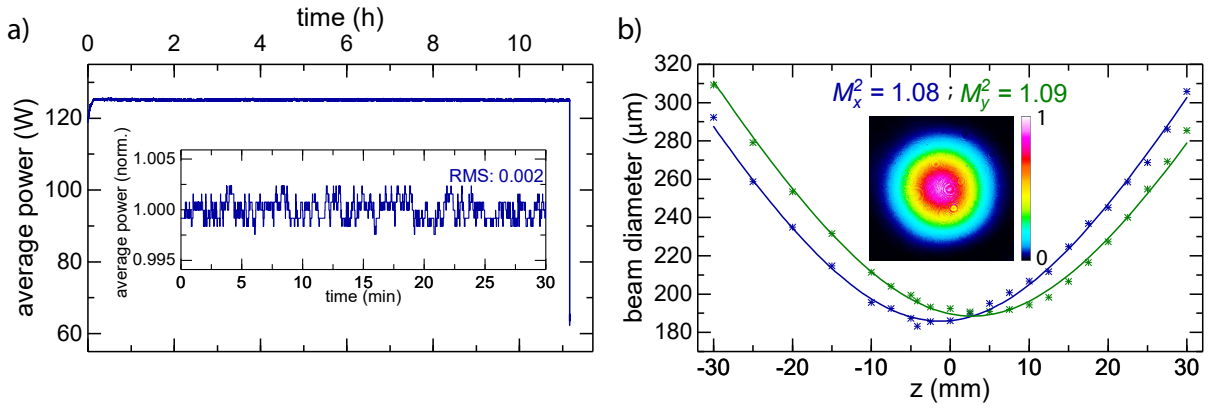

Figure 2.10: Characterization of Yb:YAG thin-disk regenerative amplifier. (a) The power stability of the regenerative amplifier after 10 h of continuous operation. Inset: normalized average power to its mean value in a time window of 0.5 h. (b) M^2 measurement of the output beam of the amplifier. Inset: output spatial profile of the regenerative amplifier. Figure (a) is adapted from [60].

2.3 Various considerations about the amplification process

As seen in the previous section, the seed pulses were successfully amplified in the regenerative amplifier and their temporal duration was compressed to 1 ps. However, there are several issues that can be observed during the operation of the regenerative amplifier. Therefore, effects such as chaotic behavior and gain narrowing are addressed in the current section.

2.3.1 Chaotic energy behavior

Unpredictable output pulse energies from a regenerative amplifier can be observed when its repetition rate is in the same order as the inverse of the upper-level lifetime of the gain medium. A chaotic energy behavior has been reported in Ref.s [67, 68] when Yb:YAG regenerative amplifiers were operated at a multi-kilohertz level while being pumped by a continuous-wave light source. Here, the population inversion of the gain medium does not entirely recover for the next extracting pulse, resulting in unstable operation. Amplified pulses experience different stored energies in the laser medium, which lead to a variation of energy extraction and random pulsing. This chaotic behavior has been numerically and experimentally presented in Ref. [67]. Moreover, a detailed study in Ref. [69] has underlined that pre-amplification of the seed pulse energy enhances the system's stability. Stable laser operation of period-doubling following this regime has been identified in Ref. [68]. The effect

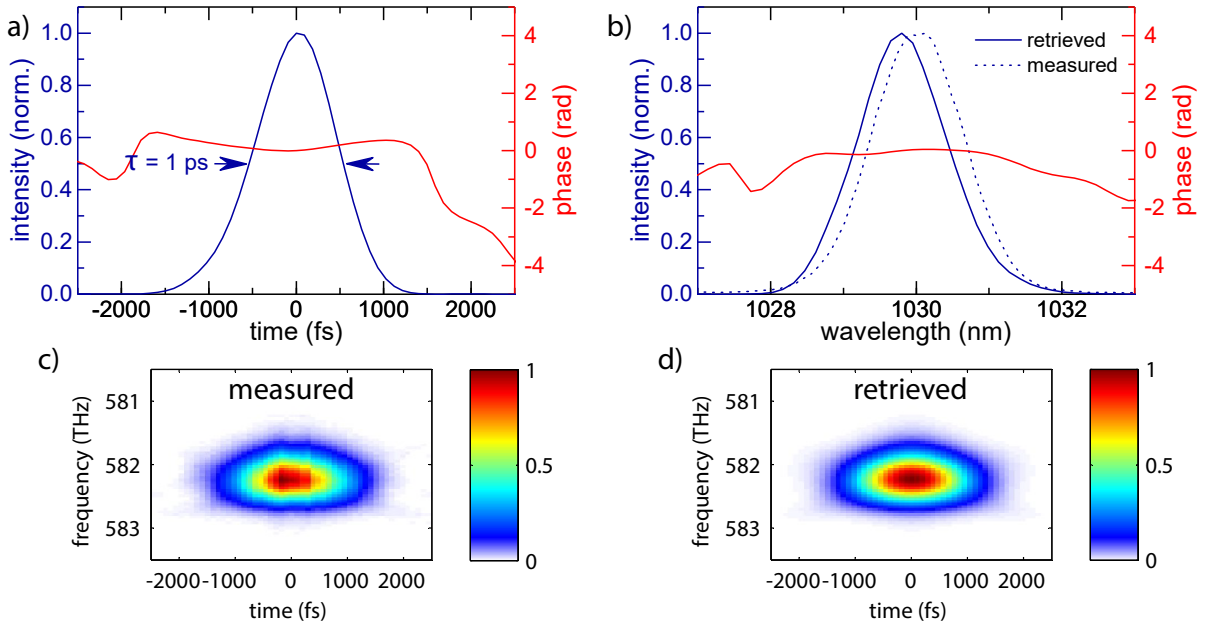

Figure 2.11: Pulse compression of Yb:YAG thin-disk regenerative amplifier. (a) The retrieved temporal intensity and (b) the retrieved spectral intensity, and the amplifier output spectrum of the laser pulses at an average power of 100 W after the gratings compressor. (c) The measured and (d) the constructed spectrographs of the compressed pulse ($G_{error} = 4 \times 10^{-3}$).

of the pump power and the round-trip number on of the bifurcation regime has been studied in Ref. [70], showing that high seed pulse energy allows shifting the bifurcation regime to lower pump power or lower round-trips. Seeding the regenerative amplifier with the energy of microjoule-level from the thin-disk Kerr-lens mode-locked oscillator ensures surpassing the bifurcation regime and running the amplifier at a stable point. Additionally, the use of a 2 μJ Yb:YAG thin-disk Kerr-lens mode-locked oscillator assists the amplification of the regenerative amplifier by decreasing the growth of the accumulated nonlinear phases, as the required round-trip number is diminished for higher input seed energy.

2.3.2 Gain narrowing

The seed pulses can experience a reduction in their bandwidth during the amplification, since the gain bandwidth of the laser medium is limited. This effect is known as gain narrowing. This is a consequence of the frequency components in the center of the spectrum encountering higher gain compared to the frequency components in the wings.

Fortunately, higher seed energy influences the amplification process and reduces the gain narrowing effect. In this respect, I experimentally investigated the impact of seed

energy on the gain narrowing. In this experiment, neutral density filters were utilized to attenuate the seed energy at different energy levels and the spectrum of the amplified pulses for each seed energy level with constant pump power was recorded. In low seed energy cases, the round-trip numbers were increased to reach maximum output power. The measured spectral bandwidth (FWHM) of the amplified pulses for different seed energies at a fixed pump power is shown in Fig. 2.12. It can be seen clearly that amplified spectral bandwidth decreases for lower seed energies due to gain narrowing. For 10 pJ seed energy, the laser operates in the period-doubling [68, 70], and it is not possible to reach stable operation, even by increasing the number of round-trips.

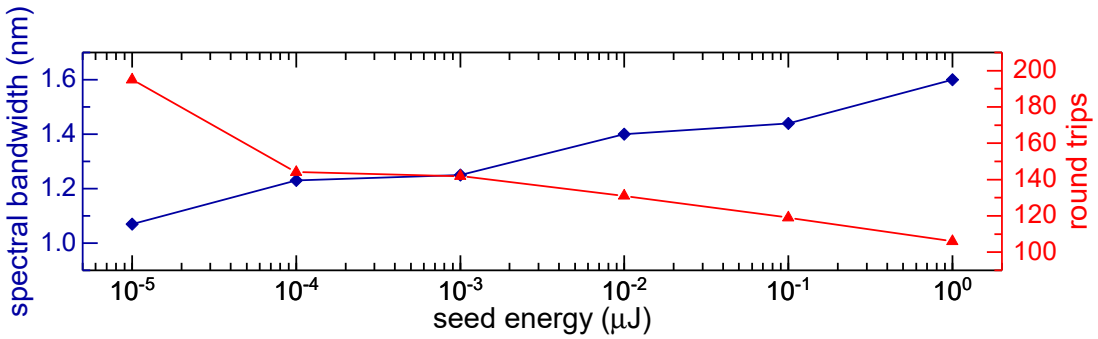

Figure 2.12: Gain narrowing effect. Seed energy versus the spectral bandwidth (FWHM) of the amplifier output and the required number of round-trips for the same output average power at 300 W of pump power. This figure is adapted from [60].

2.4 Conclusion

To conclude, I have reported on an Yb:YAG regenerative amplifier. A homemade thin-disk Kerr-lens mode-locked oscillator with a turn-key performance and pulse energy of microjoule-scale was utilized to seed the thin-disk regenerative amplifier. Microjoule seed level allows a significant reduction in the required number of round-trips for amplification in comparison to the announced results in Ref. [68], consequently, leading to a less gain narrowing effect in the spectrum of the amplified pulses. This easily facilitates overtaking the bifurcation to operate the amplifier at a very stable regime. Moreover, high-energy seed pulses assist declining the growth of the accumulated nonlinear phases, thus the amplified pulses inherit an improved temporal profile [70].

The system provides compressed pulses with a 1 ps of pulse duration (FWHM) and pulse energy of 20 mJ at a repetition rate of 5 kHz. The stability of the regenerative amplifier in combination with its turn-key performance are necessary for the generation of multi-octave, CEP-stable seed, which is treated in the next chapter. Moreover, the

performance mentioned earlier makes this amplifier an attractive pump source for OPCPA system, which is addressed in Chapter 4.

Chapter 3

CEP-Stable Supercontinuum Generation

Previously, Chapter 1 introduced the essential ingredients of the optical waveform synthesizer. Among these ingredients, I listed the CEP-stable supercontinuum generation. Today, Yb:YAG lasers are mature technology, and offer such a possibility for CEP-stable supercontinuum generation [18, 71–83]. CEP-stable, multi-octave supercontinuum generated directly from sub-picosecond Yb:YAG oscillators or picosecond amplifiers has two prominent applications: i) it can be used to seed broadband OPAs or subcycle field synthesizers pumped by high-energy, kilohertz, Yb:YAG amplifiers [17, 18, 84]; or, ii) it can be used for field- and time-resolved spectroscopy when it is driven from high average power, megahertz oscillators. However, the second application is beyond the scope of this work.

As the first application agrees with the overall subject of this work, the current chapter is devoted to the development of a compact source delivering a CEP-stable, coherent, super-octave continua spanning from visible (VIS) to MIR spectral ranges, containing more than nanojoule energy, and at kilohertz repetition rate. For a better understanding of some general terms, I initially provide a theoretical background about nonlinear optics. Thereafter, two different methods of the generation of a CEP-stable, multi-octave supercontinuum from 1 ps output pulses of an Yb:YAG thin-disk regenerative amplifier with arbitrary varying phase for seeding a high-energy field synthesis based-on OPCPA are discussed.

3.1 Theoretical foundations of nonlinear optics

In this section, I explain phenomena in nonlinear optics that happen when a nonlinear medium is irradiated with an intense light, such as a laser beam. A wide variety of superb textbooks covering the topic of nonlinear optics, such as Ref.s [85–87]. This section is

mainly adapted from Ref [85]. Starting from Maxwell's equations, the wave equation in a nonlinear medium can be derived as:

$$\nabla^2 \widetilde{E} \; - \; \frac{1}{c_0^2} \, \frac{\partial^2 \widetilde{E}}{\partial t^2} \; = \; \mu_0 \, \frac{\partial^2 \widetilde{P}}{\partial t^2} \tag{3.1}$$

where $\widetilde{E}$ is the electric field of light, c_0 is the velocity of light of free space, μ_0 is the permeability in a vacuum, and $\widetilde{P}$ is the polarization. Here, the induced polarization is not linearly proportional to the applied electric field of light. This relationship can be expressed by a Taylor expansion:

$$\widetilde{P}(t) \; = \; \epsilon_0 \, \chi^{(1)} \, \widetilde{E}(t) \; + \; \epsilon_0 \, \chi^{(2)} \, \widetilde{E}^2(t) \; + \; \epsilon_0 \, \chi^{(3)} \, \widetilde{E}^3(t) \; + \; \ldots \tag{3.2}$$

where ϵ_0 is the permittivity of free space, $\chi^{(1)}$ is the linear susceptibility of the material, and $\chi^{(2)}$ and $\chi^{(3)}$ are the second-order and third-order nonlinear susceptibilities of the material, respectively. The right-hand side of Eq. 3.2 can be rewritten into two terms:

$$\widetilde{P}(t) \; = \; \widetilde{P}^{L} \; + \; \widetilde{P}^{NL} \tag{3.3}$$

where the liner component of the polarization ($\widetilde{P}^{L}$) is given as:

$$\widetilde{P}^{L}(t) \; = \; \overbrace{\epsilon_0 \, \chi^{(1)} \, \widetilde{E}(t)}^{\widetilde{P}^{(1)}(t)} \tag{3.4}$$

Also, non-linear component of the polarization ($\widetilde{P}^{NL}$) is defined as:

$$\widetilde{P}^{NL}(t) \; = \; \overbrace{\epsilon_0 \, \chi^{(2)} \, \widetilde{E}^2(t)}^{\widetilde{P}^{(2)}(t)} \; + \; \overbrace{\epsilon_0 \, \chi^{(3)} \, \widetilde{E}^3(t)}^{\widetilde{P}^{(3)}(t)} \; + \; \ldots \tag{3.5}$$

The wave equation in a nonlinear medium can be rewritten by substituting Eq. 3.3 into Eq. 3.1:

$$\nabla^2 \widetilde{E} \; - \; \frac{n^2}{c_0^2} \, \frac{\partial^2 \widetilde{E}}{\partial t^2} \; = \; \mu_0 \, \frac{\partial^2 \widetilde{P}^{NL}}{\partial t^2} \tag{3.6}$$

where n is the refractive index of the material. The first and the second terms in Eq. 3.5 associate to the second-order ($\widetilde{P}^{(2)}(t)$) and third-order ($\widetilde{P}^{(3)}(t)$) polarization, respectively. The effects related to these terms are described in details in Sec. 3.1.1 and Sec. 3.1.2.

3.1.1 Second-order nonlinearity

In this section, I treat some phenomena related to the second-order polarization and neglect the higher-order polarization for simplicity. Second-order nonlinearity can only rise in

media with a non-centrosymmetric structure. As realized from Eq. 3.5, the corresponding nonlinear polarization is given as:

$$\widetilde{P}^{(2)}(t) \;=\; \epsilon_0 \; \chi^{(2)} \; \widetilde{E}^2(t) \tag{3.7}$$

Second-harmonic generation: It is one of the most common nonlinear processes and is also known as frequency-doubling. Here, two identical photons interact with a non-zero $\chi^{(2)}$ material to produce a new photon at double frequency of the involved photons. Suppose this material is irradiated by a single beam at a frequency of ω and its electric field can be written as:

$$\widetilde{E}(t) \;=\; E \; e^{-i\omega t} \;+\; c.c. \tag{3.8}$$

where E is the complex amplitude. Replacing the electric field in Eq. 3.7 with its expression in Eq. 3.8 obtains:

$$\widetilde{P}^{(2)}(t) \;=\; [\; \overbrace{\epsilon_0 \; \chi^{(2)} \; E^2 \; e^{-2i\omega t}}^{P(2\omega)\;(SHG)} \;+ c.c. \;] \;+\; \overbrace{2 \; \epsilon_0 \; \chi^{(2)} \; E \; E^*}^{P(0)\;\;(OR)} \tag{3.9}$$

As realized from Eq. 3.9, the first term of the second-order polarization leads to the second-harmonic generation (SHG) at frequency 2ω.

Optical rectification and Pockels effect: The second term is known as DC polarization at zero frequency and associates to the optical rectification (OR) process, which results in a change of average location of the dipole. An inverse process to the optical rectification is called Pockels effect when an external electric field (E_{ext}) is applied to a non-centrosymmetric medium. The applied electric field induces a change in the birefringence of the medium, proportional to the applied electric field. One possible application of this effect is electro-optic modulation which was previously introduced in Sec. 2.2.1 and Sec. 2.2.3, where the polarization of the incident beam is modulated by applying an external DC voltage (U) in a non-centrosymmetric crystal.

Three-wave mixing: It is a general case of second-order nonlinearity, in which two incident waves at frequencies ω_1 and ω_2 interact with a non-centrosymmetric medium, where $\omega_1 > \omega_2$. The corresponding electric field can be written as:

$$\widetilde{E}(t) \;=\; E_1 \; e^{-i\omega_1 t} \;+\; E_2 \; e^{-i\omega_2 t} \;+ c.c. \tag{3.10}$$

Substituting Eq. 3.10 in Eq. 3.7 gains:

$$\begin{aligned}\widetilde{P}^{(2)}(t) \;=\; [\; &\overbrace{\epsilon_0\,\chi^{(2)}\,E_1^2\,e^{-2i\omega_1 t}}^{P(2\omega_1)\;(SHG_1)} + \overbrace{\epsilon_0\,\chi^{(2)}\,E_2^2\,e^{-2i\omega_2 t}}^{P(2\omega_2)\;(SHG_2)} \\ &+ \overbrace{2\,\epsilon_0\,\chi^{(2)}\,E_1\,E_2\,e^{-i(\omega_1+\omega_2)t}}^{P(\omega_1+\omega_2)\;(SFG)} + \overbrace{2\,\epsilon_0\,\chi^{(2)}\,E_1\,E_2^*\,e^{-i(\omega_1-\omega_2)t}}^{P(\omega_1-\omega_2)\;(DFG)} + c.c.\;] \\ &+ \overbrace{2\,\epsilon_0\,\chi^{(2)}\,E_1\,E_1^*}^{P(0)\;(OR_1)} + \overbrace{2\,\epsilon_0\,\chi^{(2)}\,E_2\,E_2^*}^{P(0)\;(OR_2)}\end{aligned} \tag{3.11}$$

The first two terms ($P(2\omega_1)$ and $P(2\omega_2)$) in Eq. 3.11 associate to the SHG of frequency waves at ω_1 and ω_2, respectively. The third term ($P(\omega_1+\omega_2)$) shows the polarization component of sum-frequency generation (SFG) at frequency $\omega_1+\omega_2$. SFG is a general case of SHG, where two photons involve in this process at different frequencies to generate more energetic photon.

The following term ($P(\omega_1-\omega_2)$) represents difference-frequency generation (DFG) process at wave frequency $\omega_1-\omega_2$. DFG is mainly used to generate a new photon at lower frequency $\omega_3=\omega_1-\omega_2$. The weaker photon at frequency ω_2 in DFG process is amplified by the higher frequency photon (ω_1). Therefore, this process is also denominated as OPA as the process is stimulated by the presence of ω_2 photon. In OPA, the input ω_1, ω_2, and generated ω_3 frequencies are called pump, signal, and idler frequencies, respectively.

Generally, the contributions of the second-order polarization can be written as a summation form like:

$$\widetilde{P}^{(2)}(t) \;=\; \sum_n P(\omega_n)\,e^{-i\omega_n t} \tag{3.12}$$

3.1.2 Third-order nonlinearity

In this section, I describe some nonlinear processes as a consequence of the third-order polarization. The nonlinearity is dominated by third-order processes in a medium that has an inversion symmetry while the second-order susceptibility vanishes here. For simplicity, the exposed materials in this section are assumed to have an inversion symmetry structure. As seen earlier in Eq. 3.5, the third-order polarization can be expressed by:

$$\widetilde{P}^{(3)}(t) \;=\; \epsilon_0\,\chi^{(3)}\,\widetilde{E}^3(t) \tag{3.13}$$

Third-harmonic generation: By considering a single beam at frequency ω propagates in a centrosymmetric medium, the induced third-order polarization can be explicated

in the same manner of the SHG by substituting Eq. 3.8 in Eq. 3.13 to obtain:

$$\widetilde{P}^{(3)}(t) \;=\; \overbrace{\epsilon_0\;\chi^{(3)}\;E^3\;e^{-3i\omega t}}^{P(3\omega)\;(THG)} \;+\; \overbrace{3\;\epsilon_0\;\chi^{(3)}\;E^2\;E^*\;e^{-i\omega t}}^{P(\omega)\;(SPM)} \;+\; c.c. \tag{3.14}$$

The first term ($P(3\omega)$) in Eq. 3.14 associates to the polarization component of the third-harmonic generation (THG). In this process, three photons at frequency of ω involve to create a new photon at frequency of 3ω.

Self-phase modulation: The second term in Eq. 3.14 is the intensity-dependent refractive index term, which represents the polarization component corresponding to the self-phase modulation (SPM). In SPM, the pulse experiences a change in its phase due to the refractive index dependency on the pulse intensity (I). The nonlinear refractive index (n) is defined as:

$$n(t) \;=\; n_0 \;+\; n_2\;I(t) \tag{3.15}$$

where n_0 is the linear refractive index, and n_2 is the Kerr coefficient, which defines the nonlinearity strength. The coefficient n_2 is expressed as:

$$n_2 \;=\; \frac{3\;\chi^{(3)}}{2\;\epsilon_0\;c_0\;n_0^2} \tag{3.16}$$

As the pulse intensity is time-dependent, the phase change of the pulse varies with the time. As a consequence, the optical spectrum is modulated and this gives rise to a spectral broadening.

Self-focusing: Assuming that the pulse propagates in nonlinear medium with a positive value of n_2. The center of the beam experiences a higher refractive index comparing to its wings due to the spatial distribution of the beam intensity. Under these circumstances, the medium acts as a focusing lens. This phenomenon is known as a self-focusing effect. This effect is undesirable as it could cause severe damage to the optical components. Such an event would occur when the beam carries a peak power exceeding the critical power (P_{cri}), which is expressed as:

$$P_{cri} \;=\; \frac{0.146\;\lambda^2}{n_0\;n_2} \tag{3.17}$$

Cross-phase modulation: In the presence of two different beams at a frequency of ω_1 and ω_2, respectively, their interference in a centrosymmetric medium can give rise to cross-phase modulation (XPM) effect. The polarization component associated with XPM is given by:

$$P(\omega_1) \;=\; 3\;\epsilon_0\;\chi^{(3)}\;E_2\;E_2^*\;E_1\;e^{-i\omega t} \tag{3.18}$$

Here, the phase of the pulse (at frequency ω_1) experiences a variation due to the interaction with another pulse (at frequency ω_2) in the medium. This effect is called as optical Kerr effect. In a pump-probe experiment, this effect can be utilized as a method for transforming the information of a pump pulse to a probe pulse by altering the phase of the probe pulse during their interaction in a proper nonlinear material. Such as this experiment is presented in Chapter 5 and Chapter 6 when introducing the electro-optic sampling (EOS) technique.

Four-wave mixing: In the general case, the third-order polarization in a centrosymmetric medium can be induced by an incident electric field consists of three different frequencies (ω_1, ω_2, and ω_3). The total electric field is given as:

$$\widetilde{E}(t) \;=\; E_1\, e^{-i\omega_1 t} \;+\; E_2\, e^{-i\omega_2 t} \;+\; E_3\, e^{-i\omega_3 t} \;+ c.c. \tag{3.19}$$

By replacing the corresponding value of the electric field in Eq. 3.19 into Eq. 3.13, the third-order polarization becomes more complicated and contains 22 components as listed:

$$\begin{aligned}
&P(\omega_1)\ ,\ P(\omega_2)\ ,\ P(\omega_3)\ ,\ P(3\omega_1)\ ,\ P(3\omega_2)\ ,\ P(3\omega_3)\\
&P(\omega_1+\omega_2+\omega_3)\ ,\ P(\omega_1+\omega_2-\omega_3)\ ,\ P(\omega_1+\omega_3-\omega_2)\ ,\ P(\omega_2+\omega_3-\omega_1)\\
&P(2\omega_1+\omega_2)\ ,\ P(2\omega_1+\omega_3)\ ,\ P(2\omega_1-\omega_2)\ ,\ P(2\omega_1-\omega_3)\\
&P(2\omega_2+\omega_1)\ ,\ P(2\omega_2+\omega_3)\ ,\ P(2\omega_2-\omega_1)\ ,\ P(2\omega_2-\omega_3)\\
&P(2\omega_3+\omega_1)\ ,\ P(2\omega_3+\omega_2)\ ,\ P(2\omega_3-\omega_1)\ ,\ P(2\omega_3-\omega_2)
\end{aligned} \tag{3.20}$$

These components can be represented in a summation form as:

$$\widetilde{P}^{(3)}(t) \;=\; \sum_n P(\omega_n)\, e^{-i\omega_n t} \tag{3.21}$$

Cross-polarized wave generation: The generation of the cross-polarized pulses is a special case of four-wave mixing process which occurs at the degenerate frequency (ω) in a cubic crystal possessing an anisotropic third-order nonlinearity, for instance barium fluoride (BaF_2) crystal. This process leads to the generation of a new wave at the same frequency (ω) and it is perpendicularly polarized to the driving waves, as:

$$w_\perp \;=\; w_\parallel \;+\; w_\parallel \;-\; w_\parallel \tag{3.22}$$

In this process, the phase-matching between the input waves and the generated cross-polarized wave (XPW) is guaranteed due to the isotropy of the cubic crystal. The intensity of the converted wave is cubically proportional to the intensity of the driving wave. This allows for enhancing the temporal and spatial shape of the generated pulse and smoothing its spectrum. Moreover, the generated XPW pulse is compressed by a factor of $\sqrt{3}$ and

also its spectrum is broadened by a factor of $\sqrt{3}$. In the following section, the conventional methods of seed generation for OPCPAs are considered and some challenges of these methods are highlighted.

3.2 Direct seed generation from OPCPA pump source

The most common method to provide broadband seed pulses for OPCPA has been driven by low-energy lasers, such as Ti:Sa oscillators. In OPCPA, the seed pulses are amplified by high-energy pulses from a different source at higher frequencies. This imposes a need for suppressing the time jitter between the interaction pulses at the parametric stage, which can be achieved via an active temporal synchronization between the seed and pump pluses [88, 89].

In the seed generation, energy scaling of the seed pulses is prior demanded in order to enhance the conversion efficiency and minimize the superfluorescence at the OPCPA channels. Furthermore, the restricted carrier wavelength of the seed pulses can be converted to longer wavelength in MIR region [90–92]. Therefore, the complexity of this approach reduces the capability of the time synchronization system and leads to a deterioration in the CEP [93].

A substantial temporal synchronization can be attained between the seed and the pump sources of the OPCPA once the CEP-stable broadband seed pulses are directly generated from the pump pulses. This approach suppresses the mentioned drawbacks and simplifies the entire setup.

3.3 Phase-stable, multi-octave continuum

In the following, I treat the generation of a phase-stable multi-octave supercontinuum, while its implementation as a seed source in the entire system (see Fig. 1.2) is addressed in the next chapter.

The presented work in this section is based on the main Ph.D. work of Haochuan Wang and the reported results in the published article:

- H. Fattahi, H. Wang, A. Alismail, G. Arisholm, V. Pervak, A. M. Azzeer, and F. Krausz, "Near-PHz-bandwidth, phase-stable continua generated from a Yb:YAG thin-disk amplifier," *Optics Express* **24**(21), pp. 24337–24346, 2016.

Therefore, this work is briefly summarized in this section with a view to support the entire framework of this thesis.

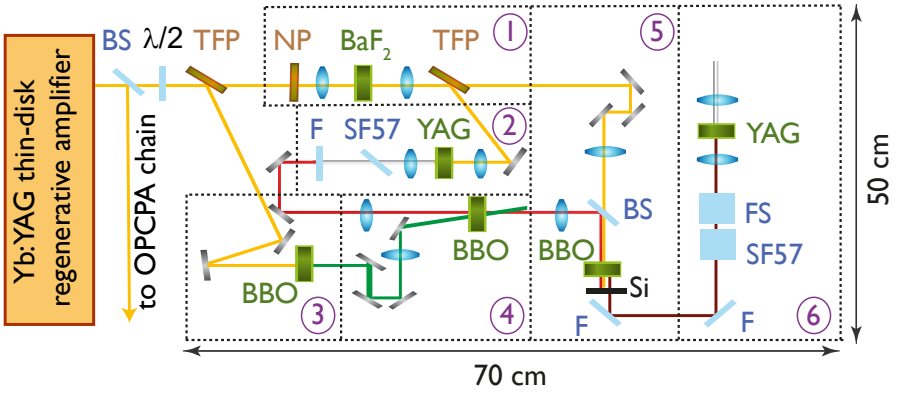

Figure 3.1: Setup layout of multi-octave, phase-stable supercontinuum. The supercontinuum is directly generated from the thin-disk Yb:YAG regenerative amplifier by utilizing a small fraction of the output energy about 1.8 mJ. In the beginning, the 1 ps pulse duration of the input pulses is reduced by a factor of $\sqrt{3}$ into a 4mm-thick BaF_2 crystal (cross-polarized wave generation) (panel 1). Next, the separated cross-polarized waves are tightly focused into a YAG crystal with a thickness of 4 mm (panel 2) for supercontinuum generation. Second-harmonic pulses at 515 nm, generated in panel 3, are used to boost the energy of supercontinuum in a non-collinear parametric amplification stage (panel 4). Subsequently, both the bandwidth of the amplified signal is shifted to longer wavelengths and the carrier-envelope phase is stabilized in a collinear difference-frequency generation stage (panel 5). Eventually, after compressing the generated pulses, second YAG crystal is used to generate another supercontinuum in order to cover the VIS spectral range (panel 6). The compact setup occupies an area of $70 \times 50\,cm^2$. BS: beam splitter, $\lambda/2$: half-wave plate, TFP: thin-film polarizer, NP: nanoparticle film polarizer, F: spectral filter, Si: silicon plate, FS: fused silica plate. This figure is adapted from [82].

As mentioned earlier, the direct seed generation from the pump source is an attractive approach since this configuration eliminates the requirement of a complex temporal synchronization system between the seed and the pump at the OPA stage [88, 89]. Direct CEP-stable, multi-octave continuum seed was generated from an Yb:YAG regenerative amplifier [82]. Scheme of the experiment setup is demonstrated in Fig. 3.1. 1.8 mJ of the output energy of the regenerative amplifier (Sec. 2.2.4) was used as the input of this setup.

The 1 ps pulses of the Yb:YAG regenerative amplifier were shortened to 650 fs via XPW to obtain a stable supercontinuum in bulk. This stage is necessary as the critical peak power of 1 ps pulses for filamentation in bulk is of the same order of magnitude as the damage threshold of the bulk [94, 95]. 140 μJ, 1 ps pulses were focused into a BaF_2 crystal with a thickness of 4 mm to generate perpendicularly polarized pulses relative to the pump pulses (see Fig. 3.1 panel 1). The XPW pulses are shortened by a factor of $\sqrt{3}$ with an enhancement of both temporal and spatial profiles. After collimating the XPW beam, a

TFP was utilized to reflect and separate the XPW from the fundamental beam. Next, the 4 μJ reflected signal was focused into a YAG crystal with a 4 mm of thickness to generate a steady filament (Fig. 3.1 panel 2) yielding a continuum spectrum covering between 550 nm to 1400 nm.

Afterwards, the supercontinuum spectrum was amplified in a saturated non-collinear optical parametric amplification (NOPA) stage utilizing a BBO type-I crystal with a thickness of 3 mm (panel 4 in Fig. 3.1). The phase-matching angle was 24.5° and the non-collinear angle was set to 2.5°. The reader is referred to Sec. 4.1 for more information about the OPA interactions. For optimum temporal overlap between the seed and pump pulses at the non-collinear parametric stage, a 4 mm-thick SF57 plate was used in the seed path. The pulse energy was scaled to 100 μJ by pumping the NOPA stage with the second-harmonic (SH) of the fundamental pulses, which was generated prior in panel 3 (Fig. 3.1). Fundamental pulse with an energy of 1.6 mJ was frequency-doubled into a BBO type-I crystal with a thickness of 1 mm ($\theta = 23°$), leading to a 515 nm pulses with approximately 1 mJ of energy. More details about the SHG characterization are provided in Sec. 4.3.

Thereafter, the amplified pulses interacted with the residual of 1030 nm pulses from panel 1 in a collinear DFG stage (Fig. 3.1 panel 5) to stabilized the CEP and shift the spectral bandwidth to MIR range. A type-I BBO crystal with a thickness of 2 mm was used for the DFG at a phase-matching angle of 20°. The generated DFG beam was filtered from the other beams by a silicon plate. The DFG pulses inherit a negative dispersion, which was compensated by using a combination of SF57 and FS glasses with the lengths of 20 mm and 10 mm, respectively. This led to a pulse duration of 32 fs. Pulse characterization was carried out by using SH-FROG employing a 100μm-thick type-I BBO crystal.

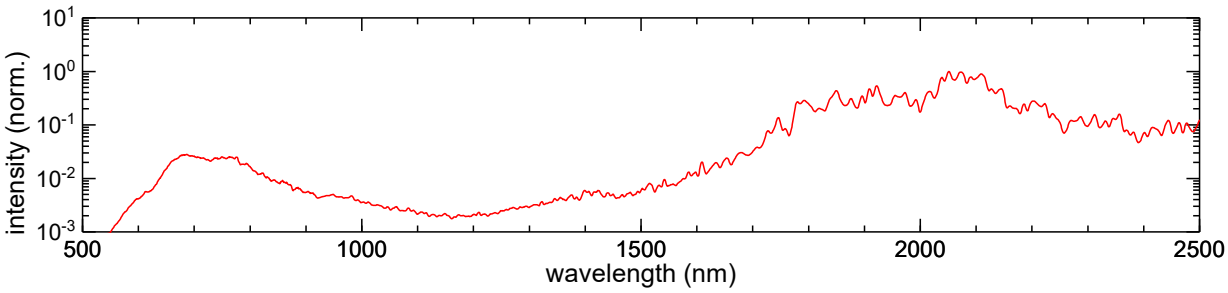

Figure 3.2: Spectrum of phase-stable multi-octave supercontinuum. The spectrum contains a pulse energy of 6 μJ and covers around 0.45 PHz of spectral bandwidth. This figure is adapted from [82].

Ultimately, the spectrum bandwidth was further extended to higher frequencies in a second YAG crystal with a thickness of 8 mm (see Fig. 3.1 panel 6). The spectrum is shown in Fig. 3.2, which was recorded by a silicon-based VIS spectrometer (Ocean Optics

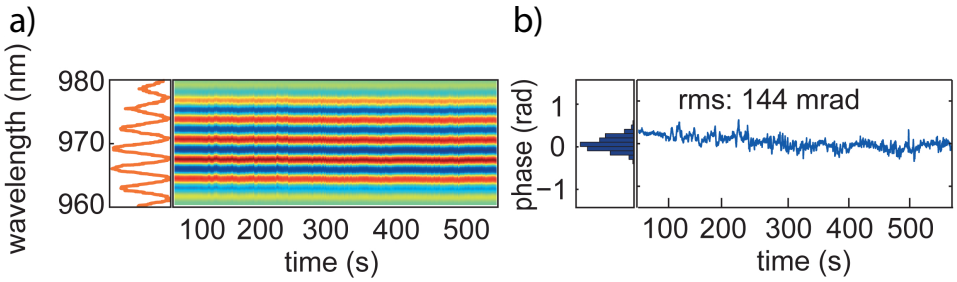

Figure 3.3: CEP stability of multi-octave supercontinuum. (a) The measured spectrogram of the interference fringes in f-2f interferometer and (b) the retrieved CEP fluctuations over a time window of 600 s. This figure is adapted from [82].

B.V, USB2000+) and two InGaAs NIR spectrometers (Ocean Optics B.V, NIRQuest-512-1.7 and NIRQuest-256-2.5). The measured spectrum, ranges from 550 nm to beyond 2500 nm, covering a spectral bandwidth of 0.45 PHz, and contains the energy of 6 μJ. The available spectrometers restricted the spectrum detection to 2520 nm, however, the retrieved spectrum of the SH-FROG measurement indicates that the seed spectrum stops at 2800 nm. The verification of the CEP stability of the generated broadband spectrum was conducted in a collinear f-2f interferometer [82]. Figure 3.3 (a) illustrates the measured trace of the CEP fluctuations of the entire spectrum over a time window of 600 s. The measurement shows an outstanding pulse-to-pulse reproducibility where the CEP jitter was approximately 144 mrad (Fig. 3.3 (b)).

3.4 Few-cycle idler generation from an angularly dispersed signal

In the current section, I propose an alternative method for generating CEP-stable MIR pulses. In the previous section, the supercontinuum pulses (Fig. 3.1 panel 2) were sent through two nonlinear stages: first, to amplify and stabilize the pulse energy via a NOPA, and, second, to CEP stabilize and shift the central frequency to the MIR in a collinear DFG. The MIR pulse generation setup in this section, the nonlinear processes were reduced by combining these stages into a single, saturated NOPA stage. However, in a NOPA due to the required non-collinear geometry for a broadband and efficient amplification, the generated idler inherits an angular dispersion, which must be compensated for. It has been shown that the angular dispersion can be compensated by using a telescope-grating after the NOPA stage [96, 97]. Alternatively, the angular dispersion can be pre-compensated by angularly dispersing the seed pulses prior to amplification [98]. I chose to compensate for the angular chirp by pre-chirping the input signal pulses to the NOPA by means of a

grating pair, motivated by the higher efficiency of grating pairs for VIS frequencies.

The presented work in this section is based on the reported results in the published article:

- A. Alismail, H. Wang, N. Altwaijry, and H. Fattahi, "Carrier-envelope phase stable, 5.4 μJ, broadband, mid-infrared pulse generation from a 1-ps, Yb:YAG thin-disk laser," *Applied Optics* **56**(17), pp. 4990–4994, 2017.

3.4.1 Experimental setup

The experimental layout is demonstrated in Fig. 3.4. 400 μJ of the total energy of the thin-disk Yb:YAG regenerative amplifier [60] was separated by using an attenuator, comprised of a TFP and a half-wave plate, which was then frequency-doubled in a BBO type-I crystal with a thickness of 1.5 mm at a phase-matching angle of 23° (Fig. 3.4 block 1).

The beam size on the crystal was adjusted to attain a peak intensity of 80 GW/cm^2. 260 μJ of energy at 515 nm was acquired, corresponding to 65 % optical-to-optical conversion efficiency. The frequency-doubling of the input pulses is necessary to ensure intrinsic CEP stability of the generated MIR pulses in the last nonlinear stage of the setup, which contains a NOPA [99].

The SH pulses are temporally shortened compared to the fundamental laser pulses at 1030 nm, due to pulse shortening based on the χ^2 effect (see Sec. 4.3.2 and Ref. [60] for more details). Afterwards, the SH beam was focused into a BaF_2 crystal with a 4 mm of thickness for XPW generation and an additional pulse shortening (see Fig. 3.4 block 2). The 466-fs-long XPW pulses were separated from the residual SH pulses by a TFP and focused in a bulk for supercontinuum generation in VIS frequencies (block 3 in Fig. 3.4) [100]. This step is necessary to achieve a stable and reproducible supercontinuum [82, 94]. Finally, the Stokes wing (lower frequencies) of the generated supercontinuum and the residual SH pulses were focused into a NOPA stage to generate broadband, CEP-stable pulses in the MIR, as shown in Fig. 3.4 block 4. More detailed discussion of each block of the setup is presented in the following sections.

3.4.2 XPW and supercontinuum driven by high-energy photons

It has been challenging to generate a supercontinuum using high-energy photons [101, 102]. As the energy of the driving photons approaches the bandgap of transparent materials, the probability of the damage due to nonlinear absorption increases. In addition, the damage threshold of transparent media is proportional to the inverse square root of the pulse-width, as a subject to the impact-ionization dynamics.

Therefore, the XPW process was used to temporally shorten the driving pulses prior to the supercontinuum generation stage due to its simplicity and self-compression, which

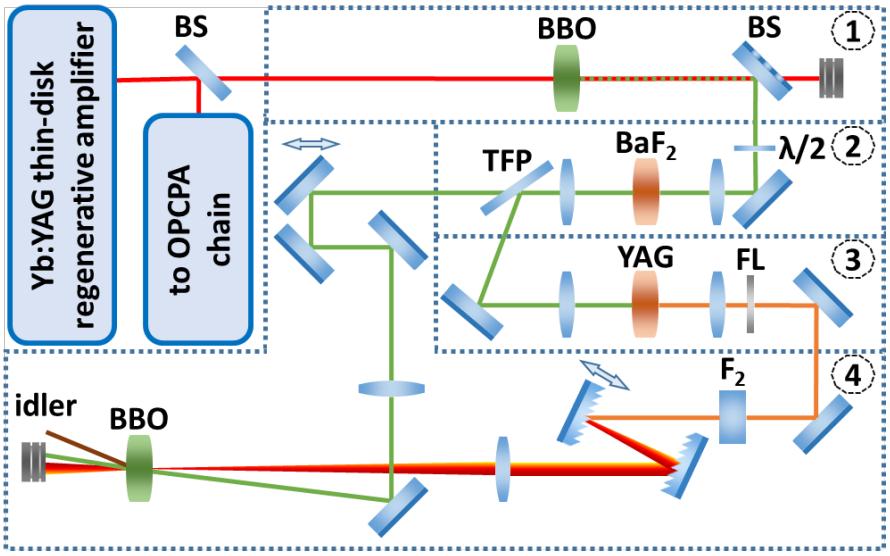

Figure 3.4: Schematic layout of a few-cycle, carrier-envelope phase-stable, idler generation. 400 μJ of a 1 ps, 20 mJ Yb:YAG, thin-disk amplifier is converted to carrier-envelope phase-stable, broadband, 5.4 μJ pulses centered at 2.1 μm. At the first, the 1 ps pulses are frequency-doubled in a BBO crystal with a 1.5 mm of a thickness (block 1). Then the 260 μJ second-harmonic beam is tightly focused into a 4-mm-thick BaF_2 crystal for cross-polarized wave generation (block 2). The 466-fs-long cross-polarized wave pulses are separated from the residual energy by means of a thin-film polarizer (block 2) and focused into a 10-mm-thick window of YAG for supercontinuum generation (block 3). The Stokes wing of the supercontinuum, centered at 680 nm, is filtered by using a 600 nm long-pass filter to serve as a signal for a NOPA. The signal pulses are sent through a grating pair and a 115-mm-thick F_2 to adjust their angular chirp and temporal duration. Finally, the signal and pump pulses are sent to a NOPA containing a 6-mm-thick BBO crystal (block 4) to generate broadband idler pulses centered at 2.1 μm. BS: beam splitter, $\lambda/2$: half-wave plate, TFP: thin-film polarizer, FL: spectral filter. This figure is adapted from [83].

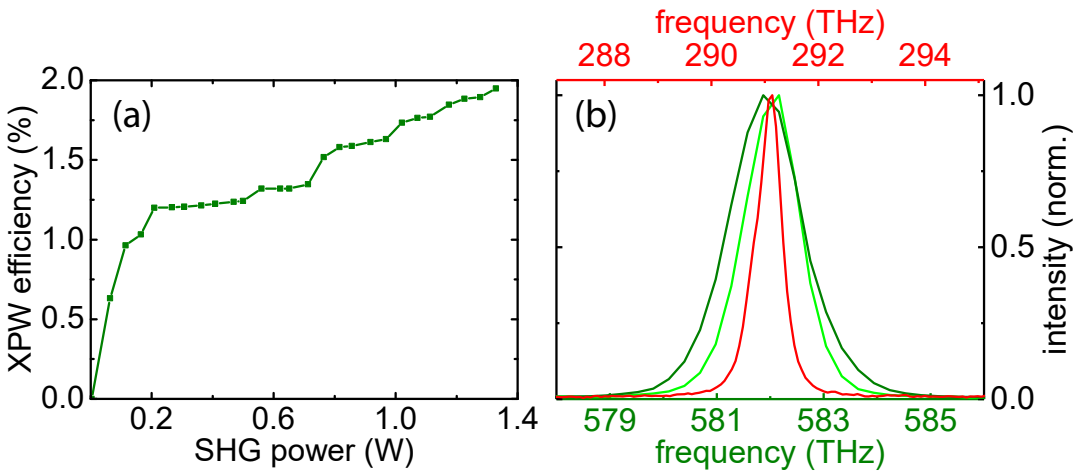

Figure 3.5: Cross-polarized waves driven by high-energy photons. (a) Optical-to-optical efficiency of the generated cross-polarized waves as a function of the power of the driving pulses (second-harmonic pulses). (b) Normalized spectra of the fundamental (red curve), the second-harmonic (light green curve), and the generated cross-polarized (dark green curve) pulses with a spectral bandwidth of 0.62 THz, 1.26 THz, and 1.64 THz (FWHM), respectively. This figure is adapted from [83].

obviates the need for any additional pulse compressor. It is known that the conversion efficiency of an XPW process is proportional to the input frequency of the driving pulses, due to the increase in the nonlinearity of materials when interacting with higher-energy photons [103]. However, for driving pulses with higher photon energies saturation occurs earlier, due to the dephasing between the driving pulses and the XPWs, limiting the conversion efficiency.

260 μJ pulses at 515 nm were used to generate XPW in a 4-mm-thick BaF_2 crystal with a holographic cut. A $f = 150$ mm convex lens was used to focus the beam, while the crystal was placed slightly after the focus. The beam size at the crystal was 260 μm at FWHM. Figure 3.5 (a) shows the optical-to-optical conversion efficiency for XPW generation. A maximum efficiency of 2 %, corresponding to 5 μJ, was achieved. Higher peak intensities on the crystal led to its optical damage. The generated XPW pulses and the residual SH pulses were both collimated by a $f = 150$ mm convex lens. A TFP was used to separate them afterward, as the XPW and SH beams have a crossed polarization. A half-wave plate before the focusing lens was used to flip the input beam polarization and to have XPW pulses reflecting from TFP. The evolution of the measured spectra at different nonlinear stages is illustrated in Fig. 3.5 (b). XPW pulses were evaluated by using a cross-correlation frequency-resolved optical gating (XFROG) employing a 100-μm-thick BBO type-I crystal. The Fourier transform-limit pulses of the Yb:YAG amplifier were used as a

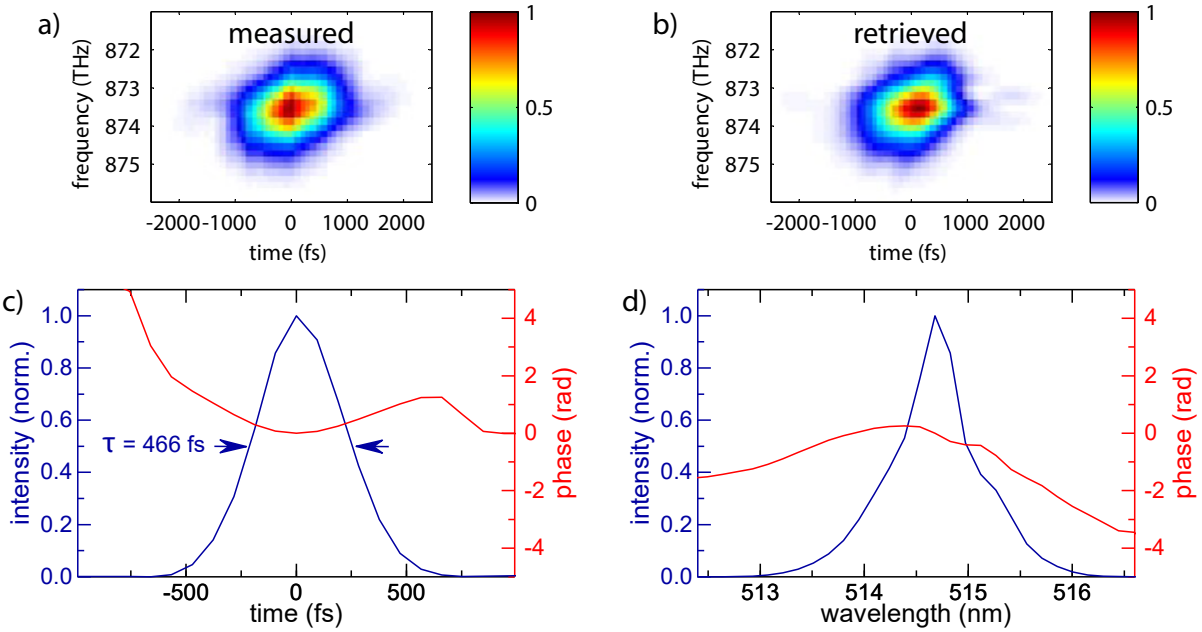

Figure 3.6: Pulse characterization of the generated cross-polarized waves. (a) Measured and (b) retrieved cross-correlation frequency-resolved optical gating spectrograms. (c) Retrieved temporal profile and the temporal phase of the cross-polarized waves with 466 fs pulse duration at FWHM. (d) Retrieved spectral intensity and the spectral phase of the cross-polarized waves ($G_{error} = 0.01544$). This figure is adapted from [83].

reference pulse for the XFROG measurement. Figure 3.6 shows the measured and retrieved XFROG spectrograms, as well as the retrieved temporal and spectral profiles of the XPW pulses with a 466 fs temporal duration (FWHM).

Thereafter, XPW pulses were focused by a $f = 125$ mm convex lens into a nonlinear medium for supercontinuum generation. I tried several nonlinear media and could achieve a stable filament only in a YAG plate with a thickness of 2 mm due to its lower critical power. This study is summarized in Table 3.1. In the final setup, I chose a 10-mm-thick plate of YAG due to the better daily reproducibility.

Figure 3.7 illustrates the spectrum and the transverse beam profiles of the generated supercontinuum in 10-mm-thick YAG. The spectra and the beam profiles of the anti-Stokes (left) and Stokes (right) wings were measured behind a 500 nm short-pass filter (Thorlabs GmbH, FES0500) and a 550 nm long-pass filter (Thorlabs GmbH, FEL0550), respectively. Both spectra were normalized to one separately. With a tighter focusing, a stable filament could be generated by using only 0.7 μJ energy and an $f = 40$ mm convex lens. However, I opted for generating a stable, single filament with the maximum pulse energy, by a careful balance between the beam size and the energy of the driving pulses. The Stokes wing of the

Table 3.1: Supercontinuum generation in different materials. The performance of different materials for supercontinuum generation driven by 466 fs pulses at 515 nm. TGG: terbium gallium garnet, ZnS: zinc sulfide. This table is adapted from [83].

crystal	thickness (mm)	critical power (MW)	band gap (eV)	filament
YAG	2	0.22	6.3	Yes
Sapphire	2	0.68	9.9	No
TGG	4	0.12	—	No
ZnS	5	0.32	3.911	No

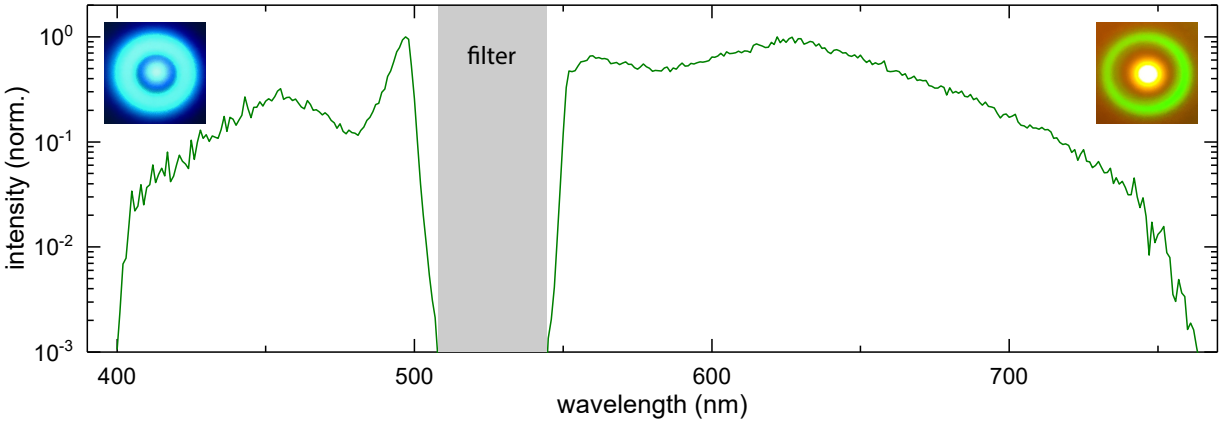

Figure 3.7: Supercontinuum driven by high-energy photons. Normalized spectrum of the generated supercontinuum in 10-mm-thick YAG. Inset: transverse beam profiles of the anti-Stokes (left) and Stokes (right) wings of the supercontinuum. This figure is adapted from [83].

supercontinuum was filtered out by a 600 nm long-pass filter (Thorlabs GmbH, FEL0600) and was collimated by a $f = 125$ mm convex lens and used to seed the NOPA stage.

3.4.3 Idler generation

To generate broadband MIR pulses, the unconverted portion of SH pulses after the XPW process (Fig. 3.4 block 2) was mixed with the Stokes wing of the supercontinuum in a NOPA. As described earlier, the generated idler in the non-collinear geometry has an angular chirp that can be pre-compensated by matching the signal pulse-front to the idler pulse-front or the propagation direction of the idler. For picosecond pump pulses, the influence of the pulse-front is insignificant and can be ignored. I chose to pre-compensate for this angular chirp by angularly dispersing the signal pulses of the NOPA, using an aluminum-coated

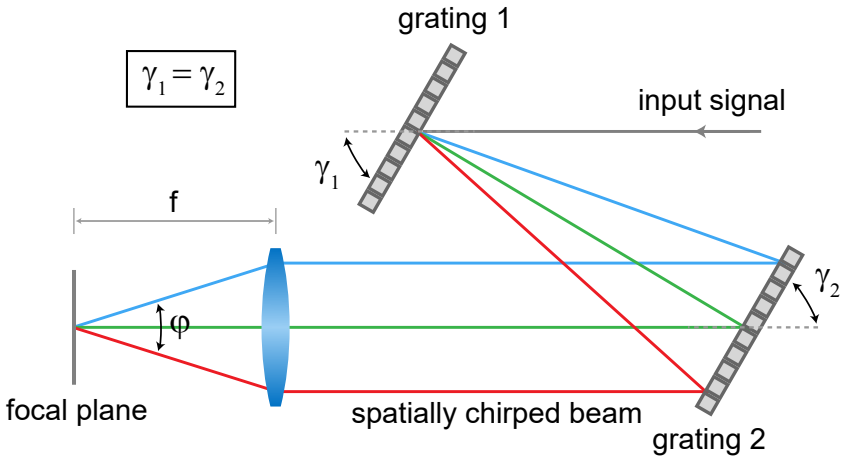

Figure 3.8: Angular dispersion of the signal beam. A spatial chirped beam is performed when the two gratings satisfy the condition $\gamma_1 = \gamma_2$. An achromatic lens focuses the frequency components of the signal at its focal plane and introduces an angular chirp in the signal's beam with a total angle of φ.

reflective grating pair, with 300 groves/mm and 8.6° blaze angle (Thorlabs GmbH, GR50-0310) [97, 98]. I avoided using a Brewster prism pair due to its undesired higher-order dispersion.

The ruled reflective diffraction grating pair produced a spatial chirp in the signal beam while ensuring the two gratings are parallel, as shown in Fig. 3.8. An achromatic lens with a focal length of 400 mm was utilized to form an angular chirp in the signal beam by focusing the different wavelengths of the signal on the same plane into the DFG crystal. For a lens with a fixed focal length, the separation between the gratings determines the applied angular dispersion to the signal. Therefore, one of the gratings was clamped on a mechanical translation stage for adjusting the distance. Increasing the distance between the grating led to the more spatial separation between the spectral components. In other words, it led to a bigger beam size on the lens and a greater angular chirp ratio ($\frac{d\varphi}{d\lambda}$). Afterwards, the angularly chirped signal pulses were amplified in a 6-mm-thick BBO type-I crystal with a phase-matching angle of 23.4° and an internal non-collinear angle of 2.4°. The pump and signal beams were focused down to 650 μm (FWHM) and overlapped spatially and temporally in the BBO crystal.

Fig. 3.9 (a) and (b) show the signal and the respective idler spectra for different cases of arrangement. In the case 1 (red curves), an angular chirp ratio of $\frac{d\varphi}{d\lambda} = 240\,\mu$rad/nm was pre-introduced to the signal. It is clear to distinguish that corresponding idler beam profile inherits an angular dispersion (Fig. 3.9 (c)). In addition to the angular chirp, the grating pair also temporally disperses the signal pulses. The GDD, induced by the grating

pair on the signal pulses, is calculated from:

$$GDD_g = -\frac{N^2\ \lambda^3}{2\ \pi\ c_0^2}\ \frac{b}{cos^3\beta} \tag{3.23}$$

where N, λ, b, c_0, and β are grating's line density, the wavelength of the incident pulse, grating separation, velocity of light, and diffraction angle from the grating of the relevant wavelength, respectively.

As a result, the signal pulses become longer than the pump pulses in the NOPA and the amplified spectral bandwidth decreases. Therefore, an additional glass plate should be added in the signal path to compensate for the introduced dispersion. The GDD given by a transmissive material can be determined by the expression:

$$GDD_m = \frac{\lambda^3}{2\ \pi\ c_0^2}\ \frac{d^2n}{d\lambda^2} \tag{3.24}$$

where n medium's refractive index of the material.

When the optimum angular chirp of the signal (220 μrad/nm) was met as case 2 (see Fig. 3.9 black curves), by adjusting the separation between the gratings precisely, the angular chirp in the idler was canceled and a nearly Gaussian beam profile was achieved (see Fig. 3.9 (d)). In this case, the decrease of the gratings separation introduces less negative GDD in the signal pulses, thus, it requires less transmissive materials for compensating the total dispersion. In the two cases, the amplification phase-matched for less bandwidth due to the residual dispersion, resulting in narrow signal and idler bandwidth.

To generate a non-angular chirp idler with a broad bandwidth, the angular chirp on the signal and its GDD need to be simultaneously controlled. Therefore, the distance of the grating pair was set to 155 mm, corresponding to a 220 μrad/nm angular chirp. In addition, a 115-mm-thick plate of flint (F_2) glass was placed in the signal beam path in order to compensate for the calculated negative chirp of the signal pulses and to adjust the temporal duration of the signal pulses within the temporal window of pump pulses at the NOPA stage. The entire GDD of the signal was estimated to be around $+300\,fs^2$. This control led to the generation of an angular-chirp-free idler, and the broadest idler bandwidth from 1.8 μm to 2.4 μm as exhibited in case 3 Fig. 3.9 (blue curves). The generated chirp-free idler pulses have similar temporal duration to the signal pulses, as their generation occurs only in the region that pump and signal pulses are temporally overlapped. The transverse spatial profile of the 5.4 μJ, broadband chirp-free idler in the far-field are shown in Fig. 3.9 (e). Table 3.2 summarizes the parameters of the three cases mentioned earlier.

The careful design of the system led to 1.35 % optical-to-optical efficiency, which is the ratio of the output pulse energy of the system to the input pulse energy. To the best of my knowledge, this is the highest reported efficiency for similar systems reported in Ref.s [82, 97, 98, 104]. Details about the comparison of these systems are summarized

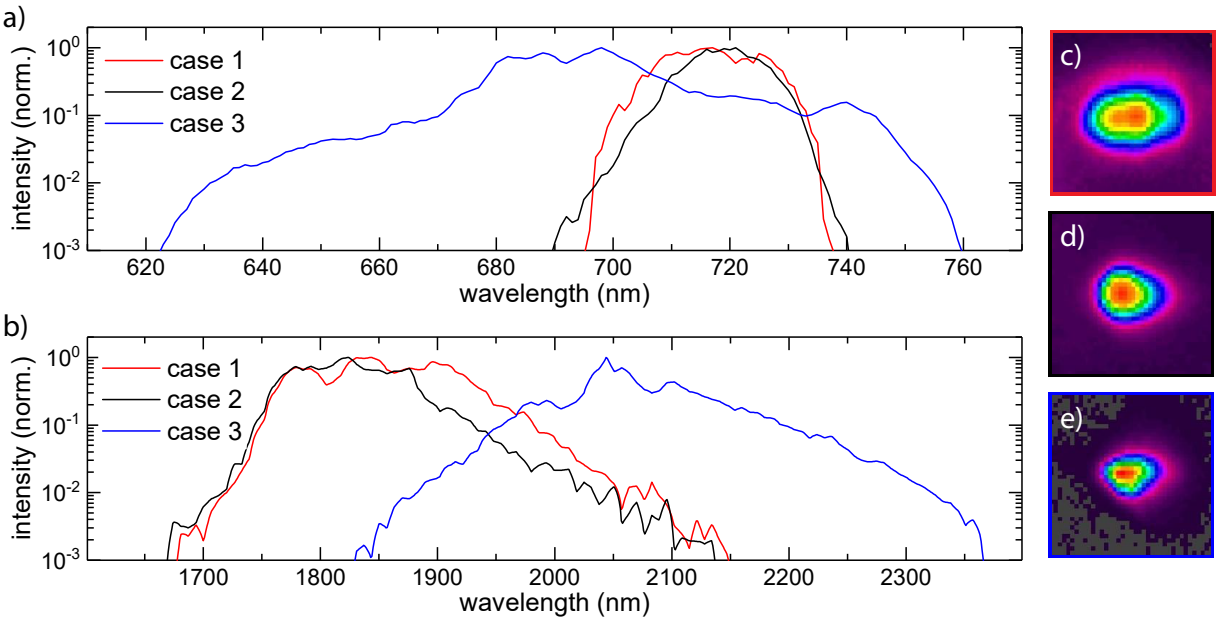

Figure 3.9: Idler generation from an angularly dispersed signal. (a) Normalized spectra of the amplified signal pulses at the NOPA containing a 6-mm-thick BBO crystal for three different cases. (b) Normalized spectra of the generated idler for three different cases. In case 3, idler's spectrum supports 37 fs (FWHM) Fourier transform-limited pulses. The transverse spatial profile of the generated idler at the focus for (c) case 1, (d) case 2, and (e) case 3. This figure is adapted from [83].

in Table 3.3. The demonstrated method in this section was motivated by scaling the efficiency of the supercontinuum generation compared to the system discussed in Sec. 3.3. However, its implantation as a seed source is beyond the scope of this thesis, since the full characterizations of this source have not been accomplished.

3.5 Conclusion

I demonstrated two compact and efficient designs to generate broadband, CEP-stable pulses driven from a 1 ps, thin-disk Yb:YAG amplifier. The first design delivers a supercontinuum with 0.45 PHz bandwidth from 550 nm to 2500 nm and 6 μJ of energy. In the second design, the broadband MIR spectrum spans from 1.83 μm to 2.36 μm and contains 5.4 μJ of energy. It is expected that the delivered pulses from this design show a similar long-term, CEP stability like the first design reported in Ref. [82].

The reported optical-to-optical conversion efficiency of the second design about 1.35 %. The microjoule, MIR pulses can be used for CEP-stable, supercontinuum generation in bulk

Table 3.2: Detailed parameters and performance of the three cases of setting reported in Fig. 3.9.

case	$\frac{d\varphi}{d\lambda}$ (μrad/nm)	GDD$_{net}$ (fs^2)	idler's bandwidth (μm)	idler's energy (μJ)
1	240	-1300	1.7-2.1	1.4
2	220	-1700	1.7-2.0	1.6
3	220	+300	1.8-2.4	5.4

Table 3.3: Efficiency comparison of several supercontinuum generation systems.

system	input energy (mJ)	output energy (μJ)	bandwidth (nm)	efficiency (%)
Ref. [97]	1.40	3.00	700-1400	0.22
Ref. [98]	0.17	0.20	1800-2400	0.12
Ref. [104]	0.65	2.40	550-1900	0.37
Ref. [104]	0.65	7.00	510-1600	1.08
Sec. 3.3 [82]	1.70	6.00	1700-2500	0.38
Sec. 3.4 [83]	0.40	5.40	1800-2400	1.35

[82, 104, 105], or hollow-core photonic crystal fibers [106], and ideal seed for broadband OPAs or waveform synthesizers, facilitating the state of the art and obviating the need for complicated optical temporal synchronization between pump and signal pulses [88, 89].

As discussed in Sec. 3.4.2, the energy threshold for generating a supercontinuum driven by 466-fs-long, 515 nm pulses is 0.7 μJ. Therefore, the required input energy to the system can be scaled down to tens of microjoules. Considering this margin, it can be simply calculated that the required input peak power to achieve a CEP-stable supercontinuum at the output of the setup is compatible with the peak power delivered by high average power oscillators such as a source reported in Ref. [57].

The opportunity of generating a super-octave, CEP-stable continuum directly from high average power, low peak power sources paves the way for a new generation of lasers, suitable for femtosecond field- and time-resolved spectroscopy in the MIR spectral range.

Chapter 4

Few-Cycle Optical Parametric Chirped Pulse Amplification Systems

The generation of few-cycle light pulses with a pulse energy of multi-millijoule is a highly focused field for a variety of applications in attosecond physics [2, 18, 107, 108] and high-field science [109, 110]. OPCPA offers few-cycle pulses that yield high pulse energies [18]. To date, OPCPA allows for broadband amplification of few-cycle pulses [111–114]. However, a modified implementation of the OPCPA scheme, which uses short pump pulses on the picosecond scale, holds promise for making this approach scalable for even higher pulse energies and average powers in the few-cycle regime [18, 91, 115]. Due to the high pump intensity in short pulse pumped OPCPA, the high single-pass gain offers for utilizing very short crystals to support broad amplification bandwidths. Despite the many benefits of pumping OPCPA with short pulses, the realizability of the mentioned approach is subject to the supply of sources that are specially tailored for this purpose. Such a pump source fulfilling these requirements have been described earlier in Chapter 2.

In the earlier chapters, the generation of the high-energy pump pulses, and the CEP-stable, multi-octave seed pulses for the OPCPA chains have been described. The current chapter focuses on the development of a few-cycle OPCPA system, consisting of NIR and MIR channels, for generating a high-energy light transient. Moreover, this chapter addresses some important considerations associated with OPA process, for instance, phase-matching condition and optical parametric gain.

The presented work in this chapter is based on the reported results in the two published articles:

- H. Fattahi, A. Alismail, H. Wang, J. Brons, O. Pronin, T. Buberl, L. Vámos, G. Arisholm, A. M. Azzeer, and F. Krausz, "High-power, 1-ps, all-Yb:YAG thin-disk regenerative amplifier," *Optics Letters* **41**(6), pp. 1126—1129, 2016.

- A. Alismail*, H. Wang*, G. Barbiero, N. Altwaijry, S. A. Hussain, V. Pervak, W.

Schweinberger, A. M. Azzeer, F. Krausz, and H. Fattahi, "Multi-octave, CEP-stable source for high-energy field synthesis," *Science Advances* **6**, p. aax4308, 2020.

4.1 Theoretical foundations of optical parametric amplification

This section studies the nonlinear interactions of OPA which was briefly described earlier in Sec. 3.1.1. There are several excellent textbooks and review articles covering the topic of OPA, such as Ref.s [85, 116–118]. This section is mainly adapted from Ref.s [85, 116]. In this process, signal and pump beams propagate in non-zero $\chi^{(2)}$ crystal (non-centrosymmetric structure). The photon energy of the pump converts to the signal photon and a new photon called idler photon. As the converted energy is conserved, the frequency components are represented as:

$$\omega_s \ + \ \omega_i \ = \ \omega_p \tag{4.1}$$

where s, i, and p indices denote for signal, idler, and pump photons, respectively.

4.1.1 Coupled-wave equations of optical parametric amplification

The physics behind the OPA process can be realized by deriving a solution of the wave equation, which was presented in Eq. 3.6. The electric field of the three waves involve in the nonlinear interaction and propagate through non-centrosymmetric crystal at z-direction describes as:

$$\begin{aligned} \widetilde{E}_s(z,t) &= A_s \ e^{i(k_s z - \omega_s t)} \ + \ c.c. \\ \widetilde{E}_i(z,t) &= A_i \ e^{i(k_i z - \omega_i t)} \ + \ c.c. \\ \widetilde{E}_p(z,t) &= A_p \ e^{i(k_p z - \omega_p t)} \ + \ c.c. \end{aligned} \tag{4.2}$$

where A is the field amplitude of the wave at a frequency of ω, and k is the wavenumber. The total electric field can be written as:

$$\widetilde{E}(z,t) \ = \ \widetilde{E}_s(z,t) \ + \ \widetilde{E}_i(z,t) \ + \ \widetilde{E}_p(z,t) \tag{4.3}$$

The polarization components of these photons can be derived from Eq. 3.7 and Eq. 4.3

as:

$$\begin{aligned}
\widetilde{P}_s^{NL} &= 4\ \epsilon_0\ d_{eff}\ A_p\ A_i^*\ e^{i(k_p-k_i)z-i\omega_s t}\ +\ c.c. \\
\widetilde{P}_i^{NL} &= 4\ \epsilon_0\ d_{eff}\ A_p\ A_s^*\ e^{i(k_p-k_s)z-i\omega_i t}\ +\ c.c. \\
\widetilde{P}_p^{NL} &= 4\ \epsilon_0\ d_{eff}\ A_s\ A_i\ e^{i(k_s+k_i)z-i\omega_p t}\ +\ c.c.
\end{aligned} \tag{4.4}$$

where $d_{eff} = \frac{\chi^{(2)}}{2}$ is the effective nonlinear coefficient. In order to introduce the signal wave equation in one-dimension, Eq. 4.3 and Eq. 4.4 are substituted into Eq. 3.6 to obtain:

$$\begin{aligned}
[\ \frac{d^2A_s}{dz^2}\ +\ 2\ i\ k_s\ \frac{dA_s}{dz}\ -\ k_s^2\ A_s\ +\ \frac{n_s^2\ \omega_s^2}{c_0^2}\ A_s\ ]\ e^{ik_s z}\ e^{-i\omega_s t}\ +\ c.c. \\
=\ -\ 4\ \epsilon_0\ \mu_0\ d_{eff}\ \omega_s^2\ A_p\ A_i^*\ e^{i(k_p-k_i)z}\ e^{-i\omega_s t}\ +\ c.c.
\end{aligned} \tag{4.5}$$

The second derivative of the complex amplitude can be neglected in this equation by assuming a slowly varying amplitude approximation, where $|\frac{d^2A_s}{dz^2}| \ll |k_s \frac{dA_s}{dz}|$. Further simplification can be made since $k_s = \frac{n_s\omega_s}{c_0}$ and $c_0 = \frac{1}{\sqrt{\epsilon_0\mu_0}}$, to gain the coupled-wave equation for signal wave:

$$\frac{dA_s}{dz} = \frac{2\ i\ d_{eff}\ \omega_s^2}{c_0^2\ k_s}\ A_p\ A_i^*\ e^{i\Delta k z} \tag{4.6}$$

where $\Delta k = k_p - (k_s + k_i)$ is the wavenumber mismatch. In the same manner, the coupled-wave equations of the idler and pump waves can be found as:

$$\begin{aligned}
\frac{dA_i}{dz} &= \frac{2\ i\ d_{eff}\ \omega_i^2}{c_0^2\ k_i}\ A_p\ A_s^*\ e^{i\Delta k z} \\
\frac{dA_p}{dz} &= \frac{2\ i\ d_{eff}\ \omega_p^2}{c_0^2\ k_p}\ A_s\ A_i\ e^{-i\Delta k z}
\end{aligned} \tag{4.7}$$

4.1.2 phase-matching

The nonlinear effects are dramatically low for a nonlinear medium under general conditions. These effects can be enhanced by decreasing the value of Δk. The amplitude of the signal wave after propagation distance of L into a nonlinear crystal can be estimated by

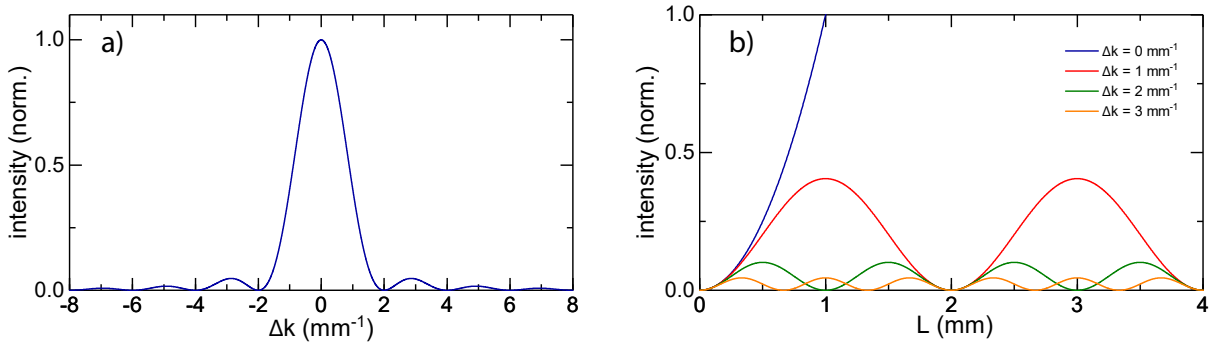

Figure 4.1: Phase-matching condition. (a) The wavenumber mismatch versus the signal intensity. (b) The evolution of the signal intensity along the crystal for different wavenumber mismatch values.

integrating Eq. 4.6 along the crystal thickness as:

$$\begin{aligned} A_s(L) &= \frac{2\ i\ d_{eff}\ \omega_s^2}{c_0^2\ k_s}\ A_p\ A_i^* \int_0^L e^{i\Delta k z}\ dz \\ &= \frac{2\ d_{eff}\ \omega_s^2}{c_0^2\ k_s}\ A_p\ A_i^*\ [\ \frac{e^{i\,\Delta k\,L}\ -\ 1}{\Delta k}\ ] \end{aligned} \tag{4.8}$$

Since the intensity of the wave at frequency ω_j is $I_j = 2\epsilon_0 c_0 n_j |A_j|^2$, the intensity of the signal wave can be evaluated as:

$$I_s = \frac{2\ d_{eff}^2\ \omega_s^2}{\epsilon_0\ c_0^3\ n_s\ n_i\ n_p}\ I_p\ I_i\ L^2\ sinc^2(\frac{\Delta k\,L}{2}) \tag{4.9}$$

As seen in Eq. 4.9, it is clear that the signal's intensity has a maximum value when $\Delta k = 0$ (see Fig. 4.1 (a)). Figure 4.1 (b) shows the intensity evolution along the crystal length. It can be observed that the intensity dramatically increases when $\Delta k = 0$. In other words, the signal's intensity can be maximized by satisfying the following:

$$k_s\ +\ k_i\ =\ k_p \tag{4.10}$$

This equation is known as the phase-matching condition. Therefore, the efficiency of the parametric amplification of the signal can be increased by fulfilling this condition. Moreover, the phase-matching condition can be also written in the form:

$$n_s\ w_s\ +\ n_i\ w_i\ =\ n_p\ w_p \tag{4.11}$$

However, this condition is difficult to achieve in usual circumstances. There are many approaches which can be used to achieve the phase-matching condition, for instance angle phase-matching, quasi-phase-matching, and temperature phase-matching. In the angle phase-matching approach, the condition satisfaction calls for the use of birefringence crystals. In these crystals, the refractive index relies on the polarization of the incident beam, its propagation direction, and the type of the crystal. The nonlinear crystals can be classified into two types: i) uniaxial crystals, and ii) biaxial crystals.

In a uniaxial crystal, an extraordinary beam, polarized along the principal plane of the crystal (contains k-vector of the propagated beam and optical axis of the crystal), faces a different refractive index compared to the ordinary beam polarized perpendicular to the principal plane. This difference can be varied by changing the angle (θ) of the incident beam with respect to the optical axis of the crystal. Therefore, the wavenumber mismatching can be minimized by controlling this variation. The refractive index as a function of the angle θ in a uniaxial crystal can be expressed as:

$$n^e(\theta) \;=\; \frac{n^o\; n^e}{\sqrt{\;(n^o)^2\; sin^2\theta \;+\; (n^e)^2\; cos^2\theta}} \tag{4.12}$$

where n^o and n^e are the refractive indices of the ordinary and extraordinary beams, respectively. The uniaxial crystals are classified into positive crystals (where $n^o > n^e$) and negative crystals (where $n^o < n^e$). There are three configurations of beam interactions in the uniaxial crystal to satisfy the phase-matching condition of the OPA process. In the case of a negative uniaxial crystal (for instance BBO crystal), these configurations are listed as:

$$\begin{aligned}
&n_s^o\; w_s \;+\; n_i^o\; w_i \;=\; n_p^e(\theta)\; w_p && (type-I, ooe-interaction)\\
&n_s^o\; w_s \;+\; n_i^e(\theta)\; w_i \;=\; n_p^e(\theta)\; w_p && (type-II, oee-interaction)\\
&n_s^e(\theta)\; w_s \;+\; n_i^o\; w_i \;=\; n_p^e(\theta)\; w_p && (type-II, eoe-interaction)
\end{aligned} \tag{4.13}$$

where θ is defined as a phase-matching angle confined between the optical axis of the crystal and the pump beam.

In biaxial crystals, such as lithium triborate (LBO) (LiB_3O_5) crystal, the three principal axes possess different refractive indices, therefore, the refractive index dependency becomes increasingly complicated comparing to uniaxial crystals. A detailed description of this dependency can be found in Ref. [119]

In the case mentioned above, all the wave-vectors of the interaction beams were supposed to have the same direction, which is denominated as collinear configuration (see Fig. 4.2 (a)). However, the signal and idler pulses temporally separate from each other after a short propagation distance (temporal walk-off) as a consequence of the disper-

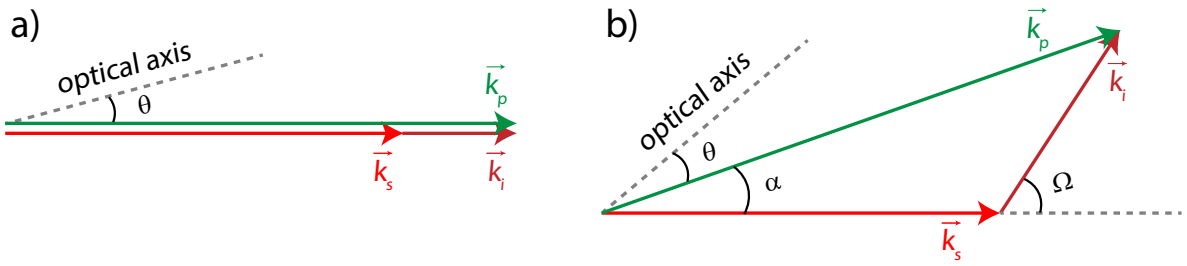

Figure 4.2: Phase-matching configuration. (a) Collinear and (b) non-collinear configurations. The angle Ω defines the angle between the signal and idler beams.

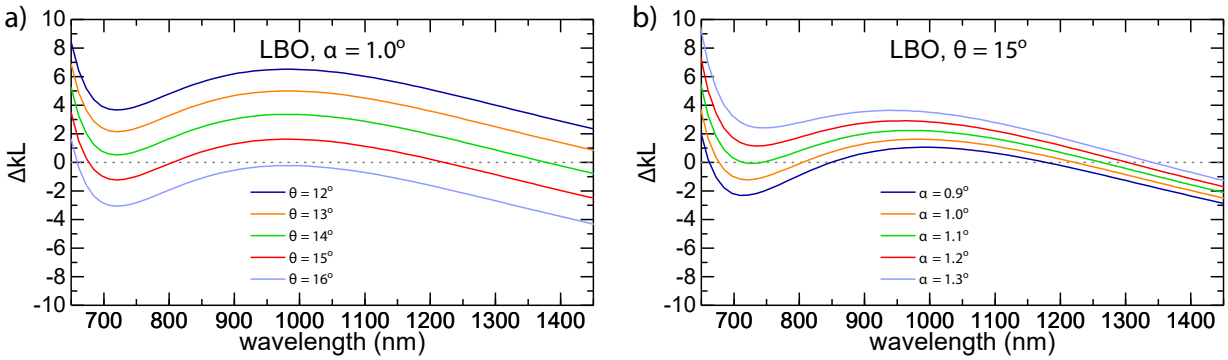

Figure 4.3: Numerical evaluation of phase-mismatch of the signal wave in an LBO crystal. The signal wavelength versus the phase-mismatch for: (a) different phase-matching angles and fixed non-collinear angle, and (b) different non-collinear angles and fixed phase-matching angle. The 4 mm LBO crystal was pumped with pulses at wavelength of 515 nm.

sion of the crystal. Therefore, this results in a limited phase-matching bandwidth. In a non-collinear configuration as shown in Fig. 4.2 (b), an internal non-collinear angle (α) is introduced between the signal and pump wave vectors which allows compensating for the temporal walk-off and supports a broader bandwidth amplification. The phase-matching condition of the NOPA can be determined as:

$$(n_i\ \omega_i)^2 \ = \ (n_p\ \omega_p)^2 \ + \ (n_s\ \omega_s)^2 \ - \ 2\ n_s\ n_p\ \omega_s\ \omega_p\ cos\,\alpha \tag{4.14}$$

Figure 4.3 shows the phase-mismatching ($\Delta k\,L$) as a function of the signal wavelength in an LBO crystal by utilizing a non-collinear configuration. The phase-mismatch was numerically evaluated by using Simulation System for Optical Science (SISYFOS) code [120] by assuming the use of 4 mm LBO type-I crystal pumped with 515 nm pulses. In Fig. 4.3 (a), the phase-mismatch was calculated for different phase-matching angles and an arbitrary non-collinear angle. While in Fig. 4.3 (b), the phase-mismatch was calculated by

varying the non-collinear angle at a fixed phase-matching angle. A broadband signal spectrum spanning from 700 nm to 1400 nm can be obtained at the optimum phase-matching angle ($\theta = 15°$) and non-collinear angle ($\alpha = 1.1°$).

4.1.3 Optical parametric gain

In this section, I treat the evolution of the optical parametric amplification along the crystal. By starting from the derivative of the coupled-wave equations of the signal (Eq. 4.6) and assuming the approximation of the undepleted pump to obtain:

$$\frac{d^2 A_s}{dz^2} \;=\; \Gamma^2 \; A_s \;+\; i \; \Delta k \; \frac{dA_s}{dz} \tag{4.15}$$

where the quantity Γ^2 is expressed as:

$$\Gamma^2 \;=\; \frac{4 \; d_{eff}^2 \; \omega_s^2 \; \omega_i^2}{c_0^4 \; k_s \; k_i} \; |A_p|^2 \;=\; \frac{2 \; d_{eff}^2 \; \omega_s \; \omega_i}{\epsilon_0 \; c_0^3 \; n_s \; n_i \; n_p} \; I_p \tag{4.16}$$

The solution of this partial differential equation (Eq. 4.16) by applying the boundary condition ($A_i(0) = 0$) can be derived as:

$$A_s(z) \;=\; A_s(0) \; e^{\frac{i \Delta k z}{2}} \; [\; cosh(gz) - i \; \frac{\Delta k}{2 \; g} \; sinh(gz) \;] \tag{4.17}$$

where the small gain (g) is expressed as:

$$g \;=\; \sqrt{\Gamma^2 \;-\; \left(\frac{\Delta k}{2}\right)^2} \tag{4.18}$$

The pump power threshold ($u_p^{(th)}$) for signal amplification can be estimated from the small gain, when $\Gamma^2 = \left(\frac{\Delta k}{2}\right)^2$, as:

$$u_p^{(th)} \;=\; \frac{\pi \; \epsilon_0 \; c_0^3 \; n_s \; n_i \; n_p \; w_p}{4 \; d_{eff}^2 \; \omega_s \; \omega_i} \; \left(\frac{\Delta k}{2}\right)^2 \tag{4.19}$$

where w_p is the pump beam radius. The intensity gain of the signal wave can be derived from the ratio of signal's intensity after the crystal ($I_s(L)$) and the initial signal's intensity ($I_s(0)$) as:

$$G(L) \;=\; \frac{I_s(L)}{I_s(0)} \;=\; 1 \;+\; \frac{\Gamma^2}{g^2} \; sinh^2(gL) \tag{4.20}$$

Figure 4.4 (a) shows the numerical simulation of the gain bandwidth of the seed pulses by using SISYFOS code [120]. Here, the seed spectrum (shown earlier in Fig. 4.3) was amplified in a single amplification stage pumped at 515 nm. The pump's beam size was

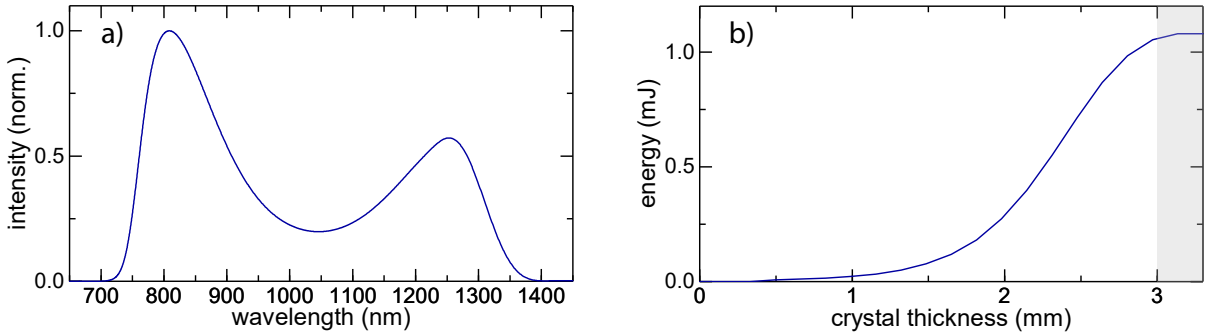

Figure 4.4: Simulated parametric gain of the signal wave in an LBO crystal. (a) The amplified signal's spectrum in an LBO crystal with a thickness of 3 mm pumped with pulses at wavelength of 515 nm. (b) The amplified pulse energy as a function of the crystal thickness. The gray-shaded area indicates the saturation zone.

adjusted to the peak intensity of 100 GW/cm^2. The parametric amplification was formed in a 3 mm LBO crystal with a phase-matching angle of 15.5°, an internal non-collinear angle of 1.05°, and d_{eff} = 0.82 pm/V. As can be seen in Fig. 4.4 (b), the amplified pulse energy reaches the saturation after a certain propagation length (gray-shaded area). The following sections is devoted to the experimental results.

4.2 Experimental setup

A layout of the OPCPA channels is depicted in Fig. 1.2. A broadband dielectric beam splitter [121] was used to divide the seed spectrum reported in Sec. 3.3 into two portions: i) NIR region from 700 nm to 1400 nm, and ii) MIR region with spectral coverage from 1600 nm to 2500 nm. The remaining energy of the Yb:YAG amplifier was frequency-doubled in a 0.5 mm-thick type-I, BBO crystal at 80 GW/cm^2 peak intensity. The SH module delivers 9 mJ pulses at 515 nm. Thereafter, the SH pulses were separated from the fundamental pulses by a dielectric beam splitter. The generation of the SH is described in sufficient detail in the next section. The spectrum in the NIR region was amplified in the NIR channel pumped by the SH pulses, while the energy of the second portion of the spectrum was boosted in the MIR channel by the fundamental pulses. An individual description of each channel is provided in Sec. 4.4 and Sec. 4.5.

4.3 Second-harmonic generation

As seen earlier, each spectral region of the broadband seed spectrum is parametrically amplified by the fundamental or lower harmonics of the pump pulses. Specifically in NIR channel, due to the condition of energy conservation, the parametric amplification calls for higher pump frequency (SHG of the Yb:YAG amplifier) compared to the seed frequencies. In the following, I deal with the SHG prior to the amplification in the NIR channel. This includes the consideration of the candidate crystals and the characterization of the conversion efficiency.

4.3.1 Crystal selection

Amongst a wide variety of nonlinear crystals for SHG, BBO and LBO were adopted as the best selections, as they offer a high nonlinear coefficient and damage threshold. The nonlinearity in BBO is greater than LBO, however, it has a larger spatial walk-off. In addition, the available aperture is limited in the case of BBO.

The performances of both crystals were analyzed and compared in a designed SHG stage by using the SISYFOS code [120]. In this code, optical parametric frequency conversions in nonlinear media are simulated in three-dimensions by utilizing a split-step Fourier method. SISYFOS code solves the coupled differential equations for the slowly varying amplitudes. This model can take into account most of the relevant physical effects in the frequency conversion such as propagation effects, second- and third-order nonlinearities, thermal effects, two-photon absorption, and non-collinear interactions. In this numerical simulation, I neglected the thermal effects, third-order nonlinear processes, and two-photon absorption. In the same fashion of the experiment, I considered the pump pulses with temporal and spatial Gaussian profiles. For BBO, phase-matching angle $\theta = 23.4°$ and a d_{eff} value of 2 pm/V were considered. For LBO, phase-matching angle of 13.7° and $d_{eff} = 0.819$ pm/V were also considered. The Sellmeier coefficients of these crystals were obtained from Ref.s [122, 123]. 1 ps (FWHM), 20 mJ pulses at 1030 nm were considered as the input of the simulation. The beam's size was adjusted for 100 GW/cm^2 peak intensity.

Figure 4.5 depicts the energy of SHG at wavelength of 515 nm versus a type-I, 3 mm-thick BBO and a type-I, 6 mm-thick LBO crystals. A similar maximum conversion efficiency can be attained in both crystals. The maximum is reached after longer propagation in LBO. This is the result of the smaller spatial walk-off between the fundamental and the SH beams in LBO crystal. The saturation of the SHG energy occurs at crystal thickness of 1.5 mm in BBO, and 3 mm in LBO crystal. After these lengths, an energy back conversion from the SH pulses to the fundamental pulses was observed. As the nonlinear coefficient of BBO is almost twice of the LBO, a shorter BBO crystal is sufficient to reach the saturation for SHG. Therefore, BBO is the more suitable choice, as the accumulated nonlinear phase

is smaller [124].

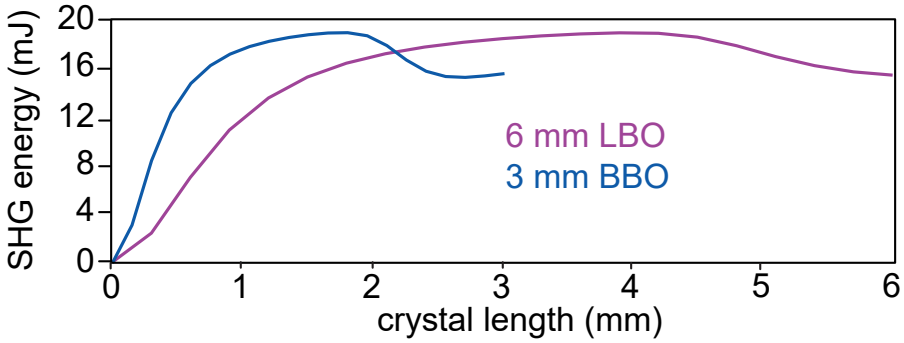

Figure 4.5: Second-harmonic generation crystals. The simulated energy of the second-harmonic generation in BBO and LBO crystals with a thickness of 3 mm and 6 mm, respectively. This figure is adapted from [60].

4.3.2 Spectral phase in saturated second-harmonic generating

High conversion efficiency has an impact on the SHG. Such impact has been numerically and experimentally investigated in Ref. [125]. A back conversion of SH photons into fundamental photons can occur at the saturation regime. This leads to pump depletion and limits the use of the unconverted pump pulses. Moreover, it is accompanied by a phase modulation on the spectral components of the SHG. These phenomena were referred to as the contribution of the cascaded second-order nonlinearity in the SHG process. In what follows, SHG characterization in BBO crystal is carried out for different conversion efficiencies.

Based on the earlier simulation, I opted for a BBO crystal with a thickness of 1.5 mm for the frequency-doubling of the output of the amplifier. 1.6 mJ at 1030 nm was sent to 1.5-mm-thick, type-I, BBO crystal (CASTECH Inc.) to generate SH pulses at 515 nm resulting in a maximum 70 % of conversion efficiency. A lens telescope was utilized before the nonlinear crystal to reduce the beam size to the peak intensity of 80 GW/cm^2. The SHG conversion efficiency is depicted in Fig. 4.6. An XFROG employing a BBO crystal with a thickness of 100 μm was used to estimate the temporal duration of the SH pulses, gated by the fundamental pulses (1 ps). SH pulse gets shorter compared to the fundamental pulse due to the second-order nonlinearity by a factor of $\sqrt{2}$. The measured pulse duration was 0.74 ps in case A (at conversion efficiency of 50 %) (see Fig. 4.7).

In order to define the ideal regime of operation, three different cases of conversion efficiency, corresponding to points A, B, and C in Fig. 4.6 were characterized. Figure 4.8 (a) illustrates the retrieved spectral intensity of the SH pulses in the three cases. It was

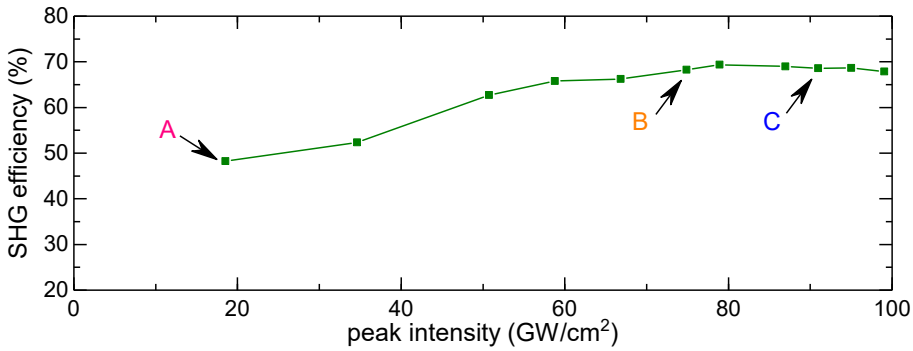

Figure 4.6: Conversion efficiency of the second-harmonic generation (SHG). The input pump peak intensity versus the experimental second-harmonic efficiency in a BBO crystal with a thickness of 1.5 mm utilizing 1.6 mJ of the amplifier output. This figure is adapted from [60].

observed that at high conversion efficiencies, the SHG spectrum is broadened and a higher-order spectral phase appears. Figure 4.8 (b) shows the group delay as a function of the wavelength for both cases. In case C, the spectrum was modulated with a central dip due to the energy back conversion. Therefore, case B with a peak intensity of 80 GW/cm^2 was chosen where the SH and the unconverted fundamental beams maintain excellent quality. Further reduction in the crystal thickness to 0.5 mm was made to equally distribute the pulse energy between the fundamental and SH pulses. Thereafter, as the two beams are orthogonally polarized, the second harmonic beam was separated from the fundamental by a harmonic beam splitter (Eksma Optics, 045-5135). In addition, the thermal effects in the SHG setup were monitored by using the total energy (20 mJ) of the amplifier, resulting in a SH pulse energy of 9 mJ at 515 nm, and no thermal load on the crystal was detected.

4.4 Near-infrared optical parametric chirped pulse amplification channel

As seen earlier in Sec. 4.2, the spectrum in the NIR region (700 nm-1400 nm) was separated from the remaining spectrum by a broadband dielectric beam splitter [121]. In this section, the amplification of this spectrum portion in the NIR channel by the SH pulses at 515 nm is discussed.

In NIR channel, the SH pump at 515 nm with energy of 0.8 mJ was temporally and spatially overlapped with the NIR spectral region of the seed in a single-stage NOPA, containing a 4-mm-thick LBO crystal at a non-collinear internal seed-pump angle of 1.05°, and a phase-matching angle of $\phi = 15°$ in type-I configuration. The crystal length was

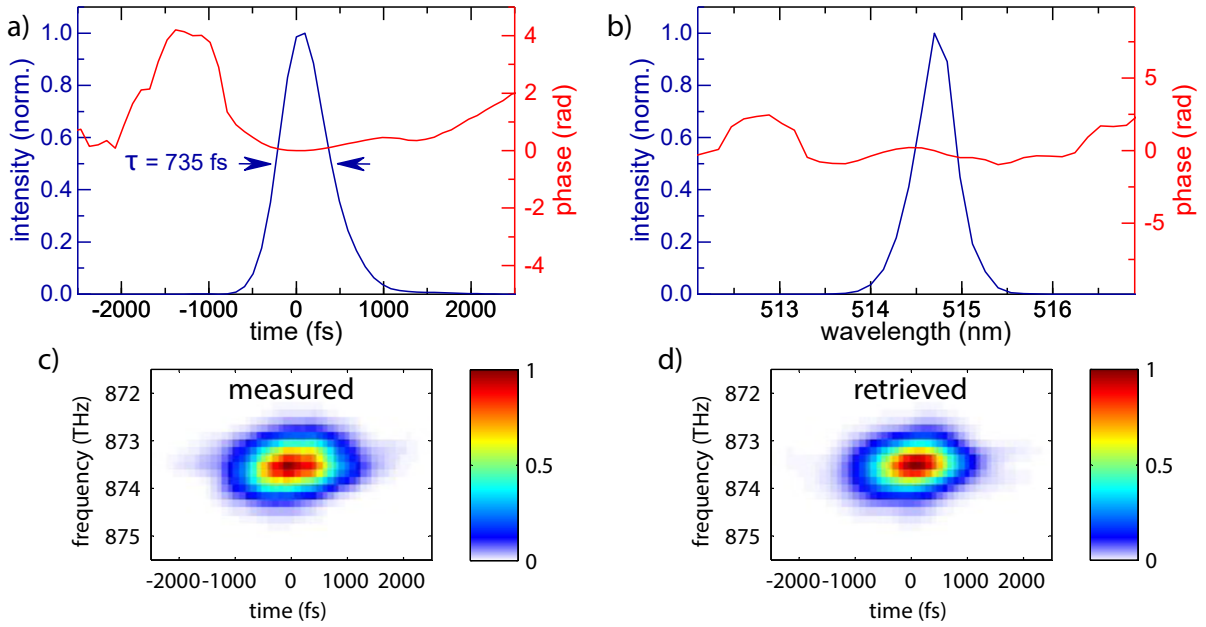

Figure 4.7: Pulse characterization of the second-harmonic generation at conversion efficiency of 50 %. (a) The retrieved temporal intensity profile and its temporal phase. (b) The retrieved spectrum including the spectral phase. (c) The measured and (d) the retrieved cross-correlation frequency-resolved optical gating spectrographs of the second-harmonic pulses ($G_{error} = 0.0138$).

chosen to reach saturation before the back conversion of signal photons into pump photons starts. The crystal was placed after the focus of the SH pump beam to diminish the influence of self-focusing. The beam size of the pump at the nonlinear crystal was 850 μm (FWHM), corresponding to a peak intensity of 130 GW/cm^2. The seed beam profile was focused by a concave spherical mirror ($R = 900$ mm) to a spot size of 650 μm (FWHM) matching approximately 80 % of the pump beam. Figure 4.9 shows the amplification gain and efficiency versus the pump energy. After the parametric gain, the amplified signal beam was collimated by another concave spherical mirror ($R = 900$ mm) and sent to a custom-designed chirped mirrors compressor. The residual pump component was removed by a 700 nm long-pass filter (Thorlabs GmbH, FEL0700) from the amplified signal.

The amplified spectrum is shown in Fig. 4.10 (orange curve). It exhibits a bandwidth of 230 THz and the amplified signal pulses yield 20 μJ of energy. The amplified pulses were initially sent to a SH-FROG, containing a 10-μm-thick BBO crystal, in order to evaluate their spectral phase. Solid curves in Fig. 4.11 (a) show the retrieved spectral phase (blue) and the group delay (GD) (red) over the entire bandwidth. This evaluation was taken into account for designing the double-angle chirped mirrors compressor. The

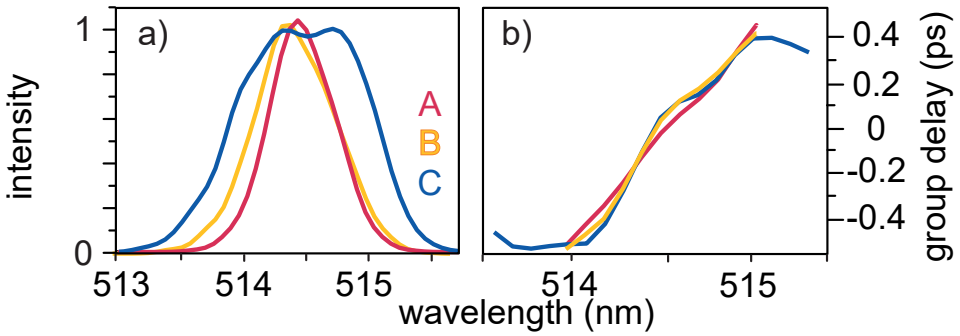

Figure 4.8: Retrieved spectrum of different second-harmonic generation efficiencies. (a) The retrieved spectral intensity and (b) the group delay of cross-correlation frequency-resolved optical gating measurements for different second-harmonic efficiencies corresponding to points A, B, and C in Fig. 4.6. This figure is adapted from [60].

design considers i) introducing smooth and negative value of GDD, ii) high-order dispersion compensation, and iii) high reflectivity along the desired wavelength range. The analytic design of double-angle chirped mirrors (UltraFast Innovations GmbH, PC132) is shown in Fig. 4.12 for two incident angles at 5° and 18°. Red and blue curves illustrate the calculated spectral oscillations and the reflectivity at incident angles of 5° and 18°, respectively. The black curve shows averaged GDD with -30 fs^2 per bounce.

Thereafter, the amplified signal pulses were compressed in a compressor setup consisting of 16 bounces. A fine compensation of the residual spectral dispersion was performed by a pair of thin fused-silica wedges inserted after the compressor at a Brewster angle. A SH-FROG containing a 10-μm-thick BBO crystal was used to characterize the compressed pulses. Figure 4.13 (a) and (b) illustrate the measured and retrieved spectrograms of the compressed pulses. The retrieved temporal intensity profile and spectral intensity of the compressed pulses are shown in Fig. 4.13 (c) and (d). A compressed pulse duration of 6 fs (FWHM) was obtained, corresponding to 1.35 cycles of the 1 μm carrier wavelength. The residual spectral phase and GD of the compressed pulses are shown in Fig. 4.11 (a) (dashed curves) and with zoom in Fig. 4.11 (b). Afterwards, the compressed signal was only guided by reflective optics to avoid introducing an additional dispersion within its propagation path.

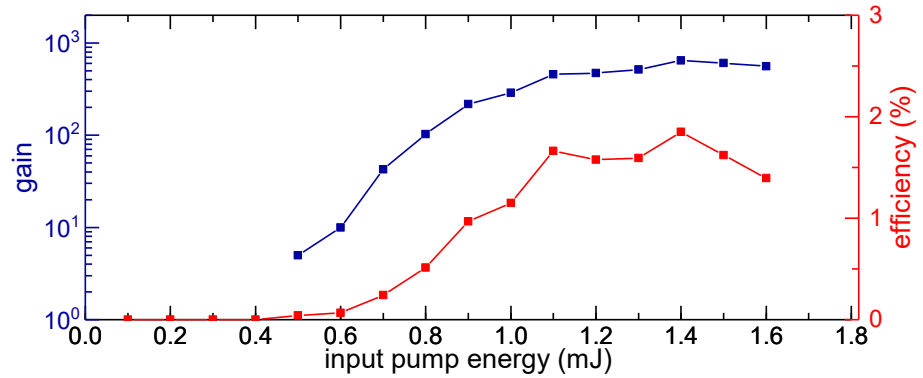

Figure 4.9: Parametric gain evaluation of the first stage of near-infrared optical parametric chirped pulse amplification channel. Gain curve and amplification efficiency as a function of the pump energy.

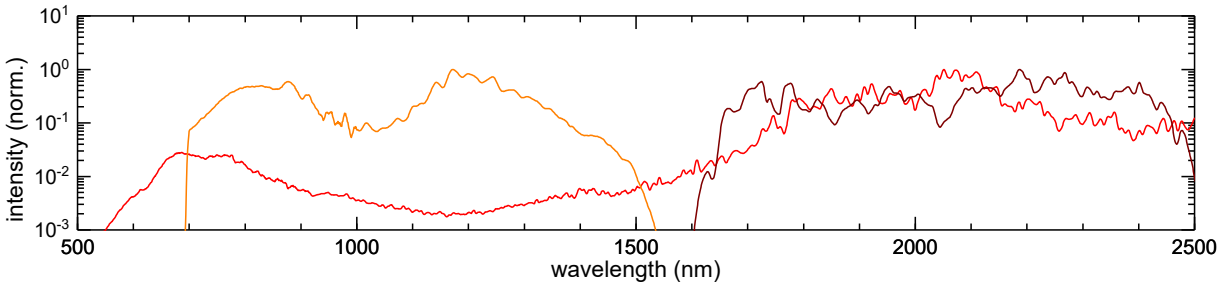

Figure 4.10: Amplified spectra in the optical parametric chirped pulse amplification channels. CEP-stable, multi-octave spectrum of seed pulses (red). Amplified spectra of near-infrared (orange) and mid-infrared (brown) optical parametric chirped-pulse amplification channels [29].

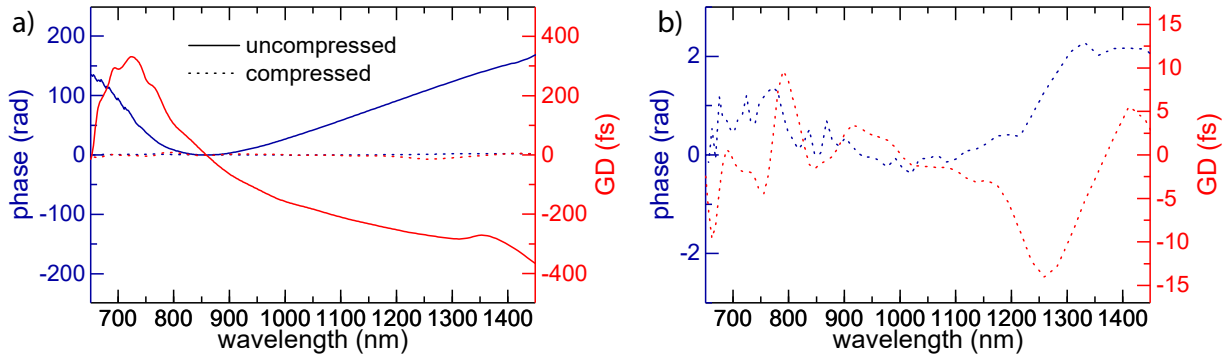

Figure 4.11: Spectral characterization of the amplified pulses in the first stage of near-infrared channel. (a) Wavelength versus the spectral phase and the group delay of the uncompressed (solid line) and compressed (dashed line) pulses. (b) Zoomed plot of the residual spectral phase and group delay (GD) of the compressed pulses.

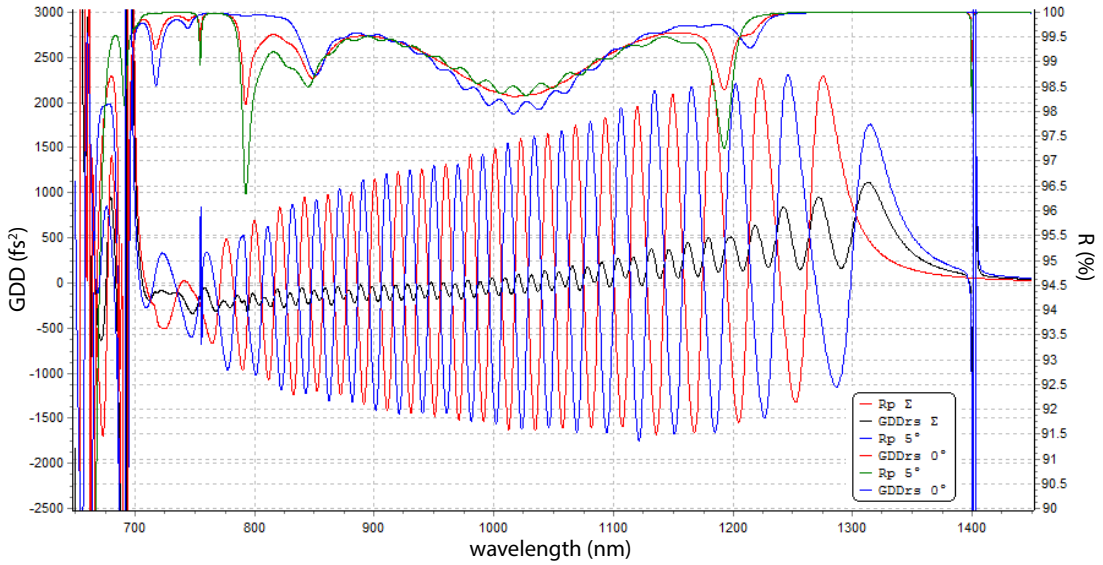

Figure 4.12: Design of the custom double-angle chirped mirrors (PC132) utilized in the first stage of near-infrared channel for temporal compression. Theoretical curves of group delay dispersion (GDD) and reflectivity (R) of the double angle chirped mirrors at incident angles of 5° (red) and 18° (blue) as function of the wavelength. The black line illustrates the average of the group delay dispersion oscillations.

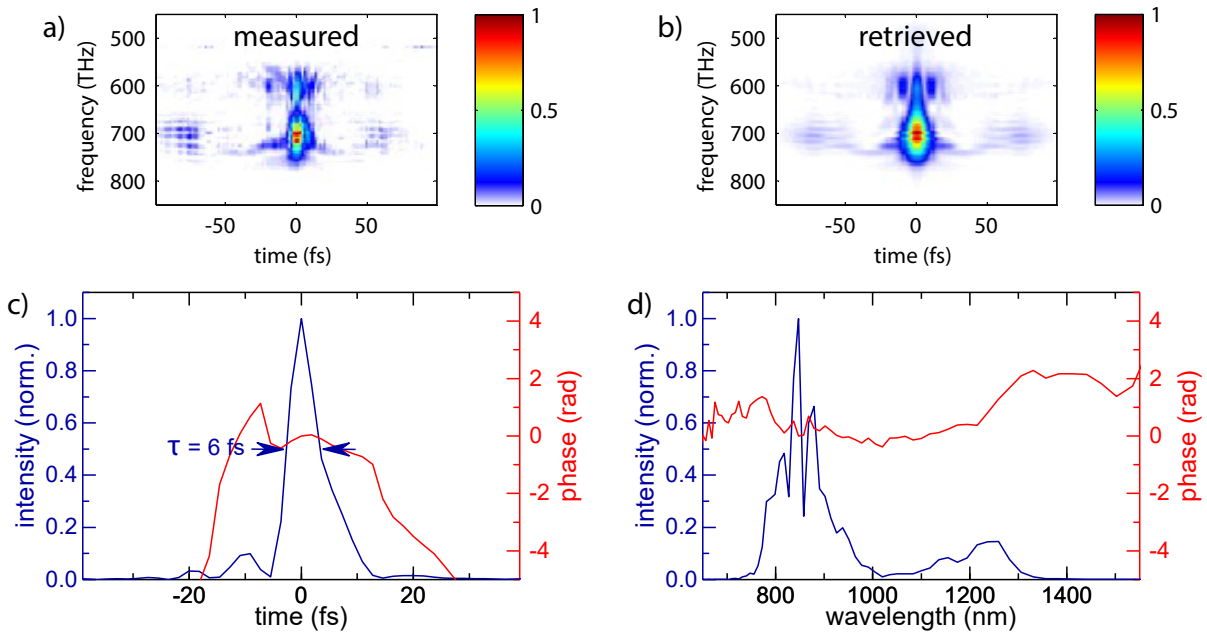

Figure 4.13: Pulse characterization of the near-infrared channel. (a) Measured and (b) retrieved second-harmonic frequency-resolved optical gating spectrograms. (c) Retrieved temporal profile and the temporal phase of the compressed near-infrared pulses with 6 fs pulse duration at FWHM. (d) Retrieved spectral intensity and the spectral phase of the compressed near-infrared pulses ($G_{error} = 0.0262$) [29].

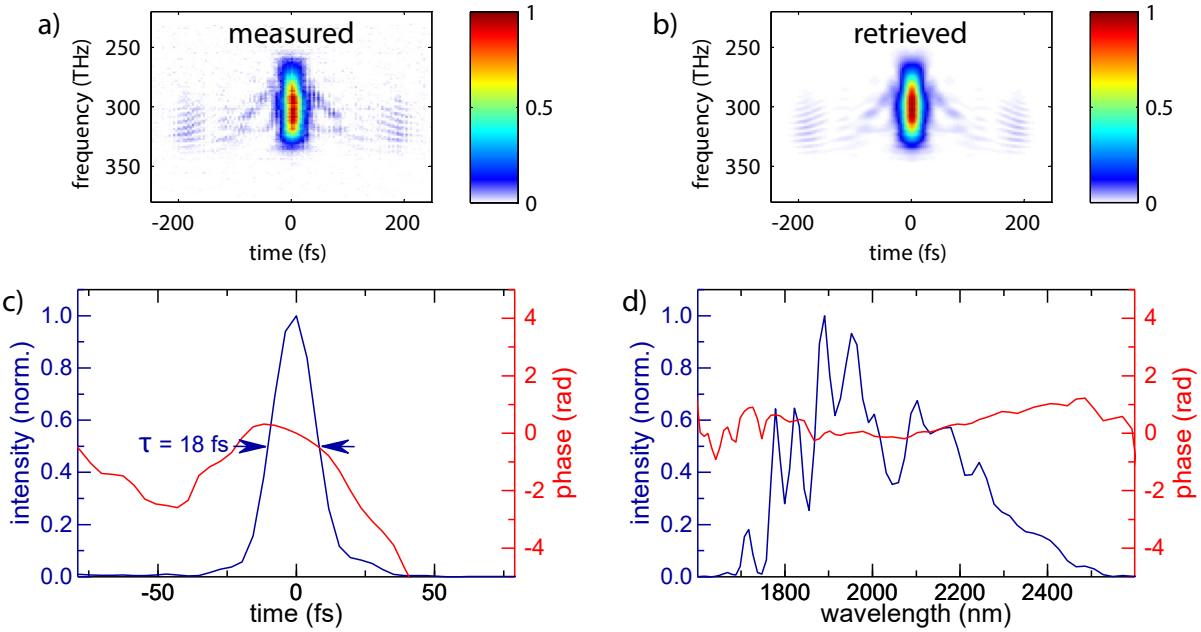

Figure 4.14: Pulse characterization of the mid-infrared channel. (a) Measured and (b) retrieved frequency-resolved optical gating spectrograms. (c) Retrieved temporal profile and the temporal phase of the compressed mid-infrared pulses with 18 fs pulse duration at FWHM. (d) Retrieved spectral intensity and the spectral phase of the compressed mid-infrared pulses ($G_{error} = 7.9 \times 10^{-3}$) [29].

4.5 Mid-infrared optical parametric chirped pulse amplification channel

The present section considers the parametric amplification of the spectrum portion in MIR region (1600 nm-2500 nm) as shown in Sec. 4.2. This spectrum was amplified by the unconverted fundamental pulses at 1030 nm after getting separated from the SH pulses (see Sec. 4.3).

The presented work in this section is based on the main Ph.D. work of Haochuan Wang. Therefore, this work is briefly summarized in this section with a view to support the entire framework of this thesis.

After the spectral separation by the dielectric beam splitter, the MIR seed pulses passed through an acousto-optic programmable dispersive filter (AOPDF) (Fastlite, Dazzler) and were amplified in a single-stage degenerate OPCPA containing a 2 mm-thick periodically poled lithium niobate (PPLN) crystal with a polling period of 30.64 μm. 180 μJ pulses at 1030 nm with the peak intensity of 70 GW/cm^2 were used to pump the MIR OPCPA stage. A 1° angle between the signal and pump beams was introduced to facilitate the separation

of the signal beam after amplification. The brown curve in Fig. 4.10 shows the spectrum of the amplified MIR pulses. The amplified spectrum covers a bandwidth of 70 THz and yields an energy of 5 μJ. The residual of the pump after the parametric amplification was filtered by a 1550 nm long-pass filter (Thorlabs GmbH, FELH1550). The amplified pulses were compressed to 18 fs by using an additional 2.5-mm-thick silicon plate in combination with the introduced phase feedback by Dazzler. Figure 4.14 (a) and (b) show the measured and retrieved spectrograms of the compressed MIR pulse. The associated retrieved temporal and spectral intensities are depicted in Fig. 4.14 (c) and (d). These measurements were done by a SH-FROG containing a 100-μm-thick BBO crystal.

4.6 Energy scaling of the few-cycle pulses

This section predicts the capability for energy scaling of the few-cycle pulses generated in both channels. Therefore, I performed three-dimensional numerical simulations by SISYFOS code [120]. Here, the energy of each OPCPA channel was individually boosted within two additional OPCPA stages by using the available pump energy. The available pump energy was equally divided between the two channels. In this numerical simulation, the thermal effects, third-order nonlinear processes, and two-photon absorption were neglected. The Sellmeier coefficients these crystals were obtained from Ref.s [123, 126].

For simulating the NIR channel, the amplified spectrum in the first stage (orange curve in Fig. 4.10) was further amplified into two additional amplification stages. The remaining energy (8.3 mJ) from the SH module at 515 nm was used to pump the second stage and recycled at the third amplification stage. The pump's beam size was adjusted to keep its peak intensity at 100 GW/cm^2. The parametric amplification was formed in an LBO crystal with a phase-matching angle of 15.5°, an internal non-collinear angle of 1.05°, and $d_{eff} = 0.82$ pm/V resulting in the amplified pulse energy of 1.8 mJ. The detailed parameters of the NIR chain are summarized in Table 4.1.

For simulating the amplified spectrum of the MIR channel (brown curve in Fig. 4.10), 8.9 mJ of pump energy at 1030 nm was used to pump two additional OPCPA stages, while the pump energy was recycled at the last stage. The pump intensity in all stages was set to 70 GW/cm^2. The signal energy was boosted to 2.2 mJ in the MIR chain by using a type-I, lithium niobate ($LiNbO_3$) crystal with a phase-matching angle $\theta = 42.9°$ and assumed d_{eff} value of 3.96 pm/V. Table 4.2 summarizes the simulation parameters of the MIR channel.

The amplified spectra of both channels after the third stage are presented in Fig. 4.15 (a) and (b). Figure 4.15 (c) and (b) show the retrieved electric fields after applying the Fourier transformation of these spectra. The simulation results show the energy of the resultant waveforms of the NIR and MIR channels can be scaled to 1.8 mJ and 2.2 mJ, respectively, by applying the available pump energy in additional amplification stages.

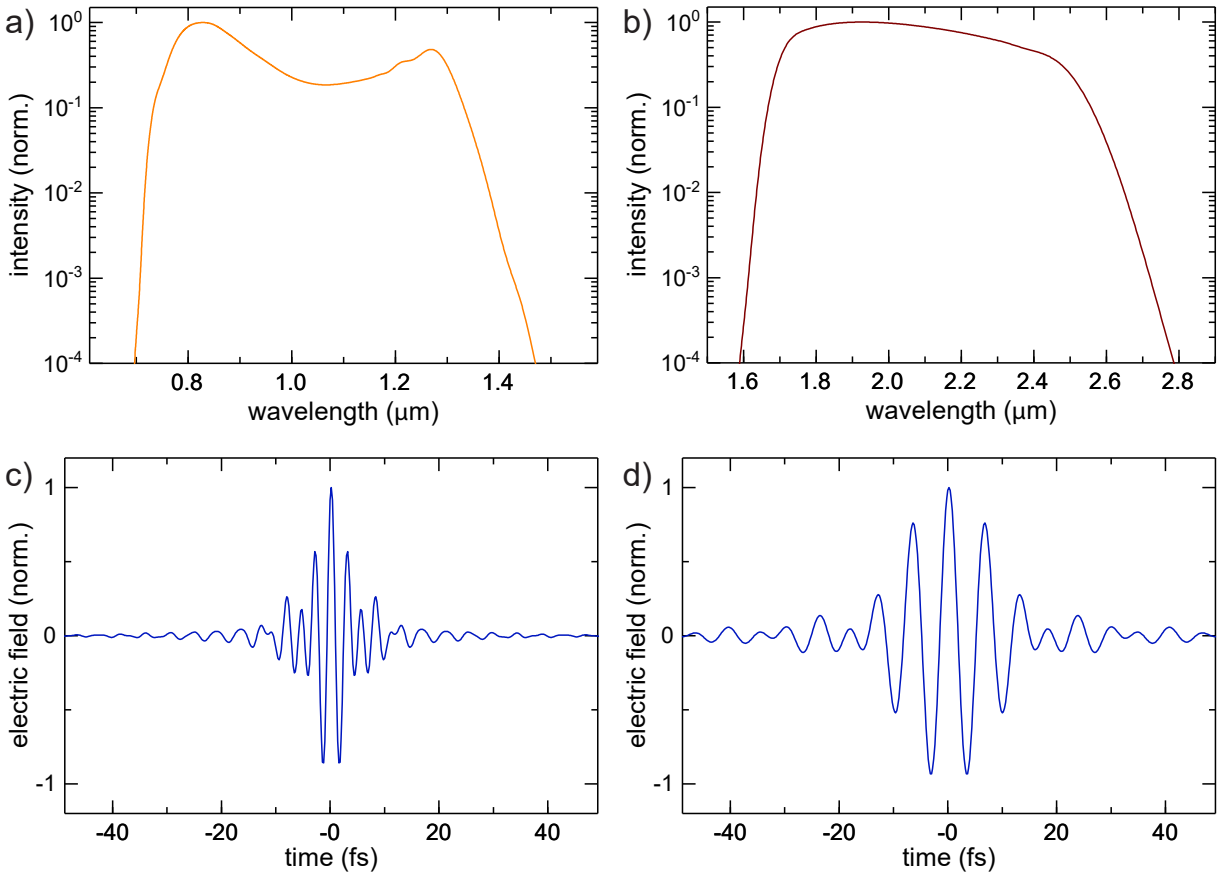

Figure 4.15: Simulated multi-millijoules, few-cycle pulses. The simulated amplified spectra in (a) near-infrared and (b) mid-infrared channels with 1.8 mJ and 2.2 mJ of energy, respectively. The associated waveforms of (c) near-infrared and (d) mid-infrared channels [29].

Table 4.1: Simulation parameters of the near-infrared channel. L: crystal thickness, E_p: input pump energy, E_s: amplified signal energy, ω_p: pump beam radius (FWHM), ω_s: signal beam radius (FWHM) [29].

stage	L (mm)	E_p (mJ)	E_s (mJ)	ω_p (mm)	ω_s (mm)	efficiency (%)
2^{nd}	2.5	8.3	1.3	1.46	1.16	15.1
3^{rd}	1.0	6.0	1.8	1.28	1.02	9.8

Table 4.2: Simulation parameters of the mid-infrared channel. L: crystal thickness, E_p: input pump energy, E_s: amplified signal energy, ω_p: pump beam radius (FWHM), ω_s: signal beam radius (FWHM) [29].

stage	L (mm)	E_p (mJ)	E_s (mJ)	ω_p (mm)	ω_s (mm)	efficiency (%)
2^{nd}	2.0	8.9	1.3	1.63	1.50	14.9
3^{rd}	1.0	6.2	2.2	1.42	1.34	13.9

4.7 Conclusion

In summary, a few-cycle OPCPA source consisting of two channels for a high-energy light transient generation was demonstrated. The frontend covers a spectral range of 700 nm to 2500 nm as stated in Sec. 3.3. The spectrum was divided prior to the parametric amplification into two spectral regions of comparable bandwidth in NIR (700 nm-1400 nm) and MIR (1600 nm-2500 nm). A 0.8 mJ, 515 nm pulses from the SHG module were used to amplify the NIR region in a 4 mm LBO crystal. 2 mm-thick PPLN was used to amplify the MIR channel pumped by 180 μJ pulses at 1030 nm. Both channels were amplified to 25 μJ, at 5 kHz repetition rates and were temporally compressed to 6 fs (NIR) and 18 fs (MIR). The simulation results show that the few-cycle pulses from both channels are further amplified in two additional subsequent OPCPA stages to the millijoule-level.

Chapter 5

Sub-Cycle, Multi-Octave Waveform Synthesizer

It has been suggested that the energy of light transients can be scaled by employing several parallel OPCPAs at different carrier frequencies prior to the temporal field synthesis [18, 34]. Before further amplification of the generated few-cycle pulses, proving the ability to synthesize the two pulses is required. In this regard, the synthesized sub-cycle light transient can be measured via attosecond streaking [2]. However, this approach is unattainable as the few-cycle pulses are limited to the sub-millijoule of energy. Therefore, an alternative approach is conducted where the electric field of the few-cycle pulses generated in MIR channel is resolved by the NIR few-cycle pulses. This approach proves the feasibility of such synthesized light transient.

In the current chapter, the generation of the sub-cycle optical transients via the OPCPA-based waveform synthesizer is addressed. Temporal drifts and relative timing fluctuations between the synthesizer's arms are discussed.

The presented work in this chapter is based on the reported results in the submitted article:

- A. Alismail*, H. Wang*, G. Barbiero, N. Altwaijry, S. A. Hussain, V. Pervak, W. Schweinberger, A. M. Azzeer, F. Krausz, and H. Fattahi, "Multi-octave, CEP-stable source for high-energy field synthesis," *Science Advances* **6**, p. aax4308, 2020.

5.1 Temporal and phase jitters

In this section, I address some vital effects that can lead to instability in the synthesized light transients such as temporal drifts and relative timing fluctuations between the synthesized pulses. In a few-cycle coherent synthesis, the relative temporal overlap between the few-cycle pulses results in a great variety of light transients [13]. Therefore, as with

any kind of interferometer, relative phase and relative timing between the two arms of the synthesizer define the ultimate stability of the generated light transient [127, 128]. In the presented scheme, the CEP stability of the seed pulses results in the stability of the absolute phase of both OPCPA channel outputs. Moreover, the direct multi-octave seed generation from the pump laser assures the intrinsic temporal synchronization and restricts the temporal jitter only to long-term drift caused by the optical path of the synthesizer. To avoid any temporal instability caused by fluctuations in the arrival of pump pulses in each OPCPA channel, the seed pulse duration was kept shorter than the pump pulse duration. This approach allows for decoupling the nonlinear amplification process from the linear temporal jitter between the pump and seed pulses.

As the few-cycle pulses from both OPCPA channels contain only two-three cycles of the electric field, the temporal jitter between the two channels has to be lower than a fraction of their half-field cycle. To prove the intrinsic synchronization between the two channels, I conducted a measurement in which the electric field of the MIR pulses is resolved in an EOS setup [22]. The 6 fs NIR pulses are utilized as probe pulses in EOS and are required to have a temporal jitter below the sub-cycle duration of the MIR pulses over the entire scanning range to allow for resolving the fast oscillating electric field of the MIR pulses. The experimental setup and results are presented in detail in the following section.

On the other hand, the residual temporal jitter concerning the long-term drift can be fairly compensated via an active optical synchronization. By using an optical technique known as balanced optical cross-correlation (BOC), a temporal stabilization with a precision of sub-100 as can be realized [19, 127, 129, 130]. This technique uses an optical cross-correlator to distinguish the time delay between the two synthesized pulses with the aid of a balanced photodiode. The BOC setup is ideally placed after coherently combining the two OPCPA channels. The detected signal from the balanced photodiode is extremely sensitive to the relative time delay and scaled with the time jitter. Unbalanced detected signal triggers a feedback loop to compensate for the temporal drift. The balanced detection allows suppressing the noise associated with the amplitude fluctuations of the OPCPA channels. An elaborate explanation of this technique can be found in Ref. [127].

5.2 Direct electric field sampling

In the current section, I represent an experiment for quantifying the temporal jitter that occurred between the two arms of the synthesizer. The experimental setup of the EOS is depicted in Fig. 5.1 (a). First, the NIR probe beam was collinearly combined with the MIR beam by using an ultra-broadband wire grid polarizer (Thorlabs GmbH, WP25L-UB). Subsequently, both beams were focused by a 2 inch focal length off-axis parabolic mirror into a 50 μm-thick BBO (type-II) crystal (CASTECH Inc.) at the phase-matching

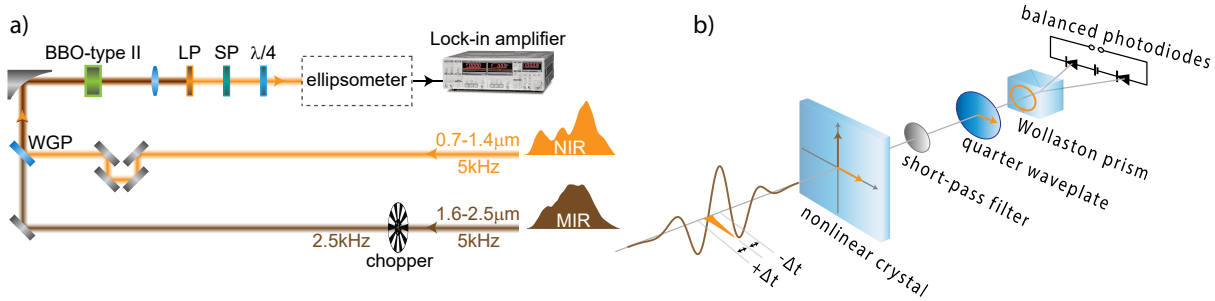

Figure 5.1: Electro-optic sampling of the mid-infrared (MIR) pulses. (a) Schematic of the electro-optic sampling setup. (b) Electro-optic sampling concept. The electro-optic sampling setup contains a 50 μm-thick BBO (type-II) crystal and an ellipsometer. The mid-infrared pulses are chopped at 2.5 kHz. The near-infrared (NIR) beam after the delay line is collinearly combined with the mid-infrared beam and both are focused in the electro-optic sampling crystal for sum-frequency generation. The generated sum-frequency signal spectrally overlaps and temporally interferes with the high-frequency components of the probe beam. Appropriate spectral filtering is used to enhance the electro-optic sampling signal. The polarization rotation as a function of time delay is detected by an ellipsometer and read out by a lock-in amplifier. WGP: wire grid polarizer, LP: long-pass filter, SP: short-pass filter, $\lambda/4$: quarter-wave plate [29]. Figure (a) is adapted from [31].

angle of $\theta = 25°$. The probe and the MIR beams are orthogonally polarized along the ordinary (o) and extraordinary (e) axes of the nonlinear crystal, respectively, as shown in Fig. 5.1 (b). By temporal and spatial overlap of the two pulses in the crystal, sum-frequency signal centered at 670 nm was generated. The sum-frequency signal is polarized along the extraordinary (e) axis of the nonlinear crystal and spectrally overlaps with the high-frequency components of the ordinary polarized probe pulses.

In order to enhance the detection sensitivity, the spectral region between 650 nm and 750 nm was filtered out by using a 650 nm long-pass (Thorlabs GmbH, FEL0650) and a 750 nm short-pass (Edmund Optics Ltd., 64-324) filters [131]. The interference between the NIR probe pulses and the sum frequency signal is assured by a quarter-wave plate (Thorlabs GmbH, AQWP05M-600). The resulted polarization rotation was read out by an ellipsometer consisting of a Wollaston prism (Thorlabs GmbH, WP10) and a home-built balanced detector as a function of the relative timing of the NIR and MIR pulses.

In the absence of the MIR beam, the ellipsometer was aligned to equally split and balance the power of the probe pulses at the pair of photodiodes. Therefore, the difference between the photocurrents of the two detectors is equal to zero. In the presence of the MIR pulses, the difference was imbalanced and varied relative to the temporal delay of the probe pulses. The electronic data from the balanced detector was recorded by using a lock-in amplifier (Stanford Research Systems, SR830-DSP) while the MIR pulses were modulated

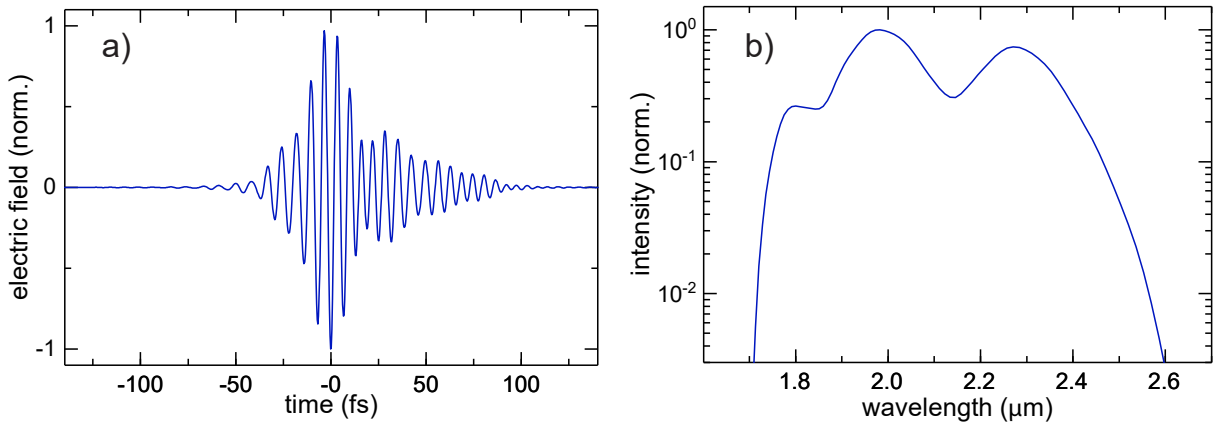

Figure 5.2: Sampled mid-infrared pulses. (a) Retrieved electric field of the few-cycle mid-infrared pulses in electro-optic sampling and (b) its retrieved spectrum.

at 2.5 kHz (half of the laser's repetition rate) with a mechanical chopper (Thorlabs GmbH, MC2000B-EC).

In parallel, for a precise temporal delay scan, the mechanical delay stage (Physik Instrumente Ltd., V-528.1AA) was tracked by a Mach-Zehnder-type interferometric delay tracking setup (SmarAct GmbH, PicoScale). The setup employs a beam of a 1.55 μm continuous-wave distributed-feedback laser diode, propagating along the MIR and NIR probe beam-paths [132].

To probe the MIR pulses, the delay stage in the probe channel was scanned over 300 μm with a speed of 1.7 μm/s, corresponding to a single shot detection at each delay position. The retrieved electric field of the MIR pulses with sub-cycle precision is shown in Fig. 5.2 (a). The retrieved spectrum was obtained by Fourier transformation of the measured electric field (Fig. 5.2 (b)). Figure 5.3 shows the actual data points measured in Fig. 5.2 over two cycles of the MIR pulses. As can be seen, there are approximately 1500 measured data points during one cycle of the MIR pulse. Assuming 6 fs pulse duration for a period, this corresponds to 4 as temporal resolution in Fig. 5.2, which was assisted by the PicoScale setup. Resolving the electric field of the MIR pulses with sub-cycle precision in the absence of active stabilization, demonstrates the short-term spatial and temporal stability of the synthesizer. As a result of the limitation of the synthesizer's stability by the long-term drift, I observed a drift after several minutes of a single EOS scan, which also degraded the equality of the following scan.

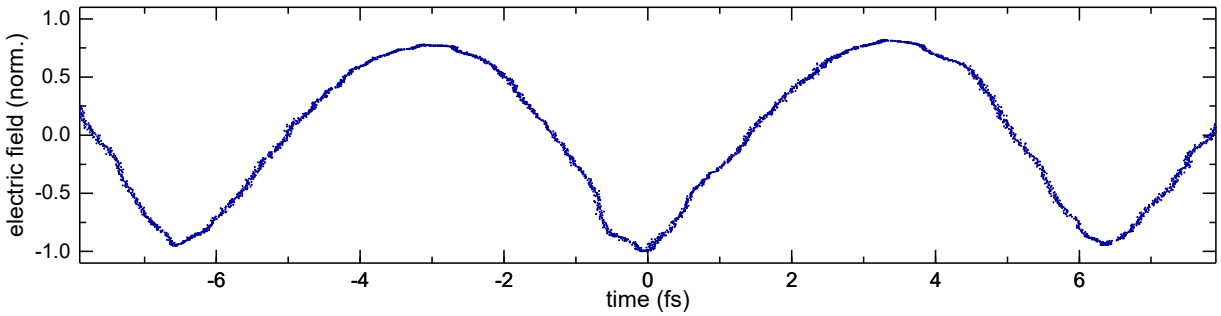

Figure 5.3: Measured data points of the sampled electric field over two cycles of the mid-infrared pulses.

5.3 Conclusion

I have demonstrated the development of OPCPA-based field synthesizer driving by all-ytterbium laser. The source is capable of delivering sub-cycle light transients. The stable CEP was ensured by generating passively CEP-stable multi-octave seed pulses directly from the Yb:YAG amplifier. The temporal jitter between the NIR and MIR pulses in this scheme is only dominated by long-term drift. This allowed for the sampling of the electric field of the MIR channel with sub-cycle resolution.

Chapter 6

Field-Resolved Spectroscopy

The current chapter is devoted to the exhibition of the concept of NIR field-resolved spectroscopy as a potential application of the few-cycle source reported in Chapter 4. This chapter is split into four sections. Initially, I address the molecular vibrations occurred in the infrared spectral range. Thereafter, I introduce a novel method of field-resolved spectroscopy in NIR region and highlight some limitations of the conventional instruments applied in NIR spectroscopy. The third section presents an overview of the theoretical model explicated the NIR spectroscopy. The last section illustrates the detection of NIR molecular response of a variety of water concentrations.

The presented work in this chapter is based on the reported results in the proceeding article:

- A. Alismail, H. Wang, G. Barbiero, S. A. Hussain, W. Schweinberger, F. Krausz, and H. Fattahi, "Near-infrared molecular fieldoscopy of water," in *Multiphoton Microscopy in the Biomedical Sciences XIX*, **10882**, p. 1088231, International Society for Optics and Photonics, 2019.

6.1 Vibrational spectroscopy

Figure 6.1 shows the electromagnetic spectrum including the transition processes at different spectral regions. Specifically, infrared spectroscopy studies the interaction between molecules and the electromagnetic radiation in the infrared region spanning from $400\,\mathrm{cm}^{-1}$ to $14000\,\mathrm{cm}^{-1}$. Infrared radiation can trigger the molecular vibrations at their resonance frequencies. Molecules that comprise polar bonds (consisted of different atoms, such as water (H_2O), and carbon dioxide (CO_2)) are infrared-active as they experience a change in their dipole moment during the vibration. On the other hand, homonuclear diatomic molecules (composed one type of atoms, such as H_2, and O_2) are not infrared-active.

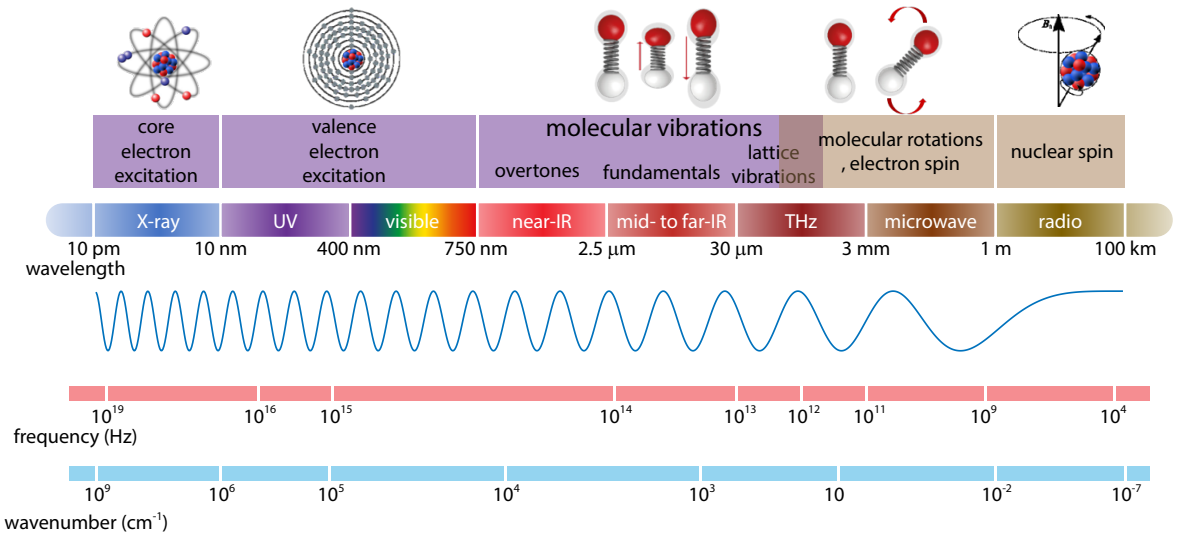

Figure 6.1: Electromagnetic spectral regions and their associated transition processes.

Fundamental vibrations (such as symmetric stretching, antisymmetric stretching, scissoring, rocking, wagging, and twisting) occur in the mid- and far-infrared ranges (400 cm^{-1} to 4000 cm^{-1}). While overtones (at integers of the fundamental vibrational frequency) and combination transitions (group of vibrations) take place in NIR range (4000 cm^{-1} to 14000 cm^{-1}).

Linear spectroscopy in NIR spectral range provides information on the molecular composition, structure, and conformation, affording tremendous potential for high-resolution, in-depth, label-free biological spectro-microscopy [133]. In NIR spectroscopy, similar information to infrared spectroscopy is obtained by exciting the first overtone of infrared-active vibrational modes. The intensity and vibrational period of these harmonics depend on the quantity and types of the present molecules in the sample. Quantitative analysis is possible when the changes in the transmitted spectrum are proportional to the concentration of chemical components of the sample under scrutiny. Therefore, NIR spectroscopy has been a popular technique for identification, quantitative and qualitative analysis, and studying structure-correlation of molecular compositions. In particular, it is routinely used for the detection of overtone and combination bands of the O-H, C-H, and N-H compositions [134]. Additionally, as the electric field in NIR spectral region supports a smaller diffraction limit than infrared, molecular information with higher spatial resolution can be obtained. Moreover, the lower cross-section of the overtone excitation allows for deeper penetration of the injected field to the sample, allowing for in-depth spectral imaging [135].

6.2 Near-infrared field-resolved spectroscopy

Previously in Chapter 4, I reported on the synchronized few-cycle pulses in the OPCPA chains composed of NIR and MIR channels. These few-cycle pulses, with bandwidths located in the NIR region, can be utilized to trigger the overtone and combination transitions when their frequencies match the resonance frequencies of the molecules. The denotation of the MIR channel can give rise to confusion, therefore, I avoid, in the following text, referring the associated pulses of this channel as MIR spectral region.

In order to quantify the electric field of light containing the molecular response, one needs to access its entire information including the intensity and phase information, where the complex electric field is defined as:

$$\widetilde{E}(\omega) \propto \sqrt{S(\omega)}\, e^{-i\varphi(\omega)} \quad \underset{IFT}{\overset{FT}{\rightleftharpoons}} \quad \widetilde{E}(t) \propto \sqrt{I(t)}\, e^{-i\phi(t)} \tag{6.1}$$

where $\widetilde{E}(\omega)$ and $\widetilde{E}(t)$ are the complex electric fields in frequency-domain and time-domain, respectively, $S(\omega)$ is the spectral intensity, $I(t)$ is the temporal intensity, and $\varphi(\omega)$ and $\phi(t)$ are the spectral and the temporal phases, respectively.

Broadband measurements in the NIR spectral region have been carried out mainly in the frequency-domain [136]. Conventional instruments used in NIR spectroscopy, such as dispersive spectrometers and Fourier transform near-infrared (FT-NIR) spectrometers, can only detect the spectral intensity. Therefore, this approach fails to provide complete information about the complex electric field. Moreover, this approach suffers from two limitations: i) the detection of small absorption is limited to the intensity noise of the source, and ii) the low detection dynamic range.

To mitigate the above-mentioned constraints, I introduce the concept of NIR field-resolved spectroscopy, as can be seen in Fig. 6.2. In NIR field-resolved spectroscopy, an ultrashort, phase-coherent pulse (in brown) is used for molecular excitation and afterward the transmitted complex electric field that contains the molecular response is directly measured by the EOS. Here, the electric field is detected in a background-free manner, eliminating the effect of the intensity noise of the source. In addition to the intensity information, measuring the complex electric field allows for extracting the full spectral phase information of the molecular response, adding a new dimension to the gained spectroscopic data.

It is well known that the interaction of broadband ultrashort pulses with an ensemble of molecules at their resonance frequencies results in coherent scattering. The delayed response of the medium, known as free-induction decay (FID) [137], can be explained by the Kramers-Kronig relation. During the interaction, photons at the resonance frequencies are slowed down compared to the other photons and appear at the trailing edge of the

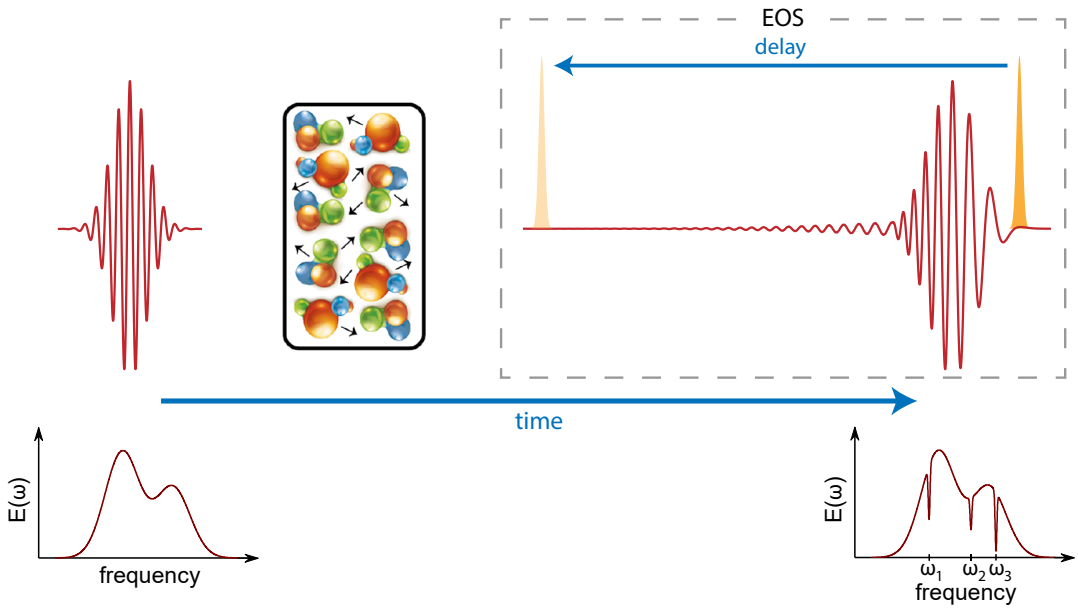

Figure 6.2: Concept of near-infrared field-resolved spectroscopy. The molecules in the sample are excited by a broadband femtosecond pulse (in brown). The electric field of the transmitted pulse contained the molecular response is detected by short sampling probe pulse (in orange) in electro-optic sampling setup. This response represents in the frequency-domain by the dips in the right spectrum due to the absorption at resonance frequencies ω_1, ω_2, and ω_3.

excitation pulse, due to the increase of the group refractive index of the medium at the vicinity of the resonance frequencies. The delayed response lasts for hundreds of picoseconds for molecules in the gas-phase and down to several picoseconds in liquid-phase. The FID carries information about the molecular composition and concentration. Therefore, by temporal detection of the coherent response, valuable spectroscopic information can be gained. Additionally, by using ultrashort pulses, the excitation pulse is confined to a time window of tens of femtosecond, which is significantly shorter than FID of the molecular sample under scrutiny. Here, the response emerging from the sample is separated temporally from the ultrashort excitation pulse, enabling for a background-free detection. As FID after the excitation pulse decreases exponentially, its earlier temporal detection results in a higher signal-to-noise ratio and therefore sensitivity.

Terahertz time-domain spectroscopy based-on EOS has been a powerful method for the direct measurement of the electric field in MIR and terahertz spectral region [1]. However, its extension to NIR has been shown just recently, due to difficulties in the generation of short, phase-stable excitation pulses that are temporally synchronized with short sampling probe pulses [22]. In the following section, I provide a theoretical basis which is relevant for the vibrational transactions.

6.3 Theoretical foundation of near-infrared spectroscopy

This section treats the physics behind the vibrational spectroscopy when molecules are irradiated by electromagnetic waves (such as laser pulses) in the NIR spectral region. There are several excellent textbooks and review articles covering the topic of NIR spectroscopy, such as Ref.s [136, 138–140]. This section is mainly adapted from Ref.s [136, 139].

Absorption can be observed once the electromagnetic wave energy meets certain energy of a chemical bond in the molecule. This absorption transfers as kinetic energy resulting in the displacement in the position of the atoms joined by the chemical bond. The absorption in a sample under scrutiny is governed by Beer's law as:

$$A = \epsilon c d = log(\frac{I_0}{I}) \tag{6.2}$$

where ϵ is the absorptivity of the sample, c is the sample's concentration, d is the sample's thickness, I_0 is the incident intensity, and I is the transmitted intensity.

In order to understand the molecular vibrations, for simplicity, suppose a molecular vibration taking place in a diatomic molecule, in which the two atoms possess masses of m_1 and m_2. The classical model treats the chemical bond as a spring between two masses (atoms) and explains the molecular vibration as a simple harmonic oscillator. The total displacement (q) of the atoms from the equilibrium position can be derived by means of

Hooke's law as:

$$F \;=\; \mu \,\frac{d^2q}{dt^2} \;=\; -\,K\;q \tag{6.3}$$

where F is the restoring force, μ is the reduced mass, and K is the force constant. The reduced mass is defined as:

$$\mu \;=\; \frac{m_1\;m_2}{m_1\;+\;m_2} \tag{6.4}$$

The general solution of Eq. 6.3 can be expressed as:

$$q \;=\; q_0\;sin(2\pi v t + \phi) \tag{6.5}$$

where q_0 is the maximum displacement, v is the vibrational frequency, and ϕ is the phase. The vibrational frequency (v) and the vibrational wavenumber ($\widetilde{v}$) are given as:

$$\begin{aligned} v \;&=\; \frac{1}{2\;\pi}\,\sqrt{\frac{K}{\mu}} \\ \widetilde{v} \;&=\; \frac{1}{2\;\pi\;c}\,\sqrt{\frac{K}{\mu}} \end{aligned} \tag{6.6}$$

The potential energy (V) of the harmonic oscillator is determined as:

$$V \;=\; \frac{1}{2}\;K\;q^2 \tag{6.7}$$

According to Eq. 6.7, the classical approach predicts the vibrational energy as a continuous profile. However, this prediction fails in a microscopic scale. In quantum mechanics, discrete energy levels are only allowed in the quantum harmonic oscillator. The system is better described by the Schrodinger equation as the following:

$$\frac{d^2\psi}{dq^2} \;=\; \frac{8\;\pi^2\;\mu}{h^2}\;(\;\frac{1}{2}\;K\;q^2\;-\;E\;)\;\psi \tag{6.8}$$

where ψ is the wavefunction, h is the Planck's constant, and E is the energy level. The proposed solution of this differential equation (Eq. 6.8) can be written as:

$$\psi(q) \;=\; C\;e^{-\frac{\alpha\;q^2}{2}} \tag{6.9}$$

Substituting Eq. 6.9 into Eq. 6.8 and applying the boundary conditions results in the

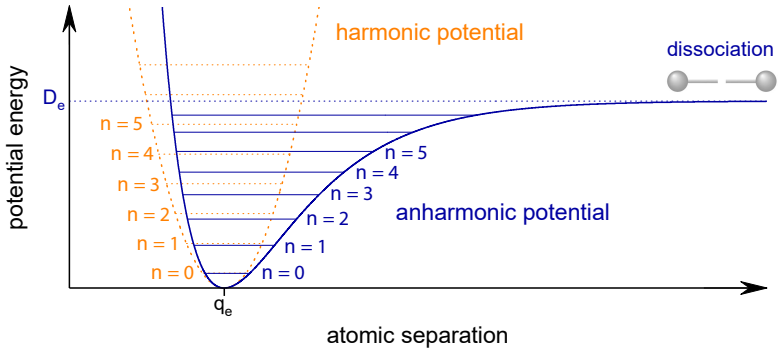

Figure 6.3: Quantum harmonic (orange) and anharmonic (blue) oscillators for a diatomic molecule.

minimum energy for the the harmonic potential:

$$E_0 \;=\; \frac{1}{2}\; h\; v \;=\; \frac{1}{2}\; h\; c\; \widetilde{v} \tag{6.10}$$

where E_0 denotes the ground state energy. The vibrational frequency (v) is expressed in the same fashion as the classical model shown in Eq. 6.6. Due to Heisenberg's uncertainty principle, this energy does not go to zero as seen earlier in the classical model. The generally normalized eigenfunctions are given as:

$$\psi_n(q) \;=\; \frac{1}{\sqrt{2^n\; n!}} \left(\frac{\alpha}{\pi} \right)^{\frac{1}{4}} e^{-\frac{\alpha\; q^2}{2}}\; H_n(\sqrt{\alpha}\; q) \tag{6.11}$$

where n is a positive integer number known as the vibrational quantum number, the coefficient $\alpha = \frac{4\pi^2 \mu v}{h}$, and H is the Hermite polynomial. The associated eigenvalues (energy levels) are given as:

$$E_n \;=\; (\; n \;+\; \frac{1}{2}\;)\; h\; v \;=\; (\; n \;+\; \frac{1}{2}\;)\; h\; c\; \widetilde{v} \tag{6.12}$$

As seen from Eq. 6.12, the energy levels are equally spaced (see harmonic potential in Fig. 6.3). The quantum model is beneficial for describing the fundamental molecular vibrations of the diatomic molecules happening in the infrared spectral region, however, it is restricted by the molecular vibrations that occurred between the adjacent energy levels. Therefore, it fails in term of explaining molecular vibrations happening in the NIR spectral region such as overtones, where $\Delta n > 1$.

In an actual diatomic molecule, the energy levels are not evenly separated and its potential energy (V) is approximated by the Morse function as:

$$V \;=\; D_e\; (\; 1 \;-\; e^{-\beta(q-q_e)}\;)^2 \tag{6.13}$$

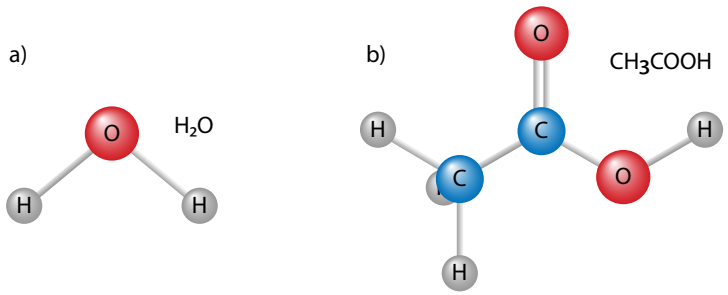

Figure 6.4: Chemical structure of (a) water and (b) acetic acid.

where D_e is the dissociation energy, β is a constant related to the curvature of the anharmonic potential, and q_e is the atomic separation in the molecule in equilibrium. The corresponding energy levels for an anharmonic potential are given by:

$$E_n = \left(n + \frac{1}{2} \right) h\, v - \left(n + \frac{1}{2} \right)^2 h\, x_e\, v + \left(n + \frac{1}{2} \right)^3 h\, y_e\, v + \ldots \quad (6.14)$$

where x_e and y_e are the first-order and second-order anharmonicity constants. Blue curve in Fig. 6.3 shows the energy levels for the anharmonic model, where their separation decrease with n. Here, the vibrations are not independent compared to the harmonic model. Therefore, the anharmonic model can successfully predict vibrations associated to combination bands in addition to the overtone bands.

6.4 Near-infrared molecular response detection

Water plays a prominent role in biological interactions and life. Figure 6.4 (a) exhibits its chemical structure. It has three fundamental vibrations in the infrared region, which are depicted in Fig. 6.5 and their parameters are summarized in Table 6.1. In the NIR region, its first overtone, in the form of a symmetric stretch vibration, appears at 1450 nm (6900 cm^{-1}). It also has a strong $v_2 + v_3$ combination band near 1930 nm (5180 cm^{-1}), as can be seen from its absorption spectrum in Fig. 6.6. Table 6.2 summarizes the parameters of its lower-order overtones and combination band. I aimed for the field detection of the water's molecular response at its combination band for various molecular concentrations. I chose acetic acid (CH_3COOH) as a background solvent due to its sparse spectral response at this range (around 1930 nm). The measured absorption spectrum of acetic acid is shown in Fig. 6.7 as a difference between the transmitted spectra of the empty cell and the 100 % acetic acid sample. The atomic structure of the acetic acid is illustrated in Fig. 6.4 (b).

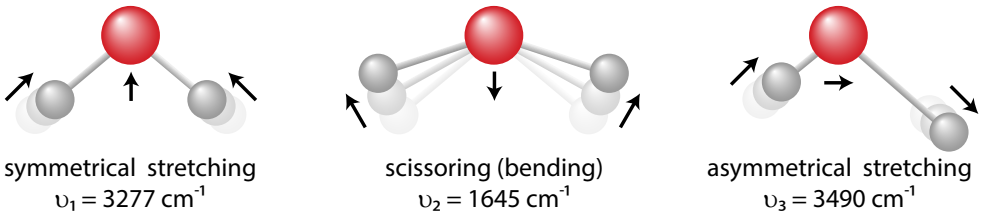

Figure 6.5: Fundamental vibrations of water.

Table 6.1: Fundamental vibrations of water in liquid-phase.

vibration	wavenumber (cm^{-1})	frequency (THz)	wavelength (nm)
v_1	3277	98	3052
v_2	1645	49	6079
v_3	3490	105	2865

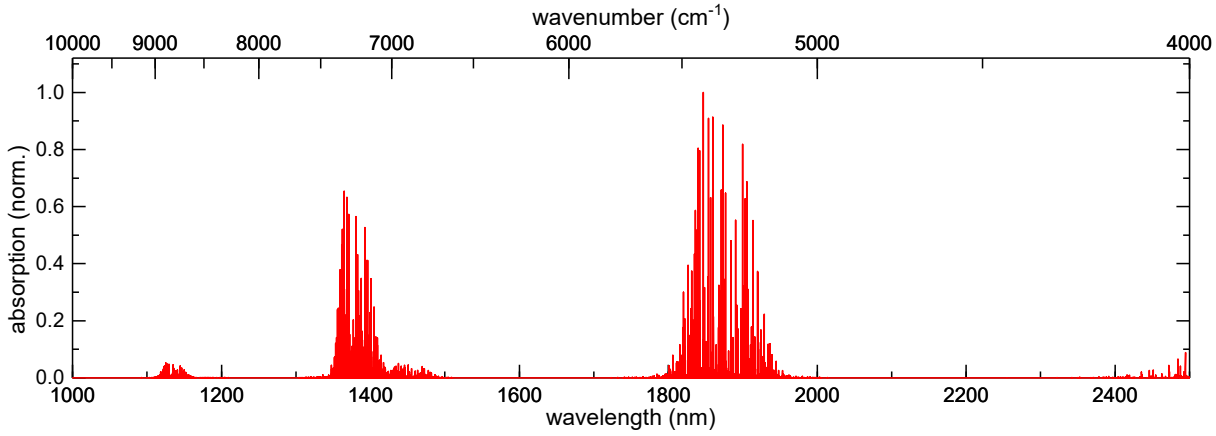

Figure 6.6: Absorption spectrum of water in near-infrared region [141].

Table 6.2: Overtone and combination transitions of water in liquid-phase in near-infrared region.

wavenumber (cm^{-1})	frequency (THz)	wavelength (nm)	assignment
5260	158	1901	$av_1 + v_2 + bv_3$, $a + b = 1$
6800	204	1471	$av_1 + bv_3$, $a + b = 2$
8330	250	1200	$av_1 + v_2 + bv_3$, $a + b = 2$
10310	309	970	$av_1 + bv_3$, $a + b = 3$
11960	359	836	$av_1 + v_2 + bv_3$, $a + b = 3$

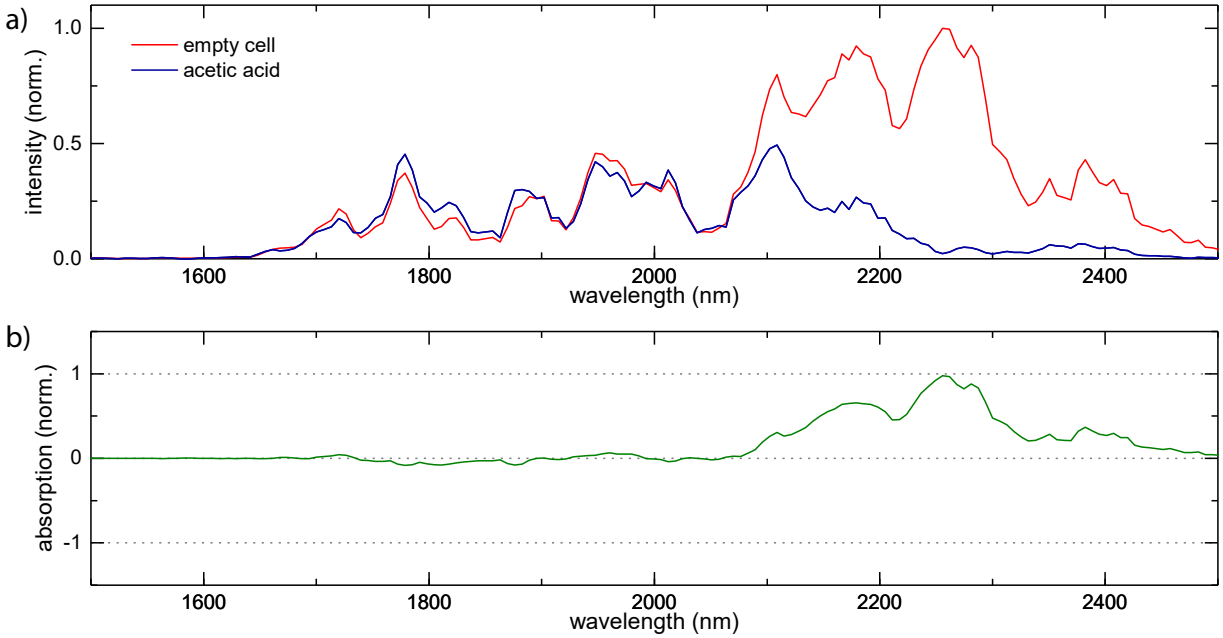

Figure 6.7: Absorption spectrum of acetic acid. (a) Measured spectra of the transmitted pulses in the absence of any sample (red) and 100 % acetic acid sample (blue). The obtained spectra were normalized then calibrated to the transmitted power. (b) Absorption spectrum in acetic acid sample by means of the difference between the two curves in (a).

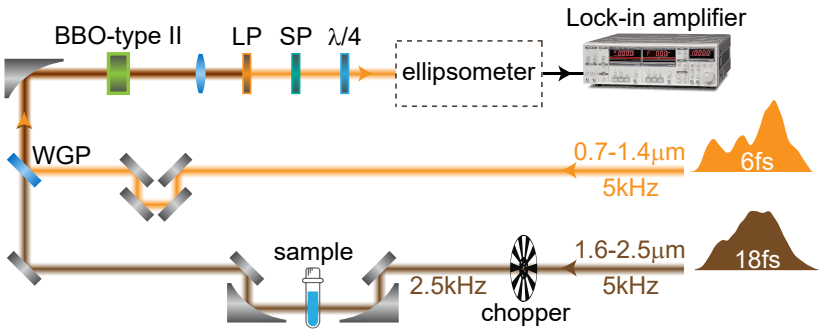

Figure 6.8: Direct electric field detection of the free-induction decay of water molecules. WGP: wire grid polarizer, LP: long-pass filter, SP: short-pass filter, $\lambda/4$: quarter-wave plate. This figure is adapted from [31].

6.4.1 Experimental setup

The experimental setup of the molecular response detection is exhibited in Fig. 6.8. It is based on the proposed experiment in Fig. 5.1, which was used for verifying the short-term stability of the synthesis, with some modification. In the modified setup, the 18 fs few-cycle pulses centered at 2 μm (depicted in Sec. 4.5) were used to excite the water molecules, focused by a 4 inch focal length off-axis parabolic mirror into the sample under scrutiny. The sample was placed slightly after the focus to avoid filamentation in the sample. The beam size on the sample was 200 μm (FWHM). Afterwards, the transmitted beam was collimated by another 4 inch focal length off-axis parabolic mirror. After collimation, the transmitted pulses, including the molecular response, were sampled and detected in a EOS setup (see Fig. 6.8), where the 6 fs few-cycle pulses centered at 1 μm (represented in Sec. 4.4) were used as a probe. The EOS concept and the data acquisition from the lock-in amplifier were also fairly described in Sec. 5.2. In what follows, before presenting the results of the sampled molecular response for different water concentrations, I evaluate the limit of EOS detection (dynamic range) in the absence of the sample.

6.4.2 Dynamic range of the detection

A series of measurements were performed to estimate the detection dynamic range of the EOS setup in the absence of the liquid sample. First, the energy of the NIR pulses was attenuated by using a series of neutral density filters with different optical densities (ODs) and afterward their electric fields were measured by EOS. Figure 6.9 (a) illustrates the sampled waveforms for different attenuations. The black curve shows the electric field of the unattenuated NIR pulses. The red curve exhibits the detectable NIR pulses by EOS with the average power of 650 nanowatts (power attenuation by filters at the OD of

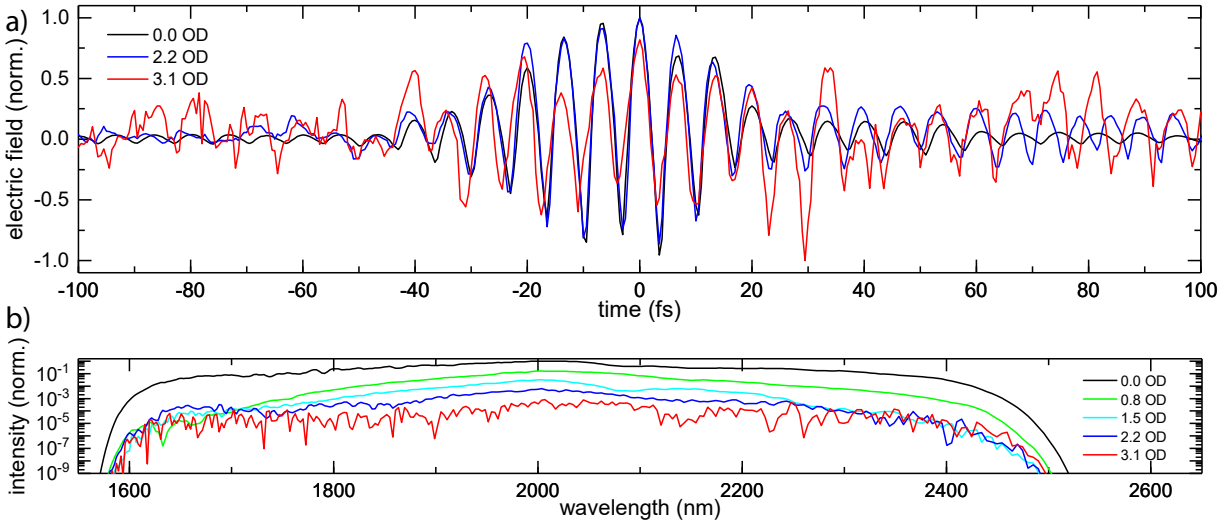

Figure 6.9: Dynamic range of the detection. (a) Measured electric field of the transmitted pulses in the absence of any sample for three different attenuations (0, 2.2, and 3.1 OD). (b) The retrieved near-infrared spectrum in the absence of any sample for five different attenuations (0, 0.8, 1.5, 2.2, and 3.1 OD). The obtained spectra were normalized then calibrated to the transmitted power. This figure is adapted from [31].

3.1). The corresponding spectra of EOS traces for five different attenuations (OD of 0, 0.8, 1.5, 2.2, and 3.1) are shown in Fig. 6.9 (b). The spectra were obtained by the Fourier transformation of the measured electric field. As can be seen, at the highest attenuation, the bandwidth of the retrieved spectrum is limited to spectral components with the highest spectral intensity. The EOS can detect the sampled waveforms with a retrievable spectrum at minimum detectable power in the level of nanowatt, corresponding to a dynamic range of 3.1 OD.

6.4.3 Sample preparation

Acetic acid (Sigma-Aldrich Inc., ReagentPlus®, $\geq 99\,\%$, A6283) and deionized water were used to create solution samples at six different concentrations between 0 Molar to 55.6 Molar (0 % - 100 %). Afterwards, different mixtures were injected into a sample holder (Harrick Scientific Products Inc., DLC-M25) consisting of two sapphire windows with a thickness of 2.3 mm. The sample's thickness for all the measurements was 500 μm.

6.4.4 Free-induction decay for different concentrations

To detect the FID of water molecules, the mixture of acetic acid and water with different concentrations was placed in the sample holder and the transmitted electric field was measured by EOS. The data of the EOS trace was gathered over 450 μm with a scanning speed of 1.7 μm/s. This corresponds to a single shot detection at each delay position by considering a 2.5 kHz as the chopped frequency of the data acquisition. Background measurements were taken with an empty sample holder and pure acetic acid serving as a blank (see Fig. 6.10 (a)). As can be seen from the inset, the electric field oscillations of the excitation pulses vanish after a temporal delay of 200 fs. By adding the sample, the molecular FID is formed and can be detected free of background at temporal delays beyond 200 fs. Figure 6.10 (b) shows the measured transmitted electric field for the mixture of water and acetic acid at two high concentrations. At high water concentrations, the transmitted main pulse is chirped. The NIR response of water molecules is clearly distinguished from acetic acid at 50 %, and 100 %. To evaluate the sensitivity of the system, measurements of lower water concentrations (10 %, 5 %, and 3 %) were carried out. As shown in Fig. 6.10 (c), the molecular response is detectable by naked eye for water concentration as low as 3 %.

A similar study [142] was reported in the frequency-domain on water molecules in methanol solvent by using a Guided Wave NIR-O$^{\text{TM}}$ process, fiber-coupled, NIR spectrometry with the core diameter of 500 μm. In this experiment, the water molecules in the methanol solvent were placed in a 10 mm-thick sample holder. The combination band of water molecules could be detected down to 0.1 % water concentration. Calibrating my measurements with a 500μm sample thickness and a 200μm laser beam size (shown in Fig. 6.10 (c)), to 10 mm of sample thickness and 500 μm of beam diameter, results in 0.075 % equivalent detectable water concentration by EOS.

In order to evaluate the absorption spectrum of water, the Fourier transform of the FID of 100 % water's concentration was performed for two different temporal delays, shaded in Fig. 6.11 (a). From the associated spectra, the absorption occurs near 1900 nm corresponding to the resonance combination band of water (Fig. 6.11 (b)). As can be seen the absorption dip over the entire scan stays at the same wavelength proofing the temporal stability of the detection. At longer time-domain the signal-to-noise ratio decreases and therefore the quality of the Fourier transform data degrades. Additionally, the observed modulations on the spectra are caused by a back reflection from the EOS crystal. However, the overtone excitation could not be detected, probably due to its very weak intensity and faster decay.

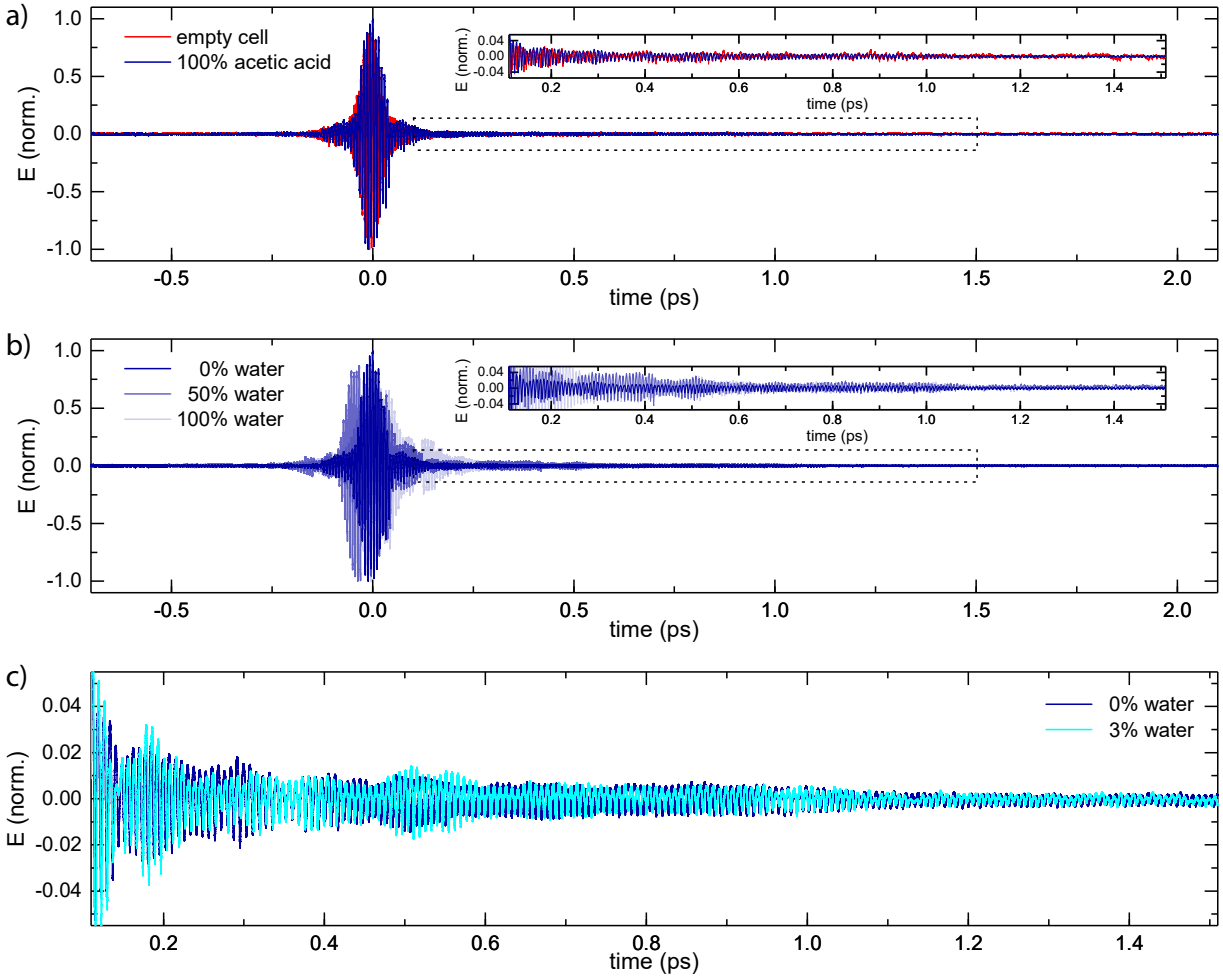

Figure 6.10: Electric field sampling of the transmitted pulses for different concentrations. (a) Measured electric field of the transmitted pulses in the absence of any sample (red) and 100 % acetic acid sample (blue). Inset: zoomed plot for the temporal delays above 100 fs. (b) Measured electric field of the transmitted pulses for the mixture of water and acetic acid for three different water's concentrations 0 %, 50 %, and 100 %. Inset: zoomed plot for the temporal delays above 100 fs. (c) Zoomed plot for the measured electric field of the transmitted pulses for water concentrations 0 % (dark blue), and 3 % (light blue). This figure is adapted from [31].

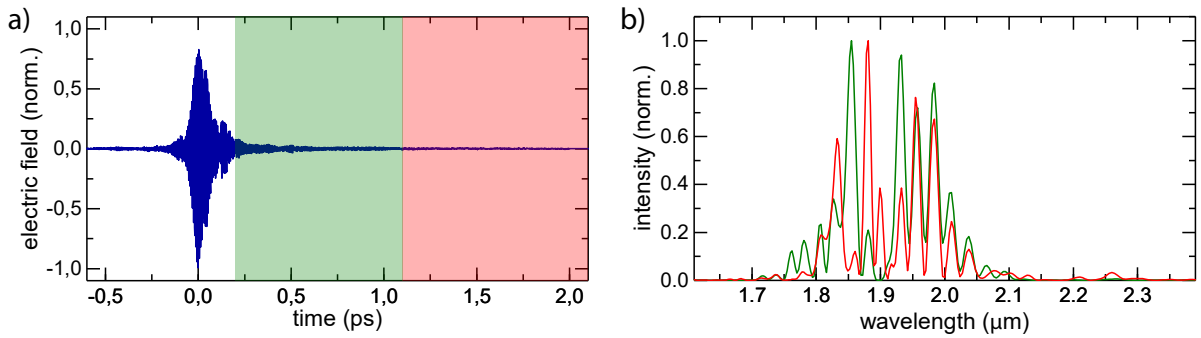

Figure 6.11: Free induction decay evaluation of 100 % water's concentration. (a) Two different temporally gated regions shaded in green and red, respectively. (b) The associated spectra, obtained from the Fourier transform, shown with the same color code. The absorption dip at 1900 nm stays at the same position for both areas demonstrating the quality of the scans.

6.5 Conclusion

I presented a novel approach, which I dubbed NIR field-resolved spectroscopy, for detection of the complex electric field of molecular response in NIR spectral range. Here, exciting molecules with ultrashort pulses allows for background-free detection of the molecular response. By employing broadband excitation pulses in combination with EOS, entire molecular vibrations can be simultaneously excited and detected.

In this regard, I demonstrated the first proof of principle field-detection of water molecule's vibration at 1.9 μm at various molecular concentrations. The achieved detection sensitivity is comparable to the conventional spectroscopy techniques and limited to the stability of the interferometer and the repetition rate of the laser. However, employing a frontend at megahertz repetition rates [18] holds promise for enhancing the detection sensitivity to unparalleled values.

Chapter 7

Conclusion and Outlook

Multi-millijoules, light transients hold promise for advancing attosecond pulse generation to higher power level and higher photon energies. Combining the concept of a lightwave synthesizer with OPCPA offers potential for the generation of multi-millijoule, watt-level light transients. In this work, a prototype based on an all ytterbium towards this potential has been reported.

In this regard, a diode-pumped Yb:YAG thin-disk regenerative amplifier based on CPA was developed. It was seeded by 2 μJ, 360 fs pulses at 1030 nm from a homemade Yb:YAG thin-disk, Kerr-lens mode-locked oscillator. Seeding the amplifier with microjoule pulses reduces the spectral narrowing effect that occurred during the amplification process. Moreover, this assists in exceeding the bifurcation regime with a smaller number of round-trips and thus shrinking the accumulated nonlinear phases. As a result, the regenerative amplifier exhibits stable operation with pulse-to-pulse stability of less than 1%. It delivers 20 mJ, 1 ps pulses at a repetition rate of 5 kHz. The achieved performance of the amplifier makes it an appropriate source for generating the CEP-stable supercontinuum and pumping the OPCPA channels.

In Chapter 3, the generation of phase-stable, multi-octave continuum pulses directly from the regenerative amplifier with a randomly varying phase was presented. The seed spectrum spans from 0.7 μm to 2.5 μm and supports a bandwidth of a 0.45 PHz, carrying an energy of 25 μJ. The method is ideally suited for seeding field synthesizers based-on multi-channel broadband parametric amplifiers.

A further method with higher optical efficiency to generate CEP-stable broadband MIR pulses, yielding 5.4 μJ of energy, is discussed. To the best of my knowledge, this approach has the highest optical-to-optical efficiency of converting 1 ps, 1 μm pulses to the CEP-stable, few-cycle, 2 μm pulses. Alternatively, this method can be combined with high-power oscillators with tens of millijoules energy to generate CEP stable, multi-octave supercontinua, suitable for field-resolved and time-resolved spectroscopy.

The parametric amplification of the phase-stable, multi-octave continuum was reported.

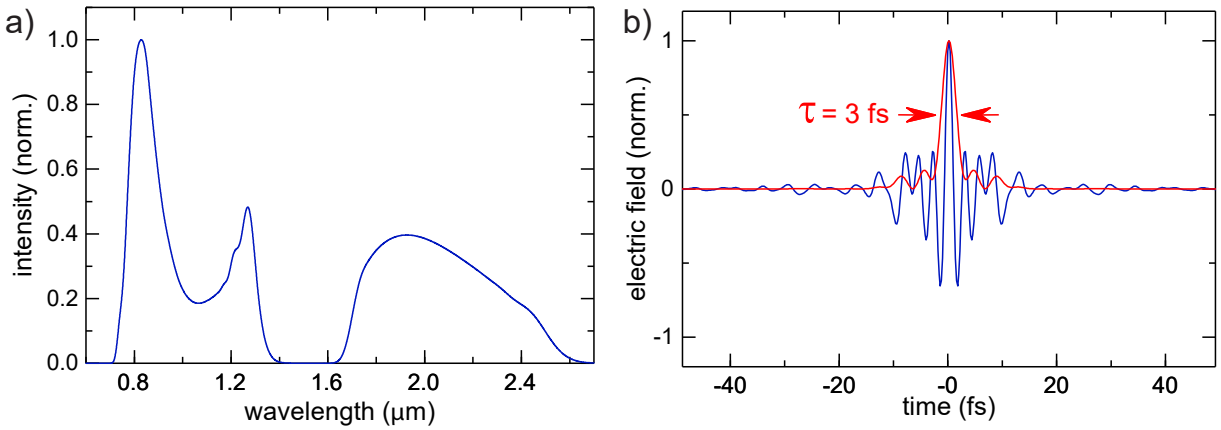

Figure 7.1: Multi-millijoules waveform synthesizer. (a) Calculated spectrum of the synthesized waveform and (b) its retrieved light transient [29].

The spectrum was split between NIR and MIR channels, then each spectral region was amplified in the respective OPCPA channel, consisting of a single amplification stage. The generated few-cycle pulses were temporally compressed to 6 fs (NIR) and 18 fs (MIR), carrying in a total energy of 25 μJ. Delivering the seed and pump pulses of the OPCPA from the same source excludes the request for active temporal synchronization between the overlapped pulses.

In order to prove the temporal and spatial stability of the coherent synthesized few-cycle pulses, the electric field of the MIR pulses was resolved with sub-cycle resolution in the absence of active stabilization via the EOS technique in the petahertz spectral region. Moreover, a numerical simulation was performed to show the source capability for scaling the few-cycle pulses, generated in the OPCPA chains, at a millijoule-level. Here, the available pump energy was used in additional amplifier stages. Based on the simulation results, the energy of the synthesized light transient can be scaled to 4 mJ. Figure 7.1 (a) shows the spectrum of the synthesized pulses. The spectrum was calculated by coherently combining the spectra reported in Fig. 4.15 (a) and (b). Each spectrum was calibrated to its energy. The associated light transient is depicted in Fig. 7.1 (b) with a temporal duration of 3 fs. Higher energy and average power can be achieved by employing a 1 kW, 200 mJ Yb:YAG amplifier [28] as the driving laser.

As a first application, a new method denominated as NIR field-resolved spectroscopy was demonstrated, where the near-infrared response of the molecules was detected by EOS. The linear absorption of the excitation pulses by molecules forms a FID at the trailing edge of the excitation pulses that lasts for several picoseconds. Therefore, the detection of the molecular response is preformed in a background-free manner, as the FID of the molecules is temporally separated from the excitation pulses. Moreover, the FID of the combination

band of water at 1.9 μm for different concentrations was measured, with an equivalent sensitivity to the FT-NIR technique. However, the detection sensitivity is restricted to the long-term stability of the EOS and the frontend's repetition rate. Utilizing a megahertz frontend has the potential for improving the detection sensitivity to a remarkable level.

In addition, combining the concept of NIR field-resolved spectroscopy with excitation nonlinear techniques such as two-dimensional spectroscopy holds promise to increase our understanding of molecular dynamics, for example in water. Water in liquid-phase, consists of a molecular network with molecular dynamics at various time scales, from several picoseconds to tens of femtoseconds. The intermolecular OH-bond stretching and bending have the shortest vibrational period at 10 fs and 20 fs, respectively. On a time scale of several hundreds of femtoseconds, liberational motions, and the H-bonds stretching and bending occur. Last but not least the exchange of hydrogen-bond partners via breaking and reforming of stable H-bonds occurs in a time range between 1-5 ps [143]. Femtosecond field-resolved spectroscopy is capable of detecting the complex electric field of the water response at all above-mentioned time scales with high sensitivity and may allow for resolving many unknown aspects of water's molecular dynamic.

Appendix A

Consideration of Peak Beam Intensity

The peak intensity of the laser beam is an essential factor in designing the stage of the non-linear interaction. The second-order nonlinearity can be triggered in non-centrosymmetric medium with a peak beam intensity around $100\,\mathrm{GW/cm^2}$, while the third-order process occurs at a peak beam intensity approximately $1\,\mathrm{TW/cm^2}$. The peak intensity (I_p) of the Gaussian beam can be calculated as:

$$I_p \;=\; \frac{0.5987\ P_{av}}{w_0^2\ \tau\ f} \tag{A.1}$$

where P_{av} is the average power, w_0 is the beam waist ($1/e^2$), τ is the pulse duration (FWHM), and f is the repetition rate of the system. Here, the beam waist is measured from the spatial intensity distribution at 13.5% of the maximum. This measurement can lead to a underestimation in the peak beam intensity as the spatial intensity decays slowly in some beam profiles. Therefore, the peak beam intensity can be properly calculated from the FWHM beam diameter as:

$$I_p \;=\; \frac{0.8297\ P_{av}}{(FWHM)^2\ \tau\ f} \tag{A.2}$$

where the two measurement methods of the beam profile is linked as:

$$FWHM \;=\; \sqrt{2\ ln2}\ w_0 \tag{A.3}$$

Appendix B

Consideration of Kramers-Kronig Relations

The refractive index of transparent material is a complex quantity, where the real and imaginary parts represent the dispersion and the absorption, respectively. Under the radiation of electromagnetic wave, the material is highly absorbent at a resonance frequency. The resonance mechanism can be characterized by Lorentz model. Figure. B.1 shows the the change of the real and imaginary part of the refractive index as a function of the frequency.

The red curve indicates that the propagation wave faces three dispersion zones. Zones shaded in red show a normal dispersion, while blue zone exhibits an anomalous dispersion. For frequencies in the vicinity of the resonance frequency, the refractive index experiences a strong variation, resulting in an increase of the group refractive index. This explains the delayed response of the molecule under scrutiny attached to the excitation wave. Moreover, the molecule response is attenuated due to the positive imaginary part of the refractive index [144, 145].

From the linear system theory, the real and imaginary parts of the refractive index are not independent. They can linked by the Kramers-Kronig relations as:

$$\begin{aligned} \mathrm{Re}\,(n(\omega)) &= 1 + \frac{2}{\pi}\, P \int_0^\infty \frac{\Omega\ \mathrm{Im}\,(n(\Omega))}{\Omega^2 - \omega^2}\, d\Omega \\ \mathrm{Im}\,(n(\omega)) &= -\frac{2\,\omega}{\pi}\, P \int_0^\infty \frac{\mathrm{Re}\,(n(\Omega)) - 1}{\Omega^2 - \omega^2}\, d\Omega \end{aligned} \tag{B.1}$$

where P is the Cauchy principal value. Analytically, the real part of the susceptibility can be expressed from the imaginary part and vice versa via the Kramers-Kronig relations. Experimentally, it is significantly easier to measure the absorption spectrum of material, which gives the imaginary part of the refractive index, and then applying the Kramers-Kronig relations to attain the real part.

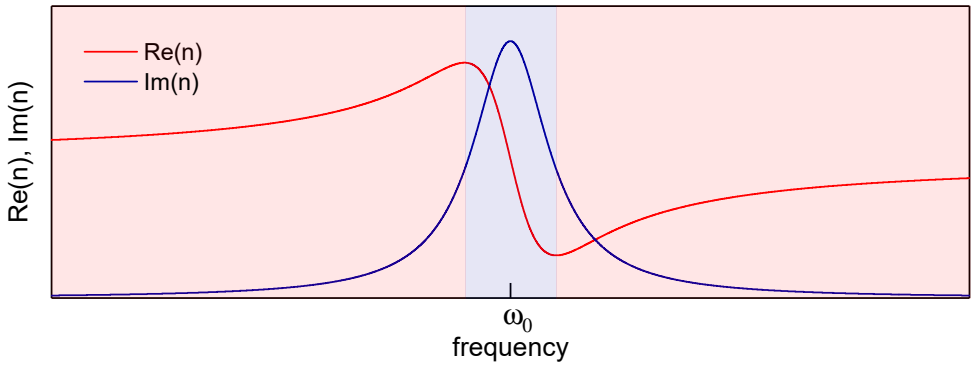

Figure B.1: Refractive index components in Lorentz model. Normal and anomalous dispersion zones are shaded in red and blue, respectively.

Appendix C

List of Publications

Peer reviewed articles:

- H. Fattahi, H. G. Barros, M. Gorjan, T. Nubbemeyer, B. Alsaif, C. Teisset, M. Schultze, S. Prinz, M. Haefner, M. Ueffing, **A. Alismail**, L. Vámos, A. Schwarz, O. Pronin, J. Brons, X. Geng, G. Arisholm, M. Ciappina, V. Yakovlev, D. Kim, A. Azzeer, N. Karpowicz, D. Sutter, Z. Major, T. Metzger, and F. Krausz, "Third-generation femtosecond technology," *Optica* **1**(1), pp. 45–63, 2014, https://doi.org/10.1364/OPTICA.1.000045.

- H. Fattahi, **A. Alismail**, H. Wang, J. Brons, O. Pronin, T. Buberl, L. Vámos, G. Arisholm, A. M. Azzeer, and F. Krausz, "High-power, 1-ps, all-Yb:YAG thin-disk regenerative amplifier," *Optics Letters* **41**(6), pp. 1126-–1129, 2016, https://doi.org/10.1364/OL.41.001126.

- T. Buberl, **A. Alismail**, H. Wang, N. Karpowicz, and H. Fattahi, "Self-compressed, spectral broadening of a Yb:YAG thin-disk amplifier," *Optics Express* **24**(10), pp. 10286–10294, 2016, https://doi.org/10.1364/OE.24.010286.

- H. Fattahi, H. Wang, **A. Alismail**, G. Arisholm, V. Pervak, A. M. Azzeer, and F. Krausz, "Near-PHz-bandwidth, phase-stable continua generated from a Yb:YAG thin-disk amplifier," *Optics Express* **24**(21), pp. 24337–24346, 2016, https://doi.org/10.1364/OE.24.024337.

- T. Nubbemeyer, M. Kaumanns, M. Ueffing, M. Gorjan, **A. Alismail**, H. Fattahi, J. Brons, O. Pronin, H. G. Barros, Z. Major, T. Metzger, D. Sutter, and F. Krausz, "1 kW, 200 mJ picosecond thin-disk laser system," *Optics Letters* **42**(7), pp. 1381–1384, 2017, https://doi.org/10.1364/OL.42.001381.

- **A. Alismail**, H. Wang, N. Altwaijry, and H. Fattahi, "Carrier-envelope phase stable, 5.4 μJ, broadband, mid-infrared pulse generation from a 1-ps, Yb:YAG thin-disk laser," *Applied Optics* **56**(17), pp. 4990–4994, 2017, https://doi.org/10.1364/AO.56.004990.

- H. Wang, **A. Alismail**, G. Barbiero, M. Wendl, and H. Fattahi, "Cross-polarized, multi-octave supercontinuum generation," *Optics Letters* **42**(13), pp. 2595–2598, 2017, https://doi.org/10.1364/OL.42.002595.

- **A. Alismail**, H. Wang, J. Brons, and H. Fattahi, "20 mJ, 1 ps Yb:YAG thin-disk regenerative amplifier," *Journal of Visualized Experiments: JoVE* (125), 2017, https://doi.org/10.3791/55717.

- H. Wang*, **A. Alismail***, G. Barbiero, R. N. Ahmad, and H. Fattahi "High energy, sub-cycle, field synthesizers," *IEEE journal of selected topics in quantum electronics* **25**(4), pp. 1–12, 2019, https://doi.org/10.1109/JSTQE.2019.2924151.

- **A. Alismail***, H. Wang*, G. Barbiero, N. Altwaijry, S. A. Hussain, V. Pervak, W. Schweinberger, A. M. Azzeer, F. Krausz, and H. Fattahi, "Multi-octave, CEP-stable source for high-energy field synthesis," *Science Advances* **6**, p. aax4308, 2020.

Conference contributions:

- T. Nubbemeyer, M. Gorjan, **A. Alismail**, M. Ueffing, H. G. Barros, T. Metzger, D. Sutter, Z. Major, and F. Krausz, "High average power kW-scale Yb:YAG thin-disk regenerative amplifier," in *The European Conference on Lasers and Electro-Optics*, pp. CA–P–1, Optical Society of America, 2015, https://www.osapublishing.org/abstract.cfm?uri=cleo_europe-2015-CA_P_1.

- H. Fattahi, H. Wang, **A. Alismail**, and F. Krausz, "Towards high-power, multi-TW light transients," in *CLEO: Applications and Technology*, pp. SM1M–6, Optical Society of America, 2016, https://doi.org/10.1364/CLEO_SI.2016.SM1M.6.

- **A. Alismail**, H. Wang, A. Azzeer, F. Krausz, and H. Fattahi, "Towards multi-mJ, OPCPA-based field synthesizer," in *The European Conference on Lasers and Electro-Optics*, pp. CG–P–20, Optical Society of America, 2017, https://www.osapublishing.org/abstract.cfm?uri=cleo_europe-2017-CG_P_20.

- H. Wang, **A. Alismail**, G. Barbiero, M. Wendl, F. Krausz , and H. Fattahi, "Cross-polarized supercontinuum generation in $LiNbO_3$ for a multi-mJ waveform synthesizer," in *The European Conference on Lasers and Electro-Optics*, pp. CG–4–2, Op-

tical Society of America, 2017, https://www.osapublishing.org/abstract.cfm?uri=cleo_europe-2017-CG_4_2.

- **A. Alismail**, H. Wang, G. Barbiero, S. A. Hussain, W. Schweinberger, F. Krausz, and H. Fattahi, "Near-infrared molecular fieldoscopy," in *CLEO: Applications and Technology*, pp. AF3K–5, Optical Society of America, 2019, https://doi.org/10.1364/CLEO_AT.2019.AF3K.5.

- **A. Alismail**, H. Wang, G. Barbiero, S. A. Hussain, W. Schweinberger, F. Krausz, and H. Fattahi, "Near-infrared molecular fieldoscopy of water," in *Multiphoton Microscopy in the Biomedical Sciences XIX*, **10882**, p. 1088231, International Society for Optics and Photonics, 2019, https://doi.org/10.1117/12.2507604.

- **A. Alismail**, H. Wang, G. Barbiero, and H. Fattahi, "All ytterbium frontend for high-energy field synthesizers," in *The European Conference on Lasers and Electro-Optics*, pp. CF–9–4, Optical Society of America, 2019, https://www.osapublishing.org/abstract.cfm?uri=CLEO_Europe-2019-cf_9_4.

- **A. Alismail**, H. Wang, G. Barbiero, F. Krausz, and H. Fattahi, "Near-infrared fieldoscopy of water," in *The European Conference on Lasers and Electro-Optics*, pp. CD–2–2, Optical Society of America, 2019, https://www.osapublishing.org/abstract.cfm?uri=CLEO_Europe-2019-cd_2_2.

Appendix D

Selected Publications

A.1 High-power, 1-ps, all-Yb:YAG thin-disk regenerative amplifier

Optics Letters

High-power, 1-ps, all-Yb:YAG thin-disk regenerative amplifier

Hanieh Fattahi,[1,2,*] Ayman Alismail,[2,3] Haochuan Wang,[1,2] Jonathan Brons,[1] Oleg Pronin,[1,2] Theresa Buberl,[4] Lénárd Vámos,[2,5] Gunnar Arisholm,[6] Abdallah M. Azzeer,[3] and Ferenc Krausz[1,2]

[1]Max-Planck Institut für Quantenoptik, Hans-Kopfermann-Str. 1, D-85748 Garching, Germany
[2]Department für Physik, Ludwig-Maximilians-Universität München, Am Coulombwall 1, D-85748 Garching, Germany
[3]Physics and Astronomy Department, King Saud University, Riyadh 11451, Saudi Arabia
[4]Techincal University of Munich, James-Franc- Str. 1, D-85748 Garching, Germany
[5]Wigner Research Center for Physics, Konkoly-Thege Miklós út 29-33, H-1121 Budapest, Hungary
[6]FFI (Norwegian Defence Research Establishment), P.O. Box 25, NO-2027 Kjeller, Norway
*Corresponding author: hanieh.fattahi@mpq.mpg.de

Received 18 January 2016; revised 9 February 2016; accepted 9 February 2016; posted 11 February 2016 (Doc. ID 257223); published 8 March 2016

We report a 100 W, 20 mJ, 1-ps, all-Yb:YAG thin-disk regenerative amplifier seeded by a microjoule-level Yb:YAG thin-disk Kerr-lens mode-locked oscillator. The regenerative amplifier is implemented in a chirped pulse amplification system and operates at an ambient temperature in air, delivering ultrastable output pulses at a 5 kHz repetition rate and with a root mean square power noise value of less than 0.5%. Second harmonic generation of the amplifier's output in a 1.5 mm-thick BBO crystal results in more than 70 W at 515 nm, making the system an attractive source for pumping optical parametric chirped pulse amplifiers in the visible and near-infrared spectral ranges.

OCIS codes: (140.0140) Lasers and laser optics; (140.3480) Lasers, diode-pumped; (140.3515) Lasers, frequency doubled; (140.3615) Lasers, ytterbium.

http://dx.doi.org/10.1364/OL.41.001126

Attosecond technology has provided direct time-domain access to the motion of electrons on the atomic time scale [1]. However, there are many exciting phenomena with significant technological and scientific implications waiting to be observed and controlled once attosecond pulses with higher flux and energy become available. Few-cycle pulses of Ti:Sa-based chirped pulse amplification (CPA) systems have been the workhorse for the generation of attosecond pulses for more than a decade [2], but their peak and average powers for few-cycle pulses are limited. As the cutoff frequency in high harmonic generation (HHG) is proportional to the energy and square of the wavelength of the driving pulses [3,4], HHGs can be dramatically changed if short pulses at a higher energy and a longer wavelength are available. Unlike CPA lasers, optical parametric chirped pulse amplifiers (OPCPA) are scalable in average and peak power and flexible in terms of the central frequency of the amplified spectrum [5,6], but their realization demands high peak-power pump lasers.

Among the currently available laser media, Yb-doped materials are most promising for scaling the average and/or peak power of few-picosecond pulses [7–11], and are therefore unrivaled pump sources for OPCPA. The medium can be pumped with cost-effective diode lasers and because of the absence of excited-state absorption, good thermal conductivity, and cubic crystal structure, they show superior performance in thin-disk geometry. Here, efficient heat transfer takes place through a heat sink attached to the laser gain medium. Due to this cooling concept, the crystal size in thin-disk amplifiers can be scaled easily, which holds promise to reach pulses with joule-level energy and kilowatt-scale average power [12,13]. However, the amplified energy is limited by amplified spontaneous emission [14].

Combining the Yb:YAG gain medium in thin-disk geometry with a CPA allows the scaling of the energy of near-1 ps pulses while keeping the B-integral in the amplifier low. This results in pulses with excellent temporal and spatial profiles, which are important to achieving high efficiency and good beam and pulse quality in an OPCPA.

In this work, we show an all-Yb:YAG thin-disk regenerative amplifier seeded with a Yb:YAG thin-disk Kerr-lens mode-locked (KLM) oscillator delivering 20 mJ, 1 ps pulses at 100 W of average power with excellent short- and long-term stability. Figure 1 outlines the scheme of the system. As described in [15], a higher seed energy results in less accumulated nonlinear phases in regenerative amplifiers. Therefore, a Yb:YAG thin-disk KLM oscillator was developed to provide a high input seed energy for the regenerative amplifier.

The front-end oscillator was designed to meet certain parameters that are critical in reaching the optimum day-to-day performance of the attached amplifier system.

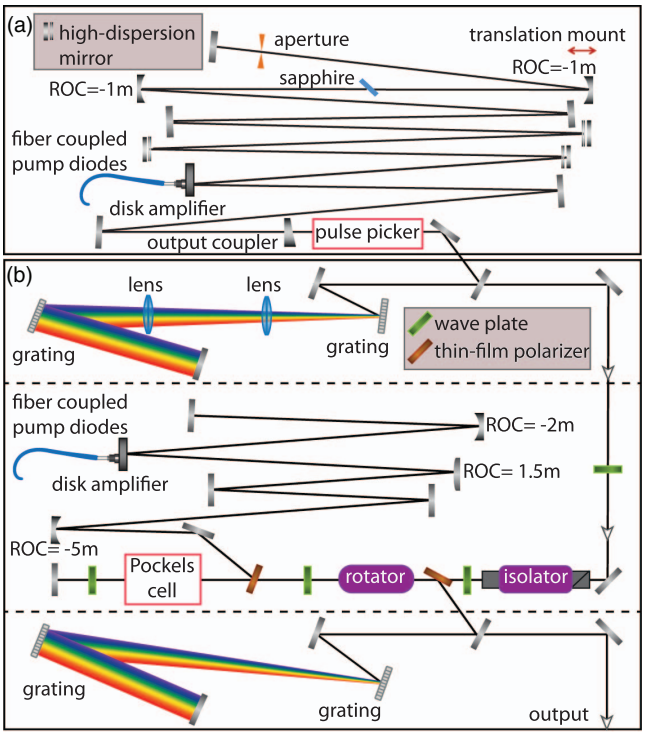

Fig. 1. Schematic layout of the Yb:YAG thin-disk regenerative amplifier. (a) The fiber-coupled diode-pumped KLM thin-disk Yb:YAG oscillator delivers 350 fs pulse at an 11 MHz repetition rate and 2 μJ of energy. A pulse picker is used to reduce the repetition rate to 5 kHz at the input of the amplifier. (b) The input seed pulses are temporally stretched before entering the regenerative amplifier. The amplifier cavity contains a fiber-coupled, diode-pumped, Yb:YAG thin-disk gain medium. The amplified pulses are coupled out using a Pockels cell and subsequently compressed in a reflective dielectric grating compressor. ROC: radius of curvature.

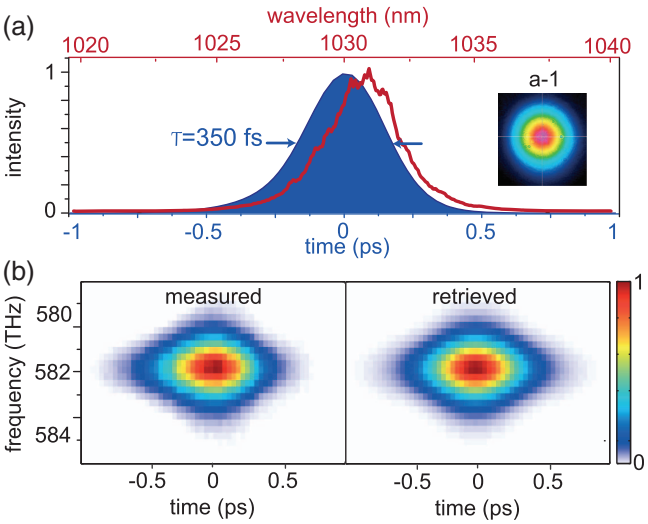

Fig. 2. (a) Oscillator's output spectrum at 25 W of average power (red) along with the retrieved temporal intensity (blue). Inset: transverse intensity profile of the oscillator. (b) Measured and retrieved SHG-FROG spectrograph of the oscillator. G_{error}: 6.8×10^{-3}.

Among them are microjoule-level pulse energy, sub-picosecond pulse duration, and low beam-pointing fluctuations, as well as good thermal and mechanical stability. Today, the highest pulse energy directly from mode-locked oscillators has been generated with thin-disk technology, mainly by employing Yb:YAG as a gain material [16–18].

The cavity setup of the oscillator is shown in Fig. 1(a). The linear cavity is bounded by a wedged output coupler with 13% transmission and a highly reflective end plane mirror, and has a total length of about 13 m. Light amplification is performed by a flat Yb:YAG thin disk that works in reflection and is pumped by fiber-coupled laser diodes at a 940 nm wavelength. Solitonic pulse shaping is supported by a net intra-cavity group-delay dispersion (GDD) of −18, 000 fs^2 per round trip, introduced by three high-dispersion mirrors. The necessary loss modulation for stable pulse generation is provided by a 1 mm-thick sapphire Kerr medium placed between two concave focusing mirrors (−1 m radius of curvature) in combination with a copper aperture and the soft aperture of the gain. Mode locking is initiated by perturbing a concave mirror on a translation stage.

Frequency-resolved optical gating based on second harmonic generation (SHG-FROG) employing a 100 μm BBO crystal is used to characterize the oscillator pulses. The output pulses are transform limited with a duration of 350 fs at the FWHM, each carrying about 2 μJ of energy (Fig. 2). During the course of a workday, the average output power is 25 W, while the root mean square (rms) intensity noise on a photodiode is less than 1% in a 1 Hz–13 MHz spectral window. The rms of the beam pointing fluctuations of the oscillator is less than 0.6% of the beam size over a measurement time window of one hour. The thermal stability of the system is sufficient for near turn-key operation such that alignment of the oscillator is not required on consecutive workdays. The most important parameters of the oscillator, such as the spectral intensity, transverse spatial intensity, and temporal intensity profile, are shown in Fig. 2.

The repetition rate of the pulse train delivered by the oscillator is reduced to 5 kHz before seeding the regenerative amplifier using a pulse picker containing a 25 mm-thick BBO crystal. A pair of gold gratings is used to stretch the high-energy seed pulses. The grating setup provides a GDD of −500 ps/nm. After the stretcher, the seed pulses have 1 μJ of energy and a 2.92 nm spectral bandwidth (FWHM). The stretched pulses are sent to the cavity of the regenerative amplifier, which contains a Faraday rotator to separate the incoming and outgoing pulses, and a Pockels cell with a 20 mm-thick BBO crystal and a clear aperture of 10 mm × 10 mm to couple out pulses from the amplifier.

An approximately 100 μm-thick Yb:YAG thin disk provided by TRUMPF Laser GmbH is used as the gain medium. The 9 mm-diameter disk has a radius of curvature of −2 m and is doped about 7%. The disk module is thermally back-contacted to a water-cooled diamond heat sink, which is connected to a chiller and is pumped with continuous-wave (cw) fiber-coupled diodes at a wavelength of 940 nm with a near-flat-top beam profile with a diameter of 3.5 mm.

At 280 W of cw pumping and after 87 round trips, 130 W of average power is achieved corresponding to an optical-to-optical efficiency of 47%. The M^2 measurement indicates that $M_x^2 = 1.08$ and $M\ 2_y = 1.07$ for the amplified beam. The beam profile and the spectrum of the amplified pulses are

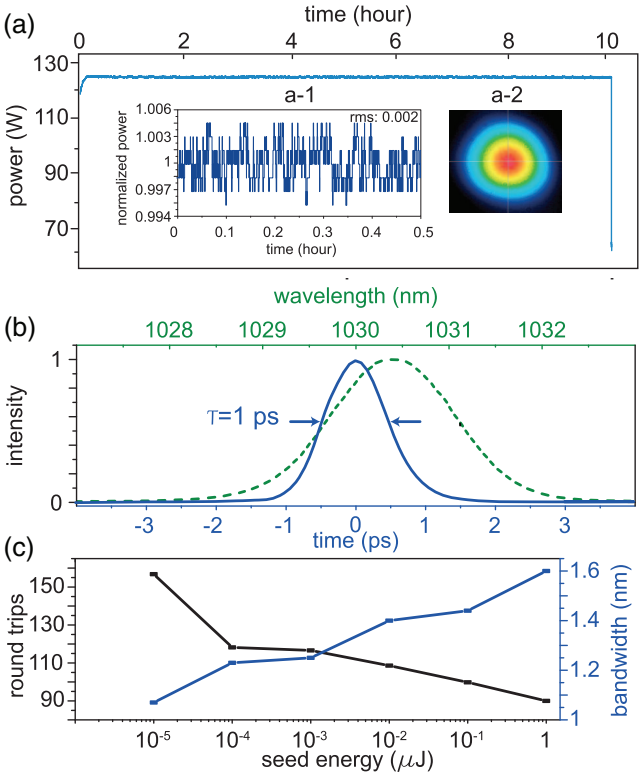

Fig. 3. (a) Average power of the Yb:YAG thin-disk laser over 10 h of continuous operation, measured with an OPHIR powermeter head (L1500W-BB-50-V2). Inset: (a-1): power normalized to its mean value in a half an hour time window. (a-2): Beam profile of the amplified pulses. (b) Output spectrum (green) and the retrieved temporal profile (blue) of the laser pulses at 100 W average power after the grating compressor. (c) Spectral bandwidth (FWHM) of the amplified pulses, and the required round trips at 300 W of pump energy versus seed energy.

shown in Figs. 3(a) and 3(b). The amplifier is operated in saturation and delivers pulses with high stability: the rms of the peak-to-peak energy fluctuations is measured to be less than 1% over a period of 2 s, while the amplifier shows outstanding average power stability over 10 h of uninterrupted operation [Fig. 3(a)]. The keys to this performance include aggressive gain saturation and optimization of the power supply of the laser diodes and the cooling system for the most stable operation.

The amplified pulses are sent to a reflective multilayer dielectric grating pair (line density of 1740 l/mm) for temporal compression with an overall throughput efficiency of 80%. Figure 3(b) shows the retrieved temporal intensity profile of the amplifier pulses, measured by using an SHG-FROG and yielding a pulse duration of 1 ps at the FWHM, which is near the 0.98 ps transform limit.

We also measured the spectral bandwidth of the amplified pulses versus the seed energy while the pump energy was fixed and the number of round trips in the amplifier was adjusted to obtain the highest output energy for each seed energy. The seed energy was reduced by neutral density filters. Figure 3(c) shows spectral bandwidth of the amplified pulse (FWHM) and the required number of round trips versus the seed energy. It is clearly seen that gain narrowing reduces the bandwidth of the amplified pulses when the seed energy is reduced. For seed energy below 10 pJ, the amplifier was unstable and it was not possible to overcome period doubling by increasing the round trip time in the cavity.

The performance reported above renders this system an ideal candidate for pumping OPCPA systems in the near-infrared and (after frequency upconversion) visible spectral ranges. Fulfilling the conservation of energy in the visible OPCPA requires the generation of low-order harmonics of the amplifier. Among the numerous available materials for SHG, critically phase-matched LBOs and BBOs are the best candidates due to their fairly high nonlinear coefficients and damage thresholds. BBO has a higher nonlinearity than LBO, but a larger spatial walk-off and it is limited in the available aperture.

The SHG stage was designed by simulating SHG in BBO and LBO using the SISYFOS code [19]. As the measured pump pulses in space and time have a near-Gaussian profile, we assumed a Gaussian spatiotemporal structure for the pump pulses. In the LBO, the phase-matching angle (θ) was 13.7° and d_{eff} was 0.819 pm/V, and in the BBO, they were $\theta = 23.4°$ and 2 pm/V, respectively. The Sellmeier coefficients were taken from [20,21].

Figure 4(a) shows the simulated energy of the SHG versus the crystal length for 1 ps pulses (FWHM) centered at 1030 nm with a pulse energy of 20 mJ and a peak intensity of 100 GW/cm^2 in type-I BBO and LBO crystals. In the case of the BBO crystal, the SHG reaches saturation in a 1.5 mm-thick crystal because a longer crystal back conversion from the second harmonic to the fundamental pulse takes place. It can be seen that because of the lower nonlinearity of the LBO as compared to the BBO, the saturation of the SHG in the LBO occurs at twice the thickness of the BBO. However, due to the smaller spatial walk-off between the second harmonic beam and the fundamental beam in the LBO, a conversion efficiency similar to the BBO can be achieved [22].

To find the optimum operation regime, SHG-XFROG measurements of pulses at 515 nm and different efficiencies were performed, where the 1 ps pulses of the amplifier were used as the gate pulse. For simplicity, this measurement was conducted in a test SHG stage, containing a 1.5 mm-thick BBO crystal, but with using only 0.5 mJ pulse energy from the amplifier. The peak intensity on the crystal was adjusted to operate the SHG stage in saturation [Fig. 4(b), black curve].

Figure 4(c) compares the retrieved spectral intensity of the experimental second harmonic pulses at different efficiency points indicated on the black efficiency curve of Fig. 4(b) as A, B, and C. For 50% conversion efficiency, the second harmonic pulses have a pulse duration of 0.89 ps, due to pulse shortening based on the χ^2 effect. At higher efficiencies, higher-order spectral phase and spectral broadening is observed. As is shown in Fig. 4(c), at point C, the spectrum is modulated and a dip appears, owing to the back conversion of energy from second harmonic pulses to fundamental pulses. Nevertheless, these chirped second harmonic pulses still maintain a good spatial and temporal quality.

Equipped with this information, the accumulation of the nonlinear phase in the experimental SHG stage was minimized by using a 1.5 mm-thick BBO crystal for the frequency doubling of the full output of the amplifier. The pump beam size was adjusted to reach the peak intensity of 80 GW/cm^2, which resulted in SHG efficiency of 70%, maintaining an excellent beam quality in both space and time [Fig. 4(b), green curve]. The second harmonic pulses have 70 W of average power, and

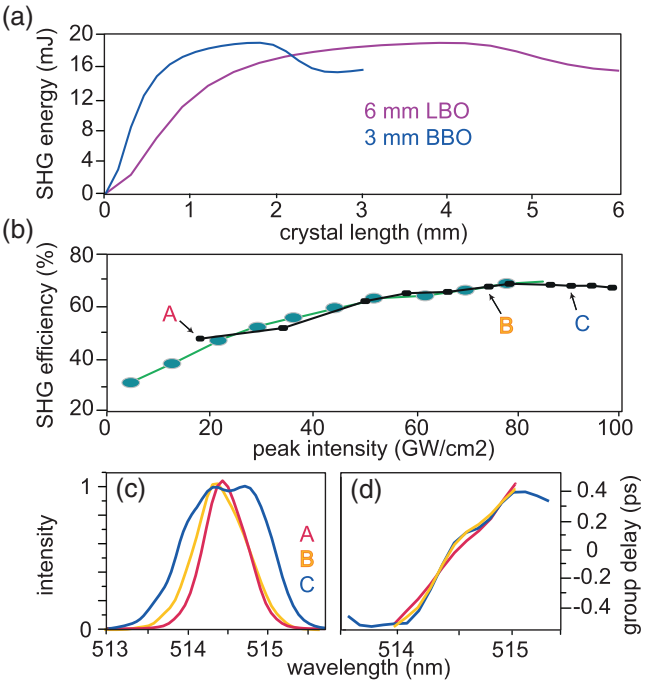

Fig. 4. (a) Simulated SHG efficiency versus crystal length in a 3 mm-thick BBO and 6 mm-thick LBO crystal. (b) Experimental SHG energy versus input pump energy in a 1.5 mm BBO crystal using 0.5 mJ (black curve) and 20 mJ (green curve) of the amplifier's energy. (c) Retrieved spectral intensity and (d) group delay of XFROG measurements of SHG at different efficiencies. Red, orange, and blue curves correspond to points A, B, and C on SHG efficiency curve (black curve in part b).

no phase mismatch due to the thermal effect or the degradation of the crystal is observed.

In conclusion, we have demonstrated an all-Yb:YAG-thin-disk laser system. By using a microjoule-scale, sub-400 fs KLM oscillator as the front end of the Yb:YAG thin-disk regenerative amplifier, the required number of round trips in the amplifier, and hence the spectral narrowing of the amplified pulses, is greatly reduced as compared to previous experiments [23]. This allows the amplification of each pulse seeded into the amplifier (as opposed to the reported period doubling [24]), and substantially improves the stability of the output pulses. As our previous study showed, higher seed energy also reduces the accumulated nonlinear phase and therefore improves the temporal phase of the amplified pulses [15].

The system delivers 1 ps pulses (FWHM) with 20 mJ energy at a 5 kHz repetition rate after the grating compressor. Frequency doubling of the amplified pulses in a simple SHG stage consisting of a 1.5 mm-thick BBO crystal results in more than 70 W of average power at 515 nm with the optical-to-optical efficiency of 70%. The turn-key performance of the amplifier combined with the demonstrated outstanding stability enables the generation of a stable, broadband supercontinuum from the same laser that pumps an OPCPA. This eliminates the need for temporal synchronization of seed and pump pulses, and together with passive carrier-envelope phase stability [24–26], it can lead to a new generation of high-energy, few-cycle OPCPA systems for exploration of new regimes in HHG and attosecond science.

Acknowledgment. We would like to thank Roswitha Graf, Martin Gorjan, Zsuzsanna Major, Moritz Ueffing, and Thomas Nubbemeyer at the Laboratory of Extreme Photonics (LEX) and Thomas Metzger and Dirk Sutter from TRUMPF Laser GmbH for their support.

REFERENCES

1. M. Hentschel, R. Kienberger, C. Spielmann, G. A. Reider, N. Milosevic, T. Brabec, P. Corkum, U. Heinzmann, M. Drescher, and F. Krausz, Nature **414**, 509 (2001).
2. A. L. Cavalieri, E. Goulielmakis, B. Horvath, W. Helml, M. Schultze, M. Fieß, V. Pervak, L. Veisz, V. S. Yakovlev, M. Uiberacker, A. Apolonski, F. Krausz, and R. Kienberger, New J. Phys. **9**, 242 (2007).
3. W. Schweinberger, A. Sommer, E. Bothschafter, J. Li, F. Krausz, R. Kienberger, and M. Schultze, Opt. Lett. **37**, 3573 (2012).
4. T. Popmintchev, M.-C. Chen, D. Popmintchev, P. Arpin, S. Brown, S. Alisauskas, G. Andriukaitis, T. Balciunas, O. D. Mücke, A. Pugzlys, A. Baltuska, B. Shim, S. E. Schrauth, A. Gaeta, C. Hernández-García, L. Plaja, A. Becker, A. Jaron-Becker, M. M. Murnane, and H. C. Kapteyn, Science **336**, 1287 (2012).
5. S. L. Cousin, F. Silva, S. Teichmann, M. Hemmer, B. Buades, and J. Biegert, Opt. Lett. **39**, 5383 (2014).
6. E. Seres, J. Seres, and C. Spielmann, Appl. Phys. Lett. **89**, 181919 (2006).
7. H. Fattahi, H. G. Barros, M. Gorjan, T. Nubbemeyer, B. Alsaif, C. Y. Teisset, M. Schultze, S. Prinz, M. Haefner, M. Ueffing, A. Alismail, L. Vámos, A. Schwarz, O. Pronin, J. Brons, X. T. Geng, G. Arisholm, M. Ciappina, V. S. Yakovlev, D.-E. Kim, A. M. Azzeer, N. Karpowicz, D. Sutter, Z. Major, T. Metzger, and F. Krausz, Optica **1**, 45 (2014).
8. O. H. Heckl, J. Kleinbauer, D. Bauer, S. Weiler, T. Metzger, and D. H. Sutter, *Ultrafast Thin-Disk Lasers* (Springer, 2016), pp. 93–115.
9. R. Fleischhaker, R. Gebs, A. Budnicki, M. Wolf, J. Kleinbauer, and D. H. Sutter, *Conference on Lasers & Electro-Optics Europe & International Quantum Electronics Conference* (CLEO, 2013), p. 1.
10. F. Röser, T. Eidam, J. Rothhardt, O. Schmidt, D. N. Schimpf, J. Limpert, and A. Tünnermann, Opt. Lett. **32**, 3495 (2007).
11. P. Russbueldt, T. Mans, G. Rotarius, J. Weitenberg, H. D. Hoffmann, and R. Poprawe, Opt. Express **17**, 12230 (2009).
12. C. Teisset, M. Schultze, R. Bessing, M. Häfner, J. Rauschenberger, D. Sutter, and T. Metzger, *Picosecond Thin-Disk Regenerative Amplifier with High Average Power for Pumping Optical Parametric Amplifiers* (OSA, 2013), paper CTh5C.6.
13. L. E. Zapata, H. Lin, A.-L. Calendron, H. Cankaya, M. Hemmer, F. Reichert, W. R. Huang, E. Granados, K.-H. Hong, and F. X. Kärtner, Opt. Lett. **40**, 2610 (2015).
14. J. Speiser, J. Opt. Soc. Am. B **26**, 26 (2009).
15. H. Fattahi, A. Schwarz, X. T. Geng, S. Keiber, D. E. Kim, F. Krausz, and N. Karpowicz, Opt. Express **22**, 31440 (2014).
16. C. J. Saraceno, F. Emaury, C. Schriber, M. Hoffmann, M. Golling, T. Südmeyer, and U. Keller, Opt. Lett. **39**, 9 (2014).
17. J. Brons, V. Pervak, E. Fedulova, D. Bauer, D. Sutter, V. Kalashnikov, A. Apolonskiy, O. Pronin, and F. Krausz, Opt. Lett. **39**, 6442 (2014).
18. D. Bauer, I. Zawischa, D. H. Sutter, A. Killi, and T. Dekorsy, Opt. Express **20**, 9698 (2012).
19. G. Arisholm, J. Opt. Soc. Am. B **14**, 2543 (1997).
20. D. Zhang, Y. Kong, and J.-Y. Zhang, Opt. Commun. **184**, 485 (2000).
21. K. Kato, IEEE J. Quantum Electron. **30**, 2950 (1994).
22. H. Fattahi, *Third-Generation Femtosecond Technology* (Springer, 2015).
23. T. Metzger, A. Schwarz, C. Y. Teisset, D. Sutter, A. Killi, R. Kienberger, and F. Krausz, Opt. Lett. **34**, 2123 (2009).
24. J. Fischer, A.-C. Heinrich, S. Maier, J. Jungwirth, D. Brida, and A. Leitenstorfer, Opt. Lett. **41**, 246 (2016).
25. H. Fattahi, A. Schwarz, S. Keiber, and N. Karpowicz, Opt. Lett. **38**, 4216 (2013).
26. A. Baltuška, T. Fuji, and T. Kobayashi, Phys. Rev. Lett. **88**, 133901 (2002).

A.2 20 mJ, 1 ps Yb:YAG thin-disk regenerative amplifier

This paper was published in Journal of Visualized Experiments (JoVE) and is made available as an electronic reprint with the permission of JoVE. The paper can be found at the following URL on the JoVE website: http://dx.doi.org/10.3791/55717.

Video Article

20 mJ, 1 ps Yb:YAG Thin-disk Regenerative Amplifier

Ayman Alismail[1,2], Haochuan Wang[1,3], Jonathan Brons[3], Hanieh Fattahi[1,3]

[1]Department of Physics, Ludwig Maximilian University of Munich

[2]Physics and Astronomy Department, King Saud University

[3]Max Planck Institute of Quantum Optics

Correspondence to: Hanieh Fattahi at hanieh.fattahi@mpq.mpg.de

URL: https://www.jove.com/video/55717
DOI: doi:10.3791/55717

Keywords: Bioengineering, Issue 125, Laser, nonlinear optics, thin-disk, regenerative amplifier, chirped-pulse amplification, second harmonic generation

Date Published: 7/12/2017

Citation: Alismail, A., Wang, H., Brons, J., Fattahi, H. 20 mJ, 1 ps Yb:YAG Thin-disk Regenerative Amplifier. *J. Vis. Exp.* (125), e55717, doi:10.3791/55717 (2017).

Abstract

This is a report on a 100 W, 20 mJ, 1 ps Yb:YAG thin-disk regenerative amplifier. A homemade Yb:YAG thin-disk, Kerr-lens mode-locked oscillator with turn-key performance and microjoule-level pulse energy is used to seed the regenerative chirped-pulse amplifier. The amplifier is placed in airtight housing. It operates at room temperature and exhibits stable operation at a 5 kHz repetition rate, with a pulse-to-pulse stability less than 1%. By employing a 1.5 mm-thick beta barium borate crystal, the frequency of the laser output is doubled to 515 nm, with an average power of 70 W, which corresponds to an optical-to-optical efficiency of 70%. This superior performance makes the system an attractive pump source for optical parametric chirped-pulse amplifiers in the near-infrared and mid-infrared spectral range. Combining the turn-key performance and the superior stability of the regenerative amplifier, the system facilitates the generation of a broadband, CEP-stable seed. Providing the seed and pump of the optical parametric chirped-pulse amplification (OPCPA) from one laser source eliminates the demand of active temporal synchronization between these pulses. This work presents a detailed guide to set up and operate a Yb:YAG thin-disk regenerative amplifier, based on chirped-pulse amplification (CPA), as a pump source for an optical parametric chirped-pulse amplifier.

Video Link

The video component of this article can be found at https://www.jove.com/video/55717/

Introduction

The generation of high-energy, few-cycle laser pulses at a high repetition rate is of great interest to applied fields, such as attosecond science[1,2,3,4] and high-field physics[5,6], which stand to directly benefit from the availability of such sources. OPCPA represents the most promising route to achieving high pulse energies and large amplification bandwidths that simultaneously support few-cycle pulses[1]. To date, OPCPA allows for ultra-broadband amplification, which generates few-cycle pulses[7,8,9,10]. However, a modified implementation of the OPCPA scheme, which uses short pump pulses on the picosecond scale, holds promise for making this approach scalable for even higher pulse energies and average powers in the few-cycle regime[1,11,12]. Due to the high pump intensity in short-pulse pumped OPCPA, the high single-pass gain allows for the use of very thin crystals to support large amplification bandwidths. Although the short-pulse pumped OPCPA has many advantages, the realizability of this approach is subject to the availability of lasers that are specially tailored for this purpose. Such pump lasers are required to deliver high-energy picosecond pulses with near-diffraction limited beam quality at repetition rates in the kHz to MHz range[13,14,15].

The introduction of ytterbium-doped lasers at different geometries, capable of delivering picosecond laser pulses with high energy and high average power, are about to change the current state of the field[1,13,14,15,16,17,18]. Yb:YAG has good thermal conductivity and a long upper-state lifetime, and it can be pumped by cost-effective diode lasers. Its performance when used in thin-disk geometry is outstanding due to the efficient cooling of the gain medium to simultaneously scale the peak and average power. Moreover, the occurrence of self-focusing inside the gain medium during the amplification process is suppressed due to the slenderness of the thin-disk in comparison to other gain medium geometries, resulting in excellent temporal and spatial profiles of the amplified pulses. Combining this concept with CPA holds promise for generating picosecond pulses with hundreds of millijoules of energy and hundreds of watts of average power[19,20].

The aim of this work is to demonstrate a turn-key Yb:YAG thin-disk regenerative amplifier with outstanding daily performance as a suitable source for pumping OPCPAs[21]. To achieve this goal, this study employs a Yb:YAG thin-disk oscillator[22] with several microjoules of pulse energy to seed the amplifier to minimize the accumulated nonlinear phase during the amplification process. This protocol provides the recipe for building and operating the laser system, which is described elsewhere[21]. Details about component implementation and control software are presented, and the alignment process of the system is described.

Protocol

Caution: Please be aware of all safety regulations that are relevant to lasers before using this equipment. Avoid exposure of the eyes or skin to direct or scattered laser beams. Please wear appropriate laser safety goggles throughout the process.

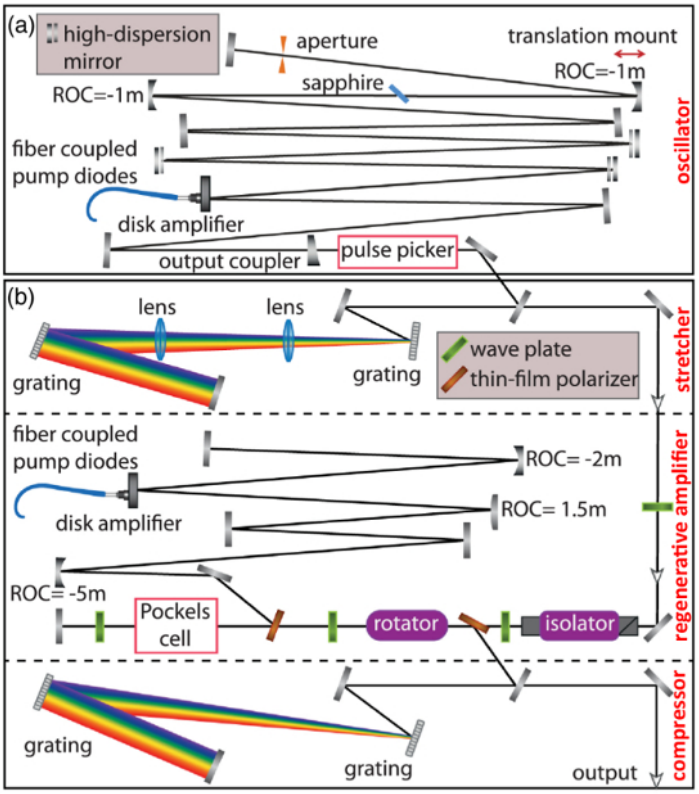

Figure 1: Schematic layout of the Yb:YAG thin-disk regenerative amplifier. (**a**) Yb:YAG thin-disk Kerr-lens mode-locked oscillator. The 13 m linear cavity of the oscillator consists of a 13% transmission output coupler, three high-dispersion mirrors with GDD of -3,000 fs^2, 1 mm sapphire Kerr medium, and a copper hard aperture. A pulse picker, containing a 25 mm-thick BBO crystal, is used to reduce the repetition rate to 5 kHz. (**b**) CPA. First block: the pulse stretcher setup containing two antiparallel gold gratings (1,740 lines/mm), where the seed pulses are temporally stretched to approximately 2 ns. Second block: the regenerative amplifier, where the seed pulse is confined in the amplifier cavity for amplification when the high voltage of the Pockels cell, which contains a BBO crystal with a thickness of 20 mm, is applied. Third block: the pulse compressor containing two parallel dielectric gratings (1,740 lines/mm), where the amplified pulses are temporally compressed down to 1 ps. This figure has been modified from Fattahi *et al.*, with permission from reference[21]. Please click here to view a larger version of this figure.

Component	ROC	Distance
	(mm)	(mm)
OC	∞	0
TD	-17000	600
M_1	-1000	5000
BP	∞	510
M_2	-1000	510
EM	∞	800

Table 1: Cavity design of the oscillator. ROC: radius of curvature, OC: output coupler, TD: thin-disk, M: mirror, BP: Brewster plate, EM: end mirror.

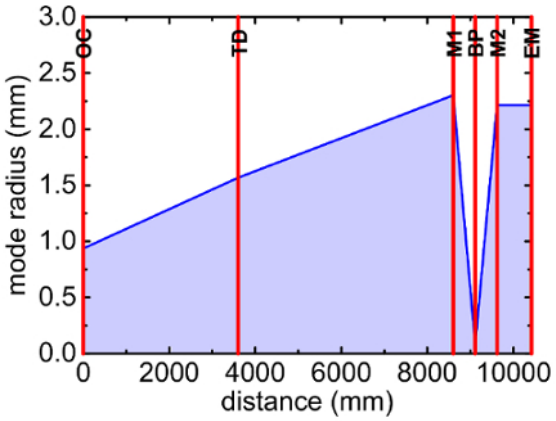

Figure 2: Oscillator cavity design. Calculated mode radius on the cavity components. OC: output coupler, TD: thin-disk, M: mirror, BP: Brewster plate, EM: end mirror. Please click here to view a larger version of this figure.

Component	ROC	Distance
	(mm)	(mm)
EM_1	∞	0
PC	∞	200
M_1	-5000	525
M_2	1500	1500
TD	-2000	1050
EM_2	-2000	2350

Table 2: Cavity design of the regenerative amplifier. ROC: radius of curvature, EM: end mirror, PC: Pockels cell, M: mirror, TD: thin-disk.

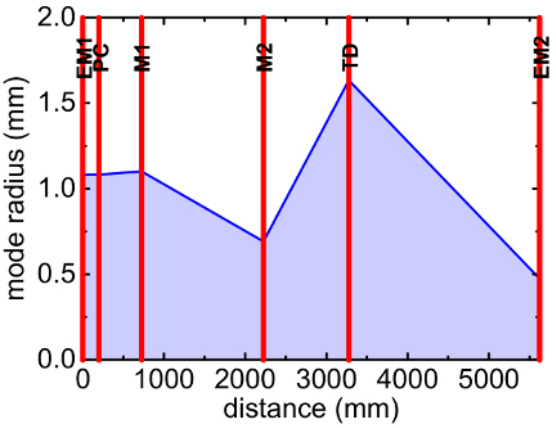

Figure 3: Regenerative amplifier cavity design. Calculated mode radius on the cavity components. EM: end mirror, PC: Pockels cell, M: mirror, TD: thin-disk. Please click here to view a larger version of this figure.

1. Oscillator

1. Turn on the cooling water for the oscillator (**Figure 1a**).
2. Switch on the cooling chillers to cool down the pump diodes, the thin-disk head, and the breadboard. Set the temperature on both chillers to 20 °C.
3. Switch on the power supply for the pump diode unit (see the **Table of Materials**, No. 1) and click the "OUTPUT ON/OFF" button.
   NOTE: A laser cavity simulation software (see the **Table of Materials**, No. 113) was used to simulate and design the oscillator and regenerative amplifier cavity (Table 1 and Table 2; **Figure 2** and **Figure 3**)[23].
4. Pump the thin-disk (see the **Table of Materials**, No. 14) via the coupled fiber at a wavelength of 940 nm by setting the "current" knob on the power supply to 26.2 A, corresponding to the 210-W output, to start the lasing in the oscillator in the continuous wave (CW) mode.
5. **To observe the output spectrum of the CW mode, connect a fiber to the spectrometer and place it before the pulse picker after using an appropriate attenuation.**
   1. In spectrometer software, select the "Spectrometer" tab and then click "Rescan Devices."
   2. Right-click on the spectrometer name and select "Spectrum Graph."

3. Click the "Accept" button on the "Choose Target" window.
4. After blocking the laser beam, click the "Store Dark Spectrum" button on the tool bar and click the "Scope Minus Dark" button to subtract the background spectrum.
5. Unblock the laser beam to observe the spectrum.

6. Observe the output power of the CW mode on the power meter before the pulse picker.
7. To operate the oscillator in pulsed mode and to initiate mode-locking, perturb the high-reflectivity mirror inside the laser cavity (on a translation stage) by mechanically pushing the stage from the back **Figure 1a**).
   NOTE: High-reflectivity mirrors with a high damage threshold were used in the oscillator and regenerative amplifier cavity (see the **Table of Materials**, No. 24 and 28).
8. Observe the spectrum and the output power of the pulsed mode before the pulse picker using a spectrometer and a power meter, respectively.
   NOTE: The oscillator output has 25 W of average power at a wavelength of 1,030 nm, an 11-MHz repetition rate, and a 4-nm spectral bandwidth (FWHM). If oscillator optimization is not required, skip steps 1.9-1.14.
9. Slightly increase the current on the power supply until a CW spike appears in the spectrum measured by the spectrometer.
10. Align the hard aperture in the oscillator (see **Figure 1a**) by tuning its micrometer screws vertically and horizontally to maximize the CW spike.
11. **Observe the depletion of the pump beam profile on the thin-disk.**
    1. Run disk camera program and select "Monochrome" from the "choose mode" window.
    2. Click the "Open camera" button on the tool bar to observe the beam spot on the thin-disk.

12. Tune the piezo linear actuators of the end mirror (motorized knobs) by pushing the "+" or "-" button on the vertical or horizontal motor from the hand-control pad in order to align this depletion to the center of the pump beam profile.
13. Slightly reduce the current on the power supply until the CW spike vanishes in the spectrum.
14. Repeat steps in 1.9-1.13 until a spectrum and an output power similar to the obtained reference levels are achieved (see the measured spectrum in **Figure 4a** (red curve) at 25 W of average power).
15. **To observe the output pulse train and to determine the pulse-to-pulse stability, connect a fast photodiode to an oscilloscope and place it before the pulse picker (after using an appropriate attenuation).**
    1. Select an appropriate trigger level by tuning the "trigger level" knob on the oscilloscope to stabilize the repeating waveforms and observe the output pulse train on the oscilloscope screen.
    2. From the "Measure" menu, select "Peak to Peak Amplitude" to determine the pulse-to-pulse stability.

16. **Observe the output beam profile before the pulse picker and determine the beam-pointing fluctuations.**
    1. Run the beam profiler software and click the "Go, start capture" button from the tool bar to observe the beam profile.
    2. From the tool bar, open the "beam wander" dialog and then click the "clear" button to start new beam-pointing stability measurement.
       NOTE: Fluctuations in the beam or a distorted beam profile (caused by optical damage, beam clipping, *etc.*) can deteriorate system stability.

17. Measure the pulse duration using frequency-resolved optical gating based on second harmonic generation (SHG-FROG)[21,24].

2. Pulse Picker and Pulse Stretcher

NOTE: Caution, be aware of all relevant electrical safety regulations before applying the high voltage on the pulse picker. Use appropriate high-voltage isolation. Remove the diagnostics from the beam path before proceeding with this section. If aligning the pulse picker and its setting is not required, skip steps 2.1, 2.3-2.6, 2.8-2.9, and 2.11.

1. Use two mirrors before the pulse picker setup to align the output beam from the oscillator through the pulse picker unit (see the **Table of Materials**, No. 5 and 7) and its 25 mm-thick beta barium borate (BBO) crystal (see the **Table of Materials**, No. 12) with the aid of the infrared viewer and the laser viewing card (**Figure 1a**).
2. Run the pulse picker program on the oscillator computer.
3. Observe the switching signal of the pulse picker and the pulse train of the oscillator on the oscilloscope (see step 1.15) with the assistance of a fast photodiode.
4. In the pulse picker program, set the delay time (delay A) from the "define delay parameters" dialog to synchronize the switching signal and the pulse train at the pulse picker crystal.
5. Set the switching time window (delay B) from the "define delay parameters" dialog box to select one pulse from the pulse train.
6. Set the internal trigger time (inhibit) from the "define delay parameters" dialog box to 200 µs to pick one pulse every 5 kHz.
7. Reduce the repetition rate of the oscillator from 11 MHz to 5 kHz by switching the power supply of the pulse picker driver to "on" to apply high voltage to the crystal.
8. Select the picked pulses from the pulse train by using a thin-film polarizer (TFP) (see the **Table of Materials**, No. 31) after the pulse picker and dump the remaining pulses into a beam dump.
9. Improve the contrast of the picked pulses by adjusting the half-wave plate (see the **Table of Materials**, No. 32) before the pulse picker.
10. Reduce the peak power of the laser pulse by passing the picked pulses through the stretcher setup to stretch the pulses to a duration of 2 ns (see **Figure 1a-b**).
11. Use two mirrors after the pulse picker setup to align the picked pulses through the stretcher setup, if required.
    NOTE: The stretcher contains two antiparallel gold gratings (see the **Table of Materials**, No. 20 and 21) with a line density of 1,740 lines/mm to stretch the pulses to a duration of 2 ns to avoid damaging the optics during the amplification process in the regenerative amplifier due to a high peak intensity. These pulses are used to seed the regenerative amplifier, as described in the next section (**Figure 1b**, top).

3. Regenerative Amplifier

Caution; Be aware of all relevant electrical safety regulations before applying the high voltage to the Pockels cell. Use appropriate high-voltage isolation. Remove the diagnostics from the beam path before proceeding with this section. Seed pulses are delivered from the Yb:YAG thin-disk Kerr-lens mode-locked oscillator. Other seed strategies can be used to seed the amplifier, such as fiber amplifiers.

1. Turn on the cooling water for the regenerative amplifier (**Figure 1b**, middle).
2. Switch on the cooling chillers to cool down the pump diodes, the thin-disk, the laser head, and the Pockels cell. Set the temperature of the chillers to 28 °C, 17 °C, and 18 °C and then activate the interlock system.
   NOTE: Misaligned seed beam can deteriorate the amplifier stability. If aligning the regenerative amplifier is not required, skip steps 3.3-3.13 and 3.25.
3. Switch on the power supply of the pump diode unit (see the **Table of Materials**, No. 2) and then click the "OUTPUT ON/OFF" button.
4. Pump the thin-disk via the coupled fiber at a wavelength of 940 nm by setting the "current" knob on the power supply to the threshold.
5. Observe the pump beam profile on the disk by using the disk camera (see step 1.11) and select "Circle Geometry" on the "Draw" menu on the disk camera program to mark the position of the beam in the camera program.
6. Reduce the power supply current to zero and then click the "OUTPUT ON/OFF" button. Switch off the power supply of the pump diode unit.
7. Use two mirrors before the regenerative amplifier to align the output beam from the stretcher (seed pulses) through the incoupling optics in the regenerative amplifier to reach the first-end mirror (behind the Pockels cell). Use the beam profiler, the infrared viewer, and the laser viewing card to help with this.
8. Close the amplifier cavity by turning the quarter-wave plate (see the **Table of Materials**, No. 33), behind the Pockels cell, eliminating the laser beam inside the cavity.
9. Tune the motorized knobs of the first-end mirror by pushing the "+" or "-" button on the vertical or horizontal motor (driver 1) from the hand-control pad to align the outcoupling beam.
10. Open the amplifier cavity by turning the quarter-wave plate (behind the Pockels cell) until maximum laser beam intensity is attained inside the cavity. Block the back-reflected beam from the second end mirror.
11. Observe the beam profile of the seed pulses on the disk camera program and overlap the beam with the marked position by tuning the knobs of one of the cavity mirrors before the thin-disk.
12. Unblock the back-reflected beam and observe its spot on the disk camera program.
13. Tune the motorized knobs of the second end mirror by pushing the "+" or "-" button for the vertical or horizontal motor (driver 2) on the hand-control pad to overlap the back reflection with the marked position.
14. From Pockels cell computer, run the Pockels cell program.
    NOTE: If the setting of the Pockels cell is not required, skip steps 3.15-3.18.
15. Observe the switching signal of the Pockels cell (see the **Table of Materials**, No. 6 and 8) and the seed pulses on the oscilloscope (see step 1.15) with the aid of a fast photodiode (**Figure 1b**, middle).
16. In the Pockels cell program, set the delay time (delay A) from the "define delay parameters" dialog box to synchronize the switching of the Pockels cell and the seed pulses at the Pockels cell crystal.
17. Set the switching time window (delay B) from the "define delay parameters" dialog box to confine one pulse inside the cavity of the regenerative amplifier to 4 µs, corresponding to 87 round trips of the pulse.
18. Set the internal trigger time (inhibit) from the "define delay parameters" dialog to "200 µs" to confine the rate to one pulse every 5 kHz.
19. Switch on the power supply of the Pockels cell driver to apply the high voltage on the crystal.
20. Switch on the power supply of the pump diode unit and click the "OUTPUT ON/OFF" button.
21. To amplify the seed pulses in the regenerative amplifier, pump the thin-disk by setting the "current" knob on the power supply to 57.7 A, corresponding to 280 W.
    NOTE: The amplified beam is separated from the seed beam by the combination of a Faraday rotator (see the **Table of Materials**, No. 19) and a TFP. The Yb:YAG oscillator is protected from the back reflection of the amplified beam by an isolator (see the **Table of Materials**, No. 18).
    NOTE: Keep the operation of the Pockels cell and the pump diode unit in the order mentioned above to avoid damaging the optics by Q-switching.
22. Observe the spectrum and the output power (see steps 1.5 and 1.6) before the compressor.
    NOTE: The amplifier output has 125 W of average power at a wavelength of 1,030 nm, a 5-kHz repetition rate, and a 1-nm spectral bandwidth (FWHM).
23. Observe the output pulse train before the compressor on the oscilloscope screen and determine the pulse-to-pulse stability with the aid of a fast photodiode (see step 1.15).
24. Observe the output beam profile before the compressor and determine the beam-pointing fluctuations (see step 1.16).
25. Finely tune the motorized knobs of the second end mirror by pushing the "+" or "-" button on the vertical or horizontal motor (driver 2) from the hand-control pad to improve the operation of the regenerative amplifier, if required.
26. **Characterize the gain-narrowing effect.**
    1. Consider the amplification for different seed energy levels by adjusting the seed energy with neutral-density filters.
    2. Change the number of round trips to obtain the highest output power for a fixed pump power of 300 W.
    3. Observe the output spectrum for each case.

4. Pulse Compressor, Beam Alignment, and Stabilization System

NOTE: Remove the diagnostics from the beam path before proceeding with this section. If aligning the compressor and the beam stabilizer unit is not required, skip steps 4.3 and 4.6.

1. Turn the motorized rotation mount of the half-wave plate (in the output path) by pushing the "+" or "-" button on motor A (driver 5) from the hand-control pad to send a few watts of the amplifier output to the compressor (**Figure 1b**, bottom).

2. Compress the laser pulse down to 1 ps by passing the amplified beam through the compressor setup.
3. Use two mirrors after the regenerative amplifier setup to align the amplified pulses through the compressor setup, if required.
   NOTE: The compressor contains two parallel dielectric gratings (see the **Table of Materials**, No. 22 and 23), with a line density of 1,740 lines/mm.
4. Switch on the power supply of the beam stabilizer unit (see the **Table of Materials**, No. 98). Run the beam stabilizer program on the beam stabilizer computer.
5. Use two mirrors before the detector setup of the beam stabilizer to align the zero-order diffraction from the first grating in the compressor to the beam stabilizer detectors.
6. Push the "regulation" button on the beam stabilizer program to lock the laser beam to avoid beam-drift after the compressor. Turn the motorized half-wave plate again to pass the full output power of the amplifier through the compressor. Adjust the gain of the beam stabilizer detectors with the aid of a neutral-density filter.
7. Characterize the time duration of the compressed pulses using SHG-FROG[21,24].

5. Pump Source of the OPCPA System

NOTE: Remove the diagnostics from the beam path before proceeding with this section.

1. From the OPCPA computer, run the program of the beam profiler.
2. Collimate and adjust the laser beam size after the compressor, using an appropriate telescope to reach the peak intensity of 80 GW/cm^2. Use the beam profiler, infrared viewer, and laser viewing card.
   NOTE: A 1.5 mm-thick BBO crystal was selected for SHG based on the results of the simulation done on the Simulation System for Optical Science (SISYFOS) code[25].
3. Guide the fundamental beam (1,030 nm) through a nonlinear crystal (1.5 mm-thick BBO; see the **Table of Materials**, No. 54) to generate the second harmonic (SH) at 515 nm.
4. Separate the SH beam from the unconverted fundamental beam by placing a harmonic separator at 45^o (see the **Table of Materials**, No. 56) after the crystal.
   NOTE: The SH beam is reflected from the harmonic separator, while the unconverted fundamental beam is transmitted through.
5. Precisely optimize the phase-matching angle of the SH by tuning the knob of the crystal mount to reach the highest conversion efficiency of the SH (70%, corresponding to 70 W).
6. Observe the power of the SH and the unconverted fundamental beams on the power meters (see step 1.6).
7. Observe the Gaussian beam profile of the SH and the unconverted fundamental beams (see step 1.16).
8. Characterize the temporal shape of the SH pulses using cross-correlation frequency resolved optical gating (XFROG)[21,24].

Representative Results

The oscillator delivers 350 fs, 2 µJ, 25-W pulses at 11 MHz repetition rate, with a pulse-to-pulse stability of 1% (rms) and beam-pointing fluctuations of less than 0.6% over 1 h of measurement (**Figure 4**).

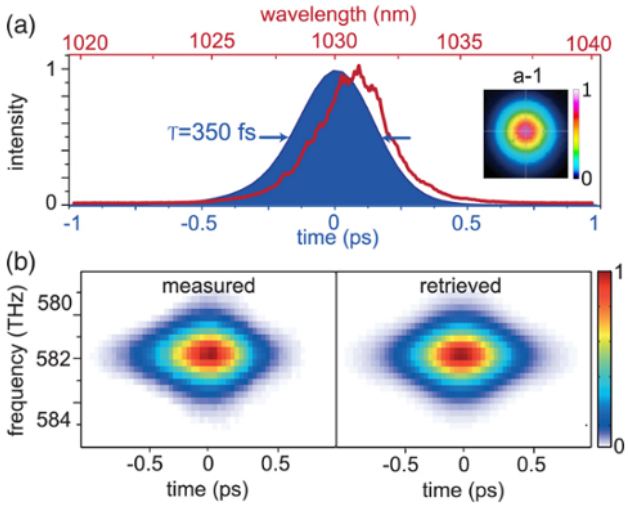

Figure 4: Yb:YAG thin-disk, Kerr-lens mode-locked oscillator. (**a**) The spectrum (red), the retrieved temporal intensity profile (blue), and the spatial profile (inset) of the oscillator pulses. (**b**) Measured and retrieved SHG-FROG spectrograph of the oscillator. This figure has been modified from Fattahi *et al.*, with permission from reference[21]. Please click here to view a larger version of this figure.

The seed pulses are amplified in the regenerative amplifier to 125 W while being pumped with a CW fiber-coupled diode at a wavelength of 940 nm at 280 W, corresponding to an optical-to optical efficiency of 47%. The pulse-to-pulse stability of the amplifier is less than 1%, and the amplifier exhibits excellent long-term stability after 10 h of continuous operation. The amplified beam has an excellent spatial profile, with a M^2 of 1 (M^2_x = 1.08 and M^2_y = 1.07) and an excellent temporal profile after compression to 1 ps (at FWHM) (**Figure 5**).

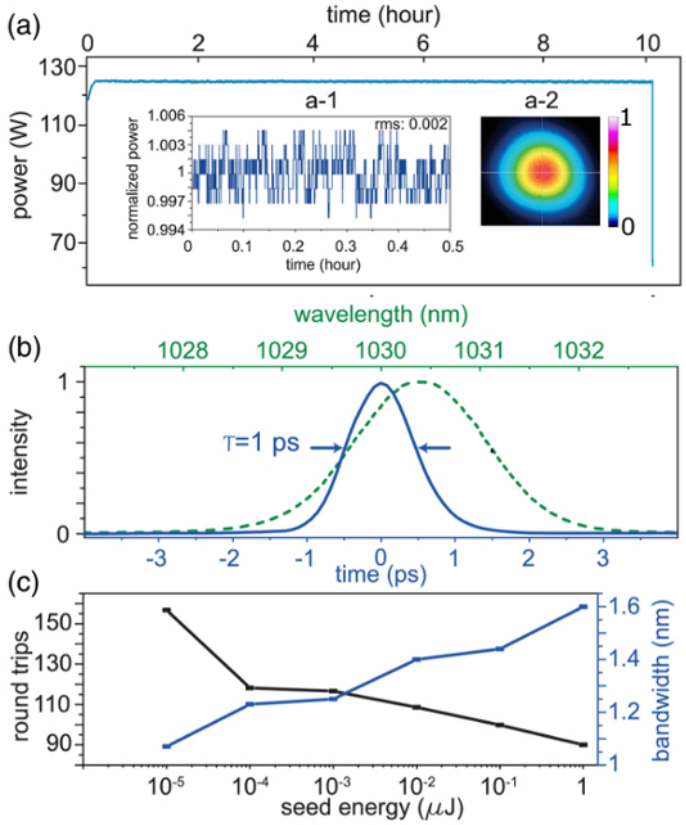

Figure 5: Characterization of the regenerative amplifier output and the gain-narrowing effect. (**a**) The stability of the regenerative amplifier average power after 10 h of continuous operation. Inset: (**a-1**) Normalized power to its mean value in a time window of 0.5 h; (**a-2**) Output beam profile of the regenerative amplifier. (**b**) Amplifier output spectrum (green) and the retrieved temporal intensity (blue) of the laser pulses at 100 W average power after the grating compressor. (**c**) Seed energy versus spectral bandwidth (FWHM) of the amplifier output and the required round trips for the same output average power at 300 W of pump power. This figure has been modified from Fattahi *et al.*, with permission from reference[21]. Please click here to view a larger version of this figure.

The SHG was analyzed using the SISYFOS code[25]. Two different crystals with the following parameters were considered: 1) a type-I, 6 mm-thick lithium triborate (LBO), with a phase-matching angle of 13.7° and a nonlinear coefficient of 0.819 pm/V, and 2) a type-I, 3 mm-thick BBO with a phase-matching angle of 23.4° and a nonlinear coefficient of 2 pm/V[26,27]. 1-ps, 20-mJ pulses at 1,030 nm and a peak intensity of 100 GW/cm^2 were considered as the input of the simulation. The simulation results showed that the BBO performance was superior to that of the LBO for SHG (**Figure 6**).

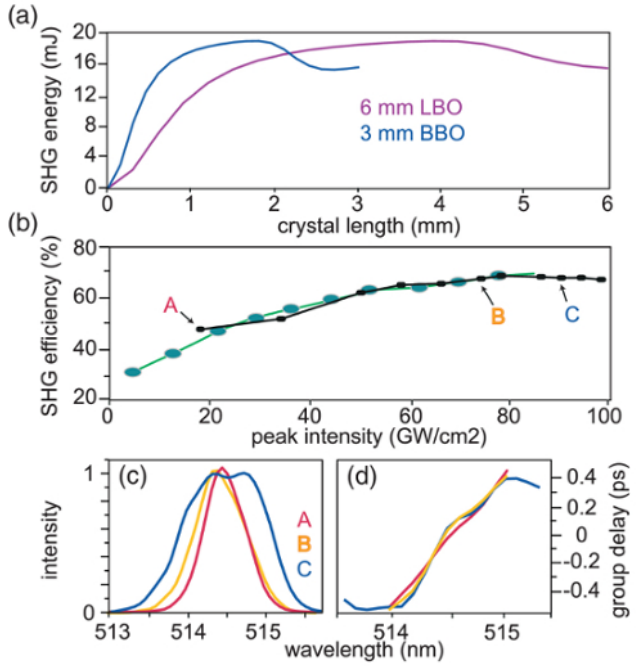

Figure 6: Second harmonic generation. (**a**) Simulated SHG energy for a 6 mm-thick LBO crystal and a 3 mm-thick BBO crystal. (**b**) Experimental SHG efficiency versus input pump peak intensity in a 1.5 mm-thick BBO crystal using 0.5 mJ (black) and 20 mJ (green) of the amplifier output. (**c**) The retrieved spectral intensity and (**d**) the group delay of XFROG measurements for different SHG efficiencies corresponding to points A, B, and C in (b). This figure has been modified from Fattahi *et al.*, with permission from reference[21]. Please click here to view a larger version of this figure.

Discussion

The turn-key operation of the oscillator is achieved by the optimum heat management of the different components of the laser. The output of the oscillator is reproducible on a daily basis, with no need for extra alignment or optimization. In addition, the pulse-to-pulse energy stability and spatial pointing stability of the seed laser fulfills the preconditions to achieving the stable operation of the regenerative amplifier.

Other low-energy seed sources, such as fiber amplifiers, can be used to seed the amplifier. In this study, a 2 µJ Yb:YAG thin-disk KLM oscillator was used to assist the amplification of the regenerative amplifier by reducing the growth of the accumulated nonlinear phases, since the required number of round trips is reduced for higher-input seed energy. Additionally, the higher seed energy influences the amplification process and reduces the gain narrowing. The measured spectral bandwidth of the amplified pulses for different seed energies at a fixed pump power is shown in **Figure 5c**. Amplified spectral bandwidth decreases for lower seed energies because of gain narrowing. For 10 pJ seed energy, the laser operates in the period doubling, and it is not possible to reach stable operation, even by increasing the number of round trips. In addition to the careful optimization of the cooling systems and the power supply of the diodes, the operation of the regenerative amplifier at saturation plays a major role in the achieved stability of the amplifier.

The fundamental or second harmonic of the laser can be used to pump an OPCPA system. For SHG, the performances of an LBO and a BBO crystal were compared, as they offer a high nonlinear coefficient and damage threshold, in spite of the larger spatial walk-off and the limited available aperture in the case of BBO. As the nonlinear coefficient of BBO is almost twice that of the LBO, a shorter crystal is sufficient to reach the saturation limit for SHG (**Figure 6a**). Therefore, BBO is the more suitable choice, as the accumulated nonlinear phase is smaller[28].

The pulse durations of the SH pulses are characterized experimentally at different conversion efficiencies. It was observed that at high conversion efficiencies, the SHG spectrum is broadened and a higher-order spectral phase appears (**Figure 6**). Therefore, case B, with the conversion efficiency of 70%, is chosen where the SH and the unconverted fundamental beams maintain excellent quality.

Disclosures

The authors have nothing to disclose.

Acknowledgements

We would like to thank Prof. Ferenc Krausz for the discussions and Najd Altwaijry for her support for finalizing the manuscript. This work has been financed by the Centre for Advanced Laser Applications (CALA).

References

1. Fattahi, H. *et al.* Third-generation femtosecond technology. *Optica.* **1** (1), 45-63 (2014).
2. Hentschel, M. *et al.* Attosecond metrology. *Nature.* **414** (6863), 509-513 (2001).
3. Cavalieri, A. L. *et al.* Intense 1.5-cycle near infrared laser waveforms and their use for the generation of ultra-broadband soft-x-ray harmonic continua. *New J Phys.* **9** (7), 242 (2007).
4. Schweinberger, W. *et al.* Waveform-controlled near-single-cycle milli-joule laser pulses generate sub-10 nm extreme ultraviolet continua. *Opt Lett.* **37** (17), 3573-3575 (2012).
5. Buck, A. *et al.* Real-time observation of laser-driven electron acceleration. *Nature Phys.* **7** (7), 543-548 (2011).
6. Zhong, H., Karpowicz, N., Zhang, X. C. Terahertz emission profile from laser-induced air plasma. *Appl Phys Lett.* **88** (26), 261103 (2006).
7. Herrmann, D. *et al.* Generation of sub-three-cycle, 16 TW light pulses by using noncollinear optical parametric chirped-pulse amplification. *Opt Lett.* **34** (16), 2459-2461 (2009).
8. Adachi, S. *et al.* 1.5 mJ, 6.4 fs parametric chirped-pulse amplification system at 1 kHz. *Opt Lett.* **32** (17), 2487-2489 (2007).
9. Adachi, S. *et al.* 5-fs, multi-mJ, CEP-locked parametric chirped-pulse amplifier pumped by a 450-nm source at 1 kHz. *Opt express.* **16** (19), 14341-14352 (2008).
10. Yin, Y. *et al.* High-efficiency optical parametric chirped-pulse amplifier in BiB_3O_6 for generation of 3 mJ, two-cycle, carrier-envelope-phase-stable pulses at 1.7 μm. *Opt Lett.* **41** (6), 1142-1145 (2016).
11. Deng, Y. *et al.* Carrier-envelope-phase-stable, 1.2 mJ, 1.5 cycle laser pulses at 2.1 μm. *Opt Lett.* **37** (23), 4973-4975 (2012).
12. Rothhardt, J., Demmler, S., Hädrich, S., Limpert, J., Tünnermann, A. Octave-spanning OPCPA system delivering CEP-stable few-cycle pulses and 22 W of average power at 1 MHz repetition rate. *Opt express.* **20** (10), 10870-10878 (2012).
13. Heckl, O. H. *et al.*Ultrafast Thin-Disk Lasers.*Ultrashort Pulse Laser Technology.* Volume 195, Nolte, S., Schrempel, F., Dausinger, F., ed., Springer International Publishing, 93-115 (2016).
14. Zapata, L. E. *et al.* Cryogenic Yb:YAG composite-thin-disk for high energy and average power amplifiers. *Opt. Lett.* **40** (11), 2610-2613 (2015).
15. Schulz, M. *et al.* Yb:YAG Innoslab amplifier: efficient high repetition rate subpicosecond pumping system for optical parametric chirped pulse amplification. *Opt Lett.* **36** (13), 2456-2458 (2011).
16. Roeser, F. *et al.* Millijoule pulse energy high repetition rate femtosecond fiber chirped-pulse amplification system. *Opt Lett.* **32** (24), 3495-3497 (2007).
17. Russbueldt, P. *et al.* 400 W Yb:YAG Innoslab fs-amplifier. *Opt Express.* **17** (15), 12230-12245 (2009).
18. Baumgarten, C. *et al.* 1 J, 0.5 kHz repetition rate picosecond laser. *Opt Lett.* **41** (14), 3339-3342 (2016).
19. Klingebiel, S. *et al.* 220mJ, 1 kHz Picosecond Regenerative Thin-Disk Amplifier. *European Conference on Lasers and Electro-Optics - European Quantum Electronics Conference.* Optical Society of America. Paper CA_10_1 (2015).
20. Nubbemeyer, T. *et al.* 1 kW, 200 mJ picosecond thin-disk laser system. *Opt Lett.* **42** (7) 1381-1384 (2017).
21. Fattahi, H. *et al.* High-power, 1-ps, all-Yb:YAG thin-disk regenerative amplifier. *Opt Lett.* **41** (6), 1126-1129 (2016).
22. Brons, J. *et al.* Energy scaling of Kerr-lens mode-locked thin-disk oscillators. *Opt Lett.* **39** (22), 6442-6445 (2014).
23. Horvath, C., Loesel, F. *WinLase home. WinLase*. http://www.winlase.com/index.html. (2016).
24. Trebino, R. *et al.* Measuring ultrashort laser pulses in the time-frequency domain using frequency-resolved optical gating. *Rev Sci Instrum.* **68** (9), 3277-3295 (1997).
25. Arisholm, G. General numerical methods for simulating second-order nonlinear interactions in birefringent media. *J Opt Soc Am B.* **14** (10), 2543-2549 (1997).
26. Zhang, D. X., Kong, Y. F., & Zhang, J. Y. Optical parametric properties of 532-nm-pumped beta-barium-borate near the infrared absorption edge. *Opt Commun.* **184** (5), 485-491 (2000).
27. Kato, K. Temperature-tuned 90^o phase-matching properties of LiB_3O_5. *IEEE J Quant Electron.* **30** (12), 2950-2952 (1994).
28. Fattahi, H. *Third-generation femtosecond technology.* Springer International Publishing. (2016).

A.3 Near-PHz-bandwidth, phase-stable continua generated from a Yb:YAG thin-disk amplifier

Research Article | Vol. 24, No. 21 | 17 Oct 2016 | OPTICS EXPRESS 24337

Optics EXPRESS

Near-PHz-bandwidth, phase-stable continua generated from a Yb:YAG thin-disk amplifier

HANIEH FATTAHI,[1,2,*] HAOCHUAN WANG,[1,2] AYMAN ALISMAIL,[2,3] GUNNAR ARISHOLM,[4] VLADIMIR PERVAK,[1,2] ABDALLAH M. AZZEER,[3] AND FERENC KRAUSZ[1,2]

[1]*Max-Planck Institut für Quantenoptik, Hans-Kopfermann-Str. 1, D-85748 Garching, Germany*
[2]*Department für Physik, Ludwig-Maximilians-Universität München, Am Coulombwall 1, D-85748 Garching, Germany*
[3]*Physics and Astronomy Department, King Saud University, Riyadh 11451, Saudi Arabia*
[4]*FFI (Norwegian Defence Research Establishment), P.O. Box 25, NO-2027 Kjeller, Norway*
[*]*hanieh.fattahi@mpq.mpg.de*

Abstract: We report on the generation of a multi-octave, phase-stable continuum from the output of a Yb:YAG regenerative amplifier delivering 1-ps pulses with randomly varying carrier-envelope phase (CEP). The intrinsically CEP-stable spectral continuum spans from 450 nm to beyond 2500 nm, covering a spectral range of about 0.6 PHz. The generated coherent broadband light carries an energy of 4 μJ, which can be scaled to higher values if required. The system has been designed and is ideally suited for seeding broadband parametric amplifiers and multi-channel synthesizers pumped by picosecond Yb:YAG amplifiers, obviating the need for active timing synchronization required in previous approaches. The presented concept paves the way to cost-effective, reliable all-Yb:YAG single-cycle sources with terawatt peak-power and tens-of-Watts average power.

OCIS codes: (140.3615) Lasers, ytterbium; (190.4223) Nonlinear wave mixing; (320.7110) Ultrafast nonlinear optics; (190.4380) Nonlinear optics, four-wave mixing; (140.7090) Ultrafast lasers.

References and links

1. A. Douhal, F. Lahmani, and A. H. Zewail, "Proton-transfer reaction dynamics," Chem. Phys. **207**, 477–498 (1996).
2. M. Drescher, M. Hentschel, R. Kienberger, M. Uiberacker, V. Yakovlev, A. Scrinzi, T. Westerwalbesloh, U. Kleineberg, U. Heinzmann, and F. Krausz, "Time-resolved atomic inner-shell spectroscopy," Nature **419**, 803–807 (2002).
3. S. R. Leone, C. W. McCurdy, J. Burgdörfer, L. S. Cederbaum, Z. Chang, N. Dudovich, J. Feist, C. H. Greene, M. Ivanov, R. Kienberger, U. Keller, M. F. Kling, Z.-H. Loh, T. Pfeifer, A. N. Pfeiffer, R. Santra, K. Schafer, A. Stolow, U. Thumm, and M. J. J. Vrakking, "What will it take to observe processes in 'real time'?" Nat. Photonics **8**, 162–166 (2014).
4. G. Sansone, L. Poletto, and M. Nisoli, "High-energy attosecond light sources," Nat. Photonics **5**, 655–663 (2011).
5. D. Shorokhov and A. H. Zewail, "Perspective: 4D ultrafast electron microscopy-Evolutions and revolutions," J. Chem. Phys. **144**, 0809011 (2016).
6. A. Gordon and F. X. Kärtner, "Scaling of keV HHG photon yield with drive wavelength," Opt. Express **13**, 2941–2947 (2005).
7. T. Popmintchev, M.-C. Chen, D. Popmintchev, P. Arpin, S. Brown, S. Alisauskas, G. Andriukaitis, T. Balciunas, O. D. Mücke, A. Pugzlys, A. Baltuska, B. Shim, S. E. Schrauth, A. Gaeta, C. Hernández-García, L. Plaja, A. Becker, A. Jaron-Becker, M. M. Murnane, and H. C. Kapteyn, "Bright coherent ultrahigh harmonics in the keV x-ray regime from mid-infrared femtosecond lasers," Science **336**, 1287–1291 (2012).
8. M. T. Hassan, A. Wirth, I. Grguraš, A. Moulet, T. T. Luu, J. Gagnon, V. Pervak, and E. Goulielmakis, "Invited article: attosecond photonics: synthesis and control of light transients," Rev. Sci. Instrum. **83**, 1113011 (2012).
9. O. D. Mucke, S. Fang, G. Cirmi, G. M. Rossi, S.-H. Chia, H. Ye, Y. Yang, R. Mainz, C. Manzoni, P. Farinello, G. Cerullo, and F. X. Kartner, "Toward waveform nonlinear optics using multimillijoule sub-cycle waveform synthesizers," IEEE J. Sel. Top. Quantum Electron. **21**, 1–12 (2015).
10. C. Manzoni, S.-W. Huang, G. Cirmi, P. Farinello, J. Moses, F. X. Kärtner, and G. Cerullo, "Coherent synthesis of ultra-broadband optical parametric amplifiers," Opt. Lett. **37**, 1880–1882 (2012).
11. H. Fattahi, H. G. Barros, M. Gorjan, T. Nubbemeyer, B. Alsaif, C. Y. Teisset, M. Schultze, S. Prinz, M. Haefner, M. Ueffing, A. Alismail, L. Vámos, A. Schwarz, O. Pronin, J. Brons, X. T. Geng, G. Arisholm, M. Ciappina, V. S.

#268771 http://dx.doi.org/10.1364/OE.24.024337
Journal © 2016 Received 27 Jun 2016; revised 2 Sep 2016; accepted 2 Sep 2016; published 12 Oct 2016

Optics EXPRESS

Yakovlev, D.-E. Kim, A. M. Azzeer, N. Karpowicz, D. Sutter, Z. Major, T. Metzger, and F. Krausz, "Third-generation femtosecond technology," Optica **1**, 45–63 (2014).
12. H. Cankaya, A.-L. Calendron, G. Cirmi, C. Zhou, O. D. Muecke, and F. X. Kaertner, "Temporal characterization of front-end for Yb-based high-energy optical waveform synthesizers," in "Conf. Lasers Electro-Optics," (OSA, Washington, D.C., 2016), p. STu4I.2.
13. H. Fattahi, H. Wang, A. Alismail, and F. Krausz, "Towards high-power, multi-TW light transients," in "Conf. Lasers Electro-Optics," (OSA, Washington, D.C., 2016), p. SM1M.6.
14. A. Dubietis, G. Jonušauskas, and A. Piskarskas, "Powerful femtosecond pulse generation by chirped and stretched pulse parametric amplification in BBO crystal," Opt. Commun. **88**, 437–440 (1992).
15. D. Herrmann, L. Veisz, R. Tautz, F. Tavella, K. Schmid, V. Pervak, and F. Krausz, "Generation of sub-three-cycle, 16 TW light pulses by using noncollinear optical parametric chirped-pulse amplification," Opt. Lett. **34**, 2459–2461 (2009).
16. S. Adachi, N. Ishii, T. Kanai, A. Kosuge, J. Itatani, Y. Kobayashi, D. Yoshitomi, K. Torizuka, and S. Watanabe, "5-fs, multi-mJ, CEP-locked parametric chirped-pulse amplifier pumped by a 450-nm source at 1 kHz," Opt. Express **16**, 14341–14352 (2008).
17. H. Fattahi, C. Skrobol, M. Ueffing, Y. Deng, A. Schwarz, Y. Kida, V. Pervak, T. Metzger, Z. Major, and F. Krausz, "High efficiency, multi-mJ, sub 10 fs, optical parametric amplifier at 3 kHz," in *CLEO Sci. Innov.* (Optical Society of America, 2012), pp. CTh1N.6.
18. K.-H. Hong, C.-J. Lai, J. Siqueira, P. Krogen, J. Moses, M. Smrz, L. E. Zapata, and F. X. Kärtner, "Multi-mJ, kHz, 2.1-μm OPCPA for high-flux soft X-ray high-harmonic radiation," in *Res. Opt. Sci.*, (OSA, 2014), paper JW2A.5.
19. Y. Deng, A. Schwarz, H. Fattahi, M. Ueffing, X. Gu, M. Ossiander, T. Metzger, V. Pervak, H. Ishizuki, T. Taira, T. Kobayashi, G. Marcus, F. Krausz, R. Kienberger, and N. Karpowicz, "Carrier-envelope-phase-stable, 1.2 mJ, 1.5 cycle laser pulses at 2.1 μm," Opt. Lett. **37**, 4973–4975 (2012).
20. S. L. Cousin, F. Silva, S. Teichmann, M. Hemmer, B. Buades, and J. Biegert, "High-flux table-top soft x-ray source driven by sub-2-cycle, CEP stable, 185-μm 1-kHz pulses for carbon K-edge spectroscopy," Opt. Lett. **39**, 5383–5386 (2014).
21. M. Puppin, Y. Deng, O. Prochnow, J. Ahrens, T. Binhammer, U. Morgner, M. Krenz, M. Wolf, and R. Ernstorfer, "500 kHz OPCPA delivering tunable sub-20 fs pulses with 15 W average power based on an all-ytterbium laser," Opt. Express **23**, 1491–1497 (2015).
22. Y. Shamir, J. Rothhardt, S. Hadrich, S. Demmler, M. Tschernajev, J. Limpert, and A. Tunnermann, "Scaling of a 2Âţm few-cycle OPCPA system to 100 kHz repetition rate and high average powers," in *2015 IEEE Photonics Conf.* (IEEE, 2015), pp. 216–217.
23. S. Prinz, M. Haefner, C. Y. Teisset, R. Bessing, K. Michel, Y. Lee, X. T. Geng, S. Kim, D. E. Kim, T. Metzger, and M. Schultze, "CEP-stable, sub-6 fs, 300-kHz OPCPA system with more than 15 W of average power," Opt. Express **23**, 1388–1394 (2015).
24. Y. Shamir, J. Rothhardt, S. Hädrich, S. Demmler, M. Tschernajew, J. Limpert, and A. Tünnermann, "High-average-power 2 μm few-cycle optical parametric chirped pulse amplifier at 100 kHz repetition rate," Opt. Lett. **40**, 5546–5549 (2015).
25. J. Rothhardt, S. Demmler, S. Hädrich, J. Limpert, and A. Tünnermann, "Octave-spanning OPCPA system delivering CEP-stable few-cycle pulses and 22 W of average power at 1 MHz repetition rate," Opt. Express **20**, 10870–10878 (2012).
26. F. Röser, T. Eidam, J. Rothhardt, O. Schmidt, D. N. Schimpf, J. Limpert, and A. Tünnermann, "Millijoule pulse energy high repetition rate femtosecond fiber chirped-pulse amplification system," Opt. Lett. **32**, 3495–3497 (2007).
27. P. Russbueldt, T. Mans, G. Rotarius, J. Weitenberg, H. D. Hoffmann, and R. Poprawe, "400W Yb:YAG Innoslab fs-Amplifier," Opt. Express **17**, 12230–12245 (2009).
28. L. E. Zapata, H. Lin, A.-L. Calendron, H. Cankaya, M. Hemmer, F. Reichert, W. R. Huang, E. Granados, K.-H. Hong, and F. X. Kärtner, "Cryogenic Yb:YAG composite-thin-disk for high energy and average power amplifiers," Opt. Lett. **40**, 2610–2613 (2015).
29. C. Baumgarten, M. Pedicone, H. Bravo, H. Wang, L. Yin, C. S. Menoni, J. J. Rocca, and B. A. Reagan, "1 J, 05 kHz repetition rate picosecond laser," Opt. Lett. **41**, 3339–3342 (2016).
30. O. H. Heckl, J. Kleinbauer, D. Bauer, S. Weiler, T. Metzger, and D. H. Sutter, *Ultrafast Thin-Disk Lasers* (2016), pp. 93–115.
31. H. Fattahi, A. Alismail, H. Wang, J. Brons, O. Pronin, T. Buberl, L. Vámos, G. Arisholm, A. M. Azzeer, and F. Krausz, "High-power, 1-ps, all-Yb:YAG thin-disk regenerative amplifier," Opt. Lett. **41**, 1126–1129 (2016).
32. H. Fattahi, C. Y. Teisset, O. Pronin, A. Sugita, R. Graf, V. Pervak, X. Gu, T. Metzger, Z. Major, F. Krausz, and A. Apolonski, "Pump-seed synchronization for MHz repetition rate, high-power optical parametric chirped pulse amplification," Opt. Express **20**, 9833–9840 (2012).
33. A. Schwarz, M. Ueffing, Y. Deng, X. Gu, H. Fattahi, T. Metzger, M. Ossiander, F. Krausz, and R. Kienberger, "Active stabilization for optically synchronized optical parametric chirped pulse amplification," Opt. Express **20**, 5557–5565 (2012).
34. I. D. Jung, F. X. Kärtner, N. Matuschek, D. H. Sutter, F. Morier-Genoud, G. Zhang, U. Keller, V. Scheuer, M. Tilsch, and T. Tschudi, "Self-starting 65-fs pulses from a Ti:sapphire laser," Opt. Lett. **22**, 1009–1011 (1997).
35. O. Pronin, M. Seidel, F. Lücking, J. Brons, E. Fedulova, M. Trubetskov, V. Pervak, A. Apolonski, T. Udem, and

Optics EXPRESS

F. Krausz, "High-power multi-megahertz source of waveform-stabilized few-cycle light," Nat. Commun. **6**, 1–6 (2015).
36. N. Tolstik, A. Pospischil, E. Sorokin, and I. T. Sorokina, "Graphene mode-locked Cr:ZnS chirped-pulse oscillator," Opt. Express **22**, 7284–7289 (2014).
37. C. Homann, M. Bradler, M. Förster, P. Hommelhoff, and E. Riedle, "Carrier-envelope phase stable sub-two-cycle pulses tunable around 1.8 Âţm at 100 kHz," Opt. Lett. **37**, 1673–1675 (2012).
38. S. Hädrich, J. Rothhardt, M. Krebs, S. Demmler, J. Limpert, and A. Tünnermann, "Improving carrier-envelope phase stability in optical parametric chirped-pulse amplifiers by control of timing jitter," Opt. Lett. **37**, 4910–4912 (2012).
39. H. Fattahi, *Third-Generation Femtosecond Technology*, (Springer International Publishing, 2015).
40. T. Metzger, "High-repetition-rate picosecond pump laser based on a Yb:YAG disk amplifier for optical parametric amplification," PhD thesis (2009).
41. O. H. Heckl, C. J. Saraceno, C. R. E. Baer, T. Südmeyer, Y. Y. Wang, Y. Cheng, F. Benabid, and U. Keller, "Temporal pulse compression in a xenon-filled Kagome-type hollow-core photonic crystal fiber at high average power," Opt. Express **19**, 19142–19149 (2011).
42. L. Lötscher and L. Vámos, "Long-term stability of nonlinear pulse compression using solid-core large-mode-area fibers," J. Lasers Opt. Photonics **02**, 1–5 (2015).
43. J. Galinis, G. Tamošauskas, I. GraŽulevičiute, E. Keblyte, V. Jukna, and A. Dubietis, "Filamentation and supercontinuum generation in solid-state dielectric media with picosecond laser pulses," Phys. Rev. A - At. Mol. Opt. Phys. **92**, 1–5 (2015).
44. A.-L. Calendron, H. Çankaya, G. Cirmi, and F. X. Kärtner, "White-light generation with sub-ps pulses," Opt. Express **23**, 13866–13879 (2015).
45. T. Buberl, A. Alismail, H. Wang, N. Karpowicz, and H. Fattahi, "Self-compressed, spectral broadening of a Yb:YAG thin-disk amplifier," Opt. Express **24**, 10286–10294 (2016).
46. G. Arisholm, "General numerical methods for simulating second-order nonlinear interactions in birefringent media," J. Opt. Soc. Am. B **14**, 2543–2549 (1997).
47. G. Arisholm, "Quantum noise initiation and macroscopic fluctuations in optical parametric oscillators," J. Opt. Soc. Am. B **16**, 117–127 (1999).
48. D. Zhang, Y. Kong, and J.-y. Zhang, "Optical parametric properties of 532-nm-pumped beta-barium-borate near the infrared absorption edge," Opt. Commun. **184**, 485–491 (2000).
49. D. Eimerl, L. Davis, S. Velsko, E. K. Graham, and A. Zalkin, "Optical, mechanical, and thermal properties of barium borate," J. Appl. Phys. **62**, 1968–1983 (1987).
50. J. C. Travers, W. Chang, J. Nold, N. Y. Joly, and P. St. J. Russell, "Ultrafast nonlinear optics in gas-filled hollow-core photonic crystal fibers [Invited]," J. Opt. Soc. Am. B **28**, A11 (2011).
51. T. Amotchkina, H. Fattahi, Y. A. Pervak, M. Trubetskov, and V. Pervak, "Broadband beamsplitter for high intensity laser applications in the infra-red spectral range," Opt. Express **24**, 16752–16759 (2016).
52. A. Wirth, M. T. Hassan, I. Grguras, J. Gagnon, A. Moulet, T. T. Luu, S. Pabst, R. Santra, Z. A. Alahmed, A. M. Azzeer, V. S. Yakovlev, V. Pervak, F. Krausz, and E. Goulielmakis, "Synthesized light transients," Science **334**, 195–200 (2011).
53. G. Krauss, S. Lohss, T. Hanke, A. Sell, S. Eggert, R. Huber, and A. Leitenstorfer, "Synthesis of a single cycle of light with compact erbium-doped fibre technology," Nat. Photonics **4**, 33–36 (2010).

1. Introduction

Femtosecond technology enabled tracking nuclear dynamics in molecules and gave birth to the novel discipline of femtochemistry [1]. Attosecond metrology and spectroscopy, in turn, opened the door for real-time observation of atomic-scale electronic motions [2]. So far, it has been restricted to the use of low-energy attosecond XUV pulses in combination with strong few-cycle near-infrared fields controlled on an attosecond time scale [3]. Exploring electron phenomena would largely benefit from attosecond pulses of higher flux and, in particular, of higher photon energy, permitting attosecond-pump, attosecond-probe spectroscopy [4] and direct access to dynamic rearrangement of atomic-scale electron distributions by diffraction imaging [5], respectively.

The cutoff energy in high-order harmonic generation (HHG) scales linearly with the peak intensity and quadratically with the wavelength of the driving pulse. Hence, two routes can be considered to extend attosecond pulses to the X-ray regime: (i) increasing the carrier wavelength of the driving laser and accepting a reduction in conversion efficiency due to its unfavorable scaling with wavelength [6, 7] or (ii) boosting its peak power whilst simultaneously temporally confining it, preferably to a single cycle or less [8], to avoid preionization of the atoms on the pulse

Optics EXPRESS

front. Preionization depletes the ground state of the medium and deteriorates phasematching, compromising thereby the efficiency of the HHG process.

We propose to take advantage of both approaches: (i) add longer wavelengths to the driving fields for being able to furnish the recolliding electron with more energy, (ii) confine the multi-octave field to a single field cycle at multi-terawatt peak power level, preferably at multi-kHz repetition rates, and (iii) tailoring the spectral chirp of the light transient for better control of tunneling ionization, releasing the electrons and of their subsequent sub-cycle trajectories. This demands a new femtosecond technology based on the phase-coherent superposition of few-cycle pulses from multiple broadband optical parametric amplifiers (OPAs) operated in different spectral ranges [9–13].

OPAs have the potential to boost the energy and average power of few-cycle pulses simultaneously, due to their broad amplification bandwidth, high amplification gain, and low heat dissipation [14]. Combined with chirped-pulse amplification (OPCPA), they have been reported to deliver few-cycle pulses with energies ranged from millijoule to the Joule level at low average-power [15–20], or with microjoule energies at high, tens-of-Watts, average power levels [21–25]. Achieving simultaneously high peak- and average powers has been hampered by the lack of (i) powerful, cost-effective pump lasers, and (ii) ultra-broadband, CEP-stable seed sources of sufficient power. The former requirement is now being met by Yb-doped lasers in fiber [26], slab [27–29], or thin-disk [11, 30, 31] geometries. The unsatisfactory state of affairs in terms of broadband seed generation (briefly reviewed in the following section) provided the motivation of the current work.

2. Seed generation for broadband OPAs

So far, the input signal for broadband OPAs has been mostly derived from low-energy broadband oscillators. In this approach the seed pulse has to be temporally synchronized with the pump pulse relying on active optical synchronization to suppress the temporal jitter accumulating through the pump amplification stages [32, 33]. Furthermore, low-energy seed pulses from oscillators cause undesirable superflourescence and low conversion efficiency in the OPCPA chain. Also, the carrier frequency of the amplified pulses is mostly restricted to the carrier frequency of the available broadband oscillators [34–36].

The energy of the oscillator's pulses could be scaled further in a separate amplifier [15] and their central frequency can be converted in nonlinear stages [18, 19, 37]. However, these schemes contain at least three laser systems and several nonlinear stages in addition to the temporal synchronization, making them complex and not robust. In addition, the residual temporal jitter between pump and seed pulses degrades the carrier-envelope-phase and energy stability of the amplified pulses [38].

Generation of multi-octave seed pulses directly from the output of the OPCPA pump source could overcome these problems and reduces the complexity and cost of the system, as here pump and seed pulses are generated from the same laser source and are intrinsically synchronized.

The architecture of a field synthesizer based on Yb:YAG thin-disk lasers is studied theoretically in [11, 39]. The apparatus consists of (i) an Yb:YAG thin-disk regenerative amplifier, followed by (ii) phase-stable multi-octave seed generation, (iii) amplification of three complementary spectral portions of the supercontinuum (SC) in OPCPA channels, and (iv) coherent recombination of the output of these channels.

CEP-stable continuum generation from narrow-band, picosecond pulses has been found to be challenging so far. Spectral broadening of picosecond pulses in waveguides has been shown to be unstable [40] or limited to energies of the order of 1-μJ [41, 42]. Filamentation in bulk does not offer a viable alternative because the critical peak power required by 1-ps-scale pulses for filamentation approaches the material's damage threshold [43, 44]. In this paper we report on the stable, reproducible generation of a multi-octave, CEP-stable continuum from 1-ps pulses for the

Optics EXPRESS

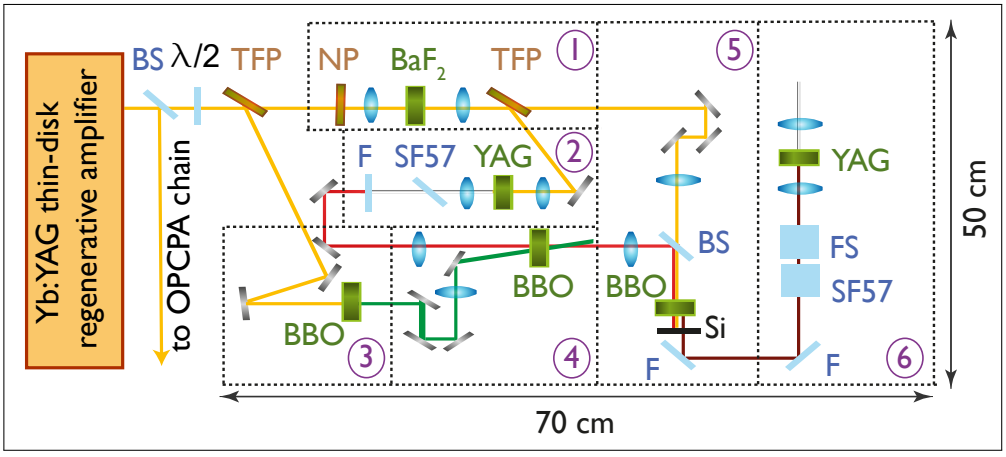

Fig. 1. Schematic layout of the setup. 1.6 mJ of the output of a 1-ps, Yb:YAG amplifier was used to generate a phase-stable multi-octave supercontinuum directly from the amplifier. At first a small portion of the 1 ps pulses was shortened to 650 fs in a cross-polarized wave generator (XPW) (block 1). Afterwards these pulses were focused into a YAG crystal to generate a supercontinuum (block 2). The rest of the energy containing 1.4 mJ was frequency doubled in a BBO crystal (block 3) and later used to amplify a small portion of the continuum in an optical parametric chirped pulse amplifier (OPCPA) stage (block 4). Later on the amplified pulses were mixed with residual energy of the XPW stage in a BBO crystal for difference frequency generation (block 5). The generated pulses were compressed to 32 fs using several fused silica plates and later on were focused into a YAG crystal for generation of a CEP-stable, multi-octave spectrum. The footprint of the setup is 70×50 cm^2. BS: beam splitter; TFP: thin film polarizer; NP: nanoparticle polarizer; F: filter; Si:silicon; FS: fused silica.

first time.

3. Experimental setup

Our experiment for the generation and characterization of the multi-octave continuum is schematically illustrated in Fig. 1. Pulses with an energy of 1.6 mJ are split off from the output of an Yb:YAG, thin-disk regenerative amplifier delivering 1-ps, 1030-nm pulses with an energy of 20 mJ at a repetition rate of 5 kHz (for more details see Ref. [31]). They drive seed generation for OPCPA chains being pumped with the remaining portion of the picosecond pulses [13].

For the stable, reproducible continuum generation, the 1-ps pulses need to be shortened, as discussed in Section 1. To this end, we compressed them to a duration of 650 fs (full width at half maximum, FWHM) in a cross-polarized wave generation (XPW) stage (block 1 in Fig. 1). XPW generates a pulse polarized perpendicularly to the input pulse, and if the process is not driven into saturation the generated pulse is shorter by a factor of 0.65 and does not carry additional chirp. In addition, the nonlinear intensity gating inherent in XPW cleans the generated pulses both temporally and spatially, resulting in improved contrast in both respects [45].

An AR-coated convex lens with a focal length of f= 75 mm was used to focus 140-μJ, 1-ps pulses into a 4-mm-thick, holographic-cut, BaF_2 crystal for XPW generation. The crystal was placed slightly behind the focus to balance the beam divergence and self-focusing, allowing a higher conversion efficiency to be achieved [45]. An additional nanoparticle-linear-film polarizer (Thorlabs) was placed before the convex lens to enhance the polarization contrast of the input beam to the XPW stage. An AR-coated convex lens (f=75 mm) was used to collimate the beam

Optics EXPRESS

and the 650-fs XPW pulses, containing 5 μJ of energy were separated from the fundamental beam using an AR-coated thin film polarizer (TFP).

The shortened pulses were then focused into a 4-mm-long YAG crystal using a convex lens (f=75 mm) and a stable filament with a spectrum spanning from 550 nm to 1400 nm was achieved (block 2 in Fig. 1).

A wavepacket with spectral components between 600-750 nm was separated from the rest of the continuum by using a custom-designed dichroic mirror and sent to an OPCPA stage (block 4 in Fig. 1) in order to boost its energy to 120 μJ in a 4-mm-thick BBO crystal (phase matching angle (θ)= 24.5^o, noncollinear angle (α)= 2.5^o) (Fig. 2(a)). The seed pulses were temporally stretched by using a 4 mm SF57 glass plate prior to the OPCPA stage in order to optimize the temporal overlap between the pump and seed pulses. The pump of the OPCPA stage was generated by frequency doubling of the Yb:YAG pulses with 1.4 mJ energy in a 1-mm-thick BBO crystal (type I, θ=32^o), resulting in 860 μJ pulses at 515 nm (block 3 in Fig. 1).

Saturated amplification in this stage provides not only the pulse energy required for subsequent spectral broadening stage but also suppresses the energy fluctuations accumulated in the preceding nonlinear stages to less than 2% (peak-to-peak).

The 120 μJ unconverted energy of the XPW stage was reused and mixed with the amplified pulses from the OPCPA in a difference frequency generation (DFG) stage, containing a 2-mm-thick BBO crystal (θ= 20^o) with type I phase matching in a collinear geometry (block 5 in Fig. 1). This geometry is necessary to avoid angular chirp of the generated difference frequency pulses. As shown in Fig. 2(b) the spectrum of the generated 4-μJ, intrinsically CEP-stable pulses, spans from 1700-2500 nm. The resultant red-shifted pulses are negatively chirped. Figure 2(c) shows the spectrum of the 720 nm-centered pulses prior and after the DFG. The difference between the input and transmitted pump spectra reflects the converted wavelength range.

The 1030 nm, high-energy pulses used for the DFG have a crucial role in achieving high conversion efficiency and broad spectral bandwidth simultaneously. For brevity, henceforth we refer to the 1030-nm and 720-nm pulses used at the DFG stage as a seed and a pump, respectively. Figure 2(d) shows the simulated difference frequency bandwidth for different seed to pump energy ratio. The SISYFOS code [46, 47] is used to perform the three-dimensional simulation. In all simulations a type-I BBO crystal is used, where the angle between the optical axis and the (collinear) pump and signal beams is 20 $^{\text{o}}$. The pump was taken to have a Gaussian beam and super-Gaussian spectrum of order 4, ranging from 650 to 800 nm and linearly chirped to 1 ps. The seed was taken to have Gaussian beam and pulse shape, centered at 1030 nm and 1 ps duration at full width at half maximum.

The d_{eff} of the BBO crystal is taken to be 2.1 pm/V and the sellmeier coefficient are taken from [48]. The coefficient for linear absorption were taken from [49]. The width of the pump beam is adjusted to provide 100 GW/cm^2 on-axis peak intensity on the crystal. The same width is used for the seed beam. The pump energy is fixed at 80 μJ, and the simulation is repeated for 0.006, 0.125, 0.625, 1, 1.25 seed to pump energy ratio. The pulse fronts of the pump and signal beams are both perpendicular to the the propagation direction of signal beam.

The crystal thickness for each seed-to-pump energy ratio is adjusted to maximize the DFG conversion efficiency. It was observed that higher seed energies result in higher conversion efficiency and a broader difference frequency spectrum. In this case the nonlinear system reaches saturation in a shorter nonlinear medium, which reduces the effect of group velocity mismatch between the interacting pulses. Conversely, low seed energies tend to narrow the spectrum of the difference frequency pulse while increasing the spectral bandwidth of the amplified seed pulses due to the broad bandwidth of the pump. As the pump pulses are not depleted in this case, their group velocity slippage with the seed pulses result in enhanced amplification of the spectral wings.

Optics EXPRESS

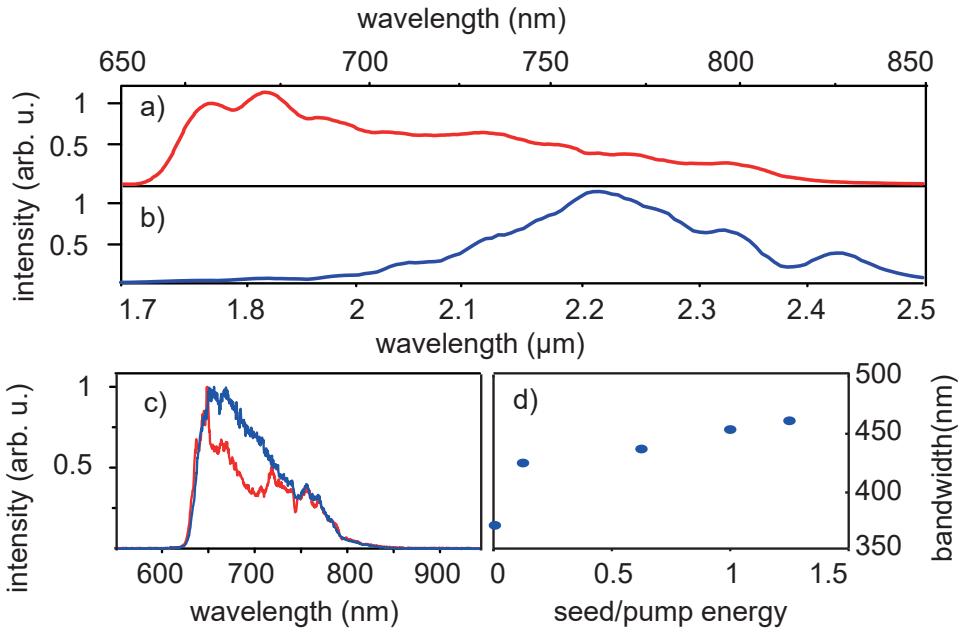

Fig. 2. a) Amplified spectrum in the OPCPA stage. b) The difference frequency generation between the OPCPA and the regenerative amplifier pulses in a 2-mm-thick BBO crystal results in a broadband spectrum centered at 2 μm. The generated pulses are intrinsically CEP-stable. c) The pump spectrum before (blue) and after (red) DFG. While the spectrum of the seed pulses stays unchanged, a hole appears in the pump's spectrum, as the signature of energy saturation. d) The simulated spectral bandwidth of the generated difference frequency pulses for different seed to pump energy ratio.

4. CEP-stable supercontinuum

The generated difference-frequency pulses were separated from the driving pulses by using a specially tailored broadband dielectric filter, and - in a preliminary study - partially compressed. The resultant 32-fs (FWHM) pulses compressed in a 20-mm-thick uncoated SF57 and a 10-mm-thick uncoated fused silica glass plates were characterized by using a frequency-resolved optical gating device (SH-FROG) containing a 200-μm-thick BBO crystal. Figure 3(a) shows the measured SH-FROG trace, its retrieved counterpart and the temporal profile of the compressed pulses. The evaluated spectral phase is well behaved and will permit the development of chirped multilayers tailored for the compression of the difference-frequency signal to its bandwidth limit.

The 32-fs pulses were then focused into a 6-mm-thick uncoated YAG crystal by using a coated CaF_2 lens (f=75 mm) for filamentation (block 6 in Fig. 1). Two grating spectrometers with silicon (USB2000+, Ocean Optics) and InGaAs detectors (NIRQuest256-2.5, Ocean Optics) were used to characterize the spectrum of the generated filament. The measured spectrum is shown in Fig. 3(b), its short-wavelength tail extends to 450 nm. The detection of wavelengths beyond 2500 nm was not possible with the available spectrometers. However our SH-FROG measurement of the generated continuum resolves spectral components up to 2800 nm.

Figure 3(b) (inset) shows the measured transverse spatial profiles of the SC after a specially designed beamsplitter for 670-1700 nm (inset-(i)) and 1700-2500 nm (inset-(ii)). The measurement for both spectral ranges is performed with a silicon charged-coupled device (CCD) camera (Dataray Wincam), making use of the two-photon absorption in silicon for detection of the spatial

Optics EXPRESS

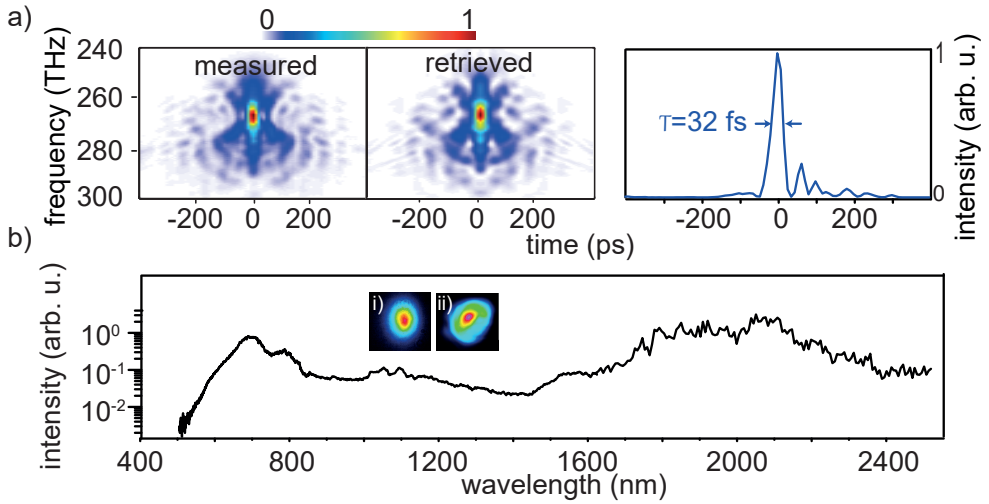

c)

	λmin:λmax	λ0 (nm)	energy	CEP-stable
Yb:YAG	1028:1032	1030	1.6 mJ	-
XPW	1025:1035	1030	5 µJ	-
first SC	550:1450	1030	0.045 µJ	-
OPCPA	630:850	720	120 µJ	-
DFG	1700:2600	2150	4 µJ	yes
second SC	450:2800	1170	4 µJ	yes

Fig. 3. a) Measured (left) and retrieved (middle) SH-FROG spectrograph and retrieved temporal intensity (right) of the difference frequency pulses. $G_{error} = 7.8 \times 10^{-3}$. The pulse is compressed to 32 fs using bulk material. b) Spectrum of the multi-octave continuum containing 4 μJ generated in a 6 mm YAG crystal. Inset: transverse intensity profile of the supercontinuum after a beamsplitter for 670-1700 nm (i) and 1700-2500 nm (ii). c) Spectral bandwidth, obtained energy, and CEP-stability at each stage of the setup. λ_0 shows the central wavelength of the generated pulses. XPW: cross-polarized wave generation; SC: supercontinuum; OPCPA: optical parametric chirped pulse amplification; DFG: difference frequency generation.

profile shown in inset (ii) of Fig. 3(b).

The SC inherits the intrinsic CEP stability of the DFG stage. To verify the pulse-to-pulse reproducibility and CEP stability of the generated multi-octave spectrum, we performed an f-2f interferometry measurement. Figure 4(a) shows the layout of the f-2f setup. A specially-designed beam splitter is used to split the SC spectrum at 1700 nm. The reflected spectral components centered at 2 μm, were frequency doubled in a 2 mm $LiNbO_3$ crystal and later interferometrically combined with the transmitted spectral components centered at 1 μm. Figure 4(b) shows the measured spectrogram of the CEP fluctuations of the SC over 10 minutes. The CEP reconstructed from this measurement, see Fig. 4(c), yields a drift of 144 mrad (detector integration time: 4 ms). The fluctuation of the CEP phase over 6000 ms and for 30 ms detector integration time yields 90 mrad jitter (Fig. 4(d)).

The spectrum of the continuum was measured for 120 s in order to study the spectral reproducibility of the continuum, particularly at the low frequency edge. The Fourier transform limit of the measured spectra shows less than 0.7 % (rms) deviation over 120 s measurement time (detector integration time: 1 ms) and excellent reproducibility.

Optics EXPRESS

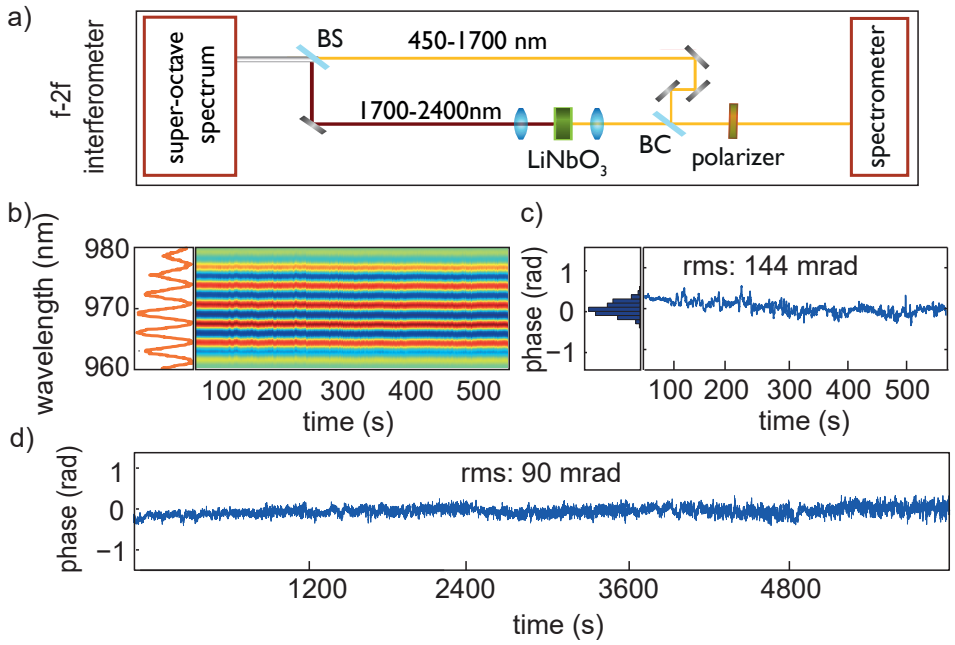

Fig. 4. a) Layout of the f-2f interferometer for monitoring the intensity and phase stability of the supercontinuum. The fundamental and its orthogonally polarized second harmonic, produced in a $LiNbO_3$ crystal are interferometrically overlapped by projecting them onto the same polarization state using a beamsplitter cube. b) The resolved fringes in the f-2f interferometer (left) and variation of the f-2f interference pattern over 600 s (right). c) Histogram (left) and reconstructed CEP fluctuations obtained from the f-2f measurement. The retrieved fluctuations yield a 144 mrad CEP jitter over 600 s measurement time (detector's integration time: 4 ms). d) reconstructed CEP fluctuations over 6000 s yielding 90 mrad jitter (detector's integration time: 30 ms). BC: beam combiner; BS: beam splitter.

5. Conclusion

We demonstrated the direct generation of CEP-stable pulses from a 1-ps, Yb:YAG thin-disk amplifier. The generated supercontinuum spans from 450 nm to beyond 2500 nm and contains 4 μJ energy. The concept demonstrated in this work is scalable to higher average and peak power, by using a gas-filled hollow waveguide for the final broadening to avoid optical breakdown and/or thermal effects [50]. The generated supercontinuum can be divided into several sub-spectral regions by using a broadband dielectric beamsplitter [51], and compressed to few-cycle pulses subsequently.

The presented compact source with a 50×70 cm^2 footprint will serve as an ideal front end for OPCPAs or field-synthesizers, simplifying the current state of the art which requires a broadband seed oscillator and complex temporal synchronization between pump and seed sources [9, 32, 33].

In broadband OPCPAs, higher seed energy reduces the amplification of superflourescence and helps the simultaneous saturation of individual frequencies of the seed pulses at the same length of the nonlinear medium [39]. On the other hand, the total optical efficiency of OPCPA is higher than the efficiency of the super-octave generator, containing cascaded nonlinear processes. As the demonstrated scheme is scalable in energy, the final output energy of the supercontinuum can be designed by taking into account the required seed energy for OPCPAs and the total efficiency of the system.

Optics EXPRESS

In addition to the mentioned applications, the generated microjoul-energy, CEP-stable multi-octave pulses are also directly applicable to femtosecond time-resolved spectroscopy. A preliminary study has revealed that the generated spectrum can be extended to a wavelength of 5 μm, by using the red wing of the first supercontinuum in a similar set up.

Advances in the Ytterbium laser technology over the last decade combined with OPCPAs present a new perspective for reaching higher peak- and average-powers. Coherent combination of several OPCPA channels hold promise for synthesizing, multi-octave waveforms and generating sub-cycle pulses [13, 52, 53] with unprecedented peak and average power. The seed generation scheme presented in this paper provides an essential step towards this goal.

Funding

This work has been supported by the Centre For Advanced Laser Applications (CALA).

Acknowledgments

We wish to thank Dr. Shawn Sederberg and Dr. Wolfgang Schweinberger for helpful discussion.

A.4 Carrier-envelope phase stable, 5.4 μJ, broadband, mid-infrared pulse generation from a 1-ps, Yb:YAG thin-disk laser

applied optics

Carrier-envelope phase stable, 5.4 μJ, broadband, mid-infrared pulse generation from a 1-ps, Yb:YAG thin-disk laser

Ayman Alismail,[1,2] Haochuan Wang,[1,3] Najd Altwaijry,[1,2] and Hanieh Fattahi[1,3,*]

[1]Department für Physik, Ludwig-Maximilians-Universität München, Am Coulombwall 1, D-85748 Garching, Germany
[2]Physics and Astronomy Department, King Saud University, Riyadh 11451, Saudi Arabia
[3]Max-Planck Institut für Quantenoptik, Hans-Kopfermann-Str. 1, D-85748 Garching, Germany
*Corresponding author: hanieh.fattahi@mpq.mpg.de

Received 14 April 2017; revised 18 May 2017; accepted 19 May 2017; posted 19 May 2017 (Doc. ID 292848); published 9 June 2017

We report on a simple scheme to generate broadband, μJ pulses centered at 2.1 μm with an intrinsic carrier-envelope phase (CEP) stability from the output of a Yb:YAG regenerative amplifier delivering 1-ps pulses with randomly varying CEP. To the best of our knowledge, the reported system has the highest optical-to-optical efficiency for converting 1-ps, 1 μm pulses to CEP stable, broadband, 2.1 μm pulses. The generated coherent light carries an energy of 5.4 μJ, at 5 kHz repetition rate, that can be scaled to higher energy or power by using a suitable front end, if required. The system is ideally suited for seeding broadband parametric amplifiers and multichannel synthesizers pumped by picosecond Yb-doped amplifiers, obviating the need for active timing synchronization. Alternatively, this scheme can be combined with high-power oscillators with tens of μJ energy to generate CEP stable, multioctave supercontinua, suitable for field-resolved and time-resolved spectroscopy.

OCIS codes: (140.3615) Lasers, ytterbium; (190.4223) Nonlinear wave mixing; (320.7110) Ultrafast nonlinear optics; (190.4380) Nonlinear optics, four-wave mixing; (140.7090) Ultrafast lasers.

https://doi.org/10.1364/AO.56.004990

1. INTRODUCTION

In femtosecond spectroscopy, the effect of a pump pulse on the envelope of a delayed probe pulse is measured, leaving effects occurring in response to the oscillating electric field unresolved [1]. On longer time scales, the polarization of a medium, in both amplitude and phase, could be retrieved from a measurement of the oscillating electric field of picosecond terahertz pulses that propagate through the medium. Access to this full polarization response, however, does rely on a gate pulse much shorter than the field cycle. This requirement had prevented the extension of the technique into the optical regime, due to the absence of sampling pulses shorter than the oscillation period of visible (VIS) or near-infrared light.

In the last decade, Ti:Sa laser technology enabled generation of coherent extreme-ultraviolet (XUV) pulses with attosecond duration and changed this scenario. Scanning the synchronized XUV pulses relative to their VIS driver pulses allowed the measurement of the light's electric field at petahertz frequencies [2]. Following recent advancement of Yb:YAG-pumped optical parametric amplifiers, field-resolved detection at kilohertz repetition rates has been extended to mid-infrared (MIR) by employing electro-optic sampling, wherein VIS, few-cycle pulses were used as a probe [3]. Field detection based on electro-optic sampling can provide a better understanding of extremely fast dynamics in solid-state materials [4] and benefits from few-cycle pulses in MIR and VIS spectral range, with carrier-envelope-phase (CEP) stability and at high repetition rates.

These applications call for compact sources, delivering CEP stable, coherent, superoctave continua spanning from VIS to MIR spectral range, beyond nanojoule energy, and at kilohertz to megahertz repetition rates. Today, Yb:YAG lasers are mature, turnkey, and cost-effective technology, and offer such a possibility [5–12].

Specifically, a CEP stable, multioctave supercontinuum generated directly from Yb:YAG, sub-ps oscillators or ps amplifiers has two prominent applications: (I) it can be used to seed broadband optical parametric amplifiers (OPAs) or subcycle field synthesizers pumped by high-energy, kHz, Yb:YAG amplifiers [5,13,14], obviating the need for complex temporal synchronization systems between two independent lasers [15,16]; or, it can be used for (II) field- and time-resolved spectroscopy when it is driven from high average-power, MHz oscillators.

MIR superoctave continua have been generated from randomly phased Yb:YAG lasers, by combining supercontinuum

generation in bulk and difference frequency generation [17,18], or by using high-energy, CEP stable MIR pulses from an OPA [19–21] and spectrally broaden them in bulk, gas, or a gas-filled hollow-core fiber [22–24]. Such supercontinua are generated in systems with very low conversion efficiency, containing several nonlinear stages and mostly with a need for an additional complex temporal synchronization stage.

In this paper, we demonstrate an efficient scheme to generate broadband, CEP stable, MIR pulses directly from a ps-long Yb:YAG, thin-disk laser at 5 kHz repetition rate. To the best of our knowledge, this system has the highest reported optical-to-optical efficiency for converting ps-long pulses at 1030 nm with randomly varying phase, to broadband, CEP stable pulses at 2.1 μm. This critical property makes this setup compatible to the output parameters of high-power, low-energy, Yb:YAG oscillators [25,26] keeping the promise to generate a CEP stable, VIS-MIR supercontinuum at MHz repetition rates to extend the filed-resolved spectroscopy [4] to a MIR spectral range.

2. EXPERIMENTAL SETUP

The experimental setup is illustrated in Fig. 1. A Yb:YAG thin-disk regenerative amplifier delivering 20 mJ, 1-ps pulses at 5 kHz repetition rate [27] is used as the front end of the system. 400 μJ of the total energy of the amplifier is separated by using an attenuator consisting of a thin-film polarizer (TFP) and a $\lambda/2$-plate, and are then frequency doubled in a 1.5-mm-thick, type-I, beta barium borate (BBO) crystal at the phase matching angle of 23°.

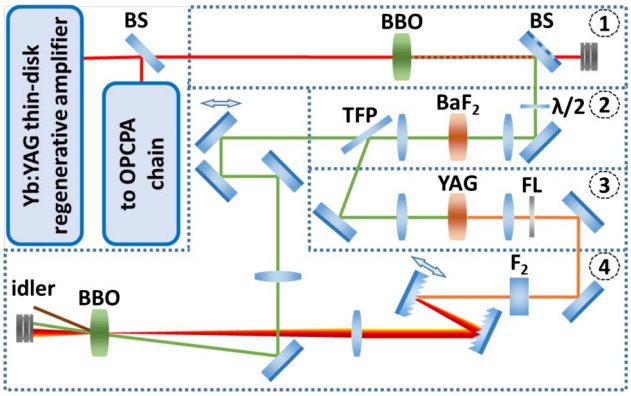

Fig. 1. Schematic of the setup to convert 400 μJ of a 1-ps, 20 mJ Yb:YAG, thin-disk amplifier to carrier-envelope phase stable, broadband, 5.4 μJ pulses centered at 2.1 μm. At first, the 1-ps pulses are frequency doubled in a 1.5-mm-thick BBO crystal (block 1). Then the 260 μJ second harmonic beam is focused into a 4-mm-thick BaF_2 crystal for cross-polarized wave generation (XPW) (block 2). The 466-fs-long XPW pulses are separated from the residual energy by means of a thin-film polarizer (block 2) and focused into a 10-mm-thick plate of YAG for supercontinuum generation (block 3). The Stokes wing of the supercontinuum, centered at 680 nm, is filtered by using a 600 nm longpass filter to serve as a seed for a noncollinear optical parametric amplifier (NOPA). The seed pulses are sent through a grating pair and a 115-mm-thick F_2 to adjust their angular chirp and temporal duration. Finally the seed and pump pulses are sent to a NOPA containing a 6-mm-thick BBO crystal (block 4) to generate broadband idler pulses at 2.1 μm. BS, beam splitter; TFP, thin-film polarizer; FL, filter.

The beam size on the crystal is adjusted to reach a peak intensity of 80 GW/cm^2, and an energy of 260 μJ at 515 nm, corresponding to 65% optical-to-optical conversion efficiency, is achieved. The frequency doubling of the input pulses is necessary to ensure intrinsic CEP stability of the generated MIR pulses in the last nonlinear stage of the setup, which contains a noncollinear optical parametric amplifier (NOPA) [28].

The second harmonic (SH) pulses are temporally shortened compared to the fundamental laser pulses at 1030 nm, due to pulse shortening based on the χ^2 effect (see Ref. [27] for details). Afterward, the SH beam is focused into a 4-mm-thick BaF_2 crystal for cross-polarized wave generation (XPW) and additional pulse shortening. The 466-fs-long XPW pulses are separated from the residual SH pulses by a thin-film polarizer and focused in a bulk for supercontinuum generation in VIS frequencies [29]. This step is necessary to achieve a stable and reproducible supercontinuum [17,30]. Finally, the Stokes wing of the generated supercontinuum and the residual SH pulses are focused into a NOPA stage to generate broadband, CEP stable pulses in the MIR.

In our previous report for generating CEP stable MIR pulses [17], the supercontinuum signal was sent through two optical parametric amplifier stages: first, to amplify and stabilize the signal energy via a NOPA, and, second, to CEP stabilize and shift the idler's central frequency to the MIR in a collinear OPA. In the current MIR pulse generation setup, the nonlinear processes are reduced by combining these two parametric amplification stages into a single, saturated NOPA stage. However, in a NOPA due to the required noncollinear geometry for a broadband and efficient amplification, the generated idler inherits an angular dispersion, which must be compensated for. We chose to compensate for this angular chirp by prechirping the input seed pulses to the NOPA by means of a grating pair, motivated by the higher efficiency of grating pairs in VIS frequencies.

In what follows, detailed discussion of each block of the setup is presented.

A. XPW and Supercontinuum Driven by High-Energy Photons

It has been challenging to generate a supercontinuum using high-energy photons [31,32]. As the energy of the driving photons approaches the bandgap of transparent materials the probability of damage due to nonlinear absorption increases. In addition, the damage threshold intensity for transparent materials increases in proportion to the inverse of the square root of the pulse duration for pulsed lasers, following the dynamics of impact ionization.

Therefore, we used the XPW process to temporally shorten the driving pulses prior to the supercontinuum generation stage due to its simplicity and self-compression, which obviates the need for any additional pulse compressor. It is known that the conversion efficiency of an XPW process is proportional to the input frequency of the driving pulses, due to the increase in nonlinearity of materials when interacting with higher-energy photons [33]. However, for driving pulses with higher photon energies saturation occurs earlier, due to the dephasing between the driving pulses and the XPWs, limiting the conversion efficiency.

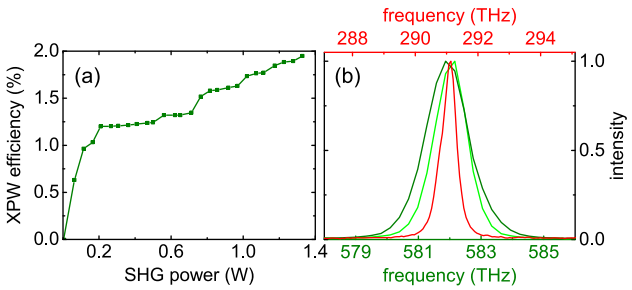

Fig. 2. (a) Optical-to-optical efficiency of the generated cross-polarized wave versus the power of the driving pulses (second harmonic pulses). (b) Normalized spectra of the fundamental (red curve), second harmonic (light green curve), and the generated cross-polarized (dark green curve) pulses with the spectral bandwidth of 0.62 THz, 1.26 THz, and 1.64 THz (FWHM), respectively.

260 μJ pulses at 515 nm are used to generate XPW in a 4-mm-thick BaF_2 crystal with a holographic cut. An $f = 150$ mm convex lens is used to focus the beam, while the crystal is placed after the focus. The beam size at the crystal is 260 μm at FWHM. Figure 2 shows the optical-to-optical conversion efficiency and the spectrum of the converted SH pulses to XPW pulses. Maximum efficiency of 2%, corresponding to 5 μJ, is achieved. Higher peak intensity on the crystal leads to its optical damage. The generated XPW pulses and the residual SH pulses are both collimated by using an $f = 150$ mm convex lens. A TFP is used to separate them afterward, as the XPW and SH beams have a crossed polarization. XPW pulses were characterized by using a cross-correlation frequency-resolved optical gating (XFROG) employing a 100-μm-thick BBO crystal. The Fourier transform limited pulses of the Yb:YAG amplifier were used as a reference pulse for the XFROG measurement. Figure 3 shows the measured and retrieved XFROG spectrograms, and the retrieved temporal profile of the XPW pulses with a 466 fs temporal duration (FWHM).

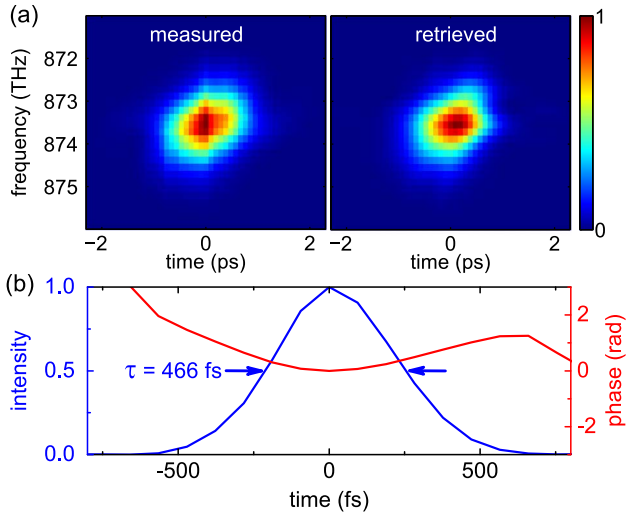

Fig. 3. Temporal profile of the generated XPW pulses at 515 nm. (a) Measured and retrieved XFROG spectrograms. (b) Retrieved temporal profile of the XPW pulses with 466 fs pulse duration at FWHM ($G_{error} = 0.01544$).

Table 1. Performance of Different Materials for Supercontinuum Generation Driven by 466 fs, 515 nm Pulses

Crystal	Thickness (mm)	Critical Power (MW)	Band Gap (eV)	Filament
YAG	2	0.22	6.3	Yes
Sapphire	2	0.68	9.9	No
TGG	4	0.12	—	No
ZnS	5	0.32	3.911	No

Thereafter, XPW pulses are focused by an $f = 125$ mm convex lens into a nonlinear medium for supercontinuum generation. We tried several nonlinear media and could achieve a stable filament only in a 2-mm-thick plate of YAG due to its lower critical power. This study is summarized in Table 1. In the final setup we chose a 10-mm-thick plate of YAG due to the better daily reproducibility.

Figure 4 shows the spectrum and the transverse beam profile of the generated supercontinuum in 10-mm-thick YAG. The anti-Stokes and Stokes wings of the supercontinuum are measured behind a 500 nm shortpass filter (FES0500, Thorlabs GmbH) and a 550 nm longpass filter (FEL0550, Thorlabs GmbH), respectively. Both wings are normalized to one separately. With a tighter focusing, a stable filament could be generated by using only 0.7 μJ energy and an $f = 40$ mm convex lens. However, we opt for generating a stable, single filament with the maximum pulse energy, by a careful balance between the beam size and the energy of the driving pulses. The Stokes wing of the supercontinuum is filtered out by a 600 nm longpass filter (FEL0600, Thorlabs GmbH) and is collimated by an $f = 125$ mm convex lens and used to seed the NOPA stage.

B. Idler Generation

To generate broadband MIR pulses, the unconverted portion of SH pulses after the XPW process are mixed with the Stokes wing of the supercontinuum in a NOPA. As described earlier, the generated idler in the noncollinear geometry has an angular chirp that can be compensated by matching the seed pulse-front to the idler pulse-front or to the propagation direction

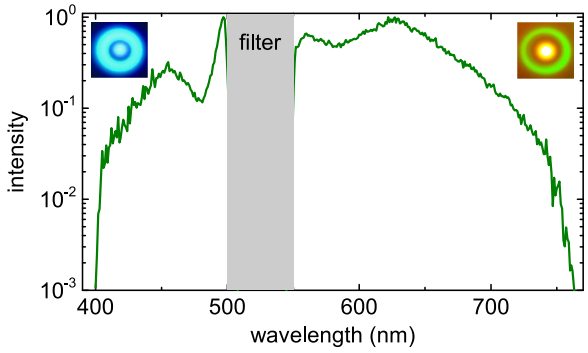

Fig. 4. Normalized spectrum and transverse beam profiles (inset) of the generated supercontinuum in 10-mm-thick YAG. The spectrum and the beam profile of the anti-Stokes and Stokes wings are measured behind a 500 nm shortpass filter and a 550 nm longpass filter, respectively.

of the idler. For ps-long pump pulses the effect of the pulse-front is negligible and can be ignored. We chose to precompensate for this angular chirp by angularly dispersing the seed pulses of the NOPA, using an aluminum-coated reflective grating pair with 300 groves/mm (GR50-0310, Thorlabs GmbH) [34,35]. We avoided using a Brewster prism pair due to its undesired higher-order dispersion.

The separation between the gratings determines the applied angular dispersion to the seed. Therefore, one of the gratings is mounted on a translation stage for adjusting the distance. Afterward the angularly chirped seed pulses are amplified in a 6-mm-thick, type-I, BBO crystal with an internal noncollinear angle of 2.4° and the phase matching angle of 23.4°. The pump and seed beams are focused down to 650 μm (FWHM) and overlapped spatially and temporally in the BBO crystal.

When the distance of the grating pair is set to 175 mm, 220 μrad/nm angular chirp is introduced to the seed pulses and an angular-chirp-free idler is generated. However, in addition to the angular chirp, the grating pair also temporally chirps the seed pulses. As a result, the seed pulses become longer than the pump pulses in the NOPA and the amplified spectral bandwidth decreases. The group delay dispersion (GDD), induced by the grating pair on the seed pulses, is calculated from Eq. (1):

$$\mathrm{GDD} = -\frac{\lambda^3 b}{2\pi c^2 d^2 \cos^3(\beta)}, \tag{1}$$

where λ, c, d, b, and β are the central wavelength of the pulse, velocity of light, grating's line density, grating separation, and diffraction angle of the grating, respectively.

Therefore, a 115-mm-thick plate of F_2 is placed in the seed beam path to compensate for the calculated, negative chirp on the seed pulses and to adjust the temporal duration of the seed pulses within the temporal window of pump pulses at the NOPA stage. The generated chirp-free idler pulses have similar temporal duration to the seed pulses, as their generation occurs only in the region that pump and seed pulses are temporally overlapped. The amplified spectrum, the idler spectrum, and the transverse spatial profile of the 5.4 μJ generated broadband chirp-free idler in the far-field are shown in Fig. 5.

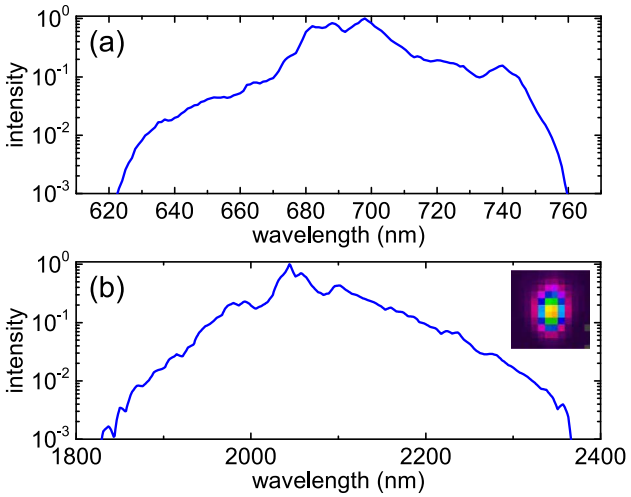

Fig. 5. (a) Normalized spectrum of the amplified seed pulses in the NOPA containing a 6-mm-thick BBO crystal. (b) Normalized spectrum of the generated chirp-free idler supporting 37 fs (FWHM) Fourier transform limited pulses. Inset: the transverse spatial profile of the generated idler at the focus.

3. CONCLUSION AND OUTLOOK

We demonstrated a compact and efficient scheme to generate broadband, CEP stable pulses at 2.1 μm, driven from a 1-ps, Yb:YAG thin-disk amplifier. The broadband MIR pulses span from 1.83 μm to 2.36 μm and contain 5.4 μJ energy. It is expected that the delivered pulses from the current system show a similar long-term, CEP stability like the previously reported work [17].

Careful design of the system led to 1.35% optical-to-optical efficiency, which is defined as the ratio of the total output pulse energy of the system to the total input pulse energy to the system. To the best of our knowledge, this is the highest reported efficiency for similar systems [17,18,34,35].

The μJ, MIR pulses can be used for CEP stable, supercontinuum generation in bulk [17,18,36], or hollow-core photonic crystal fibers [37], and can serve as an ideal front end for broadband OPAs or field synthesizers, simplifying the state of the art and obviating the need for complex temporal synchronization between pump and seed sources [15,16].

As discussed in Section 2.A, the energy threshold for generating a supercontinuum driven by 466-fs-long, 515 nm pulses is 0.7 μJ. Therefore, the required input energy to the system can be scaled down to tens of μJ. Considering this margin, it can be simply calculated that the required input peak power to achieve a CEP stable supercontinuum at the output of the setup is compatible to the peak power delivered by high average-power oscillators such as [25].

The opportunity of generating a superoctave, CEP stable continuum directly from high average-power, low peak-power sources paves the way for a new generation of lasers, suitable for femtosecond field- and time-resolved spectroscopy in the MIR spectral range.

Funding. Centre for Advanced Laser Applications (CALA).

Acknowledgment. We thank Ferenc Krausz and Maximilian Wendl for their support.

REFERENCES

1. A. H. Zewail, "Femtochemistry: atomic-scale dynamics of the chemical bond," J. Phys. Chem. A **104**, 5660–5694 (2000).
2. M. Hentschel, R. Kienberger, C. Spielmann, G. A. Reider, N. Milosevic, T. Brabec, P. Corkum, U. Heinzmann, M. Drescher, and F. Krausz, "Attosecond metrology," Nature **414**, 509–513 (2001).
3. S. Keiber, S. Sederberg, A. Schwarz, M. Trubetskov, V. Pervak, F. Krausz, and N. Karpowicz, "Electro-optic sampling of near-infrared waveforms," Nat. Photonics **10**, 159–162 (2016).
4. A. Sommer, E. M. Bothschafter, S. A. Sato, C. Jakubeit, T. Latka, O. Razskazovskaya, H. Fattahi, M. Jobst, W. Schweinberger, V. Shirvanyan, V. S. Yakovlev, R. Kienberger, K. Yabana, N. Karpowicz, M. Schultze, and F. Krausz, "Attosecond nonlinear polarization and light-matter energy transfer in solids," Nature **534**, 86–90 (2016).
5. H. Fattahi, H. G. Barros, M. Gorjan, T. Nubbemeyer, B. Alsaif, C. Y. Teisset, M. Schultze, S. Prinz, M. Haefner, M. Ueffing, A. Alismail, L. Vámos, A. Schwarz, O. Pronin, J. Brons, X. T. Geng, G. Arisholm, M. Ciappina, V. S. Yakovlev, D.-E. Kim, A. M. Azzeer, N. Karpowicz, D. Sutter, Z. Major, T. Metzger, and F. Krausz, "Third-generation femtosecond technology," Optica **1**, 45–63 (2014).

6. O. H. Heckl, J. Kleinbauer, D. Bauer, S. Weiler, T. Metzger, and D. H. Sutter, "Ultrafast thin-disk lasers," in *Ultrashort Pulse Laser Technology* (2016), pp. 93–115.
7. L. E. Zapata, H. Lin, A.-L. Calendron, H. Cankaya, M. Hemmer, F. Reichert, W. R. Huang, E. Granados, K.-H. Hong, and F. X. Kärtner, "Cryogenic Yb:YAG composite-thin-disk for high energy and average power amplifiers," Opt. Lett. **40**, 2610–2613 (2015).
8. M. Schulz, R. Riedel, A. Willner, T. Mans, C. Schnitzler, P. Russbueldt, J. Dolkemeyer, E. Seise, T. Gottschall, S. Hädrich, S. Duesterer, H. Schlarb, J. Feldhaus, J. Limpert, B. Faatz, A. Tünnermann, J. Rossbach, M. Drescher, and F. Tavella, "Yb:YAG Innoslab amplifier: efficient high repetition rate subpicosecond pumping system for optical parametric chirped pulse amplification," Opt. Lett. **36**, 2456–2458 (2011).
9. F. Röser, T. Eidam, J. Rothhardt, O. Schmidt, D. N. Schimpf, J. Limpert, and A. Tünnermann, "Millijoule pulse energy high repetition rate femtosecond fiber chirped-pulse amplification system," Opt. Lett. **32**, 3495–3497 (2007).
10. P. Russbueldt, T. Mans, G. Rotarius, J. Weitenberg, H. D. Hoffmann, and R. Poprawe, "400 W Yb:YAG innoslab fs-amplifier," Opt. Express **17**, 12230–12245 (2009).
11. C. Baumgarten, M. Pedicone, H. Bravo, H. Wang, L. Yin, C. S. Menoni, J. J. Rocca, and B. A. Reagan, "1 J, 05 kHz repetition rate picosecond laser," Opt. Lett. **41**, 3339–3342 (2016).
12. J. Novák, J. T. Green, T. Metzger, T. Mazanec, B. Himmel, M. Horáček, Z. Hubka, R. Boge, R. Antipenkov, F. Batysta, J. A. Naylon, P. Bakule, and B. Rus, "Thin disk amplifier-based 40 mJ, 1 kHz, picosecond laser at 515 nm," Opt. Express **24**, 5728–5733 (2016).
13. O. D. Mucke, S. Fang, G. Cirmi, G. M. Rossi, S.-H. Chia, H. Ye, Y. Yang, R. Mainz, C. Manzoni, P. Farinello, G. Cerullo, and F. X. Kartner, "Toward waveform nonlinear optics using multimillijoule sub-cycle waveform synthesizers," IEEE J. Sel. Top. Quantum Electron. **21**, 1–12 (2015).
14. Y. Yin, A. Chew, X. Ren, J. Li, Y. Wang, Y. Wu, and Z. Chang, "Towards terawatt sub-cycle long-wave infrared pulses via chirped optical parametric amplification and indirect pulse shaping," Sci. Rep. **7**, 45794 (2017).
15. H. Fattahi, C. Teisset, O. Pronin, A. Sugita, R. Graf, V. Pervak, X. Gu, T. Metzger, Z. Major, F. Krausz, and A. Apolonski, "Pump-seed synchronization for MHz repetition rate, high-power optical parametric chirped pulse amplification," Opt. Express **20**, 9833–9840 (2012).
16. A. Schwarz, M. Ueffing, Y. Deng, X. Gu, H. Fattahi, T. Metzger, M. Ossiander, F. Krausz, and R. Kienberger, "Active stabilization for optically synchronized optical parametric chirped pulse amplification," Opt. Express **20**, 5557–5565 (2012).
17. H. Fattahi, H. Wang, A. Alismail, G. Arisholm, V. Pervak, A. M. Azzeer, and F. Krausz, "Near-PHz-bandwidth, phase-stable continua generated from a Yb:YAG thin-disk amplifier," Opt. Express **24**, 24337–24346 (2016).
18. H. Çankaya, A.-L. Calendron, C. Zhou, S.-H. Chia, O. D. Mücke, G. Cirmi, and F. X. Kärtner, "40-μJ passively CEP-stable seed source for ytterbium-based high-energy optical waveform synthesizers," Opt. Express **24**, 25169–25180 (2016).
19. Y. Deng, A. Schwarz, H. Fattahi, M. Ueffing, X. Gu, M. Ossiander, T. Metzger, V. Pervak, H. Ishizuki, T. Taira, T. Kobayashi, G. Marcus, F. Krausz, R. Kienberger, and N. Karpowicz, "Carrier-envelope-phase-stable, 1.2 mJ, 1.5 cycle laser pulses at 2.1 μm," Opt. Lett. **37**, 4973–4975 (2012).
20. Y. Yin, J. Li, X. Ren, K. Zhao, Y. Wu, E. Cunningham, and Z. Chang, "High-efficiency optical parametric chirped-pulse amplifier in BiB_3O_6 for generation of 3 mJ, two-cycle, carrier-envelope-phase-stable pulses at 17 μm," Opt. Lett. **41**, 1142–1145 (2016).
21. C.-J. Lai, K.-H. Hong, J. P. Siqueira, P. Krogen, C.-L. Chang, G. J. Stein, H. Liang, P. D. Keathley, G. Laurent, J. Moses, L. E. Zapata, and F. X. Kärtner, "Multi-mJ mid-infrared kHz OPCPA and Yb-doped pump lasers for tabletop coherent soft x-ray generation," J. Opt. **17**, 094009 (2015).
22. F. Silva, D. R. Austin, A. Thai, M. Baudisch, M. Hemmer, D. Faccio, A. Couairon, and J. Biegert, "Multi-octave supercontinuum generation from mid-infrared filamentation in a bulk crystal," Nat. Commun. **3**, 807 (2012).
23. E. A. Stepanov, A. A. Lanin, A. A. Voronin, A. B. Fedotov, and A. M. Zheltikov, "Solid-state source of subcycle pulses in the midinfrared," Phys. Rev. Lett. **117**, 043901 (2016).
24. D. Kartashov, S. Ališauskas, A. Pugžlys, A. Voronin, A. Zheltikov, M. Petrarca, P. Béjot, J. Kasparian, J.-P. Wolf, and A. Baltuška, "White light generation over three octaves by femtosecond filament at 3.9 μm in argon," Opt. Lett. **37**, 3456–3458 (2012).
25. C. J. Saraceno, F. Emaury, C. Schriber, M. Hoffmann, M. Golling, T. Südmeyer, and U. Keller, "Ultrafast thin-disk laser with 80 μJ pulse energy and 242 W of average power," Opt. Lett. **39**, 9–12 (2014).
26. J. Brons, V. Pervak, D. Bauer, D. Sutter, O. Pronin, and F. Krausz, "Powerful 100-fs-scale Kerr-lens mode-locked thin-disk oscillator," Opt. Lett. **41**, 3567–3570 (2016).
27. H. Fattahi, A. Alismail, H. Wang, J. Brons, O. Pronin, T. Buberl, L. Vámos, G. Arisholm, A. M. Azzeer, and F. Krausz, "High-power, 1-ps, all-Yb:YAG thin-disk regenerative amplifier," Opt. Lett. **41**, 1126–1129 (2016).
28. G. Cerullo, A. Baltuška, O. Mücke, and C. Vozzi, "Few-optical-cycle light pulses with passive carrier-envelope phase stabilization," Laser Photon. Rev. **5**, 323–351 (2011).
29. A.-L. Calendron, H. Çankaya, G. Cirmi, and F. X. Kärtner, "White-light generation with sub-ps pulses," Opt. Express **23**, 13866–13879 (2015).
30. T. Buberl, A. Alismail, H. Wang, N. Karpowicz, and H. Fattahi, "Self-compressed, spectral broadening of a Yb:YAG thin-disk amplifier," Opt. Express **24**, 10286–10294 (2016).
31. M. Bradler, P. Baum, and E. Riedle, "Femtosecond continuum generation in bulk laser host materials with sub-μJ pump pulses," Appl. Phys. B **97**, 561–574 (2009).
32. P. Tzankov, I. Buchvarov, and T. Fiebig, "Broadband optical parametric amplification in the near UV-VIS," Opt. Commun. **203**, 107–113 (2002).
33. L. Canova, S. Kourtev, N. Minkovski, R. Lopez-Martens, O. Albert, and S. M. Saltiel, "Cross-polarized wave generation in the UV region," Opt. Lett. **33**, 2299–2301 (2008).
34. T.-J. Wang, Z. Major, I. Ahmad, S. A. Trushin, F. Krausz, and S. Karsch, "Ultra-broadband near-infrared pulse generation by noncollinear OPA with angular dispersion compensation," Appl. Phys. B **100**, 207–214 (2010).
35. S.-W. Huang, J. Moses, and F. X. Kärtner, "Broadband noncollinear optical parametric amplification without angularly dispersed idler," Opt. Lett. **37**, 2796–2798 (2012).
36. H. Liang, P. Krogen, R. Grynko, O. Novak, C.-L. Chang, G. J. Stein, D. Weerawarne, B. Shim, F. X. Kärtner, and K.-H. Hong, "Three-octave-spanning supercontinuum generation and sub-two-cycle self-compression of mid-infrared filaments in dielectrics," Opt. Lett. **40**, 1069–1072 (2015).
37. M. Cassataro, D. Novoa, M. C. Günendi, N. N. Edavalath, M. H. Frosz, J. C. Travers, and P. St.J. Russell, "Generation of broadband mid-IR and UV light in gas-filled single-ring hollow-core PCF," Opt. Express **25**, 7637–7644 (2017).

A.5 Near-infrared molecular fieldoscopy of water

This paper was published in SPIE and is made available as an electronic reprint with the permission of SPIE. The paper can be found at the following URL on the SPIE website: https://doi.org/10.1117/12.2507604.

Near-Infrared Molecular Fieldoscopy of Water

Ayman Alismail[a,b], Haochuan Wang[a,c], Gaia Barbiero[a,c], Syed Ali Hussain[a,c], Wolfgang Schweinberger[a,c], Ferenc Krausz[a,c], and Hanieh Fattahi[c]

[a]fakultät für Physik, Ludwig-Maximilians-Universität München, Am Coulombwall 1, D-85748 Garching, Germany
[b]Physics and Astronomy Department, King Saud University, Riyadh 11451, Saudi Arabia
[c]Max-Planck Institut für Quantenoptik, Hans-Kopfermann-Str. 1, D-85748 Garching, Germany

ABSTRACT

We introduce the concept of broadband near-infrared molecular fieldoscopy. In this scheme, molecules are excited by femtosecond pulses in near-infrared spectral range and the complex electric field of their free induction decay is directly measured by means of electro-optic sampling. Few-cycle pulses centered at 2 μm and 1 μm are generated from a 5 kHz, Yb:YAG regenerative amplifier and employed for femtosecond excitation and electro-optic sampling, respectively. We chose water in an acetic acid solvent to demonstrate the first proof of principle measurement with the novel technique. The complex electric field of the combination bond of water molecules at 1930 nm at different molecular concentrations is detected and presented. We show the detection sensitivity of our time-domain technique is comparable to conventional specral-domain techniques. However, by employing a laser frontend with higher repetition rates, the detection sensitivity can be drastically enhanced. To the best of our knowledge, this is the first detection of the complex electric field of the molecular response in near-infrared spectral range. The new method holds promise for high-resolution overtone spectroscopy and microscopy with unparalleled sensitivity and specificity over the entire molecular fingerprint region.

Keywords: time-domain spectroscopy, femtosecond fieldoscopy, near-infrared spectroscopy, Yb:YAG lasers, femtosecond spectroscopy, water, overtone excitation, background-free detection, femtosecond laser sources.

1. INTRODUCTION

Linear spectroscopy in near-infrared (NIR) spectral range provides information on the molecular composition, structure, and conformation, affording tremendous potential for high-resolution, in-depth, label-free biological spectro-microscopy.[1] In NIR spectroscopy, similar information to infrared spectroscopy is obtained by exciting the first overtone of infrared-active vibrational modes. The intensity and vibrational period of these harmonics depend on the quantity and types of the present molecules in the sample. Quantitative analysis is possible when the changes in the transmitted spectrum are proportional to the concentration of chemical components of the sample under scrutiny. Therefore, NIR spectroscopy has been a popular technique for identification, quantitative and qualitative analysis, and structure-correlation of molecular compositions. In particular, it is routinely used for the detection of the overtone and combination bands of the C-H, O-H, and N-H compositions.[2] Additionally, as the electric filed in NIR spectral region supports a smaller diffraction limit than infrared, molecular information with higher spatial resolution can be obtained. Moreover, the lower cross-section of the overtone excitation allows for deeper penetration of the injected field to the sample, allowing for in-depth spectral imaging.[3]

Broadband measurements in this spectral region have been carried out mainly in the frequency domain.[4] This approach suffers from two limitations: I) the detection of small absorption is limited to the intensity noise of the source, and II) the low detection dynamic range. To mitigate above-mentioned constraints, we introduce the concept of molecular fieldoscopy. In molecular fieldoscopy, an ultrashort, phase-coherent pulse is used for molecular excitation and afterwards the transmitted complex electric field that contains the molecular response is directly measured. Here, the electric field is detected in a background-free manner, eliminating the effect of

Further author information: (Send correspondence to HF)
HF.: E-mail: hanieh.fattahi@mpq.mpg.de, Telephone: +498932907732

Multiphoton Microscopy in the Biomedical Sciences XIX, edited by Ammasi Periasamy, Peter T. C. So, Karsten König,
Proc. of SPIE Vol. 10882, 1088231 · © 2019 SPIE · CCC code: 1605-7422/19/$18 · doi: 10.1117/12.2507604

the intensity noise of the source. Furthermore, measuring the complex electric field allows for extracting the full spectral phase information of the molecular response, adding a new dimension to the gained spectroscopic data.

It is well known that the interaction of broadband ultrashort pulses with an ensemble of molecules at their resonance frequencies, results in a coherent scattering. The delayed response of the medium, known as free-induction decay (FID), can be explained by the Kramers-Kronig relation. During the interaction, photons at the resonance frequencies are slowed down compared to the other photons and appear at the trailing edge of the excitation pulse, due to the increase of the group refractive index of the medium at the vicinity of the resonance frequencies. The delayed response lasts for hundreds of picoseconds for molecules in the gas phase and down to several picoseconds in liquid phase. The FID carries information about the molecular composition and concentration. Therefore, by temporal detection of the coherent response, valuable spectroscopic information can be gained. Additionally, by using ultrashort pulses, the excitation pulse is confined to a time window of tens of femtosecond, which is significantly shorter than FID of the molecular sample under scrutiny. Here, the response emerging from the sample is separated temporally from the ultrashort excitation pulse, enabling for a background-free detection. As FID after the excitation pulse decreases exponentially, its earlier temporal detection results in a higher detection's signal-to-noise ratio and therefore, sensitivity.

Terahertz time-domain spectroscopy based on electro-optic sampling (EOS) has been a powerful method for the direct measurement of the electric field in mid-infrared and terahertz spectral region.[5] However, its extension to NIR has been shown just recently, due to difficulties in the generation of short, phase-stable excitation pulses that are temporally synchronized with short sampling probe pulses.[6]

In what follows we report, to the best of our knowledge, the first measurement of the complex electric field of the water's molecular response by using EOS in NIR spectral range.

2. EXPERIMENTAL SETUP

Water plays a prominent role in biological interactions and life, with its first overtone of the symmetric stretch vibration appearing at 1450 nm (6900 cm^{-1}) and a strong $\nu_2 + \nu_3$ combination band near 1930 nm (5180 cm^{-1}). We aimed for the field detection of the water's molecular response at its combination band for various molecular concentration. We chose acetic acid as the background solvent due to its sparse spectral response at this range.

2.1 Near-infrared electro-optic sampling

A home-built, diode-pumped Yb:YAG thin-disk regenerative amplifier operating at 5 kHz repetition rates was used as the frontend.[7] 1.8 mJ of the output energy of the laser was used to generate a carrier-to-envelope phase-stable, multi-octave, broadband spectrum spanning from 500 nm to 2500 nm.[8] The broadband spectrum was divided into two portions: i) spectral region covering from 700 nm to 1400 nm, and ii) NIR region with spectral coverage from 1600 nm to 2500 nm. The two portions of the spectrum were amplified to the total energy of 25 μJ in two parallel single-stage optical parametric amplifiers. After amplification each channel was compressed to its Fourier transform limit, resulting in 5 fs pulses centered at 1 μm and 18 fs pulses centered at 2 μm.[9] The 18 fs, NIR pulses were used for excitation of combination bond of water molecules, while the 5 fs pulses at 1 μm were used as a probe in the EOS setup.

The experimental setup of the EOS is depicted in Fig. 1. First, the NIR beam was focused by a 4 inch focal length off-axis parabolic mirror into the sample. Afterwards, the transmitted beam was collimated by another 4 inch focal length off-axis parabolic mirror. The sample was placed slightly after the focus to avoid filamentation of the NIR pulses. The beam size on the sample was 200 μm full width at half maximum (FWHM). The probe pulses were collinearly combined with the transmitted light from the sample by using an ultra-broadband wire grid polarizer (Thorlabs, WP25L-UB). Subsequently, both beams were focused by a 2 inch focal length off-axis parabolic mirror into a 50 μm-thick BBO (Type II) crystal (CASTECH) at the phase matching angle of $\theta = 25°$. The probe and NIR beams were orthogonally polarized along the ordinary (o) and extraordinary (e) axes of the nonlinear crystal, respectively. By temporal and spatial overlap of the two pulses in the crystal, sum-frequency signal centered at 670 nm was generated. The sum-frequency signal was polarized along the extraordinary (e) axis of the nonlinear crystal and spectrally overlaps with the high-frequency components of the ordinarily polarized probe pulses.

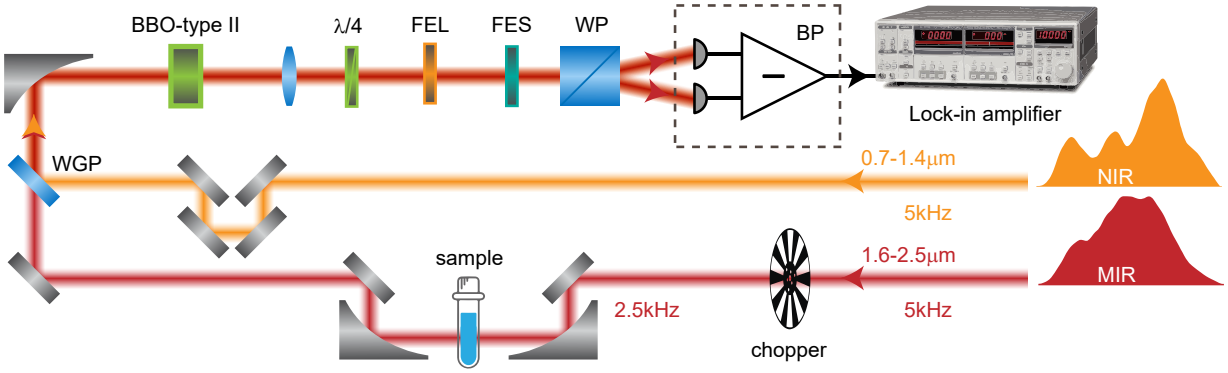

Figure 1. EOS setup consists of a 50 μm-thick BBO (Type II) crystal and an ellipsometer. The NIR beam is chopped at 2.5 KHz and transmits through a 500 μm-thick sample. The sampling beam after the delay line is collinearly combined with the transmitted NIR beam. Thereafter, they are focused in the EOS crystal for sum-frequency generation. The generated sum-frequency signal spectrally overlaps and temporally interferes with the high-frequency components of the probe beam. Appropriate spectral filtering is used to enhance the EOS signal. The polarization rotation of the probe beam as a function of temporal delay is detected by an ellipsometer and read out by lock-in amplifier. WGP: wire grid polarizer, $\lambda/4$: quarter-wave plate, FEL: longpass filter, FES: shortpass filter, WP: Wollaston prism, BP: balanced photodetector.

In order to enhance the EOS signal at the detectors, spectral region between 650 nm and 750 nm was filtered out by using a 650 nm long-pass (Thorlabs, FEL0650) and a 750 nm short-pass (Edmund Optics, 64-324) filters.[10] The generated nonlinear signal induces polarization rotation in the probe pulses as a function of the relative timing of the probe and NIR pulses. The induced electro-optic signal was detected with an ellipsometer consisting of a quarter-wave plate (Thorlabs, AQWP05M-600), Wollaston prism (Thorlabs, WP10), and a home-built balanced detector. In the absence of the NIR beam, the ellipsometer is aligned to equally split and balance the power of the probe pulses at the pair of photodiodes. Therefore, the difference between the photocurrents of the two detectors is equal to zero. In the presence of the NIR pulses, the difference is imbalanced and varies relative to the temporal delay of the probe pulses. The electronic data from the balanced detector is recorded by using a lock-in amplifier (Stanford Research Systems, SR830-DSP) while the NIR pulses were modulated at 2.5 kHz (half of the laser's repetition rate) with a mechanical chopper (Thorlabs, MC2000B-EC).

In parallel for a precise temporal delay scan, the mechanical delay stage (Physik Instrumente, V-528.1AA) was tracked with a Mach-Zehnder-type interferometric delay tracking setup (SmarAct GmbH, PicoScale). The setup employs the beam of a 1.55 μm continuous-wave distributed-feedback laser diode, propagating along the NIR and probe beam-paths.[11]

A series of measurements were performed to estimate the detection dynamic range of the EOS setup in the absence of the liquid sample. First, the energy of the NIR pulses was attenuated by using a series of neutral density filters with different optical densities (ODs) and afterwards their electric field were measured by EOS. Figure 2 a) illustrates the sampled waveforms for different attenuations. The black curve shows the electric field of the unatenuated NIR pulses. The red curve shows the detectable NIR pulses by EOS with the average power of 650 nanowatts (power attenuation by filters at the OD of 3.1). The corresponding spectra of EOS traces for five different attenuations (OD of 0, 0.8, 1.5, 2.2, and 3.1) are shown in Fig. 2 b). The spectra were obtained by Fourier transformation of the measured electric filed. As can be seen, at the highest attenuation the bandwidth of the retrieved spectrum is limited to spectral components with the highest spectral intensity.

2.2 Sample preparation

Acetic acid (Sigma-Aldrich, ReagentPlus, 99%, A6283) and deionized water were used to create solution samples at six different concentrations between 0 Molar to 55.6 Molar (0% - 100%). Afterwards, different mixtures were injected to a sample holder (Harrick Scientific, DLC-M25) consisting of two sapphire windows with a thickness of 2.3 mm. The sample's thickness for all the measurements was 500 μm.

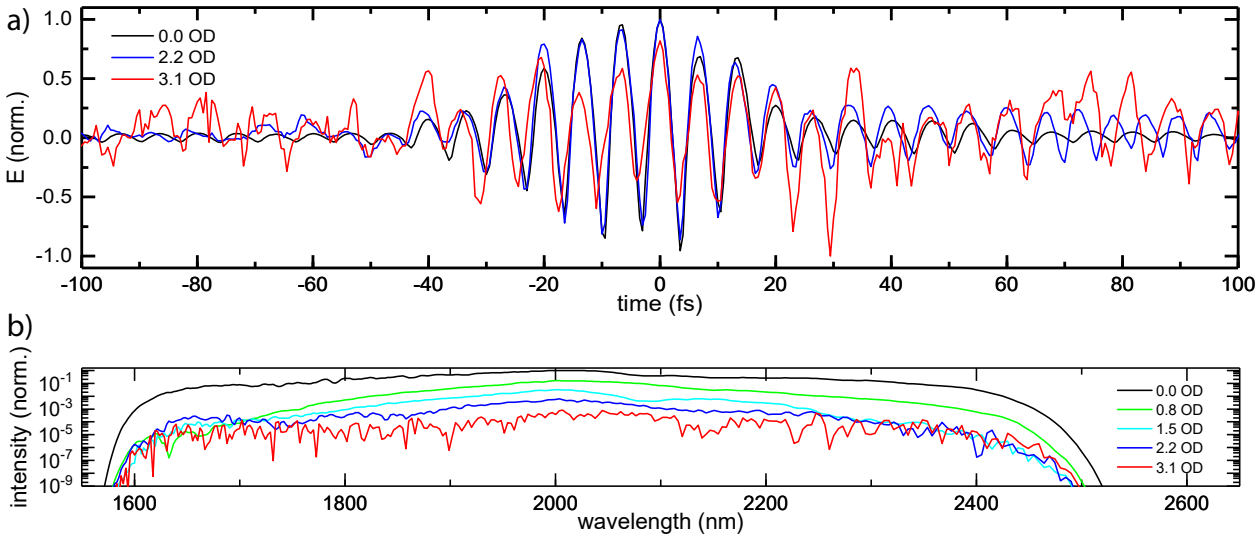

Figure 2. a) Measured electric field of the transmitted pulses in the absence of any sample for three different attenuations (0, 2.2, and 3.1 OD). b) The retrieved NIR spectrum in the absence of any sample for five different attenuations (0, 0.8, 1.5, 2.2, and 3.1 OD). The obtained spectra were normalized then calibrated to the transmitted power.

3. RESULTS AND DISCUSSION

To detect the FID of water molecules, the mixture of acetic acid and water with different concentrations was placed in the sample holder and the transmitted electric field was measured by EOS. The delay stage was scanned over 450 μm with the speed of 1.7 μm/s, corresponding to a single shot detection at each delay position. Background measurements were taken with an empty sample holder and pure acetic acid serving as blank (see Fig. 3 a)). As can be seen in the inset, the amplitude of the excitation pulses goes to zero at temporal delays above 200 fs. By adding the sample, the molecular FID is formed and can be detected free of background at temporal delays beyond 200 fs. Figure 3 b) shows the measured transmitted electric field for the mixture of water and acetic acid at two high concentrations. At high water concentrations the transmitted main pulse is chirped. The NIR response of water molecules is clearly distinguished from acetic acid at 50%, and 100%,. To evaluate the sensitivity of the system, measurements of lower water's concentrations (10%, 5%, and 3%) were carried out. As is shown in Fig. 3 c), the molecular response is detectable by naked eye for water concentration as low as 3%.

A similar study[12] was reported in the frequency domain on water molecules in methanol solvent by using a Guided Wave NIR-O Process, fiber-coupled, NIR Spectrometry with the core diameter of 500 μm. In this experiment, the water molecules in methanol solvent were placed in a 10 mm-thick sample holder. The combination bond of water molecules could be detected down to 0.1% water concentration. Calibrating our measurements with a 500μm sample thickness and a 200μm laser beam size (shown in Fig.3 c)), to 10 mm of sample thickness and 500 μm of beam diameter, results in 0.075% equivalent detectable water concentration by EOS.

4. CONCLUSION AND OUTLOOK

We presented a novel approach, which we dubbed molecular fieldoscopy, for detection of the complex electric field of molecular response in NIR spectral range. Here, exciting molecules with ultrashort pulses allows for background-free detection of the molecular response. By employing broadband excitation pulses in combination with EOS, the entire molecular vibrations in the fingerprint region can be simultaneously excited and detected.

In this regards, we showed the potential of Yb:YAG thin-disk lasers for generating the required multi-octave spectrum and demonstrated the first proof of principle field-detection of water molecule's vibration at 1.9 μm at different molecular concentrations. Our current detection sensitivity is comparable to the conventional spectroscopy techniques and limited to the stability of the interferometer and the repetition rate of the laser. However,

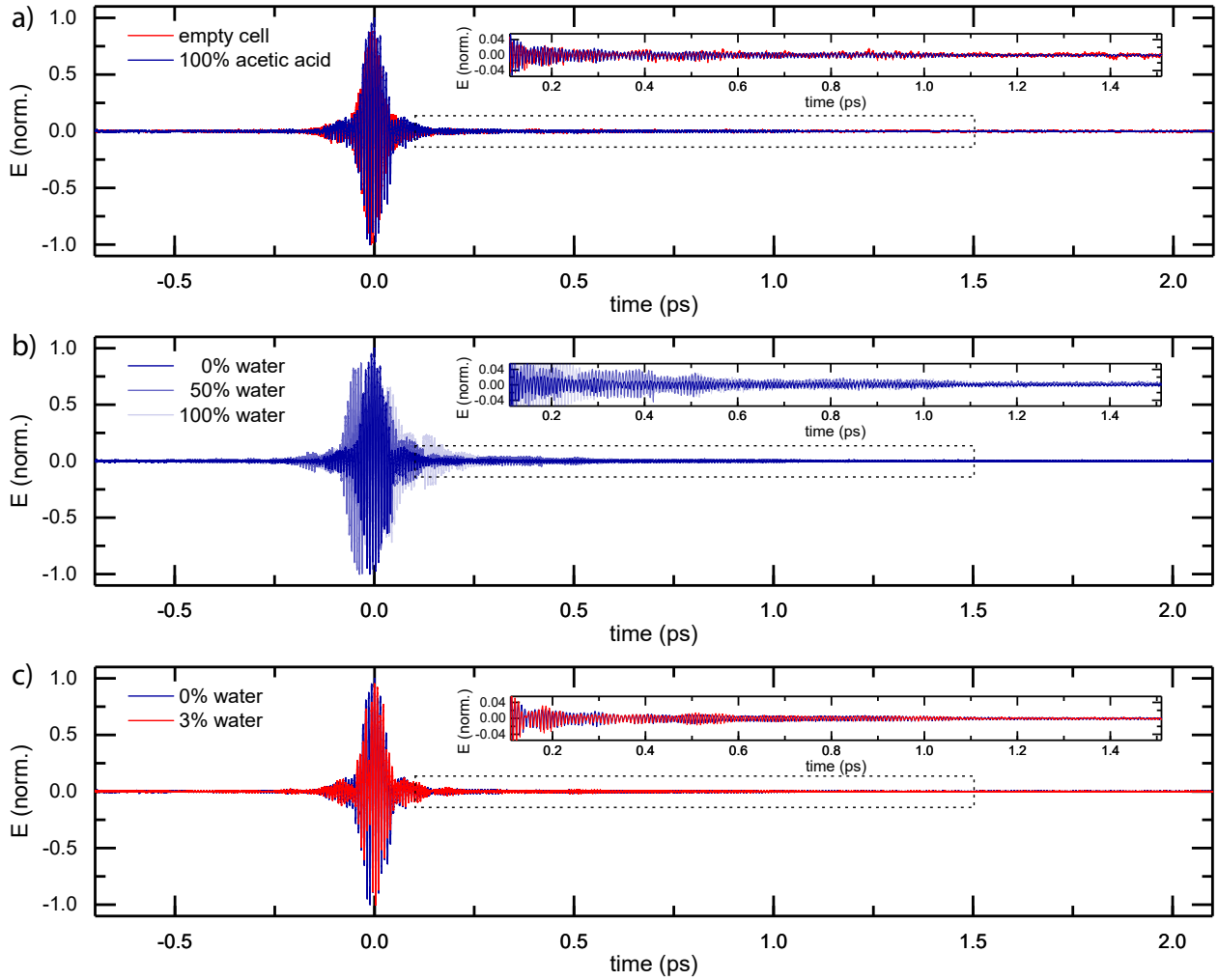

Figure 3. a) Measured electric field of the transmitted pulses in the absence of any sample (red) and 100% acetic acid sample (blue). Inset: zoomed plot for the temporal delays above 100 fs. b) Measured electric field of the transmitted pulses for the mixture of water and acetic acid for three different water's concentrations 0%, 50%, and 100%. Inset: zoomed plot for the temporal delays above 100 fs. c) Measured electric field of the transmitted pulses for the mixture of water and acetic acid for water concentrations 0% (blue), and 3% (red). Inset: zoomed plot for the temporal delays above 100 fs.

employing a frontend at megahertz repetition rates[13] holds promise for enhancing the detection sensitivity to unparalleled values.

Moreover, combining the concept of molecular fieldoscopy with exciting nonlinear techniques such as two-dimensional spectroscopy, holds promise to increase our understanding of molecular dynamics, for example in water. Water in liquid phase, consists of a molecular network with molecular dynamics at various time scales, from several picoseconds to tens of femtoseconds. The intermolecular OH-bond stretching and bending has the shortest vibrational period at 10 fs and 20 fs, respectively. On a time scale of several hundreds of femtoseconds, liberational motions, and the H-bonds stretching and bending occur. Last but not least the exchange of hydrogen-bond partners via breaking and reforming of stable H-bonds occurs in a time range between 1-5 ps.[14] Femtosecond molecular fieldoscopy is capable of detecting the complex electric field of the water response at all above-mentioned time scales with high sensitivity, and may allow for resolving many unknown aspects of water's molecular dynamic.

REFERENCES

[1] Jöbsis, F. F., "Noninvasive, infrared monitoring of cerebral and myocardial oxygen sufficiency and circulatory parameters.," *Science (New York, N.Y.)* **198**, 1264–1267 (dec 1977).

[2] Andrews, N. L. P., MacLean, A. G., Saunders, J. E., Barnes, J. A., Loock, H.-P., Saad, M., Jia, C., Ramaswamy, K., and Chen, L. R., "Quantification of different water species in acetone using a NIR-triple-wavelength fiber laser," *Optics Express* **22**(16), 19337 (2014).

[3] Wang, H.-W., Chai, N., Wang, P., Hu, S., Dou, W., Umulis, D., Wang, L. V., Sturek, M., Lucht, R., and Cheng, J.-X., "Label-Free Bond-Selective Imaging by Listening to Vibrationally Excited Molecules," *Physical Review Letters* **106**, 238106 (jun 2011).

[4] Pasquini, C., "Near Infrared Spectroscopy: fundamentals, practical aspects and analytical applications," *Journal of the Brazilian Chemical Society* **14**, 198–219 (apr 2003).

[5] Dhillon, S. S., Vitiello, M. S., Linfield, E. H., Davies, A. G., Hoffmann, M. C., Booske, J., Paoloni, C., Gensch, M., Weightman, P., Williams, G. P., Castro-Camus, E., Cumming, D. R. S., Simoens, F., Escorcia-Carranza, I., Grant, J., Lucyszyn, S., Kuwata-Gonokami, M., Konishi, K., Koch, M., Schmuttenmaer, C. A., Cocker, T. L., Huber, R., Markelz, A. G., Taylor, Z. D., Wallace, V. P., Axel Zeitler, J., Sibik, J., Korter, T. M., Ellison, B., Rea, S., Goldsmith, P., Cooper, K. B., Appleby, R., Pardo, D., Huggard, P. G., Krozer, V., Shams, H., Fice, M., Renaud, C., Seeds, A., Stöhr, A., Naftaly, M., Ridler, N., Clarke, R., Cunningham, J. E., and Johnston, M. B., "The 2017 terahertz science and technology roadmap," *Journal of Physics D: Applied Physics* **50**, 043001 (feb 2017).

[6] Keiber, S., Sederberg, S., Schwarz, A., Trubetskov, M., Pervak, V., Krausz, F., and Karpowicz, N., "Electro-optic sampling of near-infrared waveforms," *Nature Photonics* **10**, 159–162 (jan 2016).

[7] Fattahi, H., Alismail, A., Wang, H., Brons, J., Pronin, O., Buberl, T., Vámos, L., Arisholm, G., Azzeer, A. M., and Krausz, F., "High-power, 1-ps, all-Yb:YAG thin-disk regenerative amplifier," *Optics Letters* **41**, 1126–1129 (mar 2016).

[8] Fattahi, H., Wang, H., Alismail, A., Arisholm, G., Pervak, V., Azzeer, A. M., and Krausz, F., "Near-PHz-bandwidth, phase-stable continua generated from a Yb:YAG thin-disk amplifier," *Optics Express* **24**, 24337–24346 (oct 2016).

[9] Fattahi, H., Wang, H., Alismail, A., and Krausz, F., "Towards high-power, multi-TW light transients," in [*Conference on Lasers and Electro-Optics*], SM1M.6, OSA, Washington, D.C. (2016).

[10] Porer, M., Ménard, J.-M., and Huber, R., "Shot noise reduced terahertz detection via spectrally postfiltered electro-optic sampling.," *Optics letters* **39**(8), 2435–2438 (2014).

[11] Schweinberger, W., Vamos, L., Xu, J., Hussain, S. A., Baune, C., Rode, S., and Pupeza, I., "Interferometric delay tracking for low-noise Mach-Zehnder-type scanning measurements," *Accepted in Optics Express* .

[12] Wave, G., "Measuring Water Concentration in Solvents with NIR Spectroscopy."

[13] Fattahi, H., Barros, H. G., Gorjan, M., Nubbemeyer, T., Alsaif, B., Teisset, C. Y., Schultze, M., Prinz, S., Haefner, M., Ueffing, M., Alismail, A., Vámos, L., Schwarz, A., Pronin, O., Brons, J., Geng, X. T., Arisholm, G., Ciappina, M., Yakovlev, V. S., Kim, D.-E., Azzeer, A. M., Karpowicz, N., Sutter, D., Major, Z., Metzger, T., and Krausz, F., "Third-generation femtosecond technology," *Optica* **1**, 45–63 (jul 2014).

[14] Laage, D., Elsaesser, T., and Hynes, J. T., "Water Dynamics in the Hydration Shells of Biomolecules," *Chemical Reviews* **117**, 10694–10725 (aug 2017).

Data Archiving

The measured raw data, the data processing files, and the original figure files utilized in this thesis can be reached via the Data Archive Server (DAS) of the Laboratory for Attosecond Physics (LAP) at the Max Planck Institute of Quantum Optics (MPQ): `//AFS/ipp-garching.mpg.de/mpq/lap/publication_archive`. According to the thesis structure, the archive materials are divided in several folders corresponding to each chapter. Under each folder, there are subfolders, which are devoted to all figures presented in the chapter. This contains all of the relevant files such as: the raw data, MATLAB scripts in .m format, Origin projects in .opj format, drawing files in .ai format, and the figure in .pdf format. The structure of the archive materials is summarized in the following table as:

folder	subfolder	raw data	simulation	.m	.opj	.ai	.pdf
Ch. 1	Fig. 1.1	-	-	-	-	1	1
	Fig. 1.2	-	-	-	-	1	1
Ch. 2	Fig. 2.1	-	-	-	1	1	2
	Fig. 2.2	-	-	-	-	1	1
	Fig. 2.3	-	-	-	-	1	1
	Fig. 2.4	-	-	-	-	1	1
	Fig. 2.5	1	1	-	1	-	1
	Fig. 2.6	7	-	1	1	1	5
	Fig. 2.7	3	-	-	1	1	2
	Fig. 2.8	-	-	-	-	1	1
	Fig. 2.9	1	1	-	1	-	1
	Fig. 2.10	5	-	1	1	1	3
	Fig. 2.11	7	-	1	1	1	5
	Fig. 2.12	5	-	-	1	-	1
Ch. 3	Fig. 3.1	-	-	-	-	1	1
	Fig. 3.2	9	-	-	1	-	1
	Fig. 3.3	-	-	-	-	1	1
	Fig. 3.4	-	-	-	-	1	1
	Fig. 3.5	3	-	-	1	1	3
	Fig. 3.6	6	-	1	1	1	5

	Fig. 3.7	8	-	-	1	1	1
	Fig. 3.8	-	-	-	-	1	1
	Fig. 3.9	24	-	-	1	1	6
Ch. 4	Fig. 4.1	5	-	2	1	1	3
	Fig. 4.2	-	-	-	-	1	1
	Fig. 4.3	2	1	2	1	1	3
	Fig. 4.4	3	4	1	1	1	3
	Fig. 4.5	-	-	-	-	1	1
	Fig. 4.6	-	-	-	1	-	1
	Fig. 4.7	7	-	1	1	1	5
	Fig. 4.8	19	-	-	-	1	1
	Fig. 4.9	-	-	-	1	-	1
	Fig. 4.10	20	-	-	1	-	1
	Fig. 4.11	6	-	-	1	1	3
	Fig. 4.12	-	-	-	-	1	1
	Fig. 4.13	6	-	1	1	1	5
	Fig. 4.14	6	-	1	1	1	5
	Fig. 4.15	10	8	3	1	1	5
Ch. 5	Fig. 5.1	-	-	-	1	1	1
	Fig. 5.2	5	-	1	1	1	3
	Fig. 5.3	2	-	1	1	-	1
Ch. 6	Fig. 6.1	-	-	1	-	1	1
	Fig. 6.2	-	-	1	1	1	3
	Fig. 6.3	-	-	-	1	1	1
	Fig. 6.4	-	-	-	-	1	1
	Fig. 6.5	-	-	-	-	1	1
	Fig. 6.6	1	-	-	1	-	1
	Fig. 6.7	2	-	-	1	1	3
	Fig. 6.8	-	-	-	-	1	1
	Fig. 6.9	15	-	1	1	1	3
	Fig. 6.10	10	-	1	1	1	4
	Fig. 6.11	8	-	1	1	1	3
Ch. 7	Fig. 7.1	4	-	2	1	1	3
Appx. B	Fig. B.1	1	-	1	1	-	1

Bibliography

[1] S. Dhillon, M. Vitiello, E. Linfield, A. Davies, M. C. Hoffmann, J. Booske, C. Paoloni, M. Gensch, P. Weightman, G. Williams, *et al.*, "The 2017 terahertz science and technology roadmap," *Journal of Physics D: Applied Physics* **50**(4), p. 043001, 2017.

[2] M. Hentschel, R. Kienberger, C. Spielmann, G. A. Reider, N. Milosevic, T. Brabec, P. Corkum, U. Heinzmann, M. Drescher, and F. Krausz, "Attosecond metrology," *Nature* **414**(6863), p. 509, 2001.

[3] F. Krausz and M. I. Stockman, "Attosecond metrology: from electron capture to future signal processing," *Nature Photonics* **8**(3), p. 205, 2014.

[4] K. T. Kim, C. Zhang, A. D. Shiner, B. E. Schmidt, F. Légaré, D. Villeneuve, and P. Corkum, "Petahertz optical oscilloscope," *Nature Photonics* **7**(12), p. 958, 2013.

[5] A. Sommer, E. Bothschafter, S. Sato, C. Jakubeit, T. Latka, O. Razskazovskaya, H. Fattahi, M. Jobst, W. Schweinberger, V. Shirvanyan, *et al.*, "Attosecond nonlinear polarization and light–matter energy transfer in solids," *Nature* **534**(7605), p. 86, 2016.

[6] M. Schultze, M. Fieß, N. Karpowicz, J. Gagnon, M. Korbman, M. Hofstetter, S. Neppl, A. L. Cavalieri, Y. Komninos, T. Mercouris, *et al.*, "Delay in photoemission," *Science* **328**(5986), pp. 1658–1662, 2010.

[7] M. Drescher, M. Hentschel, R. Kienberger, M. Uiberacker, V. Yakovlev, A. Scrinzi, T. Westerwalbesloh, U. Kleineberg, U. Heinzmann, and F. Krausz, "Time-resolved atomic inner-shell spectroscopy," *Nature* **419**(6909), p. 803, 2002.

[8] S. R. Leone, C. W. McCurdy, J. Burgdörfer, L. S. Cederbaum, Z. Chang, N. Dudovich, J. Feist, C. H. Greene, M. Ivanov, R. Kienberger, *et al.*, "What will it take to observe processes in 'real time'?," *Nature Photonics* **8**(3), p. 162, 2014.

[9] H. Fattahi, "Sub-cycle light transients for attosecond, X-ray, four-dimensional imaging," *Contemporary Physics* **57**(4), pp. 580–595, 2016.

[10] E. J. Takahashi, P. Lan, O. D. Mücke, Y. Nabekawa, and K. Midorikawa, "Attosecond nonlinear optics using gigawatt-scale isolated attosecond pulses," *Nature communications* **4**, p. 2691, 2013.

[11] P. Tzallas, E. Skantzakis, L. Nikolopoulos, G. D. Tsakiris, and D. Charalambidis, "Extreme-ultraviolet pump-probe studies of one-femtosecond-scale electron dynamics," *Nature Physics* **7**(10), p. 781, 2011.

[12] D. Shorokhov and A. H. Zewail, "Perspective: 4D ultrafast electron microscopy—Evolutions and revolutions," *The Journal of Chemical Physics* **144**(8), p. 080901, 2016.

[13] M. Wendl, M. Högner, and H. Fattahi, "Theoretical study: high harmonic generation by light transients," *Applied Sciences* **8**(5), p. 728, 2018.

[14] S. T. Cundiff and A. M. Weiner, "Optical arbitrary waveform generation," *Nature Photonics* **4**(11), p. 760, 2010.

[15] A. Wirth, R. Santra, and E. Goulielmakis, "Real time tracing of valence-shell electronic coherences with attosecond transient absorption spectroscopy," *Chemical Physics* **414**, pp. 149–159, 2013.

[16] G. Krauss, S. Lohss, T. Hanke, A. Sell, S. Eggert, R. Huber, and A. Leitenstorfer, "Synthesis of a single cycle of light with compact erbium-doped fibre technology," *Nature Photonics* **4**(1), p. 33, 2010.

[17] O. D. Mucke, S. Fang, G. Cirmi, G. M. Rossi, S.-H. Chia, H. Ye, Y. Yang, R. Mainz, C. Manzoni, P. Farinello, *et al.*, "Toward waveform nonlinear optics using multimillijoule sub-cycle waveform synthesizers," *IEEE J. Sel. Top. Quantum Electron.* **21**(5), pp. 1–12, 2015.

[18] H. Fattahi, H. G. Barros, M. Gorjan, T. Nubbemeyer, B. Alsaif, C. Y. Teisset, M. Schultze, S. Prinz, M. Haefner, M. Ueffing, *et al.*, "Third-generation femtosecond technology," *Optica* **1**(1), pp. 45–63, 2014.

[19] C. Manzoni, S.-W. Huang, G. Cirmi, P. Farinello, J. Moses, F. Kärtner, and G. Cerullo, "Coherent synthesis of ultra-broadband optical parametric amplifiers," *Optics Letters* **37**(11), pp. 1880–1882, 2012.

[20] S.-W. Huang, G. Cirmi, J. Moses, K.-H. Hong, S. Bhardwaj, J. R. Birge, L.-J. Chen, E. Li, B. J. Eggleton, G. Cerullo, *et al.*, "High-energy pulse synthesis with sub-cycle waveform control for strong-field physics," *Nature Photonics* **5**(8), p. 475, 2011.

[21] H. Wang, A. Alismail, G. Barbiero, R. N. Ahmad, and H. Fattahi, "High energy, sub-cycle, field synthesizers," *IEEE Journal of Selected Topics in Quantum Electronics* **25**(4), pp. 1–12, 2019.

[22] S. Keiber, S. Sederberg, A. Schwarz, M. Trubetskov, V. Pervak, F. Krausz, and N. Karpowicz, "Electro-optic sampling of near-infrared waveforms," *Nature Photonics* **10**(3), p. 159, 2016.

[23] G. M. Rossi, R. E. Mainz, F. Scheiba, Y. Yang, G. Cirmi, and F. X. Kartner, "Half-cycle mJ-level CEP-stable pulses from parametric waveform synthesis," in *Conference on Lasers and Electro-Optics/Pacific Rim*, pp. F2A–1, Optical Society of America, 2018.

[24] R. E. Mainz, Y. Yang, G. M. Rossi, F. Scheiba, G. Cirmi, and F. X. Kärtner, "Controlled HHG with a sub-cycle mJ-level parametric waveform synthesizer," in *Conference on Lasers and Electro-Optics/Pacific Rim*, pp. Th3B–5, IEEE, 2018.

[25] H. Fattahi, "Design of a multi-terawatt field synthesizer (LWS-pro)," in *Third-generation femtosecond technology*, pp. 107–126, Springer, 2016.

[26] P. Russbueldt, T. Mans, J. Weitenberg, H. Hoffmann, and R. Poprawe, "Compact diode-pumped 1.1 kW Yb:YAG Innoslab femtosecond amplifier," *Optics Letters* **35**(24), pp. 4169–4171, 2010.

[27] L. E. Zapata, F. Reichert, M. Hemmer, and F. Kärtner, "250 W average power, 100 kHz repetition rate cryogenic Yb:YAG amplifier for OPCPA pumping," *Optics Letters* **41**(3), pp. 492–495, 2016.

[28] T. Nubbemeyer, M. Kaumanns, M. Ueffing, M. Gorjan, A. Alismail, H. Fattahi, J. Brons, O. Pronin, H. G. Barros, Z. Major, *et al.*, "1 kW, 200 mJ picosecond thin-disk laser system," *Optics Letters* **42**(7), pp. 1381–1384, 2017.

[29] A. Alismail, H. Wang, G. Barbiero, N. Altwaijry, S. A. Hussain, V. Pervak, W. Schweinberger, A. M. Azzeer, F. Krausz, and H. Fattahi, "Multi-octave, CEP-stable source for high-energy field synthesis," *Science Advances* **6**, p. aax4308, 2020.

[30] A. Alismail, H. Wang, G. Barbiero, and H. Fattahi, "All-ytterbium frontend for high-energy field synthesizers," in *The European Conference on Lasers and Electro-Optics*, pp. CF–9–4, Optical Society of America, 2019.

[31] A. Alismail, H. Wang, G. Barbiero, S. A. Hussain, W. Schweinberger, F. Krausz, and H. Fattahi, "Near-infrared molecular fieldoscopy of water," in *Multiphoton Microscopy*

in the Biomedical Sciences XIX, **10882**, p. 1088231, International Society for Optics and Photonics, 2019.

[32] A. Alismail, H. Wang, G. Barbiero, S. A. Hussain, W. Schweinberger, F. Krausz, and H. Fattahi, "Near-infrared molecular fieldoscopy," in *CLEO: Applications and Technology*, pp. AF3K–5, Optical Society of America, 2019.

[33] A. Alismail, H. Wang, G. Barbiero, F. Krausz, and H. Fattahi, "Near-infrared fieldoscopy of water," in *The European Conference on Lasers and Electro-Optics*, pp. CD–2–2, Optical Society of America, 2019.

[34] H. Çankaya, A.-L. Calendron, G. Cirmi, and F. X. Kärtner, "Front-end of Yb-based high-energy optical waveform synthesizer," in *2015 Conference on Lasers and Electro-Optics (CLEO)*, pp. 1–2, IEEE, 2015.

[35] F. Druon, F. Balembois, and P. Georges, "New laser crystals for the generation of ultrashort pulses," *Comptes Rendus Physique* **8**(2), pp. 153–164, 2007.

[36] D. H. Sutter, G. Steinmeyer, L. Gallmann, N. Matuschek, F. Morier-Genoud, U. Keller, V. Scheuer, G. Angelow, and T. Tschudi, "Semiconductor saturable-absorber mirror–assisted Kerr-lens mode-locked Ti:sapphire laser producing pulses in the two-cycle regime," *Optics Letters* **24**(9), pp. 631–633, 1999.

[37] U. Morgner, F. X. Kärtner, S.-H. Cho, Y. Chen, H. A. Haus, J. G. Fujimoto, E. P. Ippen, V. Scheuer, G. Angelow, and T. Tschudi, "Sub-two-cycle pulses from a Kerr-lens mode-locked Ti:sapphire laser," *Optics Letters* **24**(6), pp. 411–413, 1999.

[38] O. H. Heckl, J. Kleinbauer, D. Bauer, S. Weiler, T. Metzger, and D. H. Sutter, "Ultrafast thin-disk lasers," in *Ultrashort Pulse Laser Technology*, pp. 93–115, Springer, 2016.

[39] L. E. Zapata, H. Lin, A.-L. Calendron, H. Cankaya, M. Hemmer, F. Reichert, W. R. Huang, E. Granados, K.-H. Hong, and F. X. Kärtner, "Cryogenic Yb:YAG composite-thin-disk for high energy and average power amplifiers," *Optics Letters* **40**(11), pp. 2610–2613, 2015.

[40] M. Schulz, R. Riedel, A. Willner, T. Mans, C. Schnitzler, P. Russbueldt, J. Dolkemeyer, E. Seise, T. Gottschall, S. Hädrich, *et al.*, "Yb:YAG Innoslab amplifier: efficient high repetition rate subpicosecond pumping system for optical parametric chirped pulse amplification," *Optics Letters* **36**(13), pp. 2456–2458, 2011.

[41] F. Röser, T. Eidam, J. Rothhardt, O. Schmidt, D. Schimpf, J. Limpert, and A. Tünnermann, "Millijoule pulse energy high repetition rate femtosecond fiber chirped-pulse amplification system," *Optics Letters* **32**(24), pp. 3495–3497, 2007.

[42] P. Russbueldt, T. Mans, G. Rotarius, J. Weitenberg, H. Hoffmann, and R. Poprawe, "400 W Yb:YAG Innoslab fs-amplifier," *Optics Express* **17**(15), pp. 12230–12245, 2009.

[43] C. Baumgarten, M. Pedicone, H. Bravo, H. Wang, L. Yin, C. S. Menoni, J. J. Rocca, and B. A. Reagan, "1 J, 0.5 kHz repetition rate picosecond laser," *Optics Letters* **41**(14), pp. 3339–3342, 2016.

[44] J. Petit, P. Goldner, and B. Viana, "Laser emission with low quantum defect in Yb:$CaGdAlO_4$," *Optics letters* **30**(11), pp. 1345–1347, 2005.

[45] D. C. Brown and V. A. Vitali, "Yb:YAG kinetics model including saturation and power conservation," *IEEE Journal of Quantum Electronics* **47**(1), pp. 3–12, 2011.

[46] B. Volodin, S. Dolgy, E. Melnik, E. Downs, J. Shaw, and V. Ban, "Wavelength stabilization and spectrum narrowing of high-power multimode laser diodes and arrays by use of volume Bragg gratings," *Optics Letters* **29**(16), pp. 1891–1893, 2004.

[47] G. Huber, C. Kränkel, and K. Petermann, "Solid-state lasers: status and future," *JOSA B* **27**(11), pp. B93–B105, 2010.

[48] E. C. Honea, R. J. Beach, S. C. Mitchell, J. A. Skidmore, M. A. Emanuel, S. B. Sutton, S. A. Payne, P. V. Avizonis, R. S. Monroe, and D. G. Harris, "High-power dual-rod Yb:YAG laser," *Optics Letters* **25**(11), pp. 805–807, 2000.

[49] T. Rutherford, W. Tulloch, S. Sinha, and R. Byer, "Yb:YAG and Nd:YAG edge-pumped slab lasers," *Optics Letters* **26**(13), pp. 986–988, 2001.

[50] B. E. Schmidt, A. Hage, T. Mans, F. Légaré, and H. J. Wörner, "Highly stable, 54 mJ Yb-InnoSlab laser platform at 0.5 kW average power," *Optics Express* **25**(15), pp. 17549–17555, 2017.

[51] C.-L. Chang, P. Krogen, K.-H. Hong, L. E. Zapata, J. Moses, A.-L. Calendron, H. Liang, C.-J. Lai, G. J. Stein, P. D. Keathley, *et al.*, "High-energy, kHz, picosecond hybrid Yb-doped chirped-pulse amplifier," *Optics Express* **23**(8), pp. 10132–10144, 2015.

[52] J. Rothhardt, C. Rothhardt, M. Müller, A. Klenke, M. Kienel, S. Demmler, T. Elsmann, M. Rothhardt, J. Limpert, and A. Tünnermann, "100 W average power femtosecond laser at 343 nm," *Optics Letters* **41**(8), pp. 1885–1888, 2016.

[53] C. Teisset, M. Schultze, R. Bessing, M. Häfner, J. Rauschenberger, D. Sutter, and T. Metzger, "Picosecond thin-disk regenerative amplifier with high average power

for pumping optical parametric amplifiers," in *CLEO: Science and Innovations*, pp. CTh5C–6, Optical Society of America, 2013.

[54] J. Speiser, "Scaling of thin-disk lasers—influence of amplified spontaneous emission," *JOSA B* **26**(1), pp. 26–35, 2009.

[55] D. Strickland and G. Mourou, "Compression of amplified chirped optical pulses," *Optics Communications* **55**(6), pp. 447–449, 1985.

[56] S. Klingebiel, M. Schultze, C. Y. Teisset, R. Bessing, M. Häfner, S. Prinz, M. Gorjan, D. H. Sutter, K. Michel, H. G. Barros, *et al.*, "220 mJ ultrafast thin-disk regenerative amplifier," in *CLEO: Science and Innovations*, pp. STu4O–2, Optical Society of America, 2015.

[57] C. J. Saraceno, F. Emaury, C. Schriber, M. Hoffmann, M. Golling, T. Südmeyer, and U. Keller, "Ultrafast thin-disk laser with 80 μJ pulse energy and 242 W of average power," *Optics Letters* **39**(1), pp. 9–12, 2014.

[58] J. Brons, V. Pervak, E. Fedulova, D. Bauer, D. Sutter, V. Kalashnikov, A. Apolonskiy, O. Pronin, and F. Krausz, "Energy scaling of Kerr-lens mode-locked thin-disk oscillators," *Optics Letters* **39**(22), pp. 6442–6445, 2014.

[59] D. Bauer, I. Zawischa, D. H. Sutter, A. Killi, and T. Dekorsy, "Mode-locked Yb:YAG thin-disk oscillator with 41 μJ pulse energy at 145 W average infrared power and high power frequency conversion," *Optics Express* **20**(9), pp. 9698–9704, 2012.

[60] H. Fattahi, A. Alismail, H. Wang, J. Brons, O. Pronin, T. Buberl, L. Vámos, G. Arisholm, A. M. Azzeer, and F. Krausz, "High-power, 1-ps, all-Yb:YAG thin-disk regenerative amplifier," *Optics Letters* **41**(6), pp. 1126–1129, 2016.

[61] A. Alismail, H. Wang, J. Brons, and H. Fattahi, "20 mJ, 1 ps Yb:YAG thin-disk regenerative amplifier," *Journal of Visualized Experiments: JoVE* (125), 2017.

[62] O. Pronin and J. Brons, "Kerr-lens mode-locked high-power thin-disk oscillators," in *High Power Laser Systems*, pp. 91–110, BoD–Books on Demand, 2018.

[63] M. Roth, M. Tseitlin, and N. Angert, "Oxide crystals for electro-optic Q-switching of lasers," *Glass Physics and Chemistry* **31**(1), pp. 86–95, 2005.

[64] P. P. Fedorov, A. E. Kokh, and N. G. Kononova, "Barium borate β-BaB_2O_4 as a material for nonlinear optics," *Russian Chemical Reviews* **71**(8), pp. 651–671, 2002.

[65] O. Martinez, J. Gordon, and R. Fork, "Negative group-velocity dispersion using refraction," *JOSA A* **1**(10), pp. 1003–1006, 1984.

[66] E. Treacy, "Optical pulse compression with diffraction gratings," *IEEE Journal of Quantum Electronics* **5**(9), pp. 454–458, 1969.

[67] J. Dörring, A. Killi, U. Morgner, A. Lang, M. Lederer, and D. Kopf, "Period doubling and deterministic chaos in continuously pumped regenerative amplifiers," *Optics Express* **12**(8), pp. 1759–1768, 2004.

[68] T. Metzger, A. Schwarz, C. Y. Teisset, D. Sutter, A. Killi, R. Kienberger, and F. Krausz, "High-repetition-rate picosecond pump laser based on a Yb:YAG disk amplifier for optical parametric amplification," *Optics Letters* **34**(14), pp. 2123–2125, 2009.

[69] M. Grishin, V. Gulbinas, and A. Michailovas, "Bifurcation suppression for stability improvement in Nd:YVO_4 regenerative amplifier," *Optics Express* **17**(18), pp. 15700–15708, 2009.

[70] H. Fattahi, A. Schwarz, X. T. Geng, S. Keiber, D. E. Kim, F. Krausz, and N. Karpowicz, "Decoupling chaotic amplification and nonlinear phase in high-energy thin-disk amplifiers for stable OPCPA pumping," *Optics Express* **22**(25), pp. 31440–31447, 2014.

[71] O. Pronin, M. Seidel, F. Lücking, J. Brons, E. Fedulova, M. Trubetskov, V. Pervak, A. Apolonski, T. Udem, and F. Krausz, "High-power multi-megahertz source of waveform-stabilized few-cycle light," *Nature Communications* **6**, p. 6988, 2015.

[72] T. Südmeyer, F. Brunner, E. Innerhofer, R. Paschotta, K. Furusawa, J. Baggett, T. Monro, D. Richardson, and U. Keller, "Nonlinear femtosecond pulse compression at high average power levels by use of a large-mode-area holey fiber," *Optics letters* **28**(20), pp. 1951–1953, 2003.

[73] O. Heckl, C. Saraceno, C. Baer, T. Südmeyer, Y. Wang, Y. Cheng, F. Benabid, and U. Keller, "Temporal pulse compression in a xenon-filled Kagome-type hollow-core photonic crystal fiber at high average power," *Optics Express* **19**(20), pp. 19142–19149, 2011.

[74] F. Emaury, C. J. Saraceno, B. Debord, D. Ghosh, A. Diebold, F. Gèrôme, T. Südmeyer, F. Benabid, and U. Keller, "Efficient spectral broadening in the 100-W average power regime using gas-filled kagome HC-PCF and pulse compression," *Optics Letters* **39**(24), pp. 6843–6846, 2014.

[75] K. Mak, M. Seidel, O. Pronin, M. Frosz, A. Abdolvand, V. Pervak, A. Apolonski, F. Krausz, J. Travers, and P. S. J. Russell, "Compressing μJ-level pulses from 250 fs to

sub-10 fs at 38-MHz repetition rate using two gas-filled hollow-core photonic crystal fiber stages," *Optics letters* **40**(7), pp. 1238–1241, 2015.

[76] M. Seidel, G. Arisholm, J. Brons, V. Pervak, and O. Pronin, "All solid-state spectral broadening: an average and peak power scalable method for compression of ultrashort pulses," *Optics express* **24**(9), pp. 9412–9428, 2016.

[77] K. Fritsch, M. Poetzlberger, V. Pervak, J. Brons, and O. Pronin, "All-solid-state multipass spectral broadening to sub-20 fs," *Optics letters* **43**(19), pp. 4643–4646, 2018.

[78] I. Pupeza, D. Sánchez, J. Zhang, N. Lilienfein, M. Seidel, N. Karpowicz, T. Paasch-Colberg, I. Znakovskaya, M. Pescher, W. Schweinberger, *et al.*, "High-power sub-two-cycle mid-infrared pulses at 100 MHz repetition rate," *Nature Photonics* **9**(11), p. 721, 2015.

[79] B.-H. Chen, M. Kretschmar, D. Ehberger, A. Blumenstein, P. Simon, P. Baum, and T. Nagy, "Compression of picosecond pulses from a thin-disk laser to 30 fs at 4 W average power," *Optics express* **26**(4), pp. 3861–3869, 2018.

[80] M. Ueffing, S. Reiger, M. Kaumanns, V. Pervak, M. Trubetskov, T. Nubbemeyer, and F. Krausz, "Nonlinear pulse compression in a gas-filled multipass cell," *Optics letters* **43**(9), pp. 2070–2073, 2018.

[81] M. Kaumanns, V. Pervak, D. Kormin, V. Leshchenko, A. Kessel, M. Ueffing, Y. Chen, and T. Nubbemeyer, "Multipass spectral broadening of 18 mJ pulses compressible from 1.3 ps to 41 fs," *Optics letters* **43**(23), pp. 5877–5880, 2018.

[82] H. Fattahi, H. Wang, A. Alismail, G. Arisholm, V. Pervak, A. M. Azzeer, and F. Krausz, "Near-PHz-bandwidth, phase-stable continua generated from a Yb:YAG thin-disk amplifier," *Optics Express* **24**(21), pp. 24337–24346, 2016.

[83] A. Alismail, H. Wang, N. Altwaijry, and H. Fattahi, "Carrier-envelope phase stable, 5.4 μJ, broadband, mid-infrared pulse generation from a 1-ps, Yb:YAG thin-disk laser," *Applied Optics* **56**(17), pp. 4990–4994, 2017.

[84] Y. Yin, A. Chew, X. Ren, J. Li, Y. Wang, Y. Wu, and Z. Chang, "Towards terawatt sub-cycle long-wave infrared pulses via chirped optical parametric amplification and indirect pulse shaping," *Scientific Reports* **7**, p. 45794, 2017.

[85] R. Boyd and B. Masters, "Nonlinear Optics 3rd edn (New York: Academic)," 2008.

[86] R. L. Sutherland, *Handbook of nonlinear optics*, CRC press, 2003.

[87] N. Bloembergen, *Nonlinear optics*, World Scientific, 1996.

[88] H. Fattahi, C. Y. Teisset, O. Pronin, A. Sugita, R. Graf, V. Pervak, X. Gu, T. Metzger, Z. Major, F. Krausz, *et al.*, "Pump-seed synchronization for MHz repetition rate, high-power optical parametric chirped pulse amplification," *Optics Express* **20**(9), pp. 9833–9840, 2012.

[89] A. Schwarz, M. Ueffing, Y. Deng, X. Gu, H. Fattahi, T. Metzger, M. Ossiander, F. Krausz, and R. Kienberger, "Active stabilization for optically synchronized optical parametric chirped pulse amplification," *Optics Express* **20**(5), pp. 5557–5565, 2012.

[90] K.-H. Hong, C.-J. Lai, J. Siqueira, P. Krogen, J. Moses, M. Smrz, L. E. Zapata, and F. X. Kärtner, "Multi-mJ, kHz, 2.1-μm OPCPA for high-flux soft X-ray high-harmonic radiation," in *Quantum Information and Measurement*, pp. JW2A–5, Optical Society of America, 2014.

[91] Y. Deng, A. Schwarz, H. Fattahi, M. Ueffing, X. Gu, M. Ossiander, T. Metzger, V. Pervak, H. Ishizuki, T. Taira, *et al.*, "Carrier-envelope-phase-stable, 1.2 mJ, 1.5 cycle laser pulses at 2.1 μm," *Optics Letters* **37**(23), pp. 4973–4975, 2012.

[92] C. Homann, M. Bradler, M. Förster, P. Hommelhoff, and E. Riedle, "Carrier-envelope phase stable sub-two-cycle pulses tunable around 1.8 μm at 100 kHz," *Optics Letters* **37**(10), pp. 1673–1675, 2012.

[93] S. Hädrich, J. Rothhardt, M. Krebs, S. Demmler, J. Limpert, and A. Tünnermann, "Improving carrier-envelope phase stability in optical parametric chirped-pulse amplifiers by control of timing jitter," *Optics Letters* **37**(23), pp. 4910–4912, 2012.

[94] T. Buberl, A. Alismail, H. Wang, N. Karpowicz, and H. Fattahi, "Self-compressed, spectral broadening of a Yb:YAG thin-disk amplifier," *Optics Express* **24**(10), pp. 10286–10294, 2016.

[95] T. Metzger, C. Y. Teisset, and F. Krausz, "High-repetition-rate picosecond pump laser based on a Yb:YAG disk amplifier for optical parametric amplification," in *Advanced Solid-State Photonics*, p. TuA2, Optical Society of America, 2008.

[96] A. Shirakawa, I. Sakane, and T. Kobayashi, "Pulse-front-matched optical parametric amplification for sub-10-fs pulse generation tunable in the visible and near infrared," *Optics Letters* **23**(16), pp. 1292–1294, 1998.

[97] T.-J. Wang, Z. Major, I. Ahmad, S. A. Trushin, F. Krausz, and S. Karsch, "Ultrabroadband near-infrared pulse generation by noncollinear OPA with angular dispersion compensation," *Applied Physics B* **100**(1), pp. 207–214, 2010.

[98] S.-W. Huang, J. Moses, and F. X. Kärtner, "Broadband noncollinear optical parametric amplification without angularly dispersed idler," *Optics Letters* **37**(14), pp. 2796–2798, 2012.

[99] G. Cerullo, A. Baltuška, O. D. Mücke, and C. Vozzi, "Few-optical-cycle light pulses with passive carrier-envelope phase stabilization," *Laser & Photonics Reviews* **5**(3), pp. 323–351, 2011.

[100] A.-L. Calendron, H. Çankaya, G. Cirmi, and F. X. Kärtner, "White-light generation with sub-ps pulses," *Optics Express* **23**(11), pp. 13866–13879, 2015.

[101] M. Bradler, P. Baum, and E. Riedle, "Femtosecond continuum generation in bulk laser host materials with sub-μJ pump pulses," *Applied Physics B* **97**(3), p. 561, 2009.

[102] P. Tzankov, I. Buchvarov, and T. Fiebig, "Broadband optical parametric amplification in the near UV–VIS," *Optics Communications* **203**(1-2), pp. 107–113, 2002.

[103] L. Canova, S. Kourtev, N. Minkovski, R. Lopez-Martens, O. Albert, and S. M. Saltiel, "Cross-polarized wave generation in the UV region," *Optics Letters* **33**(20), pp. 2299–2301, 2008.

[104] H. Çankaya, A.-L. Calendron, C. Zhou, S.-H. Chia, O. D. Mücke, G. Cirmi, and F. X. Kärtner, "40-μJ passively CEP-stable seed source for ytterbium-based high-energy optical waveform synthesizers," *Optics Express* **24**(22), pp. 25169–25180, 2016.

[105] H. Liang, P. Krogen, R. Grynko, O. Novak, C.-L. Chang, G. J. Stein, D. Weerawarne, B. Shim, F. X. Kärtner, and K.-H. Hong, "Three-octave-spanning supercontinuum generation and sub-two-cycle self-compression of mid-infrared filaments in dielectrics," *Optics Letters* **40**(6), pp. 1069–1072, 2015.

[106] M. Cassataro, D. Novoa, M. C. Günendi, N. N. Edavalath, M. H. Frosz, J. C. Travers, and P. S. J. Russell, "Generation of broadband mid-IR and UV light in gas-filled single-ring hollow-core PCF," *Optics Express* **25**(7), pp. 7637–7644, 2017.

[107] A. L. Cavalieri, E. Goulielmakis, B. Horvath, W. Helml, M. Schultze, M. Fieß, V. Pervak, L. Veisz, V. Yakovlev, M. Uiberacker, *et al.*, "Intense 1.5-cycle near infrared laser waveforms and their use for the generation of ultra-broadband soft-x-ray harmonic continua," *New Journal of Physics* **9**(7), p. 242, 2007.

[108] W. Schweinberger, A. Sommer, E. Bothschafter, J. Li, F. Krausz, R. Kienberger, and M. Schultze, "Waveform-controlled near-single-cycle milli-joule laser pulses generate sub-10 nm extreme ultraviolet continua," *Optics Letters* **37**(17), pp. 3573–3575, 2012.

[109] A. Buck, M. Nicolai, K. Schmid, C. M. Sears, A. Sävert, J. M. Mikhailova, F. Krausz, M. C. Kaluza, and L. Veisz, "Real-time observation of laser-driven electron acceleration," *Nature Physics* **7**(7), p. 543, 2011.

[110] H. Zhong, N. Karpowicz, and X.-C. Zhang, "Terahertz emission profile from laser-induced air plasma," *Applied Physics Letters* **88**(26), p. 261103, 2006.

[111] D. Herrmann, L. Veisz, R. Tautz, F. Tavella, K. Schmid, V. Pervak, and F. Krausz, "Generation of sub-three-cycle, 16 TW light pulses by using noncollinear optical parametric chirped-pulse amplification," *Optics Letters* **34**(16), pp. 2459–2461, 2009.

[112] S. Adachi, H. Ishii, T. Kanai, N. Ishii, A. Kosuge, and S. Watanabe, "1.5 mJ, 6.4 fs parametric chirped-pulse amplification system at 1 kHz," *Optics Letters* **32**(17), pp. 2487–2489, 2007.

[113] S. Adachi, N. Ishii, T. Kanai, A. Kosuge, J. Itatani, Y. Kobayashi, D. Yoshitomi, K. Torizuka, and S. Watanabe, "5-fs, multi-mJ, CEP-locked parametric chirped-pulse amplifier pumped by a 450-nm source at 1 kHz," *Optics Express* **16**(19), pp. 14341–14352, 2008.

[114] Y. Yin, J. Li, X. Ren, K. Zhao, Y. Wu, E. Cunningham, and Z. Chang, "High-efficiency optical parametric chirped-pulse amplifier in BiB_3O_6 for generation of 3 mJ, two-cycle, carrier-envelope-phase-stable pulses at 1.7 μm," *Optics Letters* **41**(6), pp. 1142–1145, 2016.

[115] J. Rothhardt, S. Demmler, S. Hädrich, J. Limpert, and A. Tünnermann, "Octave-spanning OPCPA system delivering CEP-stable few-cycle pulses and 22 W of average power at 1 MHz repetition rate," *Optics Express* **20**(10), pp. 10870–10878, 2012.

[116] C. Manzoni and G. Cerullo, "Design criteria for ultrafast optical parametric amplifiers," *Journal of Optics* **18**(10), p. 103501, 2016.

[117] D. Brida, C. Manzoni, G. Cirmi, M. Marangoni, S. Bonora, P. Villoresi, S. De Silvestri, and G. Cerullo, "Few-optical-cycle pulses tunable from the visible to the mid-infrared by optical parametric amplifiers," *Journal of Optics* **12**(1), p. 013001, 2009.

[118] G. Cerullo and S. De Silvestri, "Ultrafast optical parametric amplifiers," *Review of scientific instruments* **74**(1), pp. 1–18, 2003.

[119] V. G. Dmitriev, G. G. Gurzadyan, and D. N. Nikogosyan, *Handbook of nonlinear optical crystals*, vol. 64, Springer, 2013.

[120] G. Arisholm, "General numerical methods for simulating second-order nonlinear interactions in birefringent media," *JOSA B* **14**(10), pp. 2543–2549, 1997.

[121] T. Amotchkina, H. Fattahi, Y. A. Pervak, M. Trubetskov, and V. Pervak, "Broadband beamsplitter for high intensity laser applications in the infra-red spectral range," *Optics Express* **24**(15), pp. 16752–16759, 2016.

[122] D. Zhang, Y. Kong, and J.-y. Zhang, "Optical parametric properties of 532-nm-pumped beta-barium-borate near the infrared absorption edge," *Optics Communications* **184**(5-6), pp. 485–491, 2000.

[123] K. Kato, "Temperature-tuned 90° phase-matching properties of LiB_3O_5," *IEEE Journal of Quantum Electronics* **30**(12), pp. 2950–2952, 1994.

[124] H. Fattahi, "Regenerative amplifiers," in *Third-generation femtosecond technology*, pp. 73–86, Springer, 2016.

[125] Z. Zheng, A. M. Weiner, K. R. Parameswaran, M.-H. Chou, and M. M. Fejer, "Femtosecond second-harmonic generation in periodically poled lithium niobate waveguides with simultaneous strong pump depletion and group-velocity walk-off," *JOSA B* **19**(4), pp. 839–848, 2002.

[126] D. E. Zelmon, D. L. Small, and D. Jundt, "Infrared corrected Sellmeier coefficients for congruently grown lithium niobate and 5 mol.% magnesium oxide–doped lithium niobate," *JOSA B* **14**(12), pp. 3319–3322, 1997.

[127] C. Manzoni, O. D. Mücke, G. Cirmi, S. Fang, J. Moses, S.-W. Huang, K.-H. Hong, G. Cerullo, and F. X. Kärtner, "Coherent pulse synthesis: towards sub-cycle optical waveforms," *Laser & Photonics Reviews* **9**(2), pp. 129–171, 2015.

[128] G. M. Rossi, R. E. Mainz, G. Cirmi, Y. Yang, O. D. Mücke, and F. X. Kärtner, "Orthogonal control for stable parallel waveform synthesis," in *Nonlinear Optics*, pp. NF2A–6, Optical Society of America, 2017.

[129] S.-W. Huang, G. Cirmi, J. Moses, K.-H. Hong, S. Bhardwaj, J. R. Birge, L.-J. Chen, I. V. Kabakova, E. Li, B. J. Eggleton, *et al.*, "Optical waveform synthesizer and its application to high-harmonic generation," *Journal of Physics B: Atomic, Molecular and Optical Physics* **45**(7), p. 074009, 2012.

[130] R. E. Mainz, G. M. Rossi, G. Cirmi, Y. Yang, O. D. Mücke, and F. X. Kärtner, "High-dynamic-range arrival time control for flexible, accurate and precise parametric sub-cycle waveform synthesis," *Optics Express* **25**(4), pp. 3052–3068, 2017.

[131] M. Porer, J.-M. Ménard, and R. Huber, "Shot noise reduced terahertz detection via spectrally postfiltered electro-optic sampling," *Optics Letters* **39**(8), pp. 2435–2438, 2014.

[132] W. Schweinberger, L. Vamos, J. Xu, S. A. Hussain, C. Baune, S. Rode, and I. Pupeza, "Interferometric delay tracking for low-noise Mach-Zehnder-type scanning measurements," *Optics Express* **27**(4), pp. 4789–4798, 2019.

[133] F. F. Jobsis, "Noninvasive, infrared monitoring of cerebral and myocardial oxygen sufficiency and circulatory parameters," *Science* **198**(4323), pp. 1264–1267, 1977.

[134] N. L. Andrews, A. G. MacLean, J. E. Saunders, J. A. Barnes, H.-P. Loock, M. Saad, C. Jia, K. Ramaswamy, and L. R. Chen, "Quantification of different water species in acetone using a NIR-triple-wavelength fiber laser," *Optics Express* **22**(16), pp. 19337–19347, 2014.

[135] H.-W. Wang, N. Chai, P. Wang, S. Hu, W. Dou, D. Umulis, L. V. Wang, M. Sturek, R. Lucht, and J.-X. Cheng, "Label-free bond-selective imaging by listening to vibrationally excited molecules," *Physical Review Letters* **106**(23), p. 238106, 2011.

[136] C. Pasquini, "Near infrared spectroscopy: fundamentals, practical aspects and analytical applications," *Journal of the Brazilian Chemical Society* **14**(2), pp. 198–219, 2003.

[137] R. G. Brewer and R. Shoemaker, "Optical free induction decay," *Physical Review A* **6**(6), p. 2001, 1972.

[138] Y. Ozaki, W. F. McClure, and A. A. Christy, *Near-infrared spectroscopy in food science and technology*, John Wiley & Sons, 2006.

[139] H. W. Siesler, Y. Ozaki, S. Kawata, and H. M. Heise, *Near-infrared spectroscopy: principles, instruments, applications*, John Wiley & Sons, 2008.

[140] J. R. Ferraro, *Introductory raman spectroscopy*, Elsevier, 2003.

[141] I. E. Gordon, L. S. Rothman, C. Hill, R. V. Kochanov, Y. Tan, P. F. Bernath, M. Birk, V. Boudon, A. Campargue, K. Chance, *et al.*, "The HITRAN2016 molecular spectroscopic database," *Journal of Quantitative Spectroscopy and Radiative Transfer* **203**, pp. 3–69, 2017.

[142] G. Wave, "Measuring water concentration in solvents with NIR spectroscopy," 2018. Online; accessed 25^{th} October 2019.

[143] D. Laage, T. Elsaesser, and J. T. Hynes, "Water dynamics in the hydration shells of biomolecules," *Chemical Reviews* **117**(16), pp. 10694–10725, 2017.

[144] A. Kuzmenko, "Kramers-Kronig constrained variational analysis of optical spectra," *Review of scientific instruments* **76**(8), p. 083108, 2005.

[145] K. A. Whittaker, J. Keaveney, I. G. Hughes, and C. S. Adams, "Hilbert transform: Applications to atomic spectra," *Physical Review A* **91**(3), p. 032513, 2015.

Acknowledgements

All praise belongs to Almighty Allah for giving me the blessing and the eventuality to accomplish this work. This accomplishment would not have been attained without the assist of many individuals. In what follows, I would like to drop few lines to express my eternal gratitude for all of them.

Foremost, I would like to express my deepest gratitude to Prof. Ferenc Krausz, my supervisor, who gave me the privilege to do this research, provided me with an invaluable guidance throughout my PhD journey, and allowed me access to the massive facilities in the Laboratory for Extreme Photonics (LEX Photonics).

My gratitude is extended to Dr. Hanieh Fattahi, my direct supervisor, for her continuous support, constructive suggestions, and insightful ideas. The positive research environment provided by you has been greatly appreciated.

My infinite gratitude goes to my group members, Haochuan Wang, Gaia Barbiero, Najd Altwaijry, Maximilian Wendl, and Theresa Buberl, for their assistance and cooperation throughout this project. It was an honor and a privilege to work with them.

Haochuan Wang, Gaia Barbiero, and Najd Altwaijry, thank you all very much; your help in proofreading this thesis has been invaluable. Special thanks goes to Dr. Thomas Nubbemeyer for his help in writing the Zusammenfassung.

I am overwhelmed with gratitude to Dr. Zsuzsanna Major and Dr. Helena Barros for your former direct supervision.

My endless gratitude goes to my colleagues: Dr. Thomas Nubbemeyer, Martin Kaumanns, Florian Saran, Dr. Jonathan Brons, Dr. Martin Gorjan, Dr. Lénárd Vámos, Dr. Oleg Pronin, Dr. Nicholas Karpowicz, Dr. Wolfgang Schweinberger, and Syed Ali Hussain for their contribution in this project.

I wish to express my thanks to Dr. Gunnar Arisholm, Dr. Wolfgang Schweinberger, and Dr. Moritz Ueffing for sharing their codes with me.

My deep thanks go to Dr. Vladimir Pervak and Dr. Tatiana Amotchkina for designing and fabricating the chirped mirrors and the broadband beam splitters.

I would like to acknowledge the generous sponsorship received from King Saud University. My vehement gratitude is extended to Dr. Abdallah Azzeer and Dr. Saad Aldawood for all the support you gave.

I express my appreciation to my Saudi friends in Munich, especially Dr. Abdulaziz Alhazmi and Suliman Algomiz, for all delightful memories.

To my deceased father and my mother, thank you all for your tender caring and kindness. Your spiritual support brightens my life. I also express my extreme gratitude to my brothers and sisters for their support and cordiality.

My wholehearted appreciation is expressed to my wife, Hayat, for her love. Words are powerless to express my gratitude for your infinite support and constant encouragement. Your sacrifice will not be forgotten. My heartfelt gratitude is extended to my charming sons, Mohammed and Suliman. Please accept my sincere apologies for spending less time with you during my study. You deserve warm hugs!